ScuDo
Scuola di Dottorato ~ Doctoral School
WHAT YOU ARE, TAKES YOU FAR

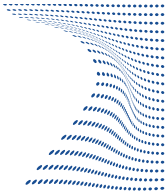

Doctoral Dissertation
Doctoral Program in Energetics (34^{th} cycle)

Multi-physics modelling of liquid metals in Advanced Nuclear Systems

Domenico Valerio
* * * * *

Supervisors
Prof. Sandra Dulla, Supervisor
Prof. Roberto Bonifetto, Co-supervisor

Doctoral Examination Committee:
Dr. Alessandro Del Nevo, ENEA Centro Ricerche Brasimone
Dr. Ion Cristescu, Karlsruhe Institute of Technology
Dr. Antonio Froio, Politecnico di Torino
Dr. Francesco Lodi, ENEA Bologna
Prof. Lluis Batet Miracle, Universitat Politècnica de Catalunya

Politecnico di Torino
July, 19^{th}

I hereby declare that, the contents and organisation of this dissertation constitute my own original work and does not compromise in any way the rights of third parties, including those relating to the security of personal data.

. . . . . .

Domenico Valerio
Turin, July, 19th

Summary

The purpose of this thesis is to discuss the use of liquid metals in next-generation nuclear fission and fusion reactors. Liquid metals can be employed as coolant (fission machines) or as coolant/breeder/carrier for the tritium exploitation (in future fusion rectors), since they present good thermo-physical and nuclear properties with respect to water. Due to the complexity of the systems where liquid metals have to be used, suitable multi-physics tools must be developed to correctly retrieve the inherent physical aspects of their employment. Several European initiatives are today supporting the research and development of this tools, as for instance, the EUROfusion consortium and the PASCAL project (where the FALCON consortium is heavily involved). Thus, the work here presented aims to verify, test and develop tools and new models for the multi-physics assessment of advanced nuclear system based on liquid metals. For this reason, two areas of activity are discussed: modelling of Liquid Metal-Cooled Reactors for future Generation IV reactors within the context of reactor physics and thermal-hydraulics assessments, and modelling of radioisotope transport in liquid metals in fusion systems.

The first part of this thesis regards the use of liquid metals in future fission nuclear reactors. The activities have been carried on with the scope to pursue the verification activities of the FRENETIC code, a multi-physics tool that has been being developed in the last years at Politecnico di Torino. Currently, the FALCON consortium and the PASCAL project are supporting the design of the ALFRED reactor in order to exploit Lead Fast Reactors technology. As a consequence, the benchmark of FRENETIC has been performed on the ALFRED core, analysing both steady state and transient coupled scenarios. To accomplish this, a temperature-dependent cross section library has been built using the Monte Carlo code Serpent-2. As second verification activities for the neutronic module, FRENETIC has been benchmarked against the SIMMER code using the same set cross sections calculated by Serpent-2.

With the aim to broaden the application domain of FRENETIC, a methodology to generate the data to simulate also secondary contributions to the total thermal power as photon heat deposition and the KERMA of neutrons has been developed. The generation of photon data (i.e, the attenuation coefficients, the deposited energy per particles, the cross section of (n, γ) interactions) has been carried out

to retrieve also the thermal power due to KERMA of neutrons and photons by a high-level detailed Serpent-2 model of the EBR-2 Sodium-cooled Fast Reactor. A previous benchmark coordinated by the IAEA on the EBR-2 reactor (SHRT-45R) has been chosen, to test also several strategies of spatial homogenisation in Serpent-2 due to the high complexity of the core configuration.

As final activity in the framework of the European project PASCAL, a preliminary design of a design-oriented-code, EFIALTE, for the deformed fuel bundle in Lead Fast Reactors has been assessed. EFIALTE is part of the suite of design-oriented-code (TEMIDE, TIFONE, ANTEO+), whose development is currently coordinated by ENEA Bologna. Its application encompasses the End-Of-Life condition and/or the accidental scenario of a fuel rod displacement. Specifically, the core solver of this code has been derived and implemented, solving the mass and momentum conservation equations - including the transverse momentum equation, accounting for possibly different pressures among sub-channels located at a given axial location.

Concerning the fusion-related activities, the design of an extractor of tritium from the PbLi by suitable numerical models to assess the tritium permeation has been carried out. The PbLi is the liquid metal breeder which is foreseen in one of the concepts of the WCLL Breeding Blanket for the future EU DEMO reactor. Several technologies are being investigated, and one of the promising solutions is based on Permeator Against Vacuum (PAV) technology. The first part of the work consists in the development of a new model for the evaluation of the permeated flux from the carrier (the PbLi) by means of an extractor where a pressure drop is established across a metallic membrane. Two regimes of permeation have been focused: the Surface-Limited, when the permeation is strongly conditioned by surface effects of the membrane, as the recombination and dissociation. The other one is called Diffusion-Limited and it is established when the the surface effects are faster than the diffusion in the bulk of membrane. The model has been developed starting from previous works and the physics modelling has been extended to the case of liquid-membrane-vacuum treating the transport from the liquid metal bulk towards the wet side of the membrane as the source of permeation.

The above-mentioned model has been used to perform efficiency analyses on the PAV mock-up that has been designed starting from the constraints of geometry prescribed in TRIEX-II facility (ENEA Brasimone). An experimental campaign was foreseen to test the technology with hydrogen. Unfortunately, due to the outbreak of COVID-19 pandemic in the 2020, the tests have been postponed beyond the ending of this PhD. The design of the mock-up has been conducted by a preliminary sizing of the vessel and holed plate where the pipes (the membrane) are located. The assessment have been performed with analytical formulas for thin shell and plates, and then verified with a set of FEM analyses considering the operational and accidental conditions. A set of CFD analyses have been assessed to study the effects of the mass flow repartition (i.e, the turbulence level in each single pipe) on

the extraction efficiency, as well as the surface conditions.

Finally, the application of the developed model has been exploited on the extractor up to EU DEMO scale. The Tritium Extraction and Removal System has been sized to achieve the required extraction efficiency foreseen in DEMO with a methodology to design the membrane, the vessel encumbrance and the number of pipes has been developed. The sizing have been carried on by changing the operative conditions, in order to find the best solution for the permeation.

Results for the fission part have shown good agreement for the activity on the FRENETIC code. On the ALFRED reactor, the benchmark between Serpent-2 and the deterministic tool has highlighted an improvement of the accordance (k_{eff} and thermal power distribution) when the geometry simulated in FRENETIC corresponds to the one of the Monte Carlo simulation. Furthermore, the verification of the neutronic solver of FRENETIC with respect to the SIMMER core has shown good results in terms of neutronic flux solution, showing the good capability of FRENETIC to simulate the neutronic flux with the diffusion theory. Regarding the EBR-2 reactor, the correctness of the methodology for the generation of photon data, as well as the spatial homogenisation optimisation, has been demonstrated. The thermal fission power and the neutron KERMA power have been correctly retrieved. On the contrary, the photon flux was not well reproduced by FRENETIC, and this discrepancy arose from the incapability of Serpent-2 to provide the photons multiplicity production which led to an underestimation of photon flux. Concerning EFIALTE, the solver has been tested with promising results on a simple undeformed test case: the exchange of flow rate is correctly retrieved when a proper driver is provided as boundary condition.

For the fusion-related activities, the new model for the permeation has been compared with another permeation model (purely diffusion-limited), showing great accordance between the evaluation of the extraction efficiency. The model is capable to encompass both surface-limited and diffusion-limited permeation regimes when the respective set of permeation properties are introduced in the model. As a consequence, the evaluation of extraction efficiency of the mock-up based on the PAV technology has been carried out together with its design. The study has also shown the main effects due to the main variables (membrane condition, temperature, pressure of H/T and PbLi mass flow rate) on the permeation efficiency. With this information, the design has been extended to EU DEMO scale, where the operating conditions of the extractor have been selected by means of a methodology developed to be compliant with the prescribed constraints of the design of extraction system.

Acknowledgements

I would like to thank from the deep of my heart my parents and my all family, for giving me the courage and incommensurable support to take on this challenge during these hard three years, especially my brother Andrea, the one that during this last period was by my side night and day to lighten my life.

Thanks to Maria Cristina and Domenico simply for loving me, for being in my life, for their encouragement to *follow my dreams*, because *indeed there will be time* to be who you have to be.

Thanks to the *Fellowship of the Hexagon*, alias Nicolò and Giuseppe for giving me the best research team ever, for sharing together the difficulties and the happiness of our work, the passion, the idea, the friendship, the hard moments.

Thanks to Sandra e Roberto, not only for their institutional supervision of my PhD program, but for their comprehension of my hard moments and their support for my personal growth.

Thanks to Andrea and Antonio for being my Friends also outside the walls of the office, for all the advice, their moral support, their knowledge and the laughter we spent together.

Thanks to Mrs. Elisabeth Rizzotti, Mr. Stefano Buono and Eng. Luciano Cinotti for the trust and the possibility to conclude this PhD program in the best way, and for the opportunity to join the project of *new*cleo. Thanks to all the *new*cleo family for their support during these months, in particular the Core Design team. Thanks to Nicolò for his gift with which *everything started*, and for being my Friend.

Thanks to Edoardo, the best *osteoguy* I have ever known, for always being present, for giving me his experience, his smile in the darkest moments and in the most serious ones. Thanks for being who you are.

To all of you, I would like to conclude with a sentence taken from my favourite book, *Canone Inverso*:

Ma chissà poi perché le parlo di queste cose, è da sciocchi parlare delle possibilità mancate, quando si sa che la vita ha una sola strada: quella che abbiamo scelto.

To all of you.
Grazie.

Alle mie nonne Elena e Mimmi, che col loro sorriso hanno innalzato la mia fantasia oltre il cielo.

Contents

List of Tables

List of Figures

Acronyms

ALFRED Advanced Lead-cooled Fast Reactor European Demonstrator. 2, 3, 9, 10, 12–18, 20, 21, 23–27, 29, 31–33, 36, 38–40, 43, 45, 111, 129, 195, 196

ANL Argonne National Laboratory. 50, 51, 55–58, 65, 69, 70, 104

BB Breeding Blanket. 4, 183, 184, 187, 194, 198

BOL Begin-Of-Life. 4, 13, 23, 112, 131, 196

CFD Computation Fluid Dynamic. 5, 159, 161, 163, 167, 168, 181, 196, 199

CR Control Rods. 12, 13, 17, 32, 33, 38, 41–44

CRP Coordinate Research Program. 48, 64, 108, 197

DCLL Dual Coolant Lithium Lead. 184

DL Diffusion-Limited. 138, 140, 145, 152, 153, 155–157, 173, 183, 193, 194, 196, 198, 199

DLM Diffusion-Limited Model. 153–156, 185, 191, 198

DOC Design-Oriented Code. 3, 4, 111, 131, 195, 198

EBR Experimental Breeder Reactor. 2

EBR-2 Experimental Breeder Reactor-2. 2, 48, 49, 52, 54, 55, 59, 62–64, 66, 67, 70–72, 75–77, 82, 84–86, 90, 91, 94–96, 100, 101, 105, 107, 108, 195, 197

EFIALTE Esame di Fasci Irregolari per Analisi Locale TErmoidraulica. 3, 4, 111, 112, 116, 118, 128, 131, 195, 196, 198

EOL End-Of-Life. 3, 112, 131, 198

EU DEMO EUropean DEMOnstrator. 4, 5, 135, 136, 139, 140, 156, 159, 161, 183–187, 193–196, 198, 199

FA Fuel Assembly. 3, 4, 10–13, 18, 22–30, 34–36, 40, 42–44, 89, 93, 96, 98, 100, 129, 131, 195

FALCON Fostering ALFRED Collaboration. 2, 195

FEM Finite Element Method. 165, 170, 181, 196, 199

FR Fast Reactor. 48, 195, 197

FRENETIC Fast REactor NEutronic/Thermal-hydraulIc Code. 3, 4, 9–11, 13, 15, 17–19, 21–32, 36–38, 40, 41, 43–45, 47, 48, 55, 57, 58, 81–83, 88–93, 95–109, 195–197

GCU Group Constant Universe. 55, 88

GIF Generation-IV International Forum. 2, 9

GLC Gas Liquid Contactor. 5, 135, 156

HFD High-Flow Driver. 49, 50

HFP Hot Full Power. 10, 29–31

HLMCR Heavy Liquid Metal Cooled Reactor. 2, 129

HWCR High Worth Control Rod. 49, 50, 52, 60, 67, 72, 73, 76, 80, 81

HWD Half-Worth Driver. 49, 50, 52

HZP Hot Zero Power. 10, 16, 24, 26, 38, 197

IB InBoard. 187

IE Initiating Event. 9, 31, 34

IF Inner Fuel. 18

KERMA Kinetic Energy Released in MAtter. 47, 88, 89, 106, 108, 109, 197

LFP Lumped-Fission-Product. 64, 65

LFR Lead Fast Reactor. 2, 12, 129, 131, 195, 196, 198

LM Liquid Metal. 1–3, 5, 10, 160, 161, 195, 196, 198

LMCR Liquid Metal Cooled Reactor. 1–4, 45, 48, 195, 196

LOFA Loss Of Flow Accident. 31, 36, 48, 108

LWR Light Water Reactor. 12

MMS Method of the Manufactured Solution. 149

MOX Mixed Oxide Fuel. 2

NE NEutronic. 2, 3, 9, 11–13, 19, 21, 25, 26, 28, 34, 35, 37, 45, 48, 89, 109, 196, 197

OB OutBoard. 187, 194

OF Outer Fuel. 18

OoA Order-of-Accuracy. 149, 156

PASCAL Proof of Augmented Safety Conditions in Advanced Liquid-Metal-Cooled Systems. 2–4, 9, 111, 112, 129, 195, 196, 198

PAV Permeator Against Vacuum. 5, 135–137, 139, 149, 156, 157, 159–163, 174, 177, 178, 181, 183–188, 190, 192–194, 196, 198, 199

PbLi Lead-Lithium. 4, 5, 135–140, 144–146, 148–150, 152, 153, 155, 156, 159–163, 165, 166, 168, 170–175, 177, 181, 183–185, 187–189, 191, 192, 194, 196, 198, 199

PH PHotonic. 3, 48, 89, 109, 195, 197

RSD Relative Standard Deviation. 20, 80

SA Sub-Assembly. 38, 40, 45, 49, 50, 52–58, 60, 62, 63, 65, 67–70, 72, 75, 78, 85, 86, 96, 108

SC Sub-Channel. 3, 4, 111–121, 123–126, 128, 129, 131, 198

SF Safety Factor. 164

SFR Sodium Fast Reactor. 2, 3, 108, 195

SHRT-17 Shutdown Heat Removal System 17. 197

SHRT-45R Shutdown Heat Removal System 45R. 48, 49, 51–55, 59, 64, 78, 108, 109, 197

SIU Super Imposed Universe. 75–77, 84, 86

SL Surface-Limited. 138–141, 146, 148, 154–157, 173, 177, 183, 191, 193, 194, 196, 198, 199

SLM Surface-Limited Model. 154, 155, 185, 191

SMR Small Modular Reactor. 12

SR Safety Rod. 12, 13, 18, 31, 34, 35, 50, 52, 53, 60, 73, 76, 80, 81

TERS Tritium Extraction and Removal System. 4, 5, 135, 136, 139, 140, 159, 174, 183–187, 193, 194, 196, 199

TH Thermal-Hydraulic. 2–4, 9, 11, 12, 21, 25, 28, 31, 34, 45, 50, 109, 163, 196

TM Thermo-Mechanic. 2, 5, 161, 163, 170

VLC Vacuum Liquid Contactor. 5, 135

VV Verification&Validation. 3, 9

WCLL Water Cooled Lithium Lead. 4, 183, 184, 187, 193, 194, 198

Chapter 1

Introduction

> *Handle so, daß die Maxime deines Willens jederzeit zugleich als Prinzip einer allgemeinen Gesetzgebung gelten könne*
>
> *Act in such a way that the maxim of your will could always hold at the same time as a principle of a universal legislation*
>
> – Immanuel Kant, Kritik der praktischen Vernunft

The purpose of this thesis is to discuss the use of Liquid Metals (LMs) in next-generation nuclear fission and fusion reactors. The general objective of this effort is to develop, verify and apply computational tools to the design and analysis of inherently multi-physics nuclear systems based onLMs.

Two areas of activity are discussed: modelling of Liquid Metal Cooled Reactors (LMCRs) for future Generation-IV reactors within the context of reactor physics and thermal-hydraulics assessments, and modelling of radioisotope transport in LM in fusion systems. These two lines of activity are discussed in different sections of the thesis.

This introductory chapter offers a brief introduction and rationale for each topic, as well as an explanation of the work objective and a perspective on the important outcomes acquired.

1.1 Liquid Metal-cooled Fast Reactors

1.1.1 Background and motivation

The Generation-IV International Forum (GIF) initiative [1] is presently pursuing the development of LMCRs. GIF promotes the development of sustainable, safe, and cost-effective nuclear reactors that minimise the creation of radioactive waste with a long half-life and reduce the danger of proliferation. Three of the six selected designs have a fast neutron spectrum, which enables the long-term radiotoxicity of nuclear waste to be reduced and the fuel usage efficiency to be increased. Two of these three selected technologies are based on LMs.

The first one implies *sodium* as coolant, namely Sodium Fast Reactors (SFRs), since the sodium presents several thermo-physical properties particularly suitable for the GIF proposal, as high thermal conductivity and low corrosion power. Moreover, the SFR technology can also exploit the use of Mixed Oxide Fuel (MOX) [2] since the coolant has also a good neutronic economy, allowing the possibility to have compact reactors and high power densities. Several sodium-cooled reactors were already commercialised from the 1970s up to 1990s for electricity production (Phénix and Super-Phénix in France), and experimental campaigns to support safety studies and development of Fast Reactors were carried on in research reactors (Experimental Breeder Reactor (EBR) and Experimental Breeder Reactor-2 (EBR-2) in USA) during the same period.

The second concept foresees the use of *lead*, which falls within the category of Heavy Liquid Metal Cooled Reactors (HLMCRs). HLMCRs have increased inherent safety features with respect to SFRs (the lead is inert), together with the potential to achieve a higher thermodynamic efficiency of the plant due to the larger margin to boiling. In this framework, the most important European initiatives now underway is the Fostering ALFRED Collaboration (FALCON) international consortium, where industries as ANSALDO Nucleare are also involved. FALCON is designing the Advanced Lead-cooled Fast Reactor European Demonstrator (ALFRED) [3], and the Proof of Augmented Safety Conditions in Advanced Liquid-Metal-Cooled Systems (PASCAL) project [4] is currently ongoing to develop computational tools and design experimental facilities to support ALFRED construction. Italy is heavily involved in PASCAL, due to the participation of universities belonging to CIRTEN consortium and research institutions as ENEA which has over 15 years of experience on lead technology.

Design of LFR cores require a multi-physics approach that must be able to deal with a large number of physical aspects coming from NEutronic (NE), Thermal-Hydraulic (TH) and Thermo-Mechanic (TM). To carry out this multi-disciplinary task, especially during the conceptual and design phase, fast computational tools are required to take into account all the safety criteria and to perform preliminary optimisation processes to respect the above-mentioned constraints. With this

mindset, in the last years Politecnico di Torino has been developing a computational tool for simulating normal operation and accidental scenarios in LMCRs, Fast REactor NEutronic/Thermal-hydraulIc Code (FRENETIC). the FRENETIC code is a multi-physics tool [5] that can perform coupled (NE+TH) steady state and transient analyses at full-core level. The TH module of the code has been already verified and validated against experimental data, and Verification&Validation (VV) activities are still ongoing for the NE module and for coupled calculations.

Another class of tools which support the designer during the early stage of the design phase are the so-called Design-Oriented Codes (DOCs). These codes are able to rapidly perform simulations in a well defined application domain, in order to suggest the best solution to optimise performance and the relationship between the interested system and the others. An example of DOC is ANTEO+ [6], a TH Sub-Channel (SC) code for the simulation of a single FA. One of the goals of the PASCAL project is the development of a DOC for the assessment of the TH of a deformed FA, a condition occurring e.g. during an accidental scenario or in the End-Of-Life (EOL) condition, when the Fuel Assembly (FA) has experienced sufficient irradiation to be deformed due to swelling of fuel. This new code, namely Esame di Fasci Irregolari per Analisi Locale TErmoidraulica (EFIALTE), is intended to perform the same analysis of ANTEO+ by also including the transverse mixing among SCs in deformed geometry.

1.1.2 Aim of the fission-related activities

This part of the work addresses the modelling of LMs for the LMCRs. Specifically, verification activities of the FRENETIC code are further carried out. To this aim, two main test-cases are studied. In the first one, a multi-physics benchmark on the ALFRED core is carried on, comparing the results calculated by FRENETIC in a coupled scenario (NE+TH) with respect to the Monte Carlo code Serpent-2 [7], which is regarded as a reference. A systematic approach is followed, in order to improve the agreement between the two tools when thermal feedback are also considered. To accomplish the verification of the NE module of FRENETIC on the ALFRED case, the code is compared with the SIMMER code [8] in a pure NE scenario, in order to assess the accuracy of the multi-group diffusion solution with respect to the transport calculation.

To complete the activities on FRENETIC, the possibility to simulate also secondary contributions to the generated thermal power inside a fission reactor such as the heat deposited by γ rays is investigated. To achieve this objective, the diffusion modelling of the NE module is adopted also for photons, and a second benchmark between the FRENETIC code and Serpent-2 (NE+PHotonic (PH)) on the test case of the EBR-2 (SFR) is presented. To accomplish this activity and therefore enlarge the application domain of the tool, the development of a methodology for the generation of effective photon data to test the capability of the PH module of

FRENETIC is needed, to correctly simulate the photon flux and the related heat deposition together with the fission power.

In the context of the development of DOCs, a multi-physics approach can be also adopted to quickly assess critical operational and/or incidental conditions. The development of the EFIALTE code, in the framework of the PASCAL project, is aimed to complement the DOCs suite of ENEA for LMCRs to be used during the design phase, before going into detailed verification analyses. With respect to ANTEO+, which is able to verify the nominal operation condition (or the BOL condition) of the FA, the target of this tool is to complete the analysis by the modelling of the deformed geometry (given as input), and on this geometry to perform the calculation of the diversion mass flow rate due to momentum difference among the SCs. These exchanges cause net mass fluxes among the gaps of SCs, therefore a suitable model of these phenomena is necessary to perform an accurate TH simulation of a deformed bundle.

1.2 Liquid metal in nuclear fusion reactors

1.2.1 Background and motivation

Pursuing fusion energy is motivated by the need of large-scale sustainable and predictable low-carbon electricity generation in a projected future world with significantly increasing global electricity demand. Nowadays the development of fusion technology is supported by EUROfusion consortium [9] and the most promising fusion reactor concept is based of the *tokamak*, in which a ionised gas (the *plasma*) reacts to establish the fusion reaction by means of a magnetic field containment.

The most promising nuclear fusion reaction to be exploited for electricity production involves deuterium and tritium as reactants [10]. While the former can be extracted, e.g., from the seawater, the latter is radioactive with an half-life of ∼12 years [11]. Therefore, it cannot be found in nature in a quantity sufficient for the fuelling of a tokamak.

The EUropean DEMOnstrator (EU DEMO) reactor [12] is expected to generate power by nuclear fusion in the 1950s [13] and show tritium self-sufficiency using a Breeding Blanket (BB) for the production of the tritium on-site [14][15]. The practicality and dependability of the tritium breeding blanket are critical for EU DEMO and commercial power plant operation. Tritium self-sufficiency demands effective breeding and extraction technologies that keep tritium inventories to a minimum. One of the developed BB designs, named the Water Cooled Lithium Lead (WCLL) BB, adopts flowing Lead-Lithium (PbLi) as breeding material. Tritium generated in the BB is subsequently transported out of the blanket by the PbLi mass flow rate and should be removed in a specific part of the PbLi loop called the Tritium Extraction and Removal System (TERS) to close the fuel cycle.

To reduce tritium losses and inventory in the machine, the TERS will be the first subsystem met by the PbLi exiting the reactor. Several technologies are being studied to extract the tritium from the LMs. These concepts of extractor were previously examined in [16], using the Gas Liquid Contactor (GLC) technology [17] (featuring two steps of extraction). Other technologies under consideration include the Vacuum Liquid Contactor (VLC) and the Permeator Against Vacuum (PAV).

The PAV has been recognised as a potential technology for the TERS in the EU DEMO perspective: liquid PbLi containing dissolved tritium will flow through channels defined by a membrane, with vacuum on the other side. Thus, the tritium will cross the membrane and be delivered to the successive stages of the tritium fuel cycle to be reprocessed, that is, combined with deuterium and injected as fuel in the core plasma.

1.2.2 Aim of the fusion-related activities

This part of the work is devoted to the design of the extractor based on the PAV technology, from the mock-up of the permeator to test the technology up to EU DEMO scale TERS. The main task is the assessment of the required membrane length to achieve the nominal extraction efficiency. For the dimensioning of the PAV membrane, a proper estimation of the tritium permeated flux in nominal operating conditions is needed. To perform this estimation, a new numerical model has to be developed in order to deal with all the possible permeation regimes.

After sizing the membrane, a design of the PAV mock-up has to be performed. The target of the analyses is the TM performances to correctly assess the integrity of the extractor during the nominal operating condition and the emergency condition. Moreover, a Computation Fluid Dynamic (CFD) study is necessary to investigate how the PbLi mass flow distribution in the component affects the extraction efficiency.

Finally, with the conclusions of the previous points, the study is extended up to the EU DEMO scale. The aim of the study is to design the extractor where the foreseen constraints for EU DEMO are considered, in terms of pressure drop, encumbrance of the extractor(s) and membrane lengths. The analysis is carried on with a parametric approach, to identify the best solutions among the possible ones to achieve the required extraction efficiency.

Part I

Liquid metal-cooled nuclear fission reactors

Chapter 2

Neutronic benchmarks of the FRENETIC code for the multi-physics analyses of Lead Fast Reactors

The most promising future fission reactor concept proposed by GIF foresees the use of lead as coolant. In the European context, Italy and Roumania are heavily involved in the development of ALFRED. Indeed, the joint European project PASCAL is ongoing to support the development of the ALFRED reactor. On the Italian scenario, research institutions as ENEA and CIRTEN consortium are involved to develop numerical codes for the design and the assessment of safety aspects, using a multi-physics approach. Indeed, in the last years, Politecnico di Torino has been developing a multi-physics code, FRENETIC, where NE and TH parameters are evaluated in a coupled scenario. FRENETIC addresses steady state and transient simulations at full-core level. The transient scenarios are simulated by Initiating Events (IEs) for both physics, with the target to give a fast response to verify and optimise the design of the reactor. The VV activities on FRENETIC have been conducted on the TH module [18], whereas for the NE module is still ongoing. In this chapter two benchmark activities performed on the FRENETIC code are described, both for the verification of the capabilities to assess coupled calculation, and for standalone NE simulations.

The first carried out activity consisted in performing a comparison between the steady-state power distribution calculated by the FRENETIC code with the Monte Carlo code Serpent-2 [7], taken as *reference solution*. The objective is to benchmark the NE module of the FRENETIC code, in order to assess its accuracy and identify possible improvements in the core modelling approximations. The model implemented in Serpent-2 is discussed, following a brief introduction to the ALFRED reactor. After that, the approach used for the effective cross sections

calculations is shown, and the comparison of Serpent-2 and FRENETIC results is provided.

The comparison with Serpent-2 allowed to develop an optimised model for FRENETIC of the ALFRED core. The barrel and the external lead have been modelled, leading to a more satisfying neutronic benchmark in Hot Zero Power (HZP) condition. This new configuration has been further verified for the accuracy also in the presence of thermal-feedback effects, and thus served as an excellent starting point for the safety and stability analyses that are required during the development of the ALFRED design.

In the second part of the benchmark the thermal feedback effects have been taken into account. The calculation is carried out in Hot Full Power (HFP) condition, with the complete geometry of ALFRED implemented in the FRENETIC code. Finally, the results of a steady-state coupled FRENETIC simulations are displayed and compared to the Serpent-2 simulation with an imposed temperature distribution consistent with FRENETIC.

The second benchmark activity addresses a standalone comparison of the NE of FRENETIC against SIMMER [8]. Here the level of discretisation for FRENETIC is deeply studied on the results of the first benchmark activity on the ALFRED rector. The input consistency between the two code is assured by a common set of cross sections calculated by Serpent-2. As for FRENETIC, the methodology used in SIMMER to solve for the thermal fission power is analysed, in order to improve the agreement between the two tools.

The study here reported is part of the works published in [19][20], and it has been performed in collaboration with Eng. Nicolo' Abrate, Dr. Giuseppe Francesco Nallo and Dr. Mattia Massone.

2.1 The FRENETIC code

The FRENETIC code simulates the neutronics and thermal-hydraulics of the reactor core, which is made up of closed hexagonal FAs, using:

- a multi-group diffusion model for neutrons, discretised with a coarse mesh nodal method at the assembly level;
- a 1D advection/diffusion model for the LM flowing within each assembly, assuming no cross-flow among drivers, but considering heat transfer between assemblies

The models and discretisation methods used are aimed at simulating core behaviour under operating and accidental settings in a computationally efficient way. The computational tool development has included a number of validation activities (e.g.,

[18][21]), which have confirmed FRENETIC capabilities and allowed for the identification of some necessary future developments, such as the inclusion of a module for the simulation of photon gamma heat and decay heat deposition [22].

The code is divided into two modules: the NE module solves the neutron flux distribution that provides the thermal energy in each FA using an *ad hoc* nodal technique to solve the time-dependent multi-group diffusion problem. The domain is discretised using a coarse mesh structure, and the flux is integrated inside the under consideration volume to retrieve the thermal power. This module solves a broad system of equations:

$$\begin{cases} \dfrac{1}{v_g}\dfrac{\partial}{\partial t}\phi_g(\mathbf{r},t) = \nabla\cdot(D_g(\mathbf{r},t)\nabla\phi_g(\mathbf{r},t)) - \Sigma_g(\mathbf{r},t)\phi_g(\mathbf{r},t) + \displaystyle\sum_{g'=1}^{G}\Sigma_{gg'}(\mathbf{r},t)\phi_{g'}(\mathbf{r},t) + \\ (1-\beta)\chi_g(\mathbf{r})\displaystyle\sum_{g'=1}^{G}\nu\Sigma_{f_{g'}}(\mathbf{r},t)\phi_{g'}(\mathbf{r},t) + \sum_{i=1}^{R}\chi_{g_i}(\mathbf{r})\lambda_i c_i(\mathbf{r},t) + S_g(\mathbf{r},t), \quad g = 1\dots\mathrm{G} \\ \dfrac{\partial}{\partial t}c_i(\mathbf{r},t) = \beta_i\displaystyle\sum_{g'=1}^{G}\nu\Sigma_{f_{g'}}(\mathbf{r},t)\phi_{g'}(\mathbf{r},t) - \lambda_i c_i(\mathbf{r},t), \qquad i = 1\dots\mathrm{R} \end{cases} \tag{2.1}$$

where R and G indicate, respectively, the delayed neutron precursor families and neutron energy groups.

The TH module solves the temperature distribution throughout the axial length of each FA using 1D modelling. When inter-assembly heat transfer is considered, neighbouring FAs are weakly connected in the radial direction. This 1D+2D technique is based on the research group prior work simulating superconducting magnets for nuclear fusion reactors [23]. The TH module solves the transient 1D mass, momentum, and energy balance implicitly in time for each FA for the z component $v(z,t)$ of the flow velocity and for the lead temperature $T_{Pb}(z,t)$ and pressure $p(z,t)$ pair, using a finer spatial mesh than the NE module. The complete set of equations for this module is available in [5].

Due to the coarser mesh along z of the neutronic module in comparison to the TH solver, two assumptions about the fuel and coolant temperatures are made:

1. the temperature profile in each pin at the coarse mesh location z_j is considered to be represented by a single averaged temperature;

2. the coolant temperature is averaged throughout the whole xy cross section of the FA.

The first point implies the following:

$$T_{c,f}(z_j) = \frac{1}{L_h}\int_{z_j-L_h/2}^{z_j+L_h/2} T_{c,f}(z')dz', \tag{2.2}$$

where L_h is the z dimension of the NE domain.

The coupling occurs through the exchange, at times steps correctly established in line with the time scales of the phenomena, of information about the power distribution (NE information sent to the TH module) and the temperature distribution (TH information provided to the NE module). The feedback effect is considered to be linear in nature and it is represented by bi-variate linear interpolations on the cross section values, starting with reference data at various temperatures:

$$\Sigma(T_c, T_f) = \Sigma(T_{c0}, T_{f0}) + \left(\frac{\partial \Sigma}{\partial T_f}\right)_{Tc} (T_f - T_{f0}) + \left(\frac{\partial \Sigma}{\partial T_c}\right)_{Tf} (T_c - T_{c0}). \tag{2.3}$$

As a result, it is necessary to generate a set of multi-group cross sections for each of the materials present in the reactor at various fuel and coolant temperatures. Due to the nonlinear nature of the TH issue, the steady-state configuration for the temperature distribution is computed using a pseudo-transient cycle, with the distribution at each computing step being transferred to the NE module.

2.2 The ALFRED reactor

ALFRED is one of the most important European initiatives for the development of LFR technologies (see Fig. 2.1). It is a 300 MW_{th} pool-type prototype system that intends to demonstrate LFR technological maturity, as well as analyse the viability of LFR Small Modular Reactors (SMRs).

The LFR core offers certain benefits over commercial Light Water Reactor (LWR). Indeed, it burns more fuel, does not require coolant pressurisation, and allows the thermodynamic cycle efficiency to be increased due to the higher operation temperature. However, because of the fast neutron spectrum and of the interest in using nuclear fuels with a certain percentage of plutonium, the resulting kinetic parameters are quite different from those of LWR cores and are associated to a faster time-dependent response, thus requiring rigorous analyses of the dynamic features under operational and accidental conditions.

Due to the faster neutron kinetics, thermal-feedback becomes much more important in controlling the reactor. As a result, in order to evaluate the core performances, a suitable modelling of the NE-TH coupling is required.

The basic design of ALFRED core consists of:

- 171 FAs, with 127 fuel pins;
- 4 Safety Rods (SRs);
- 12 Control Rodss (CRs).

Each fuel assembly is organised in a triangular lattice and a stainless steel hexagonal wrapping is present. Control and safety rods (CRs and SR, respectively) control the

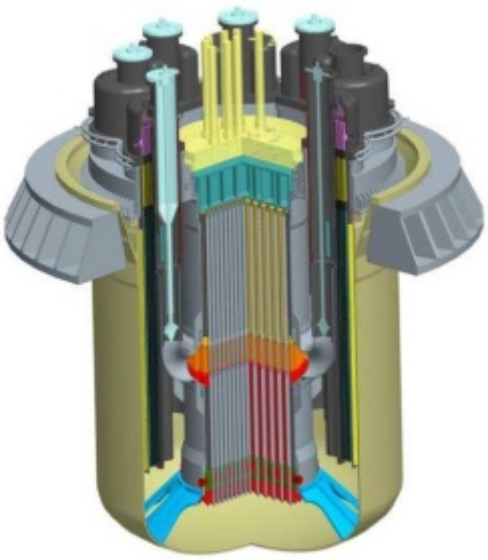

Figure 2.1: ALFRED reactor 3D sketch proposed by ANSALDO Nucleare [24].

core reactivity in both normal and unexpected operation settings. Both CRs and SRs have a B_4C poison length. An external reflector made of three rings of dummy elements, containing pins composed of zirconia, surrounds the central portion of the core, where the FAs, CRs, and SRs are located. A barrel surrounds the core, and lead is also present in the surrounding volume, which will be referred to as "external lead" in the following. This is cold lead (i.e. 400 °C) running toward the inlet plenum from the pumps.

2.3 The Serpent-2 model of ALFRED for multi-group nuclear data generation

The Monte Carlo code Serpent-2 is utilised in this study to collapse the continuous-energy nuclear data into a few-groups energy structure and to homogenise them over the reactor heterogeneous regions [25], providing the input for the FRENETIC NE module. Additionally, the same Serpent-2 model is used as a reference to compare to the FRENETIC results. The collapsing (in terms of energy) and homogenisation (in terms of space) procedures are carried out using a complete three-dimensional model of the ALFRED reactor, represented in Fig. 2.2. The core design and material compositions are compatible with the Begin-Of-Life (BOL) configuration (completely removed CRs) reported in [3]. In order to ensure the convergence of calculations, input parameters have been optimised with a convergence study, as reported in Fig. 2.3. The Shannon entropy shows that the number of inactive cycles for the fission source are sufficient to achieve its convergence.

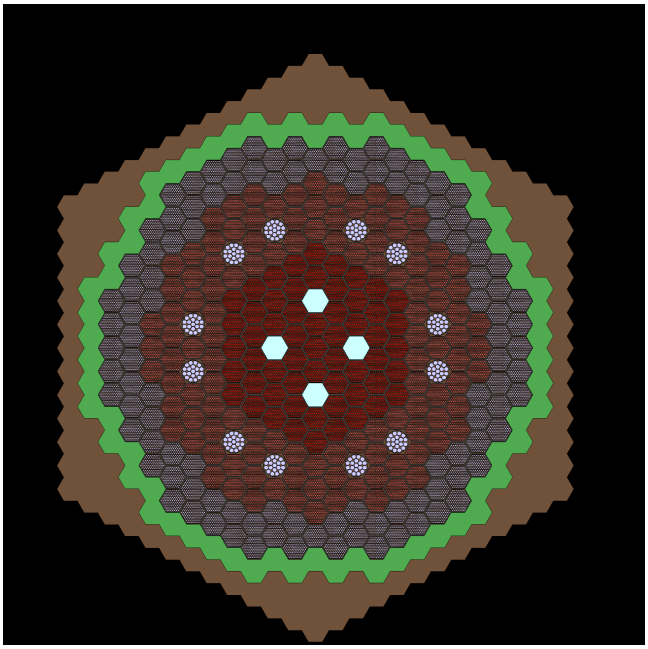

(a)

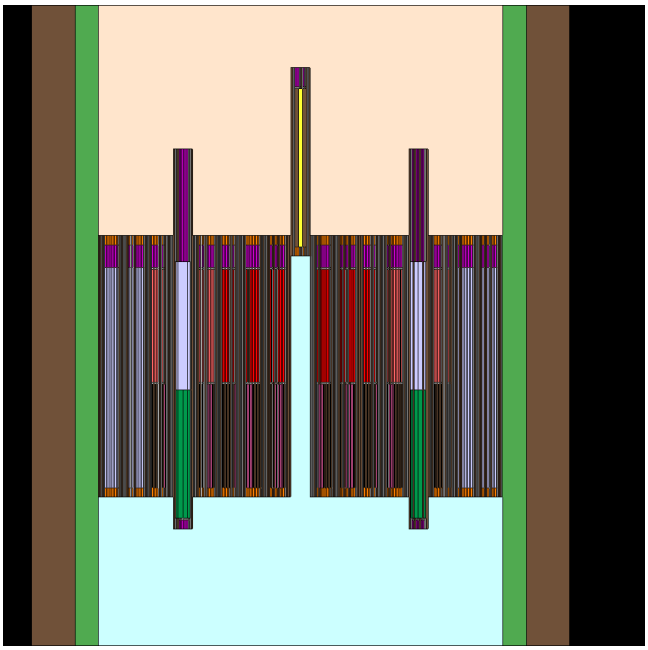

(b)

Figure 2.2: ALFRED reactor Serpent-2 model. (a): xy section; (b): yz section

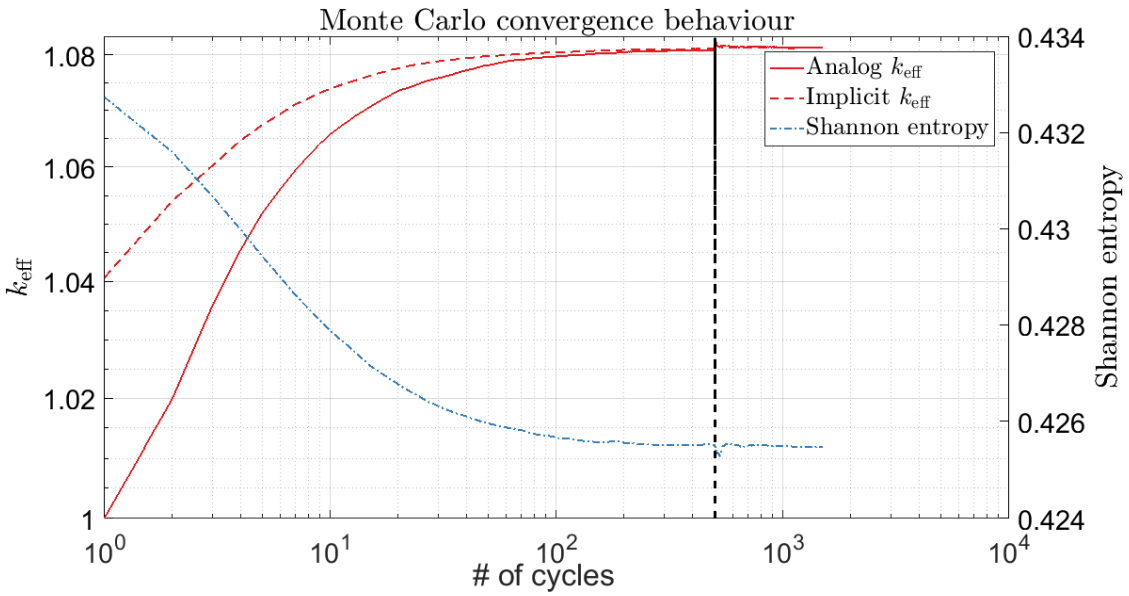

Figure 2.3: ALFRED reactor convergence analysis of the Monte Carlo simulation.

As Table 2.1 shows, these simulation parameters provide a high degree of convergence of the fission source. The indicators used were implicit and analog k_{eff}, as well as the Shannon entropy. After properly configuring a Serpent simulation, appropriate tallies (both in energy and space) must be determined in order to obtain spatially homogeneous and energy collapsed cross sections. After that, the method is repeated with varying coolant and fuel temperatures to build the cross sections library required by FRENETIC.

Table 2.1: Serpent-2 parameters for the evaluation of cross sections in the Monte Carlo ALFRED transport model.

Serpent-2 setup	Values
Particles number per batch	10E6
Inactive cycles	500
Active cycles	1000
MPI processes	8
OMP threads per MPI	12

2.3.1 Nuclear data energy collapsing

Regarding the energy groups structure, effective cross sections and other nuclear data are calculated by estimating the corresponding reaction rate on an energy

interval and then dividing it by the integrated flux on that range:

$$\Sigma_{x,g}(\boldsymbol{r}) = \frac{\int_{E_{g-1}}^{E_g} dE' \Sigma_x(\boldsymbol{r}, E') \phi(\boldsymbol{r}, E')}{\int_{E_{g-1}}^{E_g} dE' \phi(\boldsymbol{r}, E')} \tag{2.4}$$

where x is the generic reaction that a neutron can suffer along its flight, and g the generic group limited by $(\mathrm{E_{g-1}}, \mathrm{E_g})$. This ratio results in an effective cross section for that energy range that correctly retains the reaction rate (for an infinite medium).

The task of determining the number of energy intervals and their boundaries is delicate. This was accomplished in the current work by analysing neutron spectra in the most critical regions of the core, as shown in Fig. 2.4). The latter illustrates the neutron spectra as calculated by Serpent-2 in the HZP condition.

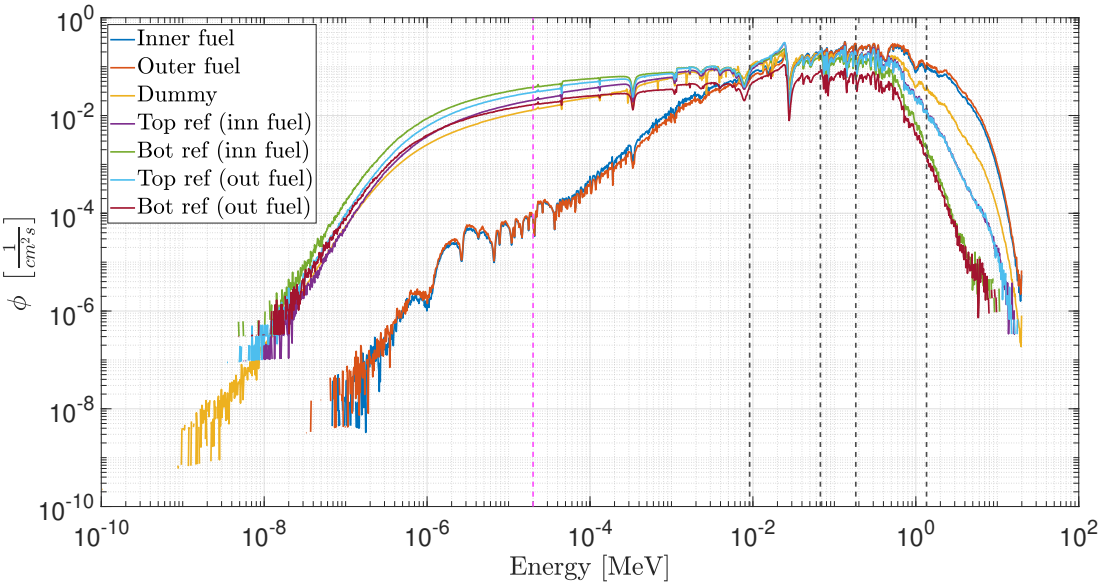

Figure 2.4: ALFRED reactor neutron flux spectra computed by Serpent-2 for selected regions of the core. Black dashed lines: energy cuts; magenta dashed line: additional group added to better account for the reflector spectrum[19].

There is a constraint in the energy discretisation for the group structure: the fifth group, with an upper energy limit of about 10^{-2} MeV, is capable of describing neutron activity in the fuel regions, but looks insufficient for the outer regions. Indeed, if a single energy group less than 10^{-2} MeV is considered, the existence of a greater proportion of thermalised neutrons in the reflectors and dummy components is entirely ignored. To address this issue, an additional energy group has been introduced, as six groups are adequate to approximate the energy distribution

behaviour of varied materials. The limits of the derived energy groups are shown in Table 2.2.

Table 2.2: Six-group data adopted to perform the macroscopic cross section energy collapsing and spatial homogenisation.

Group	Upper boundary [MeV]	Lower boundary [MeV]
1	$2.000 \cdot 10^{1}$	$1.353 \cdot 10^{0}$
2	$1.353 \cdot 10^{0}$	$1.832 \cdot 10^{-1}$
3	$1.832 \cdot 10^{-1}$	$6.732 \cdot 10^{-2}$
4	$6.732 \cdot 10^{-2}$	$9.119 \cdot 10^{-3}$
5	$9.119 \cdot 10^{-3}$	$2.000 \cdot 10^{-5}$
6	$2.000 \cdot 10^{-5}$	$1.000 \cdot 10^{-11}$

2.3.2 Spatial homogenisation

The energy collapsed cross sections must be homogenised across spatial areas in accordance with the FRENETIC code structure (i.e., homogeneous on the hexagonal fuel assembly and axially heterogeneous according to the neutronic coarse meshing). As far as the core modelling in Serpent-2 is concerned, as in Fig.2.2, some areas (most notably those located far from the fission source) were combined into a single universe for the cross section tally in order to produce a more accurate statistics.

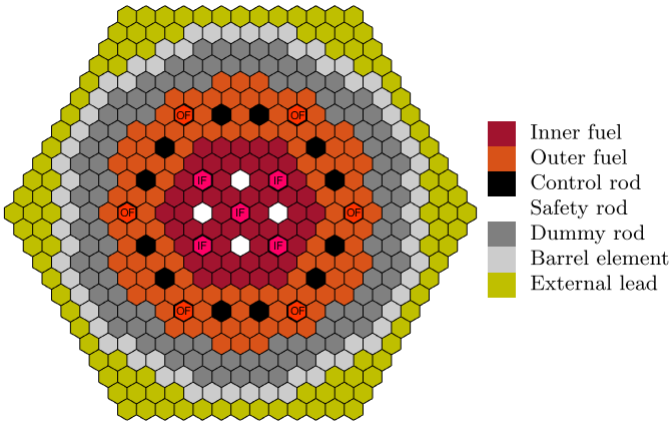

Figure 2.5: ALFRED reactor radial arrangement of the regions adopted for the cross sections homogenisation.

The outside lead (denoted by ocher in Fig.2.5), the barrel (denoted by light grey), and the dummy elements region (denoted by dark grey) are all regarded to be three distinct radial zones. Additionally, the 12 CRs are combined into a single

detector. The 4 SRs have been chosen similarly. Rather than that, it has been believed that cross sections averaged across a selection of FAs (shown in magenta in Fig. 2.5) might be typical of the complete zone for the Inner Fuel (IF) area. The Outer Fuel (OF) region has been treated similarly, with typical FAs shown in red. It should be noted that the fuel assemblies evaluated for homogenisation are those that are surrounded by similar assemblies. This option was made to strike a balance between complete homogenisation of the inner and outer fuel rings and assembly-level homogenisation, which would undoubtedly give a greater but perhaps unneeded degree of detail.

As illustrated in Fig. 2.6, the few-group cross sections assessed by Serpent-2 were first homogenised axially according to the finest attainable discretisation, which takes into consideration all of the different regions. However, the axial discretisation

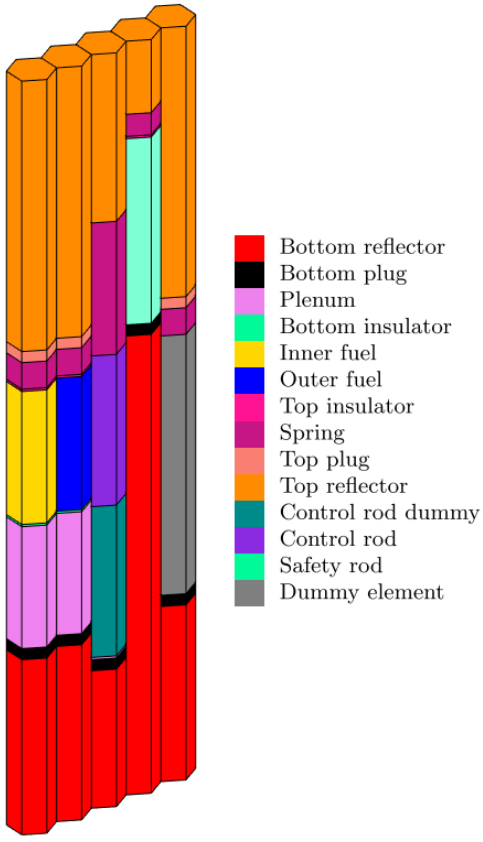

Figure 2.6: Serpent-2 axial discretisation for each radial region for the ALFRED reactor.

used for the FRENETIC code is often different, and perhaps coarser than the one used in a transport simulation. This is due to the necessity to avoid too optically thin areas, which would make difficult the convergence of the nodal method used in

FRENETIC [26] for the spatial solution of the diffusion equation. Each of the coarse axial sections in the FRENETIC model requires a single spatial value for the multi-group cross section, which has to be linked to those calculated by the transport model for the fine subdivisions that comprise that coarse axial region. This is accomplished through the use of a proper spatial *post-homogenisation* procedure that is carried out in such a way that the reaction rate for each material is preserved. The post-homogenisation procedure results in the computation of a new set of cross sections based on the flux and effective integral nuclear data of each material in the coarser regions, i.e. the FRENETIC axial mesh. The integrated data provided by Serpent-2 are integrated on the complete volume of each material and collapsed on the energy grid division, thus there are six values of integrated flux in the volume where the generic material is located, as well as the related cross section. The averaging is performed as:

$$\tilde{\Sigma}_{g,i} := \frac{\int_{V_i} d\boldsymbol{r} \int_{E_{g-1}}^{E_g} dE \Sigma(\boldsymbol{r}, E)\phi(\boldsymbol{r}, E)}{\int_{V_i} d\boldsymbol{r} \int_{E_{g-1}}^{E_g} dE \phi(\boldsymbol{r}, E)} \approx \frac{\sum_{j=1}^{N_i} h_{j,i} \int_{E_{g-1}}^{E_g} dE \Sigma_j(E)\phi_j(E)}{\sum_{j=1}^{N_i} h_{j,i} \int_{E_{g-1}}^{E_g} dE \phi_j(E)} \approx \frac{\sum_{j=1}^{N_i} h_{j,i}\Sigma_{g,j}\phi_{g,j}}{\sum_{j=1}^{N_i} h_{j,i}\phi_{g,j}} \tag{2.5}$$

where h_i is the axial length of the FRENETIC mesh and h_{Serp} is the height of the j-th Serpent-2 axial region which falls within the i$^{\text{th}}$ axial coarse mesh of FRENETIC. The index j goes from 1 to N, where N is the total number of materials (i.e., Serpent-2 regions) localised in the i$^{\text{th}}$ axial region of the FRENETIC mesh. The integration should be conducted on the right volume where the homogenisation occurs, but because the transport model provided a single value of the group-averaged flux for each material, it was assumed that the integrated flux was simply proportional to the axial length. This indicates that the flux for the g$^{\text{th}}$ group is averaged over the volume as if it were constant. Finally, the quality of results calculated by Serpent-2 regarding the thermal power is reported in Fig. 2.7.

2.4 ALFRED inner core FRENETIC simulation

The nuclear data set produced in the preceding section was used as input to the NE module of the FRENETIC code. This data-set is distributed using the radial "zoning" scheme seen in Fig. 2.8. The axial coarse regions seen in Fig. 2.6, which are each defined by a single spatial value of the cross sections, are then discretised

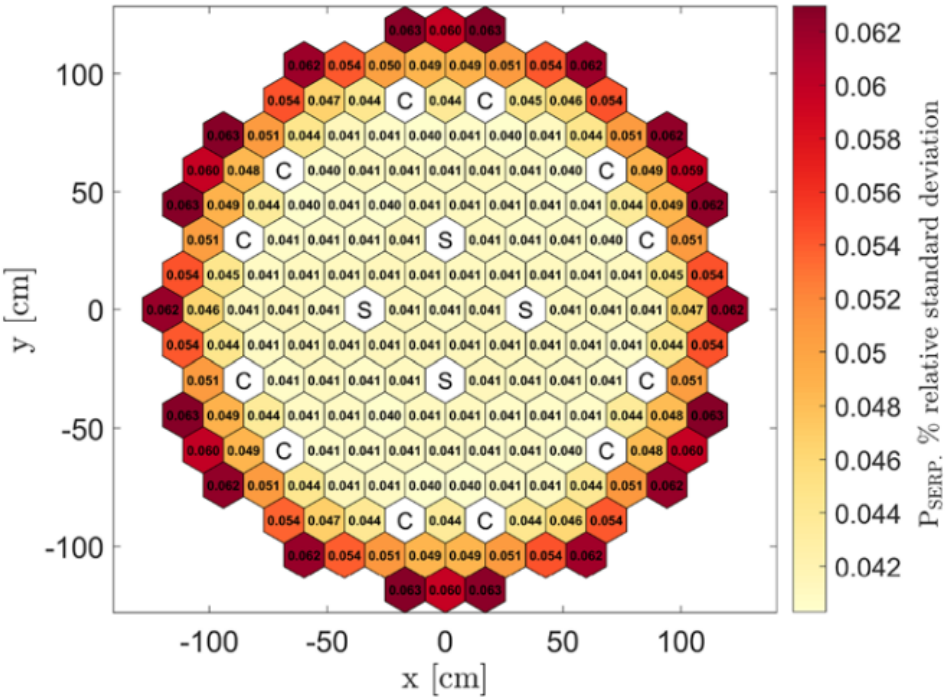

Figure 2.7: Relative Standard Deviation (RSD) of the thermal power calculated by Serpent-2 for the ALFRED reactor.

into a sufficient number of sub-nodes to guarantee that the flux solution is grid independent.

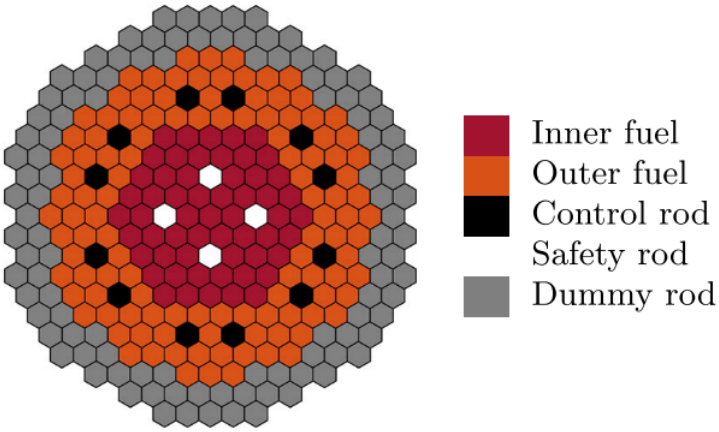

Figure 2.8: ALFRED reactor radial scheme of the FRENETIC model.

The model was compared to a steady-state reference result obtained using the identical Serpent-2 computations used to generate the cross sections set. The benchmark was carried on by imposing the identical thermal power of 300 MW_{th} and the same boundary conditions on both simulations (i.e., the transport calculation performed in Serpent-2 and the coarse-mesh diffusion calculation performed in FRENETIC). Due to the fact that this benchmark is primarily meant to verify the NE module, the temperatures of all materials in the FRENETIC core have been set to 673 K when the NE module is run in stand-alone mode. It is worth noting that the FRENETIC model of the core (Fig. 2.8) contains all parts where lead flows, but not the barrel or dummy. This restriction is caused by the thermal-hydraulic module inability to simulate assemblies with stationary lead or solid parts such as the barrel. This restriction is artificial at the moment, as the code is executing the neutronic solver standalone, and will be loosened at a subsequent step. The calculations of effective multiplication eigenvalues computed by the two codes are first compared in Table 2.3. The radial distribution of the fission power computed by Serpent-2 and FRENETIC is then shown in the Fig. 2.9. The total power is phys-

Table 2.3: Comparison between the effective multiplication eigenvalues provided by Serpent-2 and FRENETIC when the external barrel and lead are not considered.

-	Serpent-2	FRENETIC	Δk_{eff}
k_{eff}	1.08122 ± 3 pcm	1.07673	449 pcm

ically relevant because it corresponds to the exchange variable between the NE and TH modules in multi-physics simulations. A qualitative comparison demonstrates

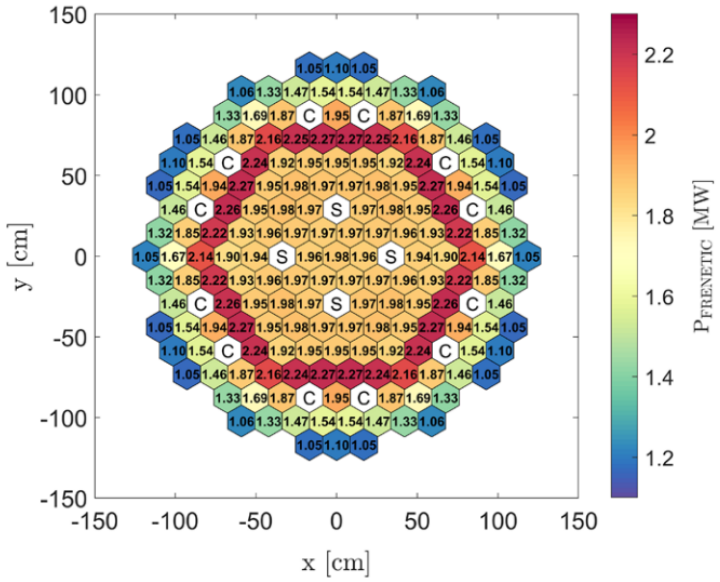

(a)

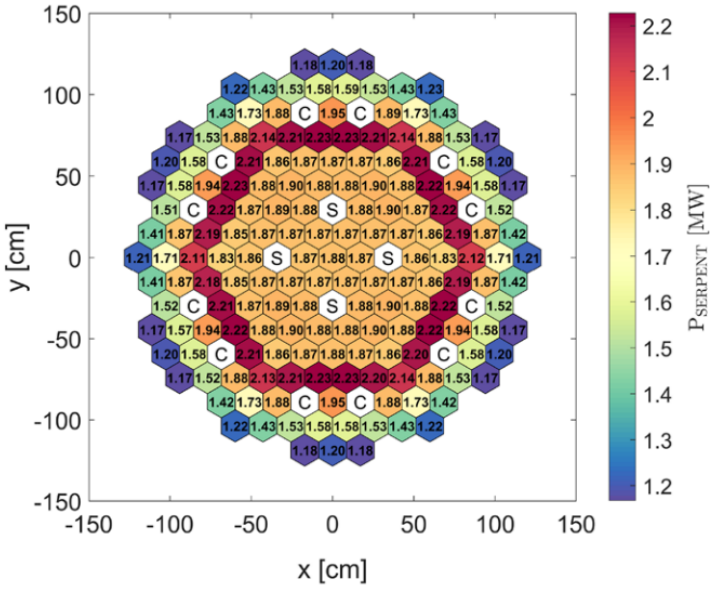

(b)

Figure 2.9: Radial power map (in MW per FA) computed by FRENETIC (a) without including barrel and external lead, and the power computed by Serpent-2 (b).

that the FRENETIC code accurately reproduces the radial power distribution: for example, in the BOL configuration studied here, the greatest value of power per FA is not found at the core centre, but at the beginning of the more richer outer fuel zone. In comparison to Serpent-2, FRENETIC correctly retrieves this particular characteristic. The Figs. 2.10 and 2.11 illustrate a more methodical comparison. Specifically, Fig. 2.10 depicts the map of the relative error between the thermal

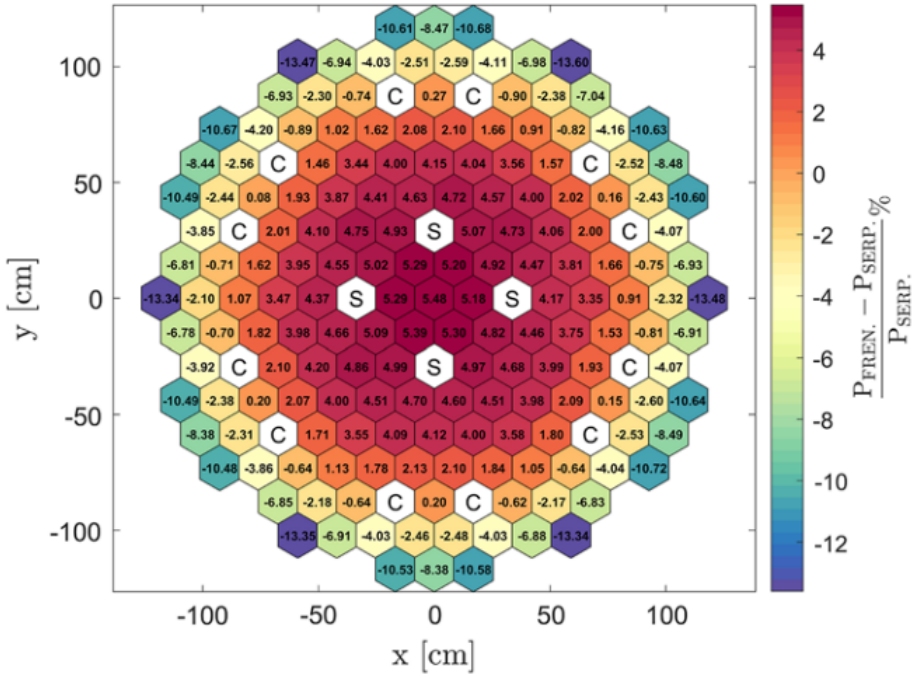

Figure 2.10: ALFRED reactor radial map of the relative error between the power per FA computed in FRENETIC and in Serpent-2.

power per FA of the two calculations, whereas Fig. 2.11 shows the axial distribution of the calculated linear power for FAs 1, 6, and 8. The relative difference, rather than the absolute value, is provided here to emphasise how FRENETIC overestimates the power per FA in the core centre, while underestimating it for FAs placed radially outside. This impact is readily apparent when a comparison is made in a radial path through the core, as seen in Fig. 2.11c. This radial distribution of the relative error indicates that the issue is with the domain extension of the two models (i.e., the absence of a barrel and external lead in the FRENETIC model), which explains in part why the multiplication constants were different between the two calculations.

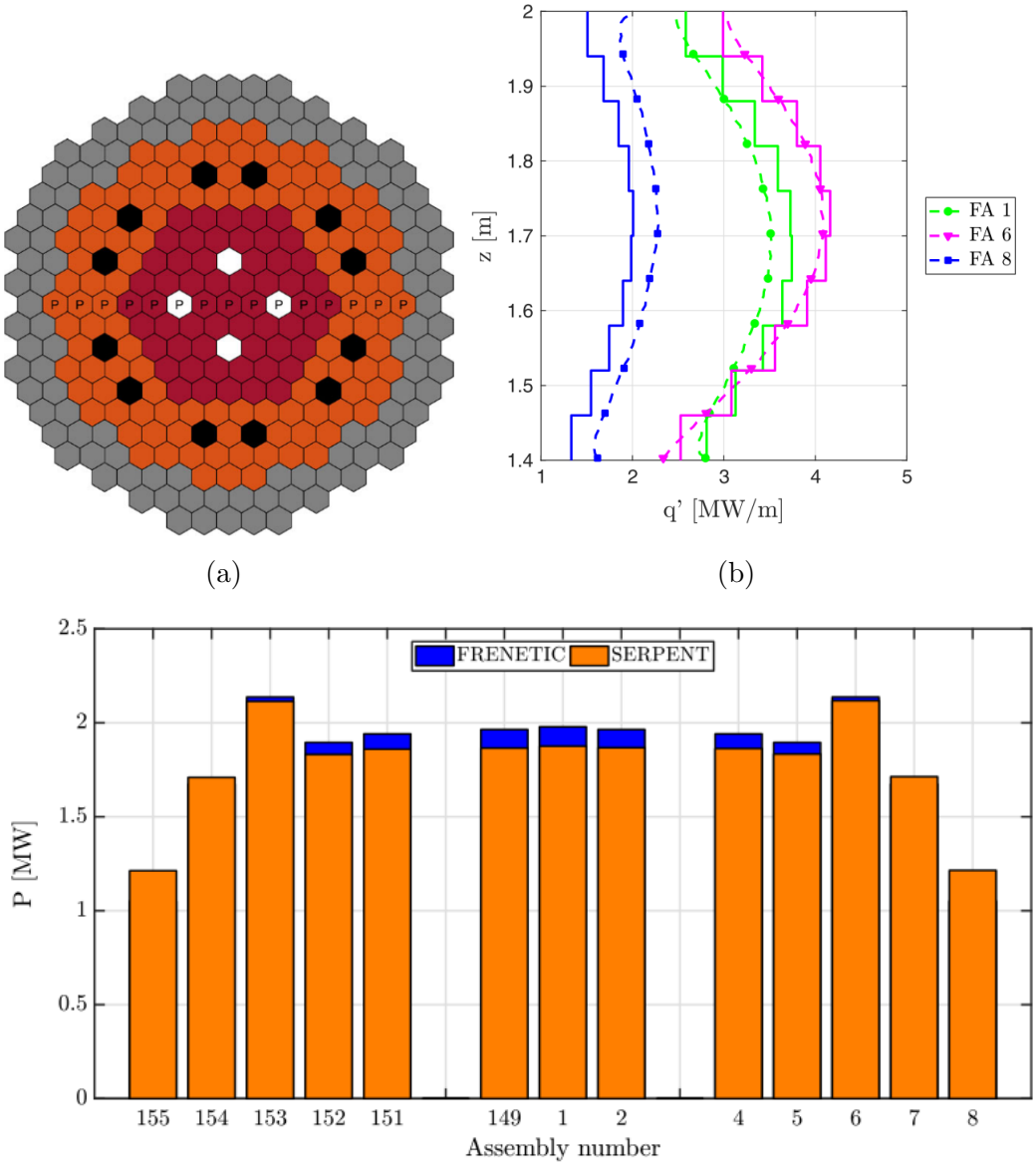

Figure 2.11: Comparison between the linear power calculated by Serpent and FRENETIC for three selected FAs for the ALFRED reactor. Serpent-2 values are represented in dashed-point line, whereas the ones calculated by FRENETIC are piece-wise constant. Comparison between the radial power profiles calculated by Serpent-2 and the FRENETIC model for some selected FAs in HZP.

2.5 Improved FRENETIC model: inclusion of barrel and external lead

Additional explanations for this mismatch include the homogeneity of space and the energy collapse of nuclear data. To distinguish between these effects, the FRENETIC model for ALFRED has been enhanced by the addition of barrel and dummy components, while keeping in mind that this expanded computational domain is viable for NE assessment but suffers from the TH module constraints. This was accomplished by introducing artificial FAs to the last two areas, as seen in Fig. 2.12a. These FAs are artificial in the sense that they do not contribute to the

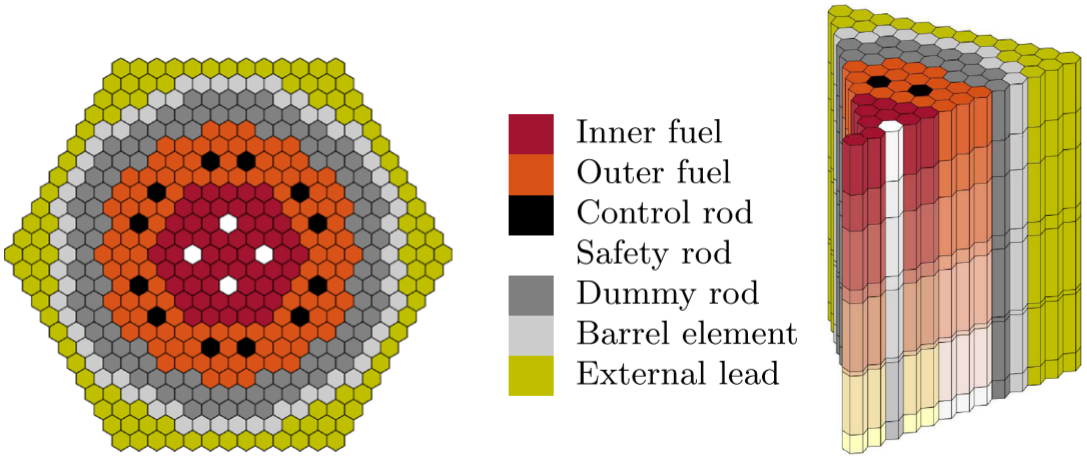

(a) (b)

Figure 2.12: ALFRED reactor radial scheme (a) and 3D sextant visualisation (b) of the improved FRENETIC model (i.e., including barrel and external lead).

thermal-hydraulic behaviour but are accounted for by the neutronic model using appropriately produced nuclear data. In this way, the core radial pattern is totally compatible with the Serpent-2 model. The radial and axial heterogeneity of the ALFRED core as implemented in the FRENETIC code is seen in Fig. 2.12b. The comparison of the effective multiplication eigenvalues calculated by the two code demonstrates the upgraded fidelity given by the improved model with respect to the Serpent-2 reference one, as reported in Table 2.4. As predicted, the results of

Table 2.4: Comparison between the effective multiplication eigenvalues provided by Serpent-2 and FRENETIC when the external barrel and lead are not considered.

-	Serpent-2	FRENETIC	Δk_{eff}
k_{eff}	1.08122 ± 3 pcm	1.08194	72 pcm

the FRENETIC NE run for the improved ALFRED model indicate that the relative error on the calculated power has been significantly decreased by including the barrel and lead outside the latter, as shown in Fig. 2.13. The relative error on

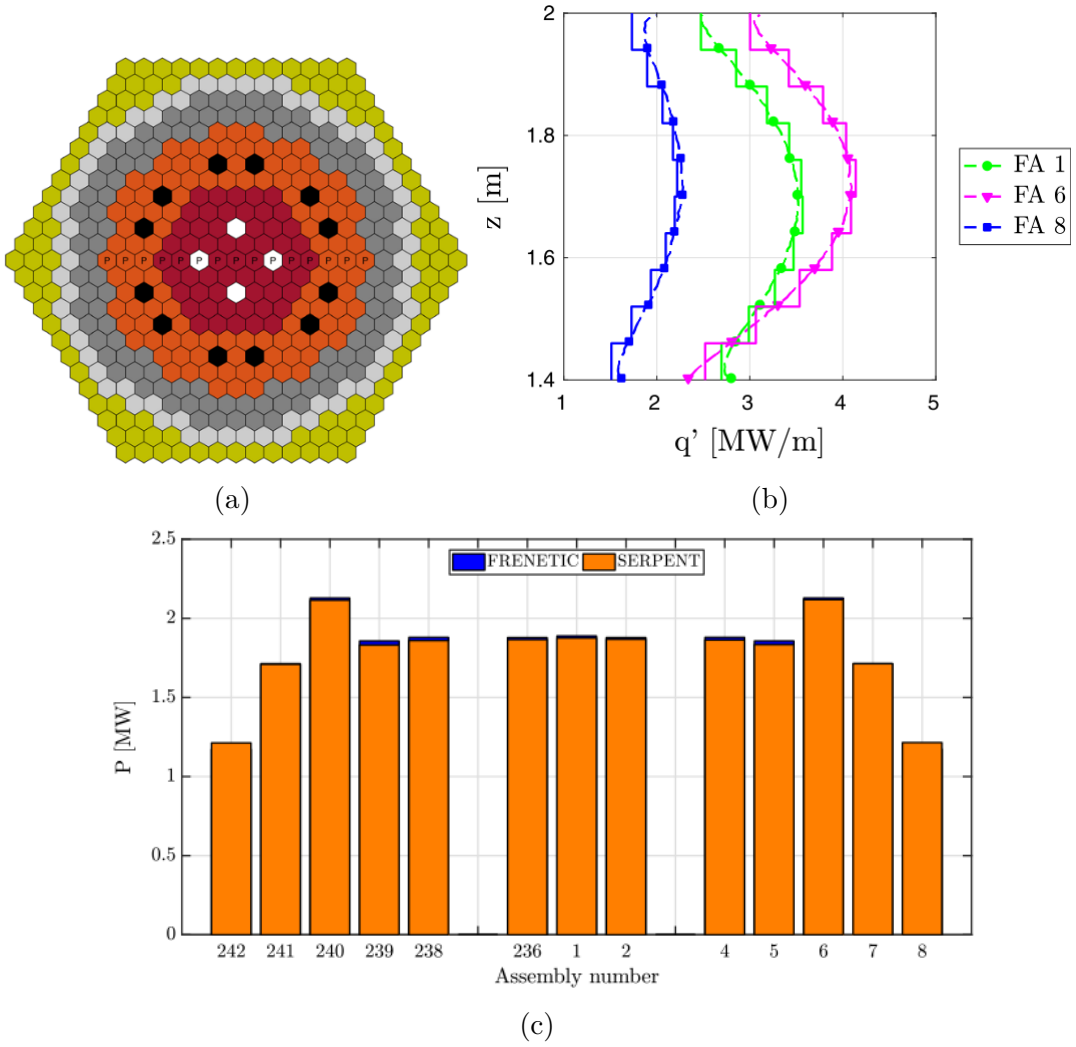

Figure 2.13: Comparison between the linear power calculated by Serpent-2 and FRENETIC for three selected FAs in HZP (b) for the ALFRED reactor. In (c) the radial power profiles calculated by Serpent-2 and the improved FRENETIC model for some selected FAs in HZP are compared.

the power produced per FA is shown in Fig.2.14, along with the statistical uncertainty of the Serpent-2 results, which naturally rises as one moves from the core centre to its perimeter. The remaining source of inaccuracies, albeit minor, is due to the energy collapsing or spatial homogenisation processes used to construct the FRENETIC data set.

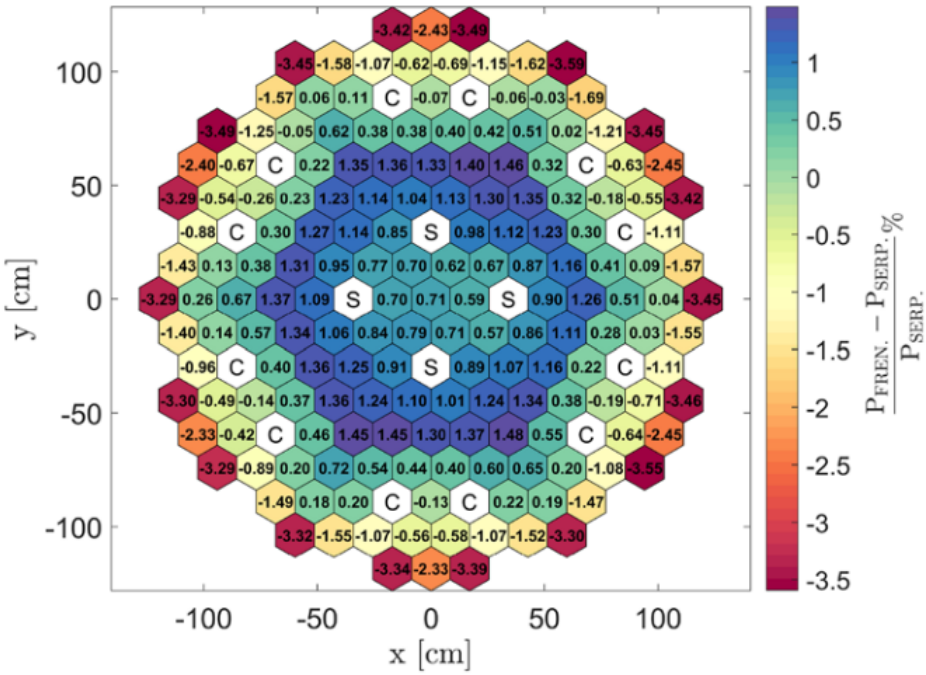

Figure 2.14: ALFRED reactor percentage relative difference between the power (in MW per FA) computed by Serpent-2 and FRENETIC.

2.6 FRENETIC coupled simulation of ALFRED in the steady-state condition

Following the successful NE benchmark exercise, a steady-state simulation in multi-physics mode, that is, with the NE-TH coupling taken into consideration, was done. As previously stated, the FRENETIC TH module does not take temperature change in the barrel or exterior lead areas into account. This enables the simulation to be run with the important NE impact linked with the existence of these locations while ignoring the (far less significant) TH effects.

2.6.1 Temperature dependence of cross sections library

The procedure mentioned above in Serpent-2 modelling has been repeated multiple times, with the temperature of the lead coolant and fuel varying, while the temperature of the structural elements has been set in Serpent based on the arithmetic average of the coolant and fuel temperatures. This procedure is required because the FRENETIC code analyses thermal-feedback by interpolating cross sections between at least two temperatures based on the local temperature of the fuel and coolant. Table 2.5 lists the fuel and coolant temperatures considered for the production of the cross section library. The lower triangular arrangement of the table is owing to the fact that the fuel temperature is always larger than the coolant temperature, at least for the reactor operational scenarios relevant for the current study.

Table 2.5: Temperatures values adopted for the Serpent-2 runs used to evaluate the few-group cross section.

T_{fuel} [K] \ $T_{coolant}$ [K]	673	1073	1473
673	×		
1073	×	×	
1473	×	×	×

2.6.2 Steady-state results of FRENETIC models for the ALFRED reactor

FRENETIC simulations generate temperature values for each FA at various z coordinate for the coolant and fuel. If such information is directly imported into Serpent-2, the input file should treat each every mesh used in the FRENETIC model as a new universe with its own temperature and composition, and the resulting memory demand becomes prohibitively large. As a result of confirming that

the greatest temperature difference between FAs within the same radial zone is less than 1 K, a collection of concentric regions has been found, each characterised by a single temperature value. All materials in the regions below the active zone have been considered to be at 673 K axially (i.e., the inlet temperature). Similarly, the regions above the active zone have the same temperature as the average core output temperature. Rather than that, the active zone of each FA has been separated into ten axial segments, each of which is defined by its corresponding average temperature as determined by FRENETIC. This results in a smaller number of areas,

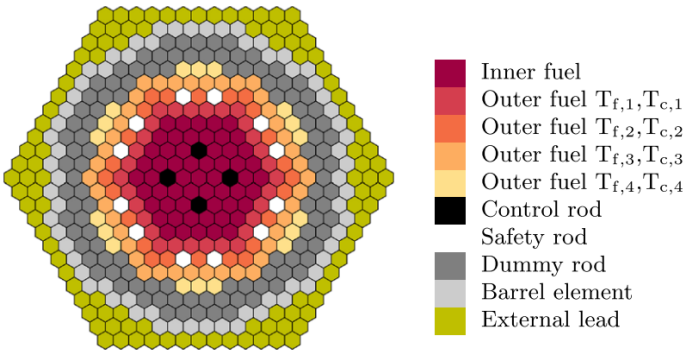

Figure 2.15: ALFRED reactor temperature distribution adopted in the Serpent-2 model operating in HFP conditions.

which enables Serpent-2 to execute a k_{eff} calculation with a physically significant temperature distribution (Fig. 2.15). The new estimations of the multiplication eigenvalue for both codes are reported in Table 2.6, showing that the validity of FRENETIC forecasts is further confirmed in the presence of thermal feedback effects. As in the prior situations, similar comparisons of power have been made.

Table 2.6: Comparison between the effective multiplication eigenvalues provided by Serpent-2 and FRENETIC when barrel and external lead are considered in HFP.

-	Serpent-2	FRENETIC	Δk_{eff}
k_{eff}	1.07848 ± 6 pcm	1.07902	54 pcm

The radial distribution of power is shown in Fig. 2.16a, whereas the linear power in three FAs is depicted in Fig. 2.16b. As final result, in Fig. 2.17 the relative error among the power calculated by the FRENETIC code and the Serpent-2 model for each FA is reported.

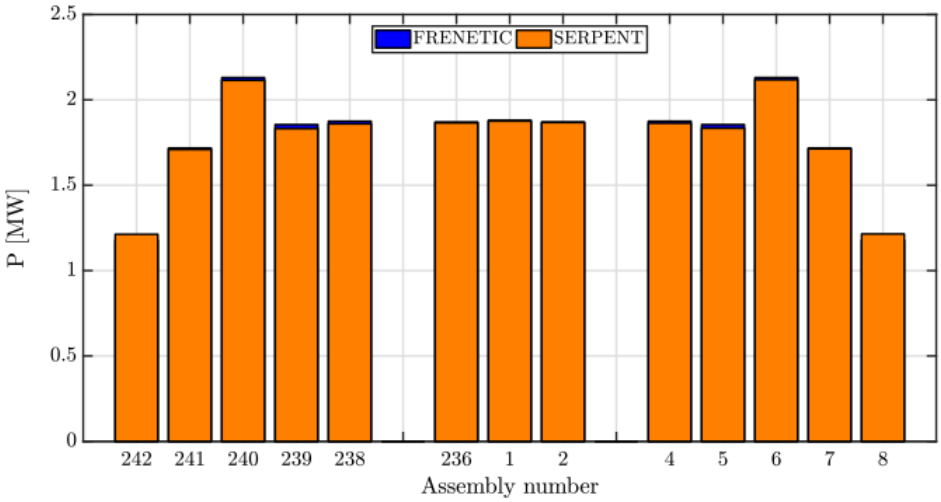

(a)

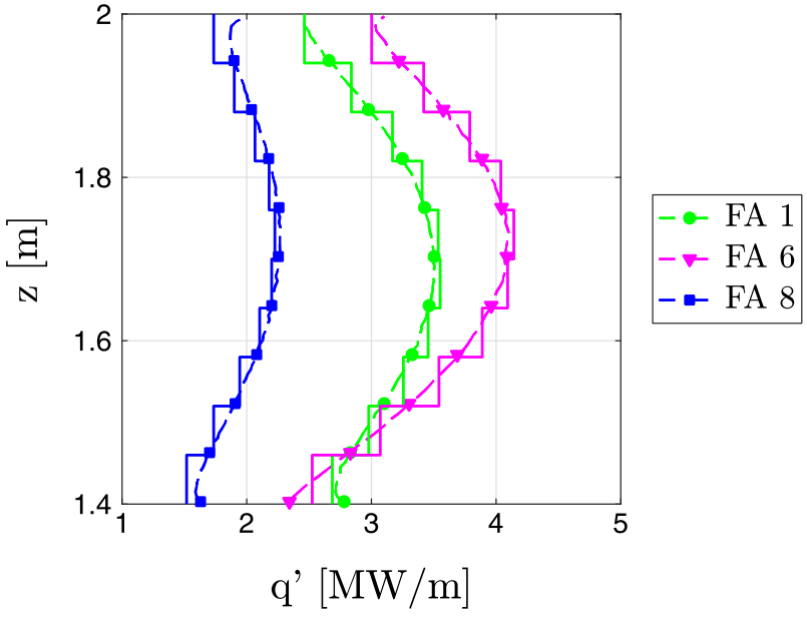

(b)

Figure 2.16: Comparison between the radial power profile calculated by Serpent-2 and FRENETIC for some selected FAs in HFP (a). In (b) the comparison between the linear power calculated by Serpent-2 and FRENETIC for three selected is shown.

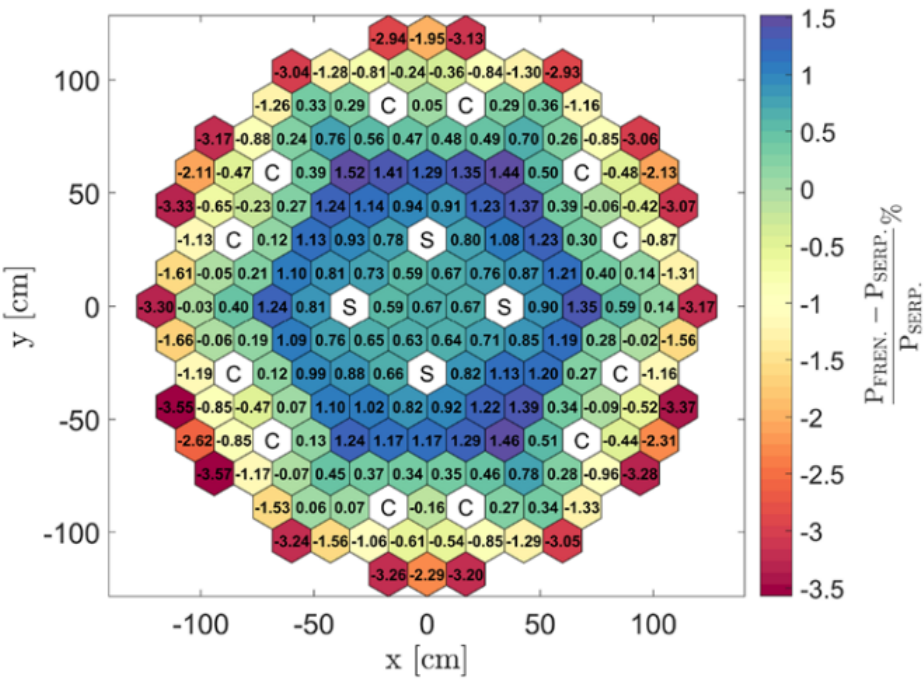

Figure 2.17: Percentage relative difference between the assembly-wise power computed by Serpent-2 and FRENETIC in HFP.

2.7 Dynamic analyses with FRENETIC of ALFRED core during emergency scenarios

On the basis of the good results of the activity performed in the frame of [19], it has been decided to proceed with the utilisation of the code FRENETIC to perform some simulations allowing to characterise the multi-physics behaviour of the ALFRED core and address some safety-relevant transient cases. In this section two relevant IEs are examined. The first regards the accidental introduction of a SR. This implies an insertion of negative reactivity with the consequent shutdown of the reactor. The second one simulates a Loss Of Flow Accident (LOFA), in which the total mass flow rate is arbitrarily decreased, in order to initiate a reactivity transient by the TH module by raising up the fuel temperature. In this scenario, the reactor is safely shut-down by passive effects due to changes in microscopic cross sections of materials and the related decrease of coolant density.

To correctly address this study, the actual steady-state condition that a multi-physics code adopts as initial condition for a transient calculation and how such steady-state is achieved. As can be seen from the previous results, the multi-physics simulation of the ALFRED core (with all SRs withdrawn) has led to a multiplication constant above criticality of around 8000 pcm. Such result is consistent with design requirements regarding excess reactivity, and such excellent reactivity is in the real

system compensated by the movement of the control and safety rods to achieve, and maintain, a critical condition during operation. When such situation is to be simulated with a multi-physics code, the common practice is to "force" the system to be critical at the beginning of the time-dependent simulation, by dividing the multiplication term in the neutron balance equations by this "initial" k_{eff}. It is however true that, if such value is far from unity, the resulting critical state may be characterised by different physical conditions, in terms of spatial and spectral neutron distribution, with influence to the following transient simulation.

For the above reason, and in order to be more representative of the ALFRED core configuration when in operation, the previous setup has been modified by changing the position of the control rods, in order to start from a configuration closer to criticality. This operation has led to the core configuration as in Fig. 2.18. In this new configuration the control rods are inserted with a $\Delta z = 29$ cm and the related FRENETIC mesh has been modified, and this has required a new spatial homogenisation procedure. In this new condition, the steady state calculation with FRENETIC gives $k_{\text{eff}} = 1.01294$. By the insertion of the CRs in such a

Figure 2.18: ALFRED core configuration with CRs position adjusted to reach a condition closer to criticality.

way to reach the criticality condition, the neutron flux is constrained to settle the power, as Fig. 2.19a shows. Therefore, the evidence of these insertions can be

easily appreciated in Fig. 2.19b, where the comparison with the previous power distribution when the CRs are extracted is performed.

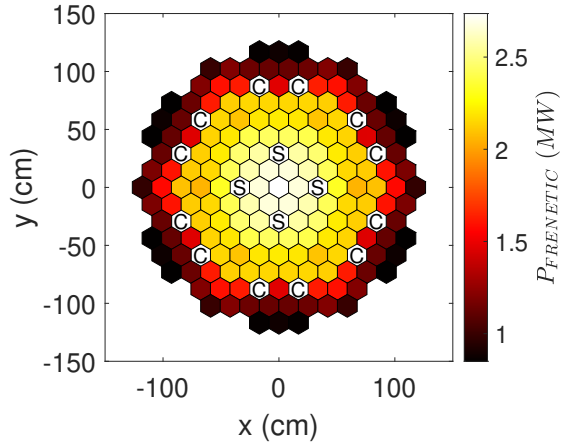

(a)

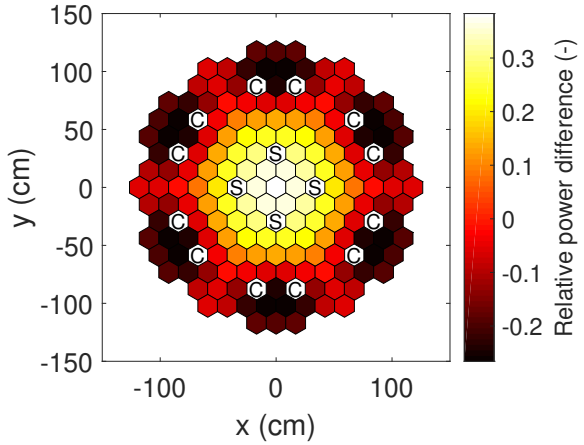

(b)

Figure 2.19: ALFRED core power distribution with rods insertion adjusted to reach a condition closer to criticality (a) and relative difference with respect to the case having withdrawn CRs (b).

2.7.1 ALFRED time-dependent purely neutronic simulation

Here the first transient is presented. In this analysis, the transient is purely neutronic without considering the thermal feedback due to changes in temperature. This can be justified by the fact that the thermal feedback are of the secondary order with respect to the great amount of reactivity due to a complete insertion of a poison length in the active length of the core. Thus, it is redundant also to

consider the passive effects on the neutronic parameters since the insertion is faster than other effects. The transient has been conducted with a total time of 9 seconds, with a change of insertion velocity at 5 seconds where a SR was faster inserted. In Fig. 2.20 the scheme of the transient is illustrated. The results (Figs. 2.21a

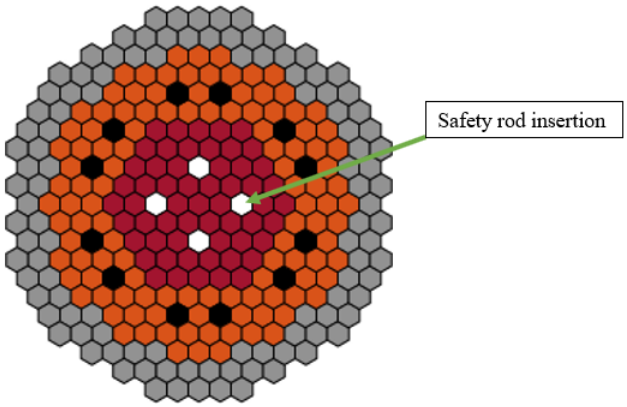

Figure 2.20: IE in the pure NE transient where a SR falls in the core.

and 2.21b) show how the insertion of the SR leads to a fast decrease of the power generation. The evident change of slope in reactivity around at 5 seconds is due to a faster insertion of the SR in the time interval (5,9) seconds. Since the rod is in a region with a high neutron importance, the effects are significant. Indeed, the power generation reach approximately zero in almost 50 seconds. However, it must be noted that if the TH feedback were present, the negative insertion of reactivity would be damped. In conclusion, this case can be considered as an estimation on the reactivity worth of one safety rod insertion. As it is evident in Figs. 2.22a and 2.22b, this transient implies a significant distortion of the radial neutron flux distribution, and therefore of the radial power map. This particular kind of transient is not suitable for simulation by means of point kinetics approach, due to fast changes of shape and amplitude of the neutron flux.

2.7.2 ALFRED time-dependent coupled NE/TH simulations

As last case proposed, here the transient due to modification of TH boundary conditions is discussed. To induce the variation, the mass flow rate of all coolant pumps is reduced following the exponential behaviour reported in Fig. 2.23, where the mass flow rate for the central FA is shown. Here the simulation is carried on in coupled conditions, since the Control System is considered out of service. Therefore, the NE solver must take into account the thermal response of the increasing in temperature values to correctly assess the temperature-dependency of

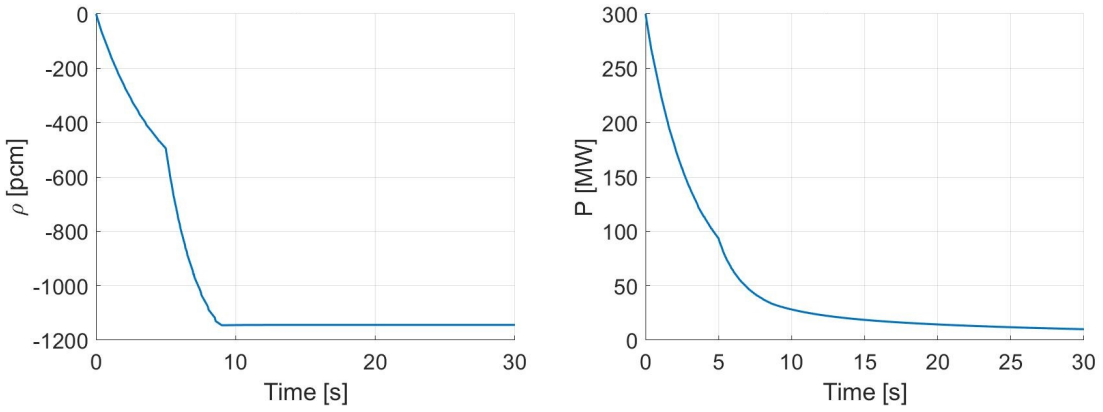

(a) (b)

Figure 2.21: Thermal power (a) and reactivity evolution in NE transient(b) due to SR insertion.

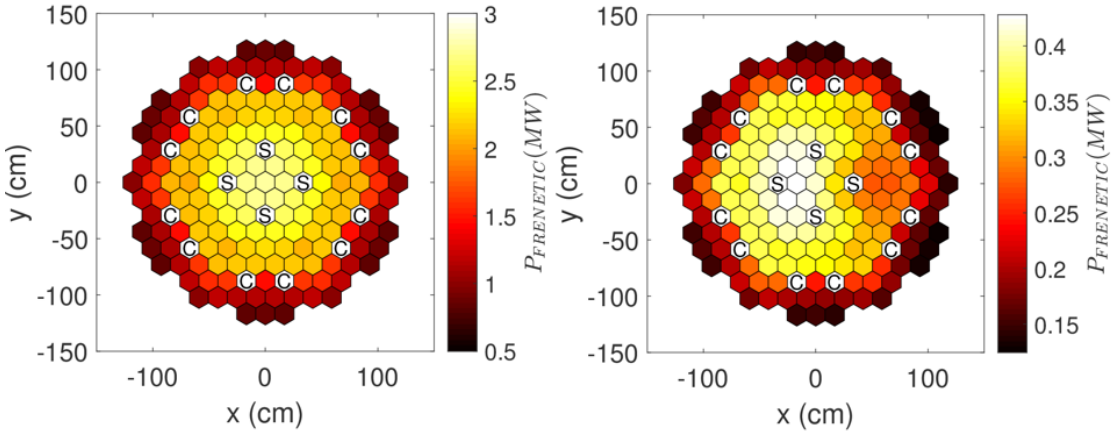

(a) (b)

Figure 2.22: Radial power map (in MW per FA) at t=0s (a) and t=7s (b) due to SR insertion.

the cross sections for the power generation. The transient has been conducted for 300 seconds, but the variation in reactivity and related thermal power are showed until 150 s. The assumed reduction of the flow rate neglects natural circulation effects too because, the quantification of which would require the presence of an external module for the primary circuit of the reactor. Therefore, this is of course a conservative estimate. This kind of transient can be suitably modelled by adopt-

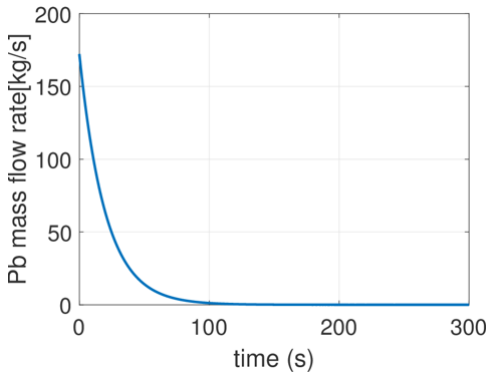

Figure 2.23: Mass flow rate reduction of the central FA.

ing a point-kinetic approach [27], since the neutron flux shape is lesser influenced by the nature of transient. On the other side, the amplitude is quite affected by thermal effects, since the absorption of the lead tends to decrease in force of the coolant density reduction, while the temperature of the fuel tends to increase. In Figs. 2.24a and 2.24b the behaviour of the reactivity and generated power during this transient is shown. As expected, feedback effects associated to the increase of the fuel temperature lead to a significant reduction of the generated power, mainly for the Doppler Effect.

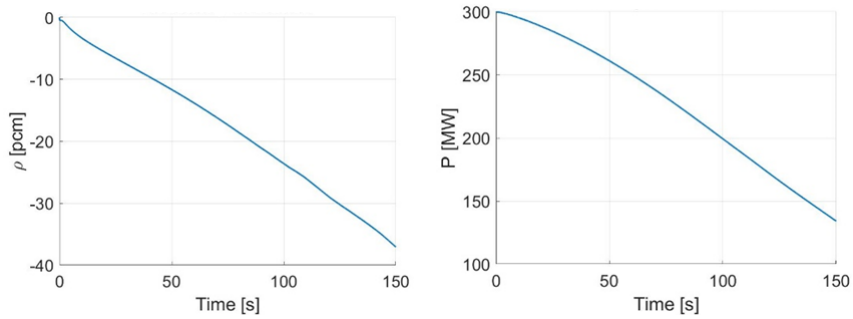

(a) (b)

Figure 2.24: Reactivity and thermal power evolution calculated by the FRENETIC code when a LOFA transient is simulated in the ALFRED reactor.

2.8 Code-to-code SIMMER/FRENETIC comparison for the neutronic simulation of ALFRED core

Here the second benchmark activity is presented. In the sections above, the neutronic module was compared against the Serpent-2, yielding quite good results in terms of assembly-wise power distribution and effective multiplication factor. The inclusion of some inactive sections, such as the core barrel and the external lead, is critical for proper evaluation of the key neutronics quantities in the reactor model. This research also examined the extremely good agreement between the thermal feedback effects evaluated by FRENETIC, which uses a library of pre-computed, temperature-dependent few-group constants, and Serpent-2, which directly changes the continuous-energy nuclear data. However, the influence of the many numerical and modelling assumptions contained in FRENETIC (e.g., nodal diffusion rather than a mesh-less transport model) should be also considered.

Therefore, FRENETIC is compared in this study to SIMMER III/IV [28], which is a reference multi-physics tool in the context of core-disruptive incidents in liquid metal-cooled fast reactors [8]. The features of SIMMER NE module, a multi-group discrete ordinates code, are well suited to the FRENETIC qualification requirements, allowing the development of a progressively detailed simulation framework, with the goal of assessing and isolating the various discrepancies between the two tools.

To achieve complete consistency of the code-to-code comparison, both codes use the identical set of homogenised few-groups data calculated with Serpent-2. Finally, some conclusions are reached, and future prospects on the optimisation of energy discretisation using a genetic algorithm [29] are considered.

2.8.1 Comparison simulation framework

Input data consistency

Because the goal of this work is to examine the influence of the various numerical and modelling methodologies used in the NE models of the two codes, it is critical to ensure that their models and input data are as consistent as feasible. The multi-group cross-section library management is a significant distinction between the two codes. FRENETIC requires a set of few-group parameters for each area given by the user, whereas SIMMER typically computes the multi-group cross-section set required for the full-core computation internally based on the actual core state. To overcome this limitation, the SIMMER code has been forced to read the same data set of cross section provided by Serpent-2 in the FRENETIC format.

ALFRED core geometry model

Another distinction between the two codes is how the core geometry is handled. FRENETIC provides for the consideration of two-dimensional systems in which the reactor is considered to be made up of flat, hexagonal SAs, as well as three-dimensional systems in which each SA is axially extruded. SIMMER, on the other hand, allows to treat the entire core with a detailed three-dimensional cartesian discretisation, or it can reduce the geometrical complexity with a cylindrical r-z discretisation, which prevents from identifying the polar localisation of specific assemblies, such as the CR. These geometrical differences have led to the suggestion that the FRENETIC 3D calculations be compared to both the 2D and 3D SIMMER models, in order to estimate the influence of the cartesian approximation of the hexagons, whose shape is slightly perturbed as sketched in Fig. 2.25, and the impact of the position of the CR rings in the cylindrical model. For the 2D analyses please refer to [20].

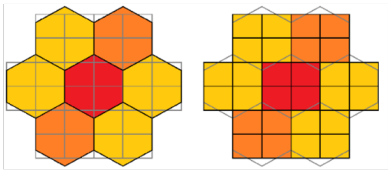

Figure 2.25: Cartesian mesh employed by SIMMER to approximate the hexagonal geometry.

Few-group constants generation

The 3D ALFRED core model used in this study for Serpent-2 calculations is the same of the previous chapter, considering the HZP condition. The various SAs (fuel, control, dummy, etc.) are represented by a pin-by-pin heterogeneous model, whilst the barrel and reflectors are considered to be built of homogeneous materials.

The Serpent-2 model is used in two configurations: in the first one, indicated in the following as *off-critical*, the CRs are completely withdrawn; in the second one, the CRs are inserted in such a way that the upper edge of the absorber zone is 11 cm above the core mid-plane, which is located at the half-height of the fuel assemblies active zone. This configuration, indicated in the following as *close-to-critical*, allows to almost achieve criticality (k_{eff}=1.00002(4)).

In Fig. 2.26 the conditions of *off-critical* and *close-to-criticality* are showed. It has to be noted that the cross sections for the above-mentioned conditions have been re-calculated according to these axial positioning, using the adopted energy grid of the previous chapter and published in [19].

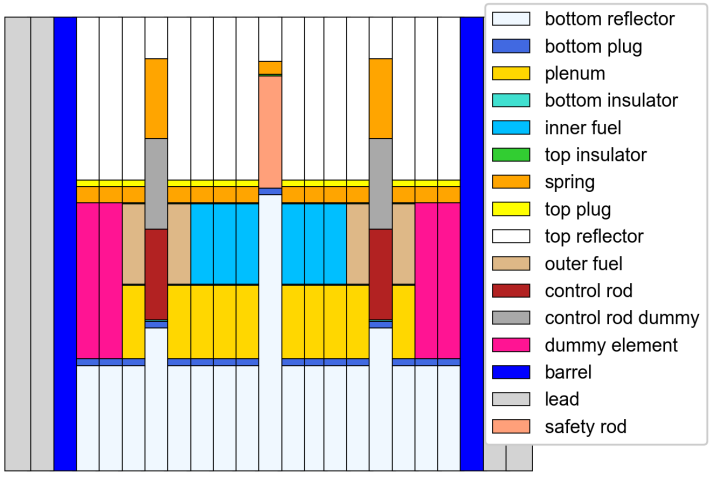

(a)

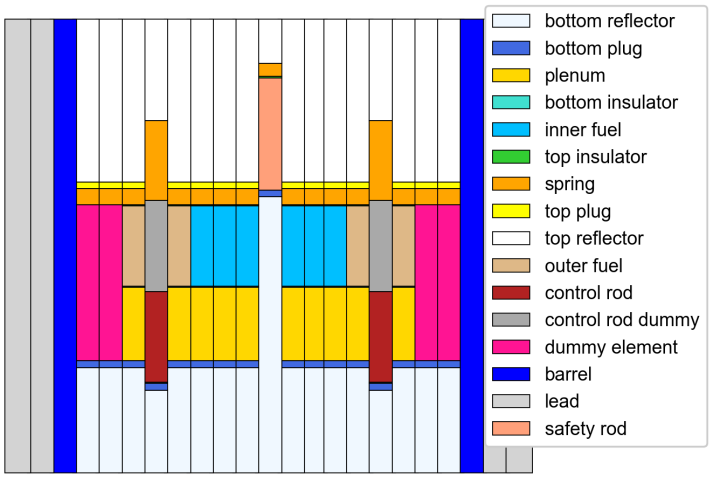

(b)

Figure 2.26: Off-critical (a) and close-to-critical (b) axial configurations of the ALFRED 3D model for the few-group constants calculation.

2.8.2 3D code-to-code comparison

The next step in the benchmark activity consists in the comparison of SIMMER and FRENETIC for the same 3D ALFRED B model, sketched in Fig. 2.27, in terms of k_{eff}, assembly-wise power distribution and linear power in two representative FAs.

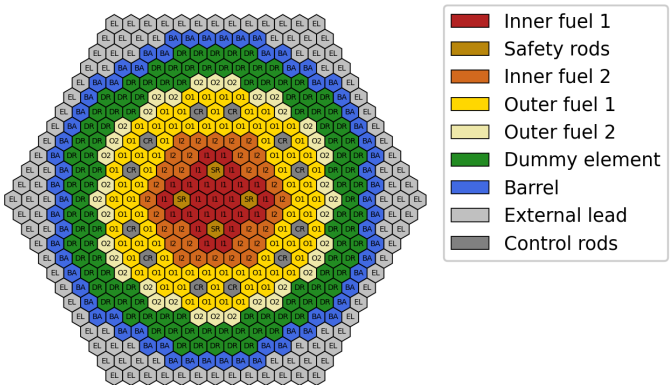

(a)

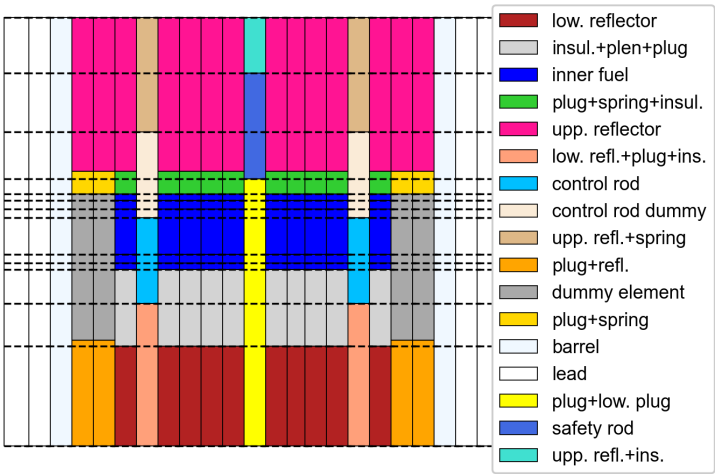

(b)

Figure 2.27: Radial (a) and axial (b) section of the ALFRED 3D model for the 3D comparison between FRENETIC and SIMMER.

Results for the close-to-critical configuration

Several S_N discretisation orders have been considered in SIMMER. The compositions along the SAs have been represented consistently between the two codes, following the procedure described in [19]. In Table 2.7, the values of k_{eff} for each SIMMER S_N order are compared with the ones calculated by FRENETIC and Serpent-2; as done in the previous sections, the latter is taken as reference.

Table 2.7: Comparison among k_{eff} provided by SIMMER (SMR) at different S_N order, and k_{eff} computed with FRENETIC (FRN) and Serpent (SRP). The reference case is provided by Serpent-2, $k_{\text{eff,SRP}} = 0.99999(8)$, whereas FRENETIC yields $k_{\text{eff,FRN}} = 0.99819$ ($\Delta k_{\text{eff,SRP-FRN}}$=172 pcm).

	S_2	S_4	S_6	S_8
$k_{\text{eff,SMR}}$	0.99631	0.99973	0.99927	0.99908
$k_{\text{eff,SMR}} - k_{\text{eff,FRN}}$ (pcm)	-188.57	154.79	108.74	89.71
$k_{\text{eff,SMR}} - k_{\text{eff,SRP}}$ (pcm)	-368.97	-25.61	-71.65	-90.68

The S_2 case, in Fig. 2.28, shows rather large discrepancies in both power and axial distributions; these differences are evident also looking at the k_{eff}, which differs from Serpent-2 and FRENETIC by more than 180 pcm. The power distribution discrepancies are affected by the cartesian-hexagonal mesh approximation, which might play a particular role in combination with the limited number of directions available for the streaming.

Excluding the S_2 case, whose behaviour has been already commented, SIMMER seems to show the tendency to converge to a k_{eff} lying between Serpent-2 and FRENETIC when the S_N order increases. Such behaviour is expected, since the cross-sections computed by Serpent-2 have been post-homogenised and therefore SIMMER should not converge to the Serpent-2 value. Notwithstanding this, SIMMER provides better results than FRENETIC, considering that the solution scheme is based on transport rather than diffusion. In general, calculations from S_4 to S_8 provide very similar results, with excellent agreement in terms of both power and linear distributions. The differences are concentrated in the neighbourhood of the CRs (with the worst behaviour observed for cells which are near two CRs), as expected with diffusion codes. The effect of the Cartesian-hexagonal mesh difference is clear in all cases, as the results do not show the 60° symmetry that is proper of the design. A closer look to Fig. 2.29, compared with Fig. 2.30 and Fig. 2.31, shows that the S_4 case provides slightly lower discrepancies between SIMMER and FRENETIC. This does not mean that the SIMMER S_4 better represents the physics, rather that it is closer to the description produced by the FRENETIC diffusion calculation. Actually, the S_4 case is already an adequate description of the core physics, as opposed to the S_2 scenario.

Results for the off-critical configuration

In order to assess the effect of the CRs on the flux and power profiles commented before, an additional case with the CRs extracted from the active region has been studied. Table 2.8 provides the multiplication factor differences calculated by FRENETIC, SIMMER and Serpent-2, and hence the worth of the CRs bank. SIMMER and FRENETIC are in very good agreement, predicting a CR worth that differ by

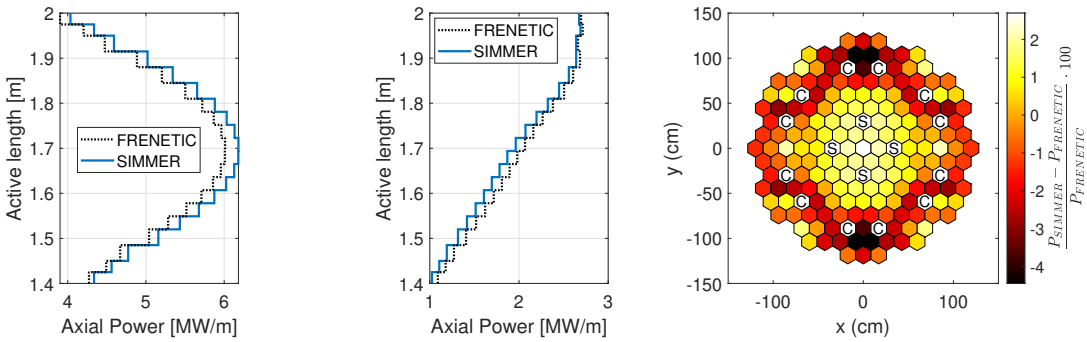

Figure 2.28: Relative difference on the assembly-wise power (right) and axial power profiles (left and centre) for the S_2 case. The left axial profiles correspond to the central FA; the centred ones, to the FA between two CRs in the 2^{nd} sextant.

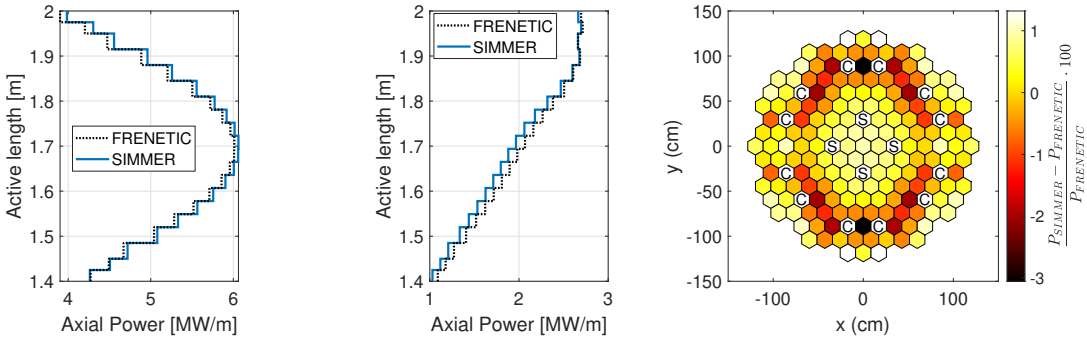

Figure 2.29: Relative difference on the assembly-wise power (right) and axial power profiles (left and centre) for the S_4 case. The left axial profiles correspond to the central FA; the centred ones, to the FA between two CRs in the 2^{nd} sextant.

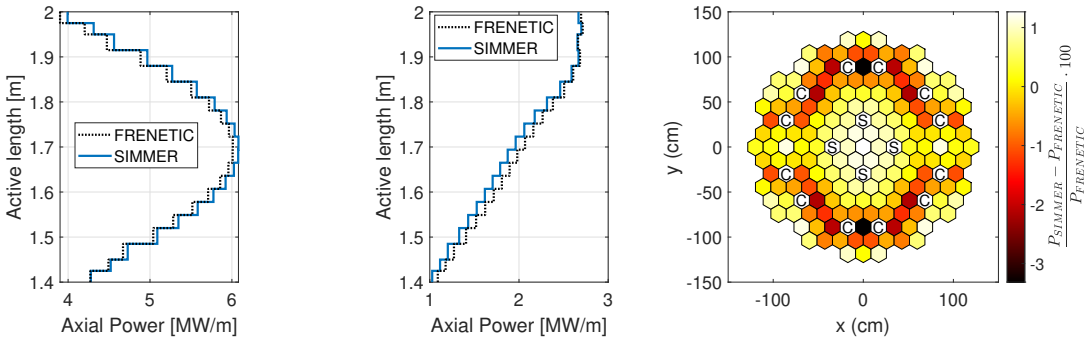

Figure 2.30: Relative difference on the assembly-wise power (right) and axial power profiles (left and centre) for the S_6 case. The left axial profiles correspond to the central FA; the centred ones, to the FA between two CRs in the 2^{nd} sextant.

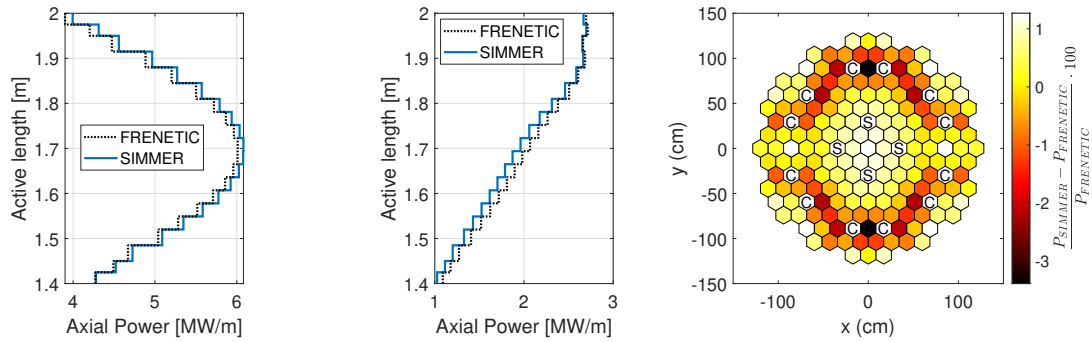

Figure 2.31: Relative difference on the assembly-wise power (right) and axial power profiles (left and centre) for the S_8 case. The left axial profiles correspond to the central FA; the centred ones, to the FA between two CRs in the 2^{nd} sextant.

just 2 %. This agreement is evident also from Fig. 2.32, showing that the CR effect

Table 2.8: Comparison among k_{eff} computed by FRENETIC, SIMMER and Serpent-2 for the configurations with CRs withdrawn and inserted.

	FRENETIC	SIMMER (3D, S_8)	Serpent-2
$k_{\text{eff,CR}_{\text{out}}}$	1.07924	1.08256	1.07616(4)
$k_{\text{eff,CR}_{\text{in}}}$	0.99818	0.99973	0.99999(8)
CR worth (pcm)	8106	8283	7616(9)

on the power per FA predicted by the two codes correspond in most of the positions. The 3D ALFRED B model is adopted for the simulation for both FRENETIC and SIMMER (S_8) employing the same number of axial nodes. The largest discrepancies are observed in the neighbourhoods of the CRs, which is in line with poor representation offered by the diffusion in presence of absorbers. In fact, diffusion fails to adequately model large anisotropies: indeed, the presence of CRs causes a large distortion in the flux - and, hence, in the power - for neighbouring FAs, both radially and axially. The central plots in Fig. 2.28 to Fig. 2.31, representing all the S_N simulations, show that the results of the two codes tend to be very different at the bottom, while the profiles agreement improves with the elevation, where the absorber effect is less significant. Considering that the CRs are inserted from the bottom, this observation is in line with the expectations, in that diffusion, as opposed to transport, is not able to correctly model the flux in the vicinity of strongly absorbing materials. This fact, together with the already commented difference in the cartesian-hexagonal modelling adopted by the codes, produces the evident difference in the radial power map in Fig. 2.31. Therefore, the power distributions of the case having the CR extracted (Fig. 2.33) presents much lower discrepancies than the corresponding case with the CRs inserted. (Fig. 2.31).

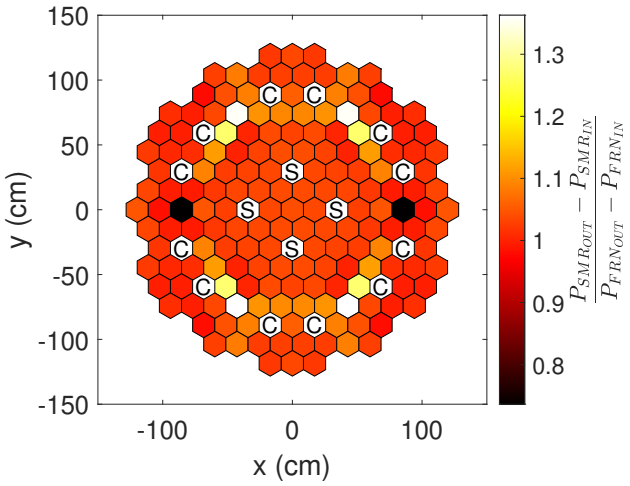

Figure 2.32: Ratio between the power differences calculated by SIMMER and the power differences computed by FRENETIC when the CRs are withdrawn/inserted.

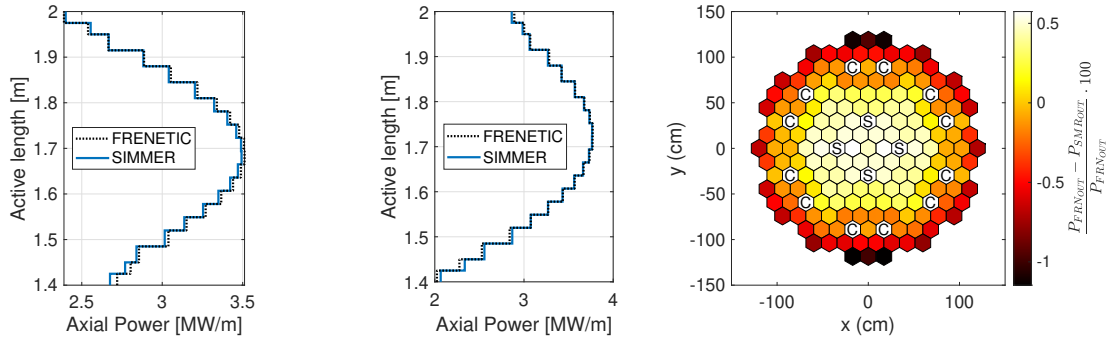

Figure 2.33: Relative difference on the assembly-wise power (right) and axial power profiles (left and centre) for the S_8 case with extracted CR configuration. The left axial profiles correspond to the central FA; the centred ones, to the FA between two CRs in the 2^{nd} sextant.

2.9 Conclusions

The purpose of the first part of the present chapter is to construct an accurate simulation model of the ALFRED core, using the Serpent-2 code as a baseline against which the outcomes of the multi-physics code FRENETIC may be compared. The FRENETIC benchmark exercise in contrast to Serpent-2 enabled the evaluation of the correctness of FRENETIC full-core simulations, while also highlighting some areas that require more research and development. The optimisation of the ALFRED model used in FRENETIC has yielded good results, with a considerable increase in prediction accuracy for neutronic simulations under various temperature settings, and indicating the next step to take in this direction. Several other advancements have been found as a result of these findings:

- extension of the TH module to allow modelling of assemblies with stagnant lead in linked NE-TH mode without the use of fictional assemblies;
- enhancement of the energy group structure by the use of more sophisticated techniques [29].

Regarding dynamic simulation performed with FRENETIC on the ALFRED reactor, the setup of the simulation has been further improved to correctly represent the critical, equilibrium condition of the system, and different perturbations have been introduced to study the most significant physical phenomena of this design. The simulations performed also allowed to identify some limitation in the applicability of FRENETIC for what regards the computational efficiency, related to some optimisation aspects of the NE module currently not exploited totally in the coupled simulation mode. This observation is now leading the current research work, to improve the computational performances of FRENETIC.

In the last part, the comparison between the FRENETIC code and SIMMER has been addressed. Different options for the geometrical representation of a hexagonal core in SIMMER were compared to the coarse-mesh approach adopted in FRENETIC, which is tailored for hexagonal SAs. Neutronic simulations were performed, carefully ensuring the consistency of the nuclear data fed to the two codes, showing that the FRENETIC diffusion solution is in very good agreement with the SIMMER S_N transport solution. As perspectives, the natural prosecution of this benchmark activity would be represented by considering the multi-physics NE-TH coupling in both codes, which would allow to further qualify the FRENETIC code for the multi-physics simulation of LMCRs.

Chapter 3

Neutron-gamma coupled simulation of the EBR-2 during the SHRT-45R

In a fission reactor, the thermal power is mainly due to the energy released by fission. There are also minor contributions to the total thermal power, given by the γ releasing and energy released in matter by the travel of particles. The gamma contribution can be divided into prompt γ , mainly due to fission events, or delayed γ (and β) by emission of delayed neutrons and radioactive decays. Furthermore, the inelastic scattering or radiative captures of neutrons produces γ. The last contributions are quite minor with respect to the former, and it due to kinetic energy released in matter, as known as KERMA. These contributions arise from the travelling of particles (neutrons) and radiation (γ) that, in principle, lose their energy by ionisation and collision. In fact, when a particle is absorbed, the carried energy is deposited in the absorption site.

The FRENETIC code solves the multi-group diffusion equation for neutrons, and in first approximation, the same strategy can be applied also model the diffusion of photons [22]. To perform this, a suitable set of data for the deposited energy by neutrons (KERMA and fission) and gamma rays (KERMA and heat transported by the radiation) must be provided to the code, to correctly simulate the total heat deposition. Thanks to the similarity in the modelling of photons diffusion and neutrons, a set of effective nuclear data must be retrieved from a tool which is able to describe the interaction of photons with matter. To accomplish this, Serpent-2 has been used to compute the attenuation coefficients (Compton and photo-electric effects, Rayleigh scattering and pairs production) for photons, as well as the effective cross sections for neutrons and their related γ production cross section. Therefore, a methodology has been elaborated [30] to calculate from Serpent-2 the entire data set for neutrons and photons.

To test the FRENETIC code when the photons diffusion is included, the case

test of the EBR-2 has been selected. These analyses were previously performed in [27] without considering the photon heat deposition contextually to a Coordinate Research Program (CRP) organised by the IAEA [31]. In this CRP, a set of experimental data collected during two tests were delivered to allow the validation of computational codes for the design of FRs. In this chapter, the description of the test case is provided, with particular emphasis on the test setup during the Shutdown Heat Removal System 45R (SHRT-45R) and on the methodology to build the 3D Serpent-2 model. Afterwards, the discussion about the energy collapsing and spatial homogenisation procedures are presented. From these analyses, the results of the Monte Carlo model are used to generate a cross sections library for neutrons, and the attenuation coefficients for photons. With this set of nuclear data, the steady state simulation during the configuration proposed in the SHRT-45R is carried on with FRENETIC in a coupled scenario NE-PH. The results of FRENETIC simulations are compared with the ones provided by Serpent-2 both for neutrons and photons, to verify both the generation of effective data by means a spatial/energy homogenisation, and the correctly assessment of photon distribution.

3.1 SHRT-45R Test

The SHRT-45R program was carried out in the EBR-2 reactor between 1984 and 1986. Its aim was to support liquid metal reactors design, by providing experimental data for the validation of computer codes for the design. Several tests were conducted, including Loss Of Flow Accident (LOFA) of the primary loop when an unprotected transient is concerned, in order to assess the safety of passive systems and the physical mechanisms for the reactor shutdown as reactivity feedback. Concerning the latter, in a LMCR the shutdown is accomplished for the major part by the Doppler effect in the fuel and its thermal deformation. Other important effects are the deformation of structural materials and the change of coolant density due to temperature distribution. The geometry variations increase the neutron leakage, which implies the lowering of power generation (i. e., changing in neutron spectrum and spatial distribution) and therefore, the passive shutdown of the core.

In this framework, the SHRT-45R test was conducted by simulating an unprotected LOFA both for core and the system at large. The tripping of the primary and the secondary loops was done and the SCRAM procedure was intentionally prevented from being activated. Fuel and sodium temperatures quickly increased, keeping however acceptable values from the boiling point as the power generation was lowered by the passive reactivity feedback. During the transient, the sodium temperature was measured in two different locations inside the core: the first set of measurements was collected in a fuel-loaded assembly (XX09), whereas the other one was assessed by a dummy elements in stainless steel (XX10).

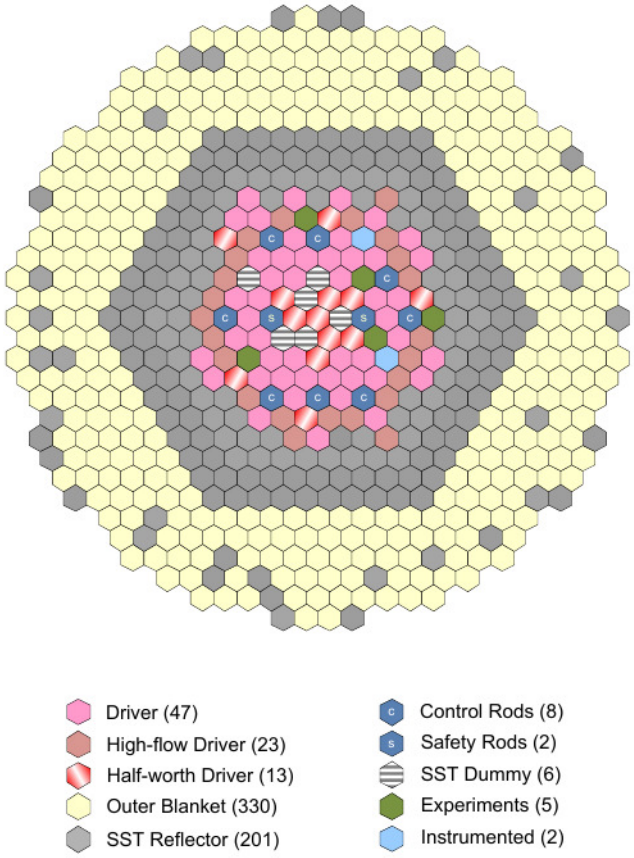

Figure 3.1: EBR-2 core pattern (Run 138B) for the SHRT-45R. In the legend, the typologies of sub-assemblies are also reported.

3.1.1 EBR-2 core configuration in the SHRT-45R

During the SHRT-45R, the EBR-2 core was loaded with a configuration named **Run 138B**. The core was composed by a large variety of Sub-Assemblys (SAs), encompassing also several experimental and two instrumented elements. In Fig. 3.1 the adopted core pattern is shown. Regarding the fuel elements, the inner region of the core was loaded with three types of sub-assemblies: the Half-Worth Driver (HWD), High-Flow Driver (HFD) and nominal driver. The HWDs were nominal drivers where half of the fuel was loaded; the HFDs were drivers with larger sodium mass flow rate from the high-flow plenum with respect to the nominal ones. The control of the reactor was accomplished by 8 High Worth Control Rods (HWCRs). Notwithstanding they were considered as control elements, they were fuelled and completely extracted during the test. By means of this extraction the poison length, constituted by B_4C, was outside the active length of the core. Thus, to give the maximum contribution in terms of reactivity, their active lengths were partially

aligned with the nominal position of the active length of the core. The same criteria was decided for the 2 Safety Rods (SRs), where the insertion led to have the active length below the nominal active length position of the rest of the core. As a consequence, the upper stainless steel reflector inside the driver was partially aligned with the other fuel elements. To allow the extraction/insertion, both HWCRs and SRs were inserted in a hexagonal guide tube fixed to the high-pressure plenum of the core. A group of dummy sub-assemblies in stainless steel were inserted in the central region of the core, denoted by SST Dummy. Other SAs were mainly experimental and they will be described in the next section. To conclude the general overview of the loaded pattern of the inner region of the core, particular attention has to be placed on the instrumented drivers XX09 and XX10, in which the measurements of sodium temperature were carried on. The XX09 was fuelled, whereas the XX10 was totally made in stainless steel. Outside, several rings made in stainless steel enclosed the inner region and they formed the reflector. The latter had the function to increase the neutron flux in the core and, concurrently, to lower the energy of neutrons in order to promote the capture events inside the blanket. The blanket, indeed, was completely loaded with depleted uranium aiming the fertilisation of U-238 and even isotopes of plutonium.

To correctly locate each SA in the core, Argonne National Laboratory (ANL) proposed an identification convention. The core was divided into 6 sextants from A to F, as shown in Fig. 3.2. Moving from the centre to the outside direction in each sextant, a first number could be assigned to the row ($\#_r$) and a second one to the distance from the central SA ($\#_c$). The numeration must follow the reference dashed line of each sextant. In this way, each SA could be identified with an alpha-numerical code $\#_c X \#_r$, where the couple $\#_c \#_r$ was allocated in the sextant X.

3.1.2 Sub-assembly geometry - Core

Generally, all the fuelled SAs inside the inner region of the reactor could be divided into three axial macro regions: the first and the third region were axial reflectors in stainless steel, and the second one contained the active length with fuel. Going into the detail of the geometry description, the fuelled drivers were further divided into two other groups, depending on the manufacturing. The **MARK-IIAI** presented a difference in the fuel elements length with respect to the reference SA of the group **MARK-IIA**. Moreover, the MARK-IIAI drivers belonging to the HFDs presented a bigger hole in the nozzle, in order to increase the sodium mass flow rate. In the 138B configuration, the HWDs belonged to the group of MARK-IIAI. This implied a different geometry for the modelling into the transport code, with higher values of mass flow rate for the TH analyses. Regarding the structural materials, two different stainless steels were used. The SS316 was implied with structural function, as in the wrapper of the SA, the fuel cladding and the wire spacer among

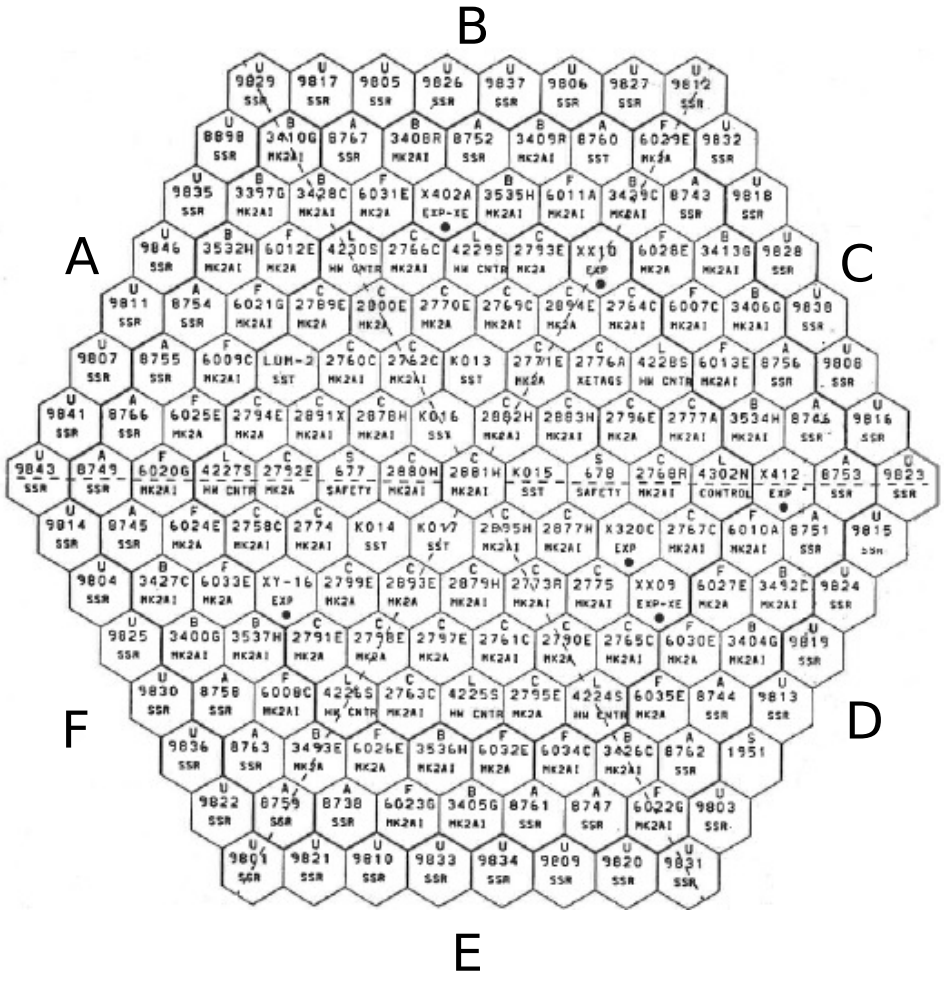

Figure 3.2: SHRT-45R core pattern: sextant division proposed by ANL.

the pins. The SS304 was used for the axial reflectors, for the nozzle in the lowest region of the SA and for the upper fixture in the upper plenum. However, nozzles and upper plenum are not modelled, since the modelling regards the core and not the components of the primary system.

MARK-IIA and MARK-IIAI

The geometrical details for the MARK-IIA and MARK-IIAI are reported in Fig. 3.3. Concerning the details of the fuel disposition, both MARK-IIA and MARK-IIAI presented the same configuration, which also included the case of the HWD where the half of fuel rods were dummy elements made in SS316. Moving to the axial

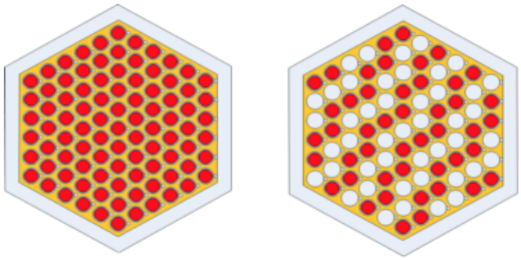

(a) (b)

Figure 3.3: Cross sections of MARK-IIA/MARK-IIAI (a) and the MARK-IIAI partially loaded (b) in the EBR-2 during the SHRT-45R.

description, an example for the MARK-IIAI is shown in Fig. 3.4. The general division among the three regions is clearly visible: the lower and upper shield were made in SS304; in the fuel plenum, He was present to allow thermal-dilatation or deformation induced by fission reaction. It is pivotal to show how, in this type of fuel elements, the gap between the fuel and the cladding was filled by sodium. For the detailed description of each blue prints, please refer to [32].

HWCRs and SRs

The HWCRs and the SRs were manufactured as MARK-IIS driver. They were located in a hexagonal guide tube (thimble), in order to allow the extraction/insertion. This wrapper was fixed and completely made in SS316, whereas the structural material of the SA was made in SS304. As stated before, both HWCRs and SRs were fuelled. With respect to internal structure, the cross section is reported in Fig. 3.5. The HWCRs/SRs presented 61 fuel pins wire-spaced in SS316. The fuel cladding was in SS316, as the hexagonal internal wrapper.

As for the MARK-IIA/I, the axial division was quite the same [32], but the poison elements of B_4C were placed in the upper reflector region. The HWCRs carried 7 poison pins, each of ones had a gas plenum, a spring and an axial reflector

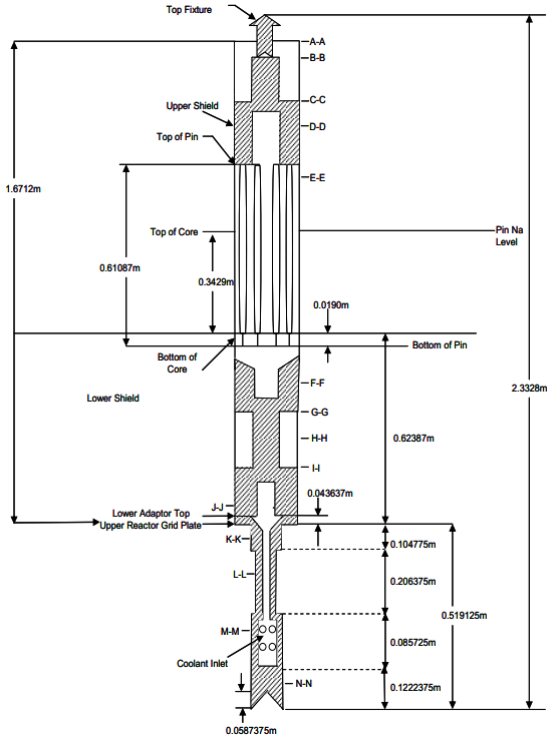

Figure 3.4: Axial scheme of the MARK-IIAI fuel driver.

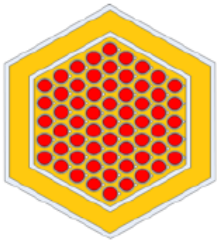

Figure 3.5: Cross section of MARK-IIS in the EBR-2 during the SHRT-45R.

in SS304. Instead, the SRs did not contained poison elements, but a longer axial reflector with respect to the MARK-IIA/I SA.

XX09, XX10, SST-K, XY-16, X320C, X402A, X412 and XETAGS

To conclude the description of the SA typology in the core, a description of the experimental and instrumented drivers. The SST-K dummy element was made entirely in SS304, composed by 7 pins enclosed inside a hexagonal wrapper with the same dimensions of the generic fuel driver.

The XX09 and the XX10 were the instrumented SAs used for temperature measurements. Both SAs were included in a thimble, as in the MARK-IIS. In [32]

the axial scheme of the XX09 is reported. For the location of the thermo-couples, please refer to [32]. Regarding the XX10, there was no fuel in the active region. In fact, its structure was more similar to a dummy element (SST-K) with all the pins in SS304. The XX10 included 19 dummy elements long as the MARK-IIA fuel element. As in the XX09, the flow mixer and the same thermo-couples were also installed in it.

Regarding the experimental elements, they were actually ascribable to the already mentioned MARK-IIA/I, MARK-IIS and SST-K dummy. They are indicated in Fig. 3.2 as XY-16, X320C, X402A, X412 and XETAGS. The XY-16 had 61 solid elements in SS304 with the design of the MARK-IIS, thus, it was located inside a thimble. The X320C was an assembly for structural irradiation, therefore it could be comparable to a SST-K dummy element. The X402A and the X412 were considered as a MARK-IIA element, whereas the XETAGS was a MARK-IIAI completely fuelled, in which Xe TAG gas was loaded into the fuel plenum.

3.1.3 Sub-assembly geometry - Reflector and Blanket

Moving outside, the EBR-2 presented 4 rings for the reflector in SS304. The internal structure was composed by a unique elements with hexagonal shape and 6 cuts to allow the sodium passage. The whole structure (SA wrapper and its internal structure) was composed by SS304. In [32] the axial description is reported. The last region of the core was the blanket, where the fuel elements were fuelled for the major part with depleted uranium, together with fission products and actinides [32]. The typical fuel element for the blanket was formed by 19 pins, wire-spaced inside the hexagonal wrapper (Fig. 3.6). The whole structure, including the cladding for the fuel elements, were made in SS304.

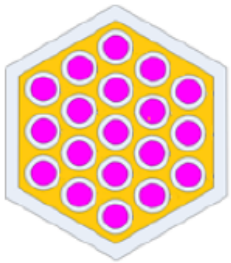

Figure 3.6: Cross sections of blanket elements in the EBR-2 during the SHRT-45R.

3.2 EBR-2 3D Monte Carlo model for the generation of nuclear data

3.2.1 Aim of the study

The methodology to build the Monte Carlo model for the EBR-2 reactor during the SHRT-45R for the generation of collapsed nuclear data for neutrons and attenuation coefficients for γ rays is explained. The evaluation is carried out with a few-groups energy structure by means of a 3D full-core simulation. This level of detail is necessary in order to:

- model the high level of heterogeneity in composition and in-core configuration;
- preserve the differences among the classes of SAs involved during the test;
- optimise the data generation (collapsing domain) for neutrons and γ rays, which is not predictable *a priori*.

The 3D transport model has been organised using the approach in the following. The methodology for the input pre-processing is divided into 4 modules. Each *module* is supposed to treat a different aspect of the methodology. The **geometry module** creates the geometry of the core (radially and axially), mapping ANL labelling with respect to the one adopted in FRENETIC. Subsequently, each class of SA is discretised in coarser regions in order to perform a homogenisation for materials along the axial direction.

The **material module** elaborates the whole inventory of materials in the reactor. The composition for each fuelled element is assessed, using the available data from [32]. For the structural materials and sodium, an average mass composition has been used, as well as for xenon and helium.

The information processed by geometry and materials modules are then passed to the **mesh module**: the geometry of each sub assembly class is coupled with its related composition, to build the core geometry at full level element-by-element. The generation of integral data is in charge to the Group Constant Universe (GCU) module, in which the strategy to collapse few-groups energy constants is optimised both for neutrons and γ particles.

3.2.2 Geometry

Core map

In the Run 138B, the core was loaded with 637 SAs with a regular pattern for each sextant. Each sextant contained 160 SAs, with the exception of the sextant A, where the central assembly belonged to. A pure geometrical construction has been performed to obtain the coordinates of each driver, ensuring the above-mentioned

correspondence with ANL convention. To construct the core geometry, some considerations about the SAs geometries must be done: all the loaded drivers presented the same maximum encumbrance, although they could have different internal organisation. This encumbrance is delimited by the external wrapper which is the same for all the assemblies, as shown in Fig. 3.7. To model also the clearance of

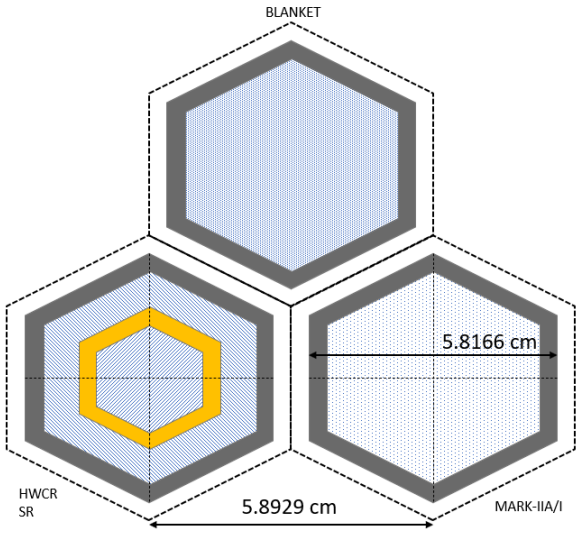

Figure 3.7: Details of the radial geometry for the construction of the core in the transport model.

coolant among the drivers, the maximum encumbrance has been virtually extend to a larger hexagonal area, whose apothem is half of the drivers pitch as to take the same amount of sodium per SA. In Fig. 3.7, the clearance of sodium can be seen in the blank area delimited by the wrapper (grey) and the external dashed line. The pitch between two SAs was 5.8929 cm with the distribution reported in Tab. 3.1. The generic coordinates of the driver centre in the sextant A are given by

Table 3.1: Number of SAs in each sextant.

I_r	1	2	3	4	5	6	7	8	9	10	11	12	13
I_{FA}	13	12	12	11	10	9	9	8	7	6	4	3	2

$$\begin{cases} x_{c,A} = x_0 - p(\mathrm{I_{FA,i}} - 1) + \dfrac{\mathrm{p}}{2}(\mathrm{I_r} - 1) \\ \\ y_{c,A} = y_0 + l\left[1 + \sin\left(\dfrac{\pi}{6}\right)\right](\mathrm{I_r} - 1) \end{cases} \tag{3.1}$$

where the factor I_r refers to i^{th} row from 1 to 13, $I_{FA,i}$ considers the element number in the same row (up to I_{FA}) , l is the hexagon side, p is the pitch and $(x_0,\ y_0)$ are

the coordinates of the second driver with $(-p,\ 0)$ centre. The latter translation is necessary to not to consider the central element since it is in common with the other sextants. With these information, the sextant A can be built.

Setting the angle θ of rotation to 60°, the integer $\mathrm{I_{sext}}$ is changed from 0 to 5 (A to F) according to the sextant that has to be built, and due to the symmetry, the centres of the sextant A can be easily rotated over the entire angle in order to obtain the whole set of coordinates.

$$\begin{bmatrix} x'_{c,sext} \\ y'_{c,sext} \end{bmatrix} = \begin{bmatrix} \cos(\mathrm{I_{sext}}\theta) & \sin(\mathrm{I_{sext}}\theta) \\ -\sin(\mathrm{I_{sext}}\theta) & \cos(\mathrm{I_{sext}}\theta) \end{bmatrix} \begin{bmatrix} x_{c,A} \\ y_{c,A} \end{bmatrix} \tag{3.2}$$

The nomenclature proposed by ANL is expressed by the relationship

$$\begin{cases} X_{col} = \mathrm{I_{FA,i}} + \mathrm{I_r} \\ Y_{row} = \mathrm{I_r} \end{cases} \tag{3.3}$$

where $\mathrm{I_{FA,i}}$ encompasses from 1 to $\mathrm{I_{FA}}$, and $\mathrm{I_{FA}}$ and $\mathrm{I_r}$ have the same meaning (and reciprocal relation) of the previous equations. In this way, the equivalence between the geometrical position of SAs and the alpha-numerical nomenclature can be used to link the geometry to the reactor configuration. The Table 3.2 shows the results of the geometry modelling, and by means of this set of coordinates, for each sextant from A to F the relationship between the ANL convention and the geometry of the model can be assessed to properly collocate each driver.

Table 3.2: Correspondence between the core geometry and the nomenclature proposed by ANL.

$\mathrm{x_c}$ [cm]	$\mathrm{x_c}$ [cm]	$\mathrm{X_{col}}$	S	$\mathrm{Y_{row}}$
0	0	1	A	1
−5.892900	0	2	A	1
−11.78580	0	3	A	1
−17.67870	0	4	A	1
−23.57160	0	5	A	1
−29.46450	0	6	A	1
−35.35740	0	7	A	1
−41.25030	0	8	A	1
−47.14320	0	9	A	1
−53.03610	0	10	A	1
−58.92900	0	11	A	1
−64.82190	0	12	A	1
−70.71480	0	13	A	1
−76.60770	0	14	A	1

With the same approach, the core map can be retrieved also for FRENETIC. Since the mesh is the same for both codes, the geometrical disposition of core elements does not change. On the contrary, the element numeration for FRENETIC

follows a different logic: the core lattice is filled moving in the opposite direction along the x axis, keeping the same orientation for the y axis. This can be obtained by inverting the rotation direction:

$$\begin{bmatrix} x'_{c,FRN} \\ y'_{c,FRN} \end{bmatrix} = \begin{bmatrix} \cos(\mathrm{I}_{\mathrm{sext}}\theta) & -\sin(\mathrm{I}_{\mathrm{sext}}\theta) \\ \sin(\mathrm{I}_{\mathrm{sext}}\theta) & \cos(\mathrm{I}_{\mathrm{sext}}\theta) \end{bmatrix} \begin{bmatrix} x_{c,A} \\ y_{c,A} \end{bmatrix} \tag{3.4}$$

In this way, the orientation to map the sextants is kept since the reference axis is always tilted by 60°. Refer Fig. 3.8 for the correspondence.

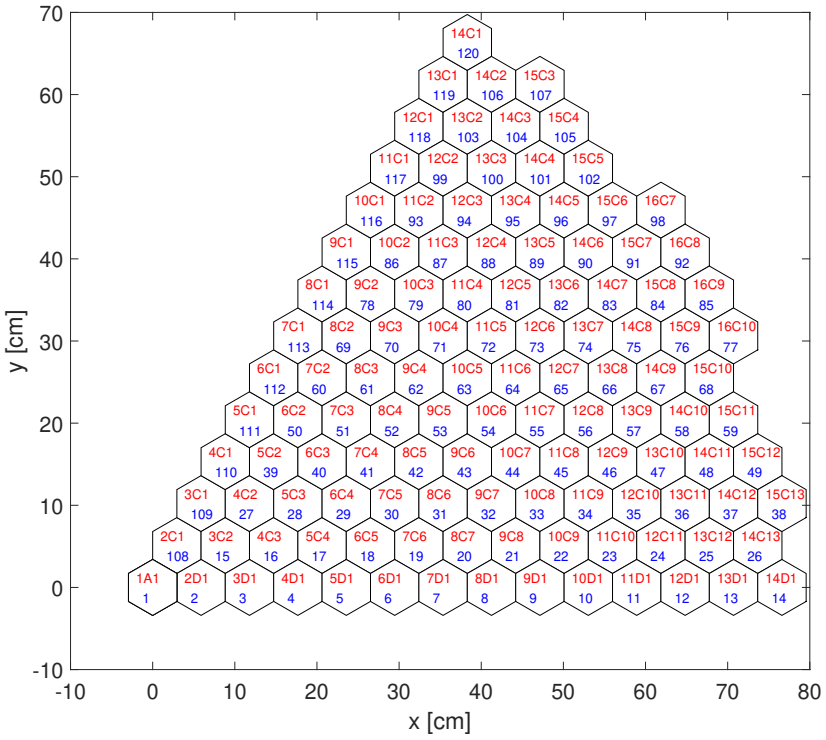

Figure 3.8: Core map with the ANL label and related numeration in FRENETIC. In red the ANL convection and in blue the numeration in FRENETIC are, respectively, reported.

The guideline to correctly load the core pattern is given by Fig. 3.2. Each element can be classified with respect to its typology, taking also into account the level of fuelling. For instance, a driver of the MARK-IIAI class could have the half of fuel and this leads to have a further division among drivers of this family. In Fig. 3.9 the core map for the Monte Carlo model is shown: this fine classification of SAs takes into consideration not only the geometry of the driver itself (along the axial direction), but also the mass of fissile material.

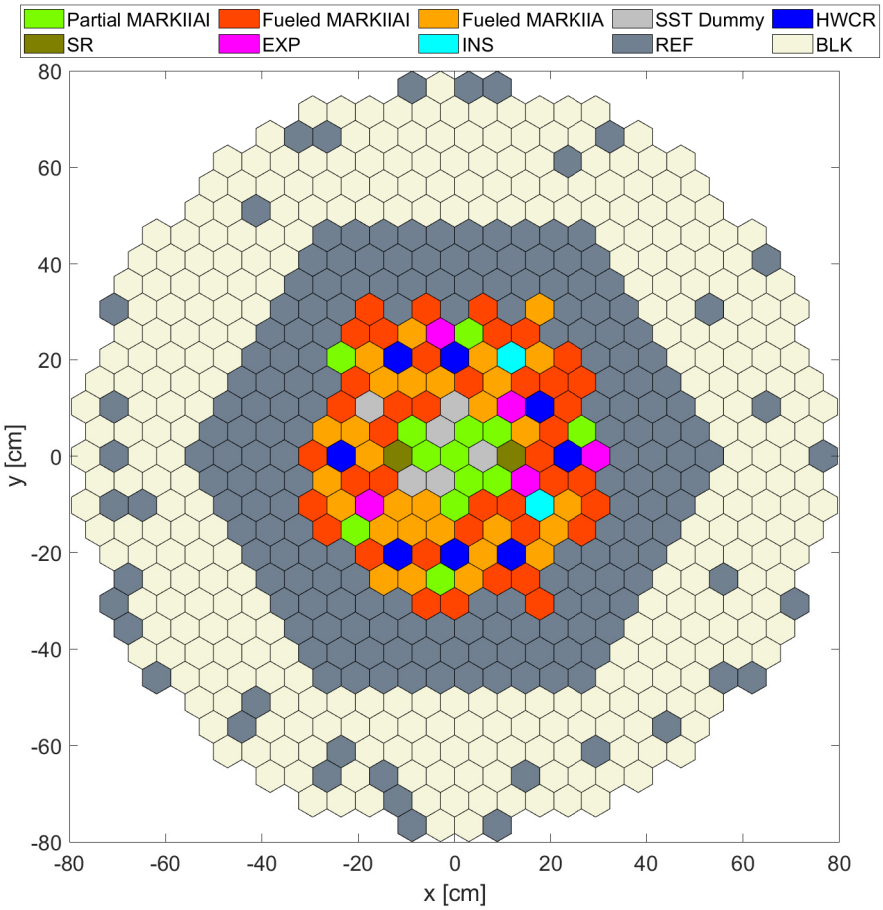

Figure 3.9: Core map of the EBR-2 3D Monte Carlo model during the SHRT-45R.

Sub-assembly axial discretisation

The axial modelling has been carried on using the detailed geometries in available in [32]. The target is to provide the volume fractions of each material in each type of SA. By means of this, the spatial homogenisation technique has been adopted. The hypothesis behind this approach is related to the expected neutron behaviour: the core geometry was relatively small if it is compared with the mean free path of neutrons, therefore the spatial effects inside the SA can be considered negligible. This practice is well accepted in fast systems, taking also in account the smallness of the SAs.

As specified in the benchmark deliverable, the experimental drivers (XY16, X320C, X402, XETAGS and X412A) can be adequately associated to the already discussed SAs. Therefore, the structures to be analysed are:

- MARK-IIAI partially loaded;
- MARK-IIAI fully loaded (containing XETAGS);
- MARK-IIA (containing X402 and X412A);
- HWCR MARK-IIS;
- SR MARK-IIS;
- SST-K dummy element (containing XY16 and X320C);
- Radial reflector;
- Blanket fuel assembly;
- Instrumented driver (XX09 and XX10).

Secondly, for each type a coarse discretisation has been introduced to separate all the regions where there are significant differences in geometry and/or composition. The axial discretisation is reported in the next table. As said before, the generic SA can be divided into 3 main regions: lower reflector, active length, upper reflector. Notwithstanding this, the active length (when present) has been to further separated by the plenum region to isolate the fuel from other non fissile materials (helium in particular).

The next step is the calculation of the real volumes of each materials, accordingly to the considered structure moving along the axial direction:

$$V_{\mathrm{TOT_i}} = \sum_{i=1}^{N_{\mathrm{reg}}} V_i = \sum_{i=1}^{N_{\mathrm{reg}}} A_i \Delta z_i \tag{3.5}$$

where

- $\mathrm{N_{reg}}$ is the number of region where the $\mathrm{i^{th}}$ material is present
- A_{i} is the $\mathrm{i^{th}}$ area of the considered material
- Δz_i is the height of the volume concerning the $\mathrm{i^{th}}$ material

In this way the total volume $V_{\mathrm{TOT_i}}$ of the $\mathrm{i^{th}}$ material is calculated for each coarse region.

The last step is the calculation of the volumes fraction with respect to a reference volume. The latter is assumed to be:

$$V_{\mathrm{ref}} = A_{\mathrm{hex}}(z_n - z_{n-1}) \tag{3.6}$$

where A_{hex} is the hexagonal cross section area that embraces also the sodium clearance between contiguous assemblies. To be more understandable, please refer to Fig. 3.10: the grey area represents the area occupied by the generic assembly, as

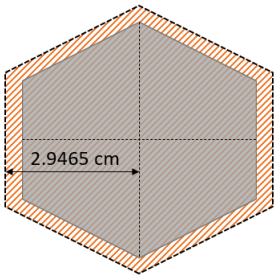

Figure 3.10: Reference area for the axial homogenisation (not in scale)

they had the same encumbrance. The dashed orange area regards the external clearance of the generic assembly. In this way, each driver includes also the related portion of sodium among the others in order to consider the volume of sodium of the clearance. The value 2.9465 cm is the half of the pitch. The difference $z_n - z_{n-1}$ is the distance between the generic two planes which defines the coarse region in where the homogenisation is performed. Thus, the homogenisation procedure is carried on according to:

$$x_{V_{j,n}} = \frac{V_{TOT_j}}{V_{ref}} = \frac{\sum_{i=1}^{N_{reg}} A_i \Delta z_i}{A_{hex} \Delta z_n} \text{ with } \mathrm{n} = 1, ..., \mathrm{N_{hom}}, \mathrm{j} = 1, ..., \mathrm{N_{mat}} \tag{3.7}$$

where $\mathrm{N_{hom}}$ is the number of homogenised regions and $\mathrm{N_{mat}}$ is the number of materials. Depending on materials which are involved (fuel, stainless steel, plenum gas or $\mathrm{B_4C}$), the sodium volume is computed as the difference with respect to the others. Moreover, although there may be negligible differences in composition of SS304 and SS316, their respective volume fractions are calculated by considering

Table 3.3: Example of volume fractions calculated for the MARK-IIAI fully loaded.

Driver type	Coarse regions	Materials	Fractions
MARK-IIAI	Lower Ref	SS304	0.5108
		SS316	0.0669
		Na	0.4223
	Active length	fuel	0.2694
		SS304	0
		SS316	0.2230
		Na	0.5408
	Plenum	He	0.2964
		SS304	0
		SS316	0.2271
		Na	0.4615
	Upper Ref	SS304	0.4748
		SS316	0.0669
		Na	0.4583

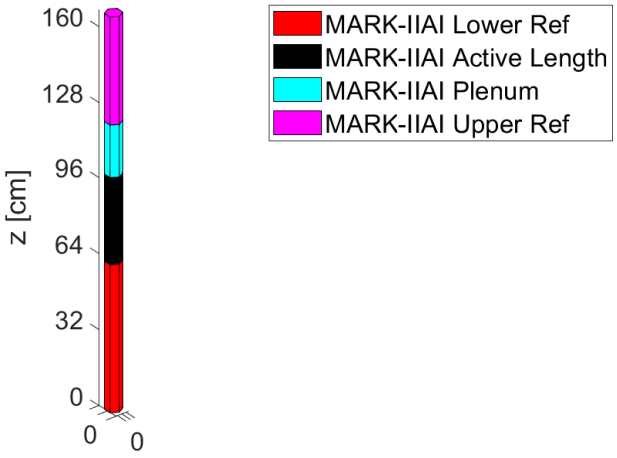

Figure 3.11: Example of axial discretisation in the 3D Monte Carlo model of the EBR-2: the homogenised regions are reported for the SA class MARK-IIAI (fully loaded)

them as different. An example of the output of the procedure is reported in Table 3.3. In this example the division in coarse regions is expanded with the detail about the materials and their volume fractions. Similar results have been obtained for the whole set of SA classification, which is not reported in this study to simplify the discussion. The Fig. 3.11 represents the coarse regions (for the MARK-IIAI) where the homogenisation has been performed.

In the next flowchart (Fig. 3.12) the procedure is resumed. This method has been applied for each SA class of the entire core, to provide a complete description of the geometry starting from detailed information and moving towards the simulated model.

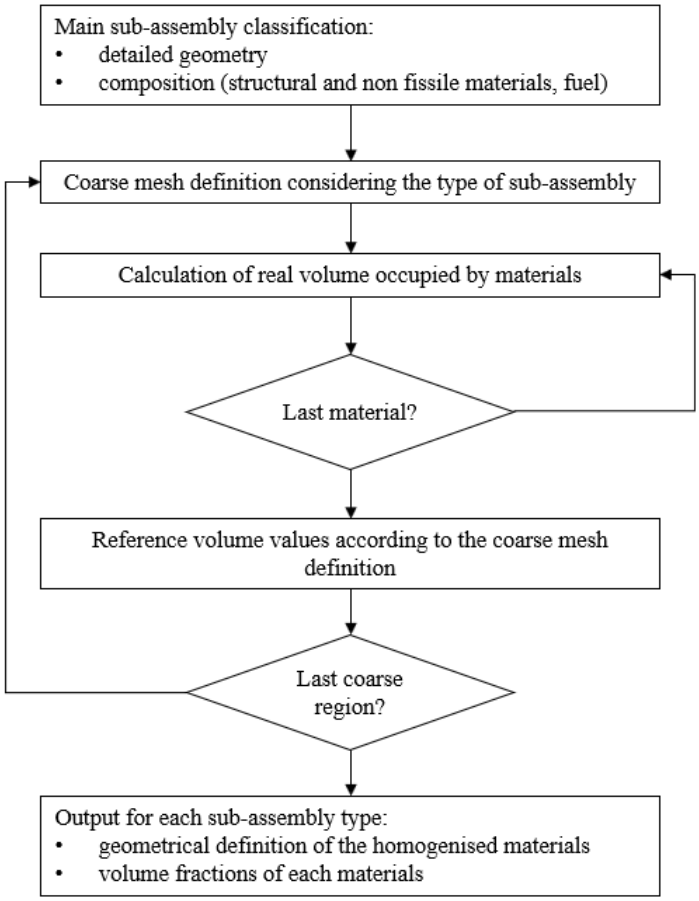

Figure 3.12: Flowchart of the spatial homogenisation for the axial modelling in the 3D Monte Carlo model of the EBR-2.

3.2.3 Material inventory

After the geometry modelling, the materials inventory has been analysed. The benchmark specifications gives the whole isotopic composition for the inner core and the blanket. The nominal fuel employed in the EBR-2 was the U-5Fs, although the core was partially depleted before running the SHRT-45R test. Therefore, the isotopic composition has been given after a burnup corresponding to the fuel swelling of 6.88%, which made necessary the inclusion of fission products and actinides in the original composition. These information are specified for three equal segments along the active length, where the first is lower part, the second the middle one and the third the last one. The Table 3.4 shows the table-type with the isotopic composition for each assembly. The Lumped-Fission-Product (LFP) entries indi-

Table 3.4: Example of isotopic composition in [atoms/(barn cm)] for the MARK-IIAI fuel assembly 1A1.

Isotope	**1A1$_1$**	**1A1$_2$**	**1A1$_3$**
U-234	8.32093489023E-08	9.89178923581E-08	7.19888149055E-08
U-235	3.45383816412E-03	3.44914295295E-03	3.46751551840E-03
U-236	1.75723381505E-05	1.73345154977E-05	1.53747751836E-05
U-238	1.74865995117E-03	1.74814960213E-03	1.74957857944E-03
Np-237	1.29516379409E-07	1.44908506460E-07	1.06754812219E-07
Pu-236	8.46740506475E-14	1.14073217454E-13	6.06560041200E-14
Pu-238	7.61553044693E-10	8.29153878552E-10	5.60322418162E-10
Pu-239	4.88128442942E-06	4.86668844687E-06	4.27090697740E-06
Pu-240	8.72196716598E-09	7.98951422355E-09	6.70047461794E-09
Pu-241	1.31241359165E-11	1.15726748345E-11	8.79862159181E-12
Pu-242	1.38488315535E-14	1.20707754976E-14	8.03667047486E-15
Am-241	4.54547476100E-14	4.02155043639E-14	2.99135986394E-14
Am-242m	3.23745017110E-17	2.80712386044E-17	1.86655057945E-17
Am-243	1.04172446076E-17	8.68971310664E-18	5.38622376975E-18
Cm-242	1.00274400107E-16	8.69318348011E-17	5.77990701932E-17
Cm-243	3.16120402450E-20	2.40149844333E-20	1.63679144157E-20
Cm-244	1.79030443285E-20	3.55805143812E-21	2.20572855153E-21
Cm-245	4.07166671213E-24	4.02992016064E-25	2.79742722868E-25
Cm-246	3.59918557076E-28	2.35607737876E-29	1.51736976618E-29
LFP:U-235	2.94226428628E-04	2.99156400355E-04	2.82825231071E-04
LFP:U-238	2.52969812222E-06	2.97870320774E-06	2.18368147300E-06
LFP:Pu-239	7.34810754989E-08	7.92980338586E-08	5.55484309261E-08
LFP:Pu-240	3.27429737180E-11	3.41801166150E-11	2.13305484821E-11
LFP:Pu-241	1.09959804191E-13	1.02202498781E-13	6.30781206645E-14
La-139	1.89359907857E-05	1.92820074350E-05	1.81755707159E-05
Nd-148	5.01356690063E-06	5.10645042594E-06	4.81320386747E-06
Fissium	6.71053356410E-04	6.71053356410E-04	6.71053356410E-04

cate the sum of atomic composition derived from the fission of the father-isotopes. These values have been specified in a second document during the CRP. The last row named Fissium reports other fission products, which were present only in the

inner core. As for the LFP, the Fissium entries were released later. The information provided for the LFP reports the absolute composition of the other isotopes that has to be normalised with respect to the total quantity reported in the rows "LFP:Z-A", where Z is the element and A is the mass number. The composition of LFP is normalised as

$$x_{\mathrm{LFP,i}} = \frac{m_{\mathrm{LFP,i}}}{\sum_{j=1}^{\mathrm{N_{LFP}}} m_{\mathrm{LFP,j}}} \ , \ i = 1, ..., \mathrm{N_{LFP}} \tag{3.8}$$

where $\mathrm{N_{LFP}}$ is the total number of LFP isotopes. Then, the set of LFP for each father-isotope is obtained with

$$\boldsymbol{V}_{\mathrm{LFP:Z-A}} = \boldsymbol{X}_{\mathrm{LFP}} M_{\mathrm{LFP:Z-A}} \tag{3.9}$$

where $\boldsymbol{V}_{\mathrm{LFP:Z-A}}$ indicate the vector of normalised LFP normalised on the $\mathrm{i^{th}}$ LFP value, the $\boldsymbol{X}_{\mathrm{LFP}}$ are the mass fractions vector and $M_{\mathrm{LFP:Z-A}}$ the total quantity of LFP reported in Table 3.4. The same approach is adopted for the Fissium entry, as the mass fractions for Fissium isotopes are also provided.

The composition tables refer to the cross section area with the half of the pitch, as in the radial description is defined. Each composition is processed following the next procedure:

1. the $\mathrm{i^{th}}$fuel assembly is selected
2. the composition is read from the data of the benchmark specification. For each segment of the active length:
   (a) the LFPs are calculated
   (b) the Fissium composition is calculated
   (c) the complete set of isotopes is retrieved
3. the isotope name is converted into the library format of the transport code, associating the provided calculation to the $\mathrm{i^{th}}$ fuel assembly label

In this way, each SA accords with its fuel composition in format proposed by ANL, that is then passed to the mesh module to construct the input for the simulation. The above algorithm is repeated for each composition presents in the data of the benchmark. Due to the large computational resources to store all the data for each fuel assembly, an average fuel composition has been derived from this level of detail. In fact, the mentioned procedure is performed at each level of the fuel and consequently, the memory usage for each SA is multiplied by a factor 3. Moreover, there are negligible differences among the most important isotopes in the three levels of the active length. The average value for the generic isotope $\mathrm{x_{th,avg}}$ is simply

calculated by a weighted average on the volume but, due to the same volume of each segment, it results as

$$x^i_{\text{avg}} = A_{\text{ref}} H \frac{x^i_1 + x^i_2 + x^i_3}{3 A_{\text{ref}} H} = \frac{x^i_1 + x^i_2 + x^i_3}{3}, \; i = 1, ..., \text{N}_{\text{itp}} \tag{3.10}$$

where x^i_1, x^i_2, x^i_3 are the related concentrations in each segment for the isotope i, H is the total height of the active length and A_{ref} is the hexagonal cross section area referred to the pitch and N_{itp} is the total number of isotope in the fuel. It should also point out that no information are available about the mass density of the fuel at this burnup, therefore the hypothesis to keep the dependency on the temperature only for the microscopic cross section has been adopted, keeping constant the atomic densities. With this assumption, the information about the temperature is inserted in the fuel inventory by changing the reference temperature in the microscopic cross section libraries, whereas the mass density is given by the sum of atomic densities.

As already mentioned, the structural materials employed were two austenitic stainless steels. The SS316 was used mainly for the cladding of the fuel rods, for the wrapper of the MARK-IIA/I and the MARK-IIS, whereas the SS304 for the external thimble in the MARK-IIS, in the blanket, in the radial reflector and for the lower/upper shields. As for the fuel, both compositions are calculated in such way that the homogenisation with the other materials is straight forward. The reference compositions are provided in mass fractions and they are reported in Tab. 3.5

Table 3.5: Mass composition for the SS316 and SS304 in the EBR-2.

Element	**SS316**	**SS304**
C	0.00070	0.00080
Cr	0.17000	0.19000
Fe	0.66605	0.68845
Mn	0.02000	0.02000
Ni	0.11000	0.09000
P	0.00045	0.00045
S	0.00030	0.00030
Si	0.01000	0.01000
Mo	0.02250	0
Sum	1	1

Each element is assumed to be composed by the most abundant isotope in the natural composition. With respect to the assumptions for the fuel about the temperature dependency, here the effect is taken into account for the mass density too. In other words, the microscopic cross section from the library will be loaded at the modified temperature, as well as the mass density will be changed according to the new value.

The EBR-2 was cooled by sodium. Since there are no information about its composition, the latter has been assumed to be composed by pure sodium. The mass density value (g/cm^3) is selected according to [33].

The last material to describe is the absorber in the HWCRs. The neutronic poison consisted of B_4C, with the natural B composed by B-10 and B-11. As specified in the benchmark document, the mass density is assumed to be independent of temperature and it is fixed at 2.40 g/cm^3. The mass fractions are reported in Table 3.6.

Table 3.6: Composition of B_4C expressed by mass fractions for the poison length of the HWCR in the EBR-2.

Isotope	**Mass fraction**
B^{10}	0.1449
B^{11}	0.6377
C^{12}	0.2174
Sum	1

3.2.4 Serpent-2 input

The aim of this part of the pre-processing is the coupling of what has been done in the geometry with respect to the assembly typology, and the related information about the composition of the entire set of materials in each assembly. The functions of the mesh module are:

- to extract the geometry from the ith assembly of each coarse region;
- to create the homogenised composition library for each coarse region;
- to build the Serpent-2 input.

The geometry of each coarse region is constant with respect to the position in the core, therefore a data-set for the generic assembly typology can be constructed. In this data-set, the information related to the heights of coarse regions are reported since the reference cross section area is constant. Other information required are the materials and their quantities. As Table 3.7 shows, in the last column a Serpent-2 identifier is defined: these labels allow the code to correctly identify the region, i. e. the material mixture with a unique name for that specific class of SA. As a consequence, it is not to further necessary to define the common materials among the same typology: the only region which is crucial to distinguish is the *active length* since the fuel volume contains a different material depending on the core position, although the volume fractions are constant. This allows to save computational memory because the material mixture not fuel-inclusive is always the same

Table 3.7: Example of the generic assembly data-set used by the mesh builder for Serpent-2.

MARK-IIAI	**[z_{n-1} z_n] cm**	**x_v**	**Materials**	**Serpent-2 entry**
Lower Ref	0 - 62.387	0.0669 0.5108 0.4233	SS316 SS304 Sodium	MARKIIAIf_LR
Active Length	62.387 - 99.037	0.2693 0.2230 0 0.5077	Fuel SS316 SS304 Sodium	MARKIIAIf_AL
Plenum	99.037 - 121.574	0.2964 0.2271 0 0.4615	He SS316 SS304 Sodium	MARKIIAIf_PL
Upper Ref	121.574 - 167.12	0.0669 0.4748 0.4583	SS316 SS304 Sodium	MARKIIAIf_UR

for the considered class of SA. Moreover, this common definition enlarges the computational domain in which the scoring is performed, thus increasing the quality of results.

The material libraries are calculated for each data-sets. For mixtures that are not depending on the core position, the respective volume fractions are considered and the homogenised composition is created in this way:

1. to read the Serpent-2 identifier from the SA class data-set;
2. to identify the respective volume fractions;
3. to create the mixture with the Serpent-2 identifier

The mixing operation is obtained by using the *mix* command of Serpent-2. The latter can be used to facilitate the generation of materials in such a way to get the access to the general database where the composition inventory is stored, and then to perform the homogenisation by weighting the masses on the volume fractions. Results of this procedure are shown in Table 3.8. Concerning the active lengths, the mixing procedure must take into account the specific composition or, in other words, the core position. In fact, a proper mixed material has to be generated according to SA class and the related composition. It should be emphasised that the fuel composition is already normalised on the reference cross section area on which the volume fractions are calculated, therefore the fuel composition was first divided by its volume fraction in the materials inventory, and afterwards multiplied again by the same in the mixing operation. This operation is consistent since the fact that the volume in which the mixture is then positioned (the computational volume in the Serpent-2 mesh) is the same of the homogenisation procedure. Going back to

Table 3.8: Homogenised composition example for Serpent- 2.

Mixture	**Volume fractions**
mix MARKIIAIf_LR	
SS316	6.688239E-02
SS304	5.107714E-01
Sodium	4.223462E-01
mix MARKIIAIf_PL	
He	2.964E-01
SS316	2.271E-01
SS304	0.0000
Sodium	4.615E-01
mix MARKIIAIf_UR	
SS316	6.688239E-02
SS304	4.748473E-01
Sodium	4.582703E-01

the generation of the mixture for the active length, each SA in its class is thus processed with the association of ANL label: according to the SA classification, the active region is uniquely identified with its core position and it contains its average fuel composition. An example is given in Table 3.9, which reports the whole set of mixtures for a generic assembly belonging to the MARK-IIA class.

Table 3.9: Example of mixtures set for the MARK-IIA class used in Serpent-2.

mix MARKIIA_LR	
SS316	6.688239E-02
SS304	5.107714E-01
sodium	4.223462E-01
mix MARKIIA_AL_4A1	
fuel_4A1	2.692672E-01
SS316	2.230324E-01
sodium	5.077004E-01
mix MARKIIA_PL	
He	3.013099E-01
SS316	2.270846E-01
sodium	4.688164E-01
mix MARKIIA_UR	
SS316	6.688239E-02
SS304	4.701310E-01
sodium	4.629866E-01

Now the the geometry in Serpent-2 can be created following the next logic:

1. creating the reference geometry of the generic SA (hexagonal base area, infinite in z direction);

2. filling the above surface with each material as it was axially infinite;

3. cutting the material with the respective planes considering the proper axial discretisation;

4. putting this portion of the infinite material into the respective volume in the considered assembly identified by ANL label;

5. filling the core lattice using ANL label.

This approach gives the possibility to extract singularly the integral nuclear data of a single region (axially) or to compute them by integrating all over the volume. In fact, the way of how to perform the scoring depends not only on compositions/geometry, but also on the position. Therefore, to be more flexible as possible the input has been prepared to calculate the parameters at the lowest geometrical level, i. e, the single axial region in each SA. The points 1 and 2 produce a list of materials that are all infinite along the z direction inside a hexagonal surface. Since Serpent-2 is universe-based, each material fills the reference surface in order to have a *material-universe*, which is easier to collocate inside the final geometry. Refer Fig. 3.13. The points 3 and 4 complete the final assembly geometry: each

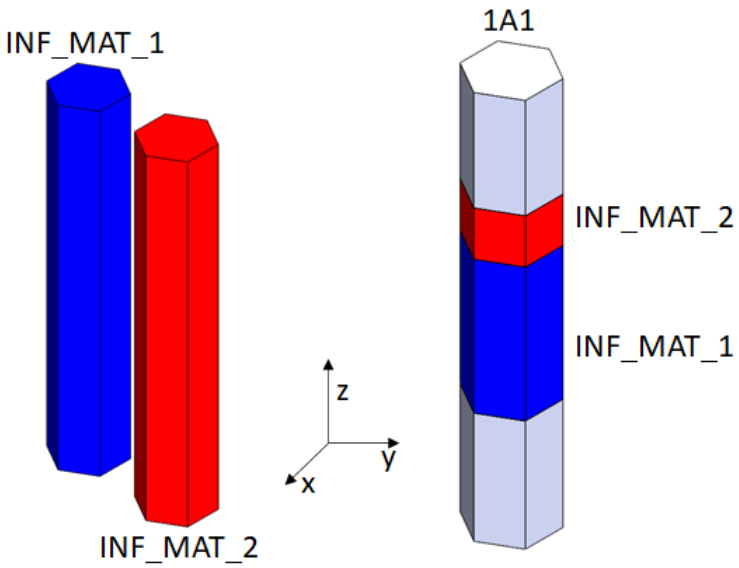

Figure 3.13: Example of Serpent-2 filling procedure to create the mesh in the 3D Monte Carlo model for the EBR-2.

material-universe is cut by its couple of planes along the axial direction, and then it is filled in the final universe of the i^{th} SA. In this way, each core driver has its proper description along the vertical axis, each region is a defined universe where Serpent-2 can perform the collapsing, and finally the entire SA can be placed in the core lattice (point 5).

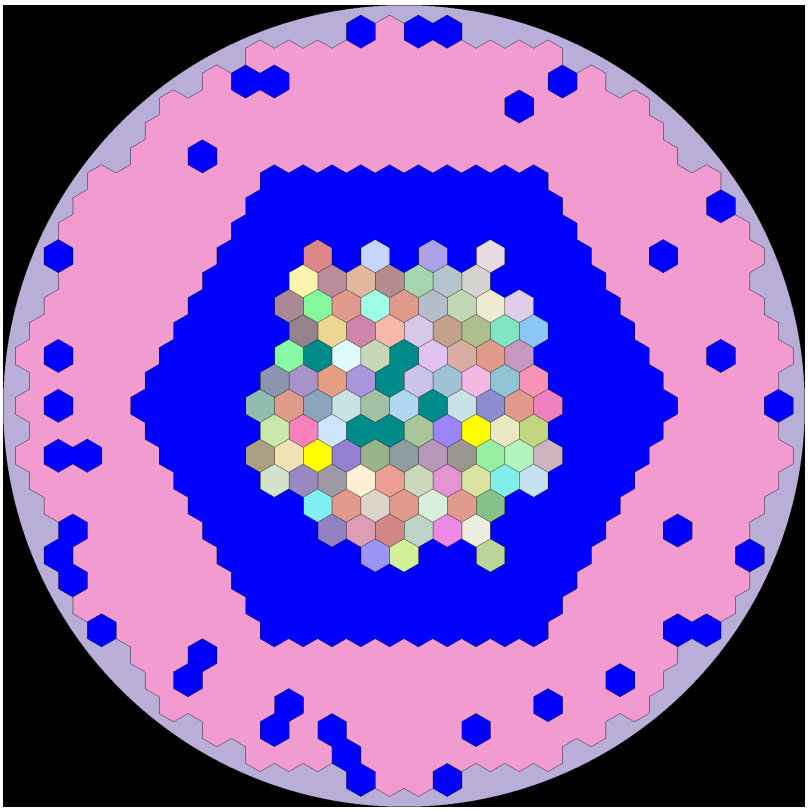

Figure 3.14: EBR-2 core lattice simulated in Serpent-2 in the plane (x, y).

The results of this methodology are reported in the next two figures. Fig. 3.14 shows the core lattice at the middle active length in the plane xy. Each colour represents the mixed composition with structural materials, sodium and fuel in each element. Due to the fact of having different fuel vectors, the heterogeneity can be appreciated since each SA has a slightly different composition. The blue region corresponds to the SS304 radial reflector and now homogenised in stainless steel and sodium; the pink region is the blanket, which appears filled with the same material. In fact, to optimise the memory consumption, an average composition for this region has been calculated: the presence of U-235 is negligible since the blanket was designed to hold fertile materials as U-238, Th-232 or plutonium even isotopes. Therefore, a low neutrons importance can be expected as well as their energy distribution. Moreover, the discrepancy among the average blanket composition and the original one-by-one is quite low, thus the approximation is well justified.

In Fig. 3.15 the section is taken along the y axis in the centre of the core, showing the plane (x, z). The internal description of fuel assemblies is pointed out. The

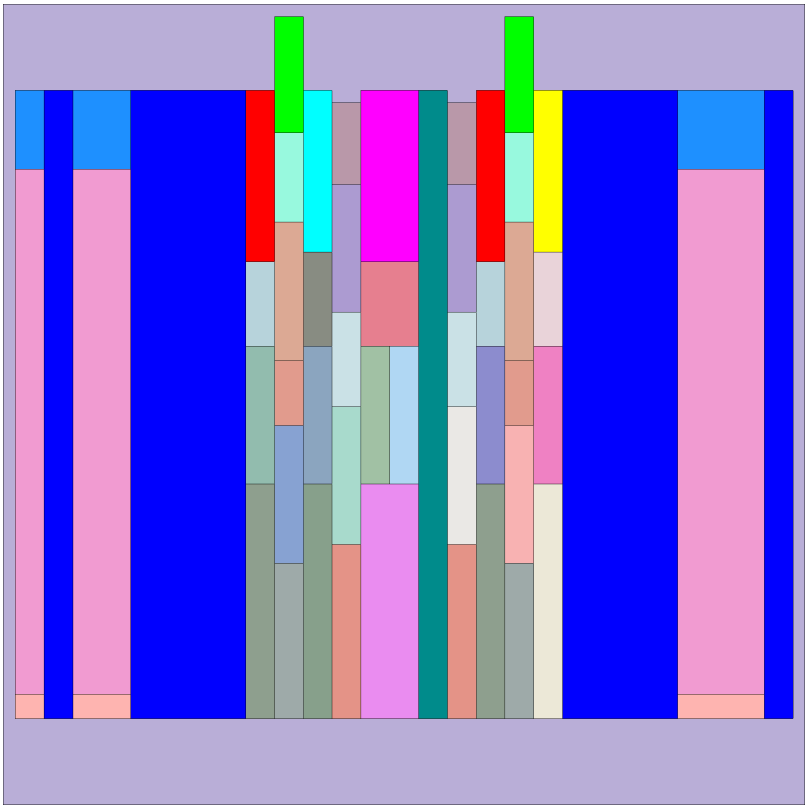

Figure 3.15: EBR-2 core lattice simulated in Serpent-2 in the plane (x, z) at y = 0.

common materials have the same colour, whereas the active regions are different as said in the previous paragraph. In Fig. 3.16 the position of the HWCRs can be also

noticed: the level of withdrawal was such that the bottom of the fuel bundles of the HWCR was lower of 21.06 cm than the bottom of the fuel bundle of the generic fuelled driver. In this position, the B_4C did not face the active region of the core, setting up the condition for an unprotected accident. For the SR (not reported in figure), the insertion level was of 15.97 cm below the active length of the active region, in order to have the fuel bundle of the SR partially inserted in the colder region of the core.

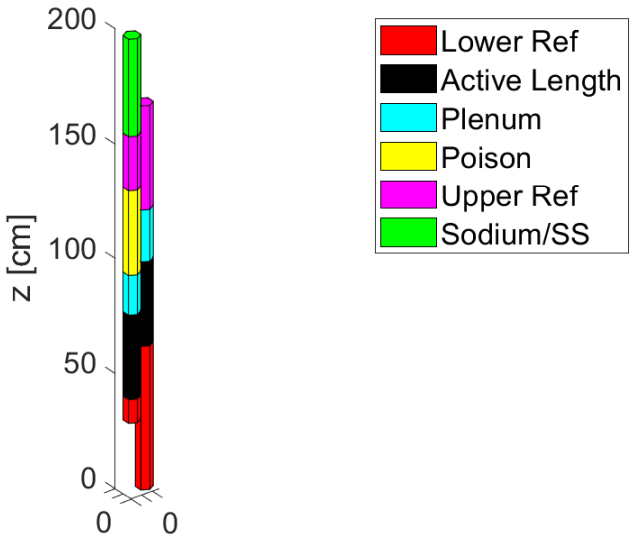

Figure 3.16: Relative position of the HWCR with respect to the common fuelled driver.

3.2.5 Neutron spectra and spatial distribution analyses

The homogenisation of nuclear parameters for both neutrons and photons requires further considerations for the group constant generation, for the spatial definition of the integration domain and the energy structure of the collapsing groups. The ENDF/B-VIII library has been used [34] in Serpent-2 calculations, together with an additional library for photons from the MCNP code at temperature of 400 K.

As far as the energy discretisation of the neutrons energy is concerned, the group-structure can be defined by analysing the spectra of fuel elements one-by-one. Fig. 3.17 shows the spectra of the fuel assemblies in the inner core by integrating the flux in the active region. This result indicates that the neutrons energy distributions are quite the same at the higher energy moving from the centre of the core (fuel elements with index 1S#) towards the periphery (fuel elements with row 7S#) as S is the generic sextant and # is the elevation with respect the core centre. Moving

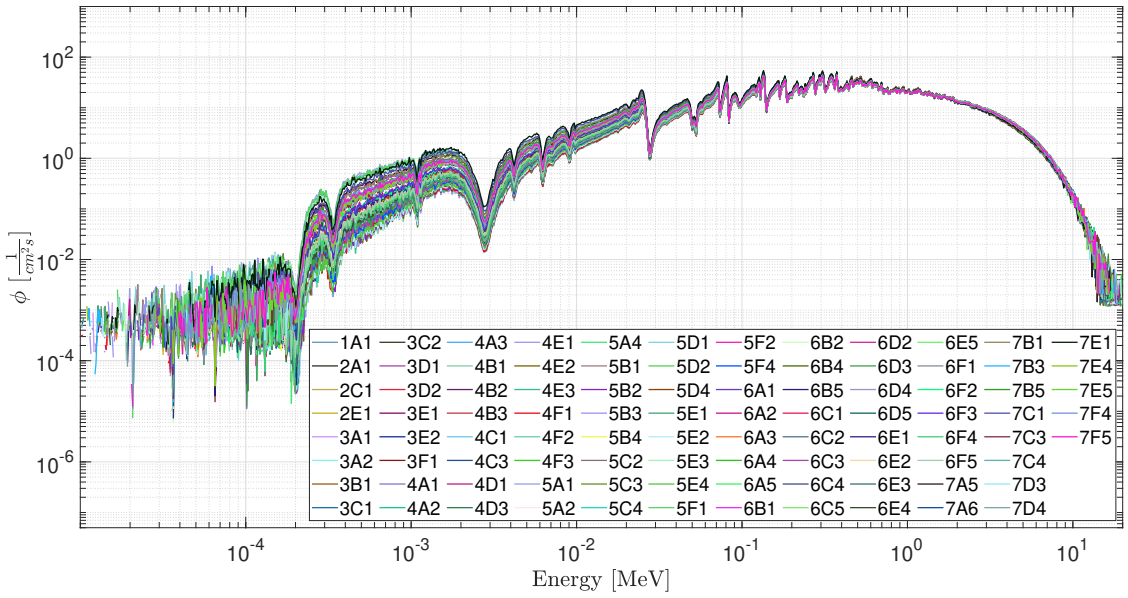

Figure 3.17: Active length spectra of the inner core.

close the radial reflector, the probability to have a neutron with the energy between 2E-4 MeV and 1E-2 MeV tends to be higher. This effect can be explained with the scattering of the stainless steel at lower energies for the external fuel elements. As the system considered is fast, at energy lower than 2E-4 MeV, the statistical quality worsen since the total interaction rate is quite low.

Regarding the blanket and radial reflector, the spectra have been calculated considering their respective entire domains. The statistical quality is better, since the results are evaluated on a larger spatial domain with respect to the single fuel assembly. In fact, the neutrons in the inner region of core have a mean free path of order of 5 cm, which is almost twice the physical dimension of the single core element. Moreover, considering what has been said in the material processing, the blanket region has a proper average composition, thus the local spatial information on fuel discrepancies is lost. Going trough the analysis of these spectra (Fig. 3.18), the radial reflector energy distribution confirms the influence on the peripheral fuel elements of the inner core about the increasing of the interaction probability: in the energy range $[1E-4; 1E-3]$ MeV the spectrum presents a relative maximum. Also at lower energies (below 1E-4 MeV), neutrons collide inside the reflector, a non-negligible fraction travel towards the blanket with even lower energy. The effect is clearly visible in the spectrum of the blanket. The energy range around 1E-5 MeV presents the characteristically captures by plutonium isotopes and U-238. This implies that the final energy structure for the homogenisation has to take into account also what happens below 1E-4 MeV, despite the bad quality of results for the inner core region. Moreover, the photon production is expected to be

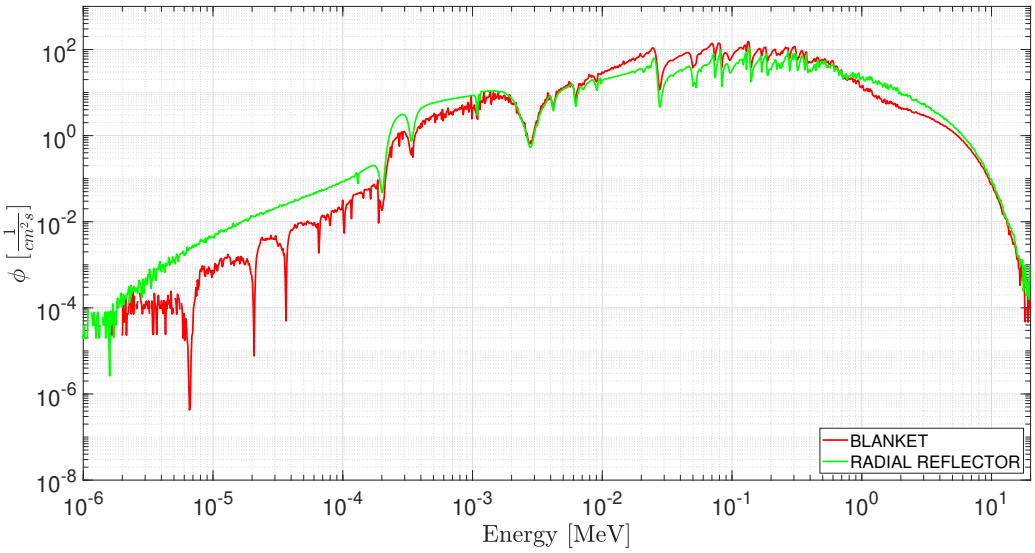

Figure 3.18: Reflector and Blanket spectra for the EBR-2 using the Super Imposed Universes (SIUs) for the spatial homogenisation.

important due to capture events in the by fertile isotopes, confirming the necessity of having a group energy structure that is able to describe the above-mentioned phenomena.

By means of these analyses, some preliminary conclusions about the spatial definition of the collapsing domains can be drawn. The relative position among SAs of the same class is quite negligible if it is compared with the length travelled by a neutron arising from the inner region of the core, since the spectra have the same distribution nearby the centre. Therefore the entire inner active region could be described by a single domain between the centre and the radial reflector. To verify this hypothesis, a more general space definition to calculate the spectrum of the core has been introduced in the model. Radially, the core has been divided into 3 regions:

- the **inner core**, in turn divided into 3 axial parts:
  - the lower part corresponding to the **lower axial reflector**;
  - the active part corresponding to the **active length**;
  - the upper part corresponding to the **upper axial reflector**;
- the **radial reflector**;
- the **blanket**.

The lower part of the inner region has been defined considering the dimensions of the lower reflector of the generic MARK-IIA/I SA, since it is the most representative

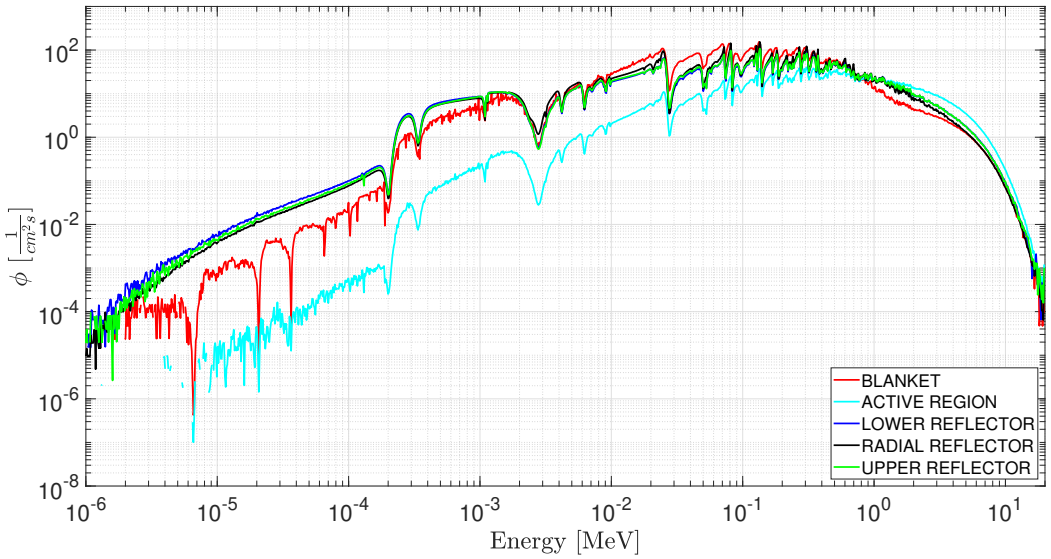

Figure 3.19: EBR-2 spectra of the SIUs for the group constant generation analysis.

fuel assembly in the inner core. The same consideration has been done for the upper one. As a consequence, the shifting of HWCRs and SRs is lost in this process due to the partial insertion of their active lengths inside the considered domain. Results are shown in Fig. 3.19. With respect to Fig. 3.18, the blanket and the reflector do not present any difference, since the integration domains are the same. On the contrary, the spectrum calculated on the volume corresponding to the active length of the generic MARK-IIA/I presents a better statistic at lower energy. Apart from this secondary effect, mainly due to the increase of the integration volume, the shape remains quite the same. This confirms the above-supposed hypothesis about the low effect of the related positioning among the fuel assemblies, in that neutrons are not dramatically affected by discontinuity in element geometry due to the high value of their mean free path as compared to the pitch of core elements. Upper and lower axial reflectors present the same behaviour of the radial reflector, supporting the effect of the scattering of neutrons also in the axial direction. At this point, a few-group energy structure can be adopted for neutrons. The tally used here is the same presented in [35] (Table 3.10). This energy subdivision aims to represent the considerations already illustrated. In Fig. 3.20 the energy structure is reported on the spectra. The first group preserves mainly the fission spectrum, since at those energies the major events are the emission of fast neutrons; the second and the third groups isolate the absorption due to sodium; the fourth takes into account the absorption due to manganese present in the stainless steel; the fifth group gives importance to the scattering effects provided by stainless steel and finally the sixth one allows to take into account for the capture events in the blanket. This

Table 3.10: Six-group data adopted to perform the group constant energy generation.

Group	Upper boundary [MeV]	Lower boundary [MeV]
1	$2.0 \cdot 10^{1}$	$4.0 \cdot 10^{-1}$
2	$4.0 \cdot 10^{-1}$	$6.0 \cdot 10^{-2}$
3	$6.0 \cdot 10^{-2}$	$1.0 \cdot 10^{-2}$
4	$1.0 \cdot 10^{-2}$	$1.5 \cdot 10^{-3}$
5	$1.5 \cdot 10^{-3}$	$2.5 \cdot 10^{-4}$
6	$2.5 \cdot 10^{-4}$	$1.0 \cdot 10^{-11}$

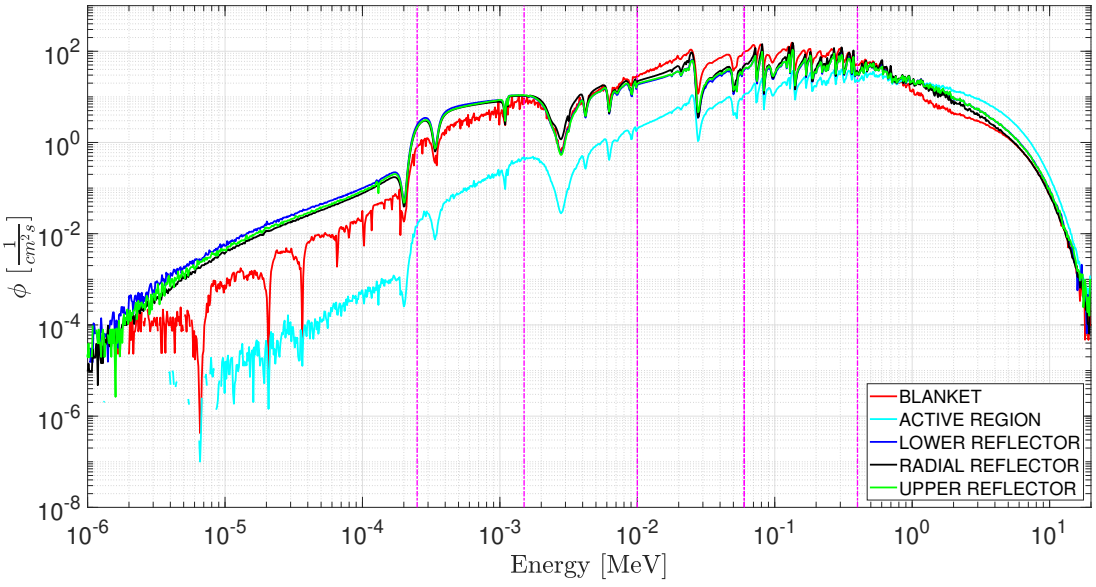

Figure 3.20: Energy group structure applied to the EBR-2 spectra (spatial collapsing in SIUs) for the group constant generation for neutrons.

energy grid has been already employed in [35] to study the transient of the SHRT-45R, where the reactor was modelled as a homogeneous cylinder to calculate the cross sections for neutrons. Furthermore, since this model improves the geometrical description of the system preserving the local position of core elements, the previous analysis has pointed out that the geometrical effects (positioning, differences in SA classes) have a low effect on the energy distribution of particles, thus it is reasonable to adopt the same energy structure.

To complete the discussion, the spatial neutron flux distribution has been analysed taking advantage of the previous spectral analyses. Figure 3.21 reports the flux distributions in the plane (x, y) with the adopted energy sub-division, spatially integrated along the axial length. These results are in good agreement with the conclusions arisen from the energetic analyses: neutrons travel long distances without experiencing relevant distortions at higher energies (Figs. 3.21a, 3.21b and 3.21c), where the majority of fast fission occurs. As the energy decreases, the radial reflector presents higher value of the flux, which means that neutrons are decreasing their energy due to scattering after the shortening of their mean free path (Figs. 3.21d, 3.21e). The last group shows (Fig. 3.21f) a lesser presence of neutrons in the inner regions of the system. The latter explains the darker colour in the inner region with respect to Fig. 3.21e, whereas the reflector continues to have particles at thermal energy.

As Serpent-2 performs the estimation of reaction rates by using Monte Carlo techniques, quantitative information related to the accuracy of results are also provided. The entire estimation has been carried out by using the parameters reported in Table 3.11. The last point for the neutron constants generation regards

Table 3.11: Serpent-2 parameters for the evaluation of spatial homogenisation domains and the few-structure energy grid.

Serpent-2 setup	Values
Particles number per batch	5E6
Inactive cycles	50
Active cycles	500
MPI processes	8
OMP threads per MPI	12

the analyses of the cross section, which resumes the accuracy of the line of reasoning to build the temperature-dependent library. In Table 3.12 the effective total cross sections for the considered domains are reported. First, the 1st group shows the order of magnitude of the mean free paths in the respective region: the maximum length that a neutron can be travelled is around 5 cm, which is almost the dimension of a single core element. As the lowest group is concerned, the mean free path is reduced below 1 cm, especially in the radial reflector. This confirms the hypothesis

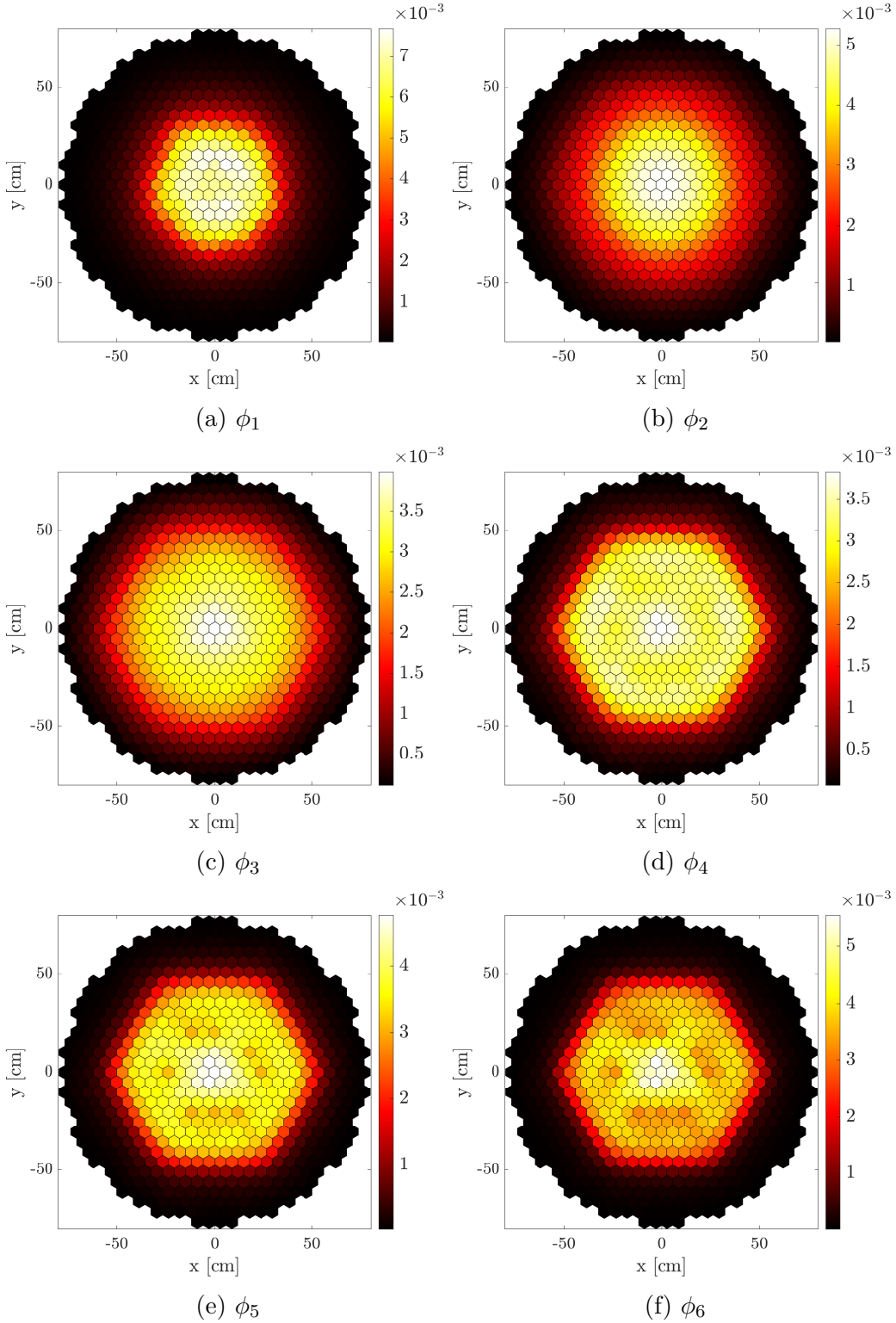

(a) ϕ_1 (b) ϕ_2

(c) ϕ_3 (d) ϕ_4

(e) ϕ_5 (f) ϕ_6

Figure 3.21: Spatial distribution of neutron flux in the six group energy structure.

Table 3.12: Σ_t calculated with the six groups energy structure according to the five coarse regions. Results are in cm^{-1}.

Domain	$\Sigma_{t,1}$	$\Sigma_{t,2}$	$\Sigma_{t,3}$	$\Sigma_{t,4}$	$\Sigma_{t,5}$	$\Sigma_{t,6}$
LOWER REF	0.18160	0.19828	0.28167	0.48957	0.49172	1.1989
ACTIVE CORE	0.18841	0.23361	0.31620	0.46287	0.45204	0.97528
UPPER REF	0.11843	0.14055	0.20899	0.39260	0.37534	0.96883
RADIAL REF	0.20996	0.22865	0.32860	0.55543	0.62305	1.5748
BLANKET	0.29913	0.39251	0.47708	0.55627	0.52463	0.94770

to have a great amount of particles in this region, therefore it is reasonable to expect an important generation of photons in this volume.

Concerning the Relative Standard Deviation (RSD) of Serpent-2 results, the values are reported in Table 3.13. The highest value is in the core, according to have very few interactions in that region with energies in the considered range. Notwithstanding this, the value is still acceptable since the thermal flux is very low, as Fig. 3.21f shows.

Table 3.13: RSD of the Σ_t calculated with the six groups energy structure according to the five coarse regions.

Domain	$RSD_{t,1}$	$RSD_{t,2}$	$RSD_{t,3}$	$RSD_{t,4}$	$RSD_{t,5}$	$RSD_{t,6}$
LOWER REF	1.38e-05	1.74e-05	2.60e-05	3.00e-05	3.00e-05	5.6e-04
ACTIVE CORE	5.00e-06	7.60e-06	1.50e-05	6.60e-05	7.20e-05	1.4e-03
UPPER REF	3.40e-05	3.00e-05	4.60e-05	7.00e-05	9.80e-05	6.6e-04
RADIAL REF	9.60e-06	9.20e-06	1.26e-05	1.16e-05	1.64e-05	3.6e-04
BLANKET	1.02e-05	9.20e-06	1.22e-05	3.20e-05	3.60e-05	5.2e-04

A further level of description of the system can be obtained with the evaluation of cross sections inside some critical sub-domains as the HWCRs, SRs, and the other classes of core elements that are different from the common fuel elements. In fact, the location of experimental driver, instrumented and control ones can be preserved by calculating the data inside their volume. For instance, the effect of the poison length inside the HWCRs can be accurately assessed by collapsing in there the cross sections. The same logic can be adopted for the cold assemblies as the dummy elements SST-K and the XX10, avoiding the thermal power generation which derives from the integration with the other fuelled drivers. Results for the HWCRs of this calculation are reported in Table 3.14. The HWCRs were located in proximity of the radial reflector and partially extracted. As a consequence, the extraction level implies the inclusion of fission reaction rates in those regions that are at zero fission power (LOWER and UPPER REF in the inner core) and a larger statistics in the 6^{th} group due to scattering of the reflector. Moreover, the presence of the B_4C is a singularity in the modelling when the diffusion theory is used, for

Table 3.14: Σ_t calculated with the six groups energy structure into the HWCRs poison length domain. Results are in cm^{-1}.

Domain	$\Sigma_{t,1}$	$\Sigma_{t,2}$	$\Sigma_{t,3}$	$\Sigma_{t,4}$	$\Sigma_{t,5}$	$\Sigma_{t,6}$
$5A1_{B4C}$	0.22423	0.30067	0.38922	0.55051	0.56975	1.2801
$5B1_{B4C}$	0.22366	0.30081	0.38973	0.54955	0.56844	1.2843
$5B3_{B4C}$	0.22378	0.30064	0.38996	0.54974	0.56840	1.2784
$5C3_{B4C}$	0.22370	0.30073	0.39003	0.54947	0.56822	1.2817
$5D1_{B4C}$	0.22425	0.30074	0.38939	0.55085	0.56814	1.2778
$5E1_{B4C}$	0.22371	0.30076	0.38964	0.55039	0.56801	1.2840
$5E3_{B4C}$	0.22356	0.30078	0.39009	0.54965	0.56688	1.2805
$5F1_{B4C}$	0.22395	0.30071	0.38939	0.55054	0.56840	1.2794

instance in the FRENETIC code. To overcome this, a detailed analysis has been conducted. Results show that there are negligible differences among the HWCR elements for the whole set of energy groups. On the other hand, their inclusion in the coarse domains of the inner core would lead to an under-estimation of reaction rates if they were integrated with the other elements. Furthermore, the poison will be virtually dislocated inside the inner core, losing the information of spatial effect due to local absorption. These effects can be avoided by defining a proper sub-domain for the integration of data, in order to average the cross sections all over the HWCR drivers. Details on SST-K dummy or SR elements are not discussed due to their collocation nearby the centre where the interactions are considerably at higher energy, therefore it is reasonable to assume that the positioning is unimportant for spectral effects.

To conclude the analysis on neutrons cross sections generation, the discussion on the spatial integration has led to the definition of the collapsing domain with the next guideline. The relative positioning at higher energy has a negligible influence with respect to the heterogeneity in composition and geometry. Relevant effects are appreciable at lower energy, where the mean free path of neutrons are quite smaller than the assembly geometry and the particles become sensible to difference in compositions. An example is the capturing in the blanket by the plutonium isotopes. The former are also present in the fuel elements of the inner region, but the the spectra analysis does not show evidence of appreciable capturing events. Thus, since the inner region faces the major part of fast neutron flux, an element-by-element approach is redundant. This suggests to preserve the heterogeneity in those assemblies that are dummy or instrumented ones, to avoid the generation of power if the entire inner region is used for the cross sections homogenisation. Therefore, the power generation can be taken as a first criterion for the domains generation. This first approach identifies the domains on which the cross sections ca be generated, and they are resumed in Table 3.15.

Table 3.15: EBR-2 general collapsing domain for the homogenisation of integral data.

INNER CORE	RADIAL REFLECTOR	BLANKET
Lower reflector Active region Upper reflector HWCRs SRs SST-K X320C, XY16 XX10, XX09	Reflector elements	Blanket driver Reflector elements

3.2.6 Generation of the attenuation coefficients for photons

Regarding the photons production and their propagation, some clarifications for the next discussion are required. At the moment Serpent-2 is not well optimised for the generation of the attenuation coefficients, alike for neutron cross sections. First, the code is not able to calculate the multi-group data with the same straightforward approach used for neutrons: the limitation on the multi-group constants generation arises from the impossibility to reconstruct the scattering matrix if a few-group energy grid is provided. Therefore, all the calculations for the generation of attenuation coefficients here discussed are assumed to be in a mono-kinetic approach. Secondly, Serpent-2 cannot currently model photo-nuclear reactions as (γ, n), thus only the photo-atomic ones can be simulated, as *Compton scattering*, *photo-electric effect*, *Rayleigh scattering* and *pair productions*. However, in the next future the capability to take into account also photo-nuclear reactions will be available, as reported in [36].
A strategy to overcome these limitations has been studied to retrieve attenuation coefficients to be used in the FRENETIC code. The general definition to calculate the effective attenuation coefficient in a certain group for the x^{th} reaction can be written as

$$\bar{\mu}_{x,g}(\boldsymbol{r}) = \frac{\int_{E_{i-1}}^{E_i} dE' \phi_p(\boldsymbol{r}, E') N(\boldsymbol{r}) \sigma_x(E')}{\int_{E_{i-1}}^{E_i} dE' \phi_p(\boldsymbol{r}, E')} \tag{3.11}$$

if the (E_{i-1}, E_i) energy interval is considered. As mentioned above, the incapability to generate multi-group constants leads to the collapsing of energy-dependent quantities on the whole energy axis. Therefore, the 3.11 for the g_{th} group can be generalised in

$$\bar{\mu}_{x}(\boldsymbol{r}) = \frac{\int_{-\infty}^{\infty} dE' \phi_p(\boldsymbol{r}, E') N(\boldsymbol{r}) \sigma_x(E')}{\int_{-\infty}^{\infty} dE' \phi_p(\boldsymbol{r}, E')} \tag{3.12}$$

By knowing the photon flux and its distribution, the microscopic cross section for the x^{th} photon reaction and the atomic composition distribution the parameter can be assessed. Here comes the advantage of having defined the material as a mixtures: the dependency on the space is lost, and the integration for the x^{th} photo-reaction in a single homogenised region becomes

$$\bar{\mu}_x = \frac{\int_{-\infty}^{\infty} dE' \phi_p(E') N \sigma_x(E')}{\int_{-\infty}^{\infty} dE' \phi_p(E')}. \tag{3.13}$$

The above relation is correct only if the composition is made by a single nuclide. Since the attenuation coefficient represents the probability per unit length to suffer a collision for a given element as the photon travels along its direction, the total probability in a mixture to suffer a collision per unit length is given by

$$\bar{\mu}_x = \bar{\mu}_{x,1} + \bar{\mu}_{x,2} + \bar{\mu}_{x,3} + ... + \bar{\mu}_{x,N} \tag{3.14}$$

if N is the total number of elements involved in the mixture in the integration domain. Therefore, the generic attenuation coefficient for a given mixture in a defined domain using the mono-kinetic approach can be finally expressed as

$$\bar{\mu}_x = \sum_{i=1}^{N} \frac{\int_{-\infty}^{\infty} dE' \phi_p(E') N_i \sigma_{x,i}(E')}{\int_{-\infty}^{\infty} dE' \phi_p(E')} \tag{3.15}$$

where N is the number of involved elements in each region. This implies that Serpent-2 has to score only the photon flux since the homogenised mixture is known by the input, and the microscopic cross sections are retrieved for each element by the code with a separate routine. To be useful for FRENETIC, the photo-atomic reactions have been re-organised as in the next, since the code is not able to manage secondary photons:

- Rayleigh and Compton scattering summed in a *scattering coefficient* μ_s;
- pairs-production and photo-electric effect summed in an *absorption coefficient* μ_a.

The last element to complete the set of data required for FRENETIC is the diffusion coefficient D_γ. Serpent-2 does not provide an estimation for the diffusion coefficient for photons, thus an approximation for it must be adopted with the available data. Assuming that photons are well treated by a single group diffusion equation, a first approximation of D_γ can be formulated using the P_1 definition as

$$D_\gamma = \frac{1}{3\left(\mu_t - \mu_{s,1}\right)} \tag{3.16}$$

where μ_t is the total attenuation coefficient as the sum of the above-defined scattering and absorption coefficients, and $\mu_{s,1}$ is the first moment of the scattering coefficient. Due to the lack of information about the scattering moments, the diffusion of photons is assumed to be isotropic and the previous definition degenerates in:

$$D_\gamma = \frac{1}{3\mu_t} \tag{3.17}$$

Although this definition is correct in the framework of photon modelling by diffusion theory, other studies have investigated the dependency of the diffusion coefficient on the absorption coefficient. In [37], an alternative definition is exposed and the diffusion coefficient is assumed to be independent on the absorption coefficient. In conclusion, the definition here used to retrieve the D_γ is

$$D_\gamma = \frac{1}{3\mu_s} \tag{3.18}$$

Photon flux distribution and spectral analyses

In Fig. 3.22 the energy distributions of photons inside the main coarser regions adopted for neutrons are shown, (without the refinement proposed in Table 3.15) to allow a consistent comparison. Scattering phenomena (Rayleigh and Compton)

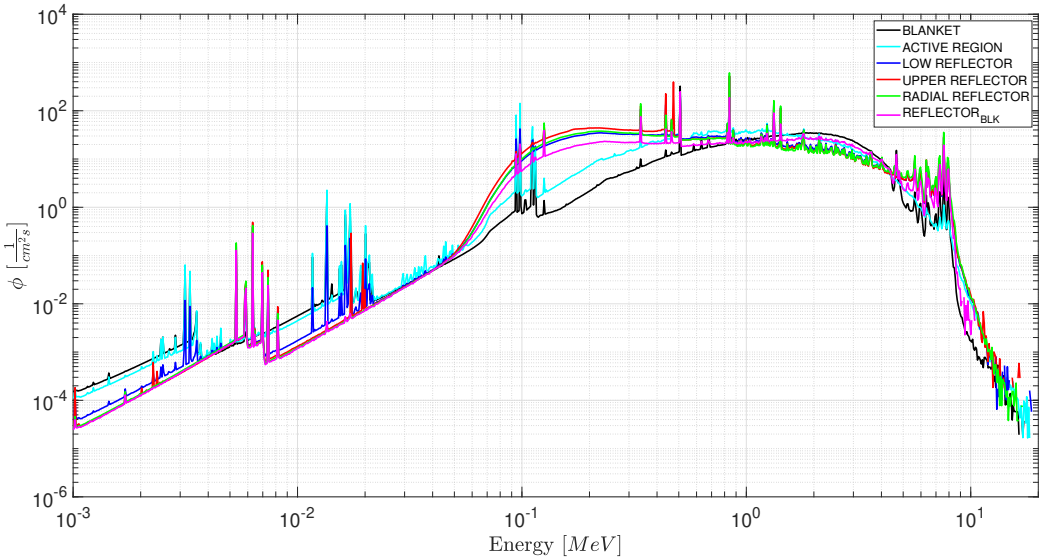

Figure 3.22: Photon spectra in the EBR-2 integrating in the SIUs used for neutrons.

are evident at lower energy than 10^{-1} MeV. The stainless steel elements present a larger probability to have photons with energy in the range of (10^{-1}, 1) MeV, which is reasonable with respect to the related distribution of neutrons in the same range. Regarding the energy range of fast fission, Serpent-2 associates a γ ray release in

places where fission happen, therefore the spectrum related to the active region follows with quite accuracy the one of neutrons in the active region reported in Fig. 3.20. It is also evident that the pairs-production is negligible, since there are no depressions around 1.022 MeV in the all considered regions.

Regarding the spatial distribution of photons, in Fig. 3.23 the distribution of photon flux is shown, in order to how particles are propagated. To conclude the dis-

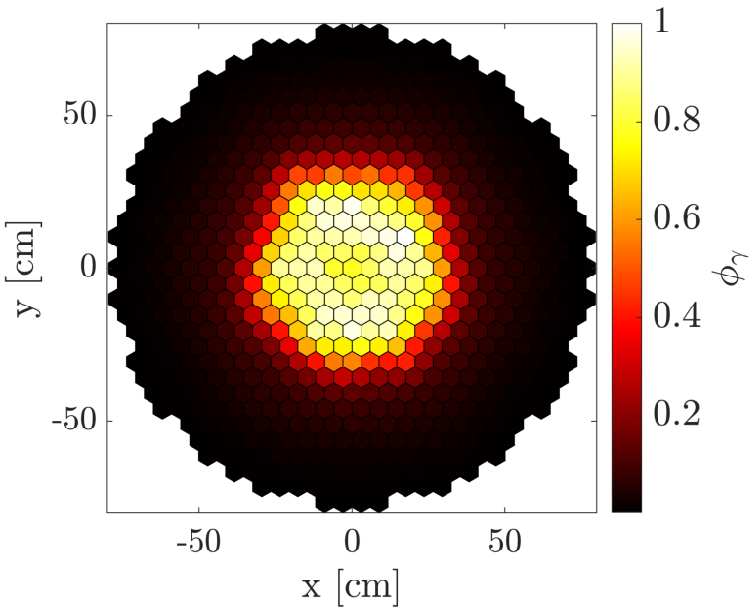

Figure 3.23: Photon distribution in the EBR-2, normalised on the maximum.

cussion on the spatial distribution, the coarse regions (Table 3.15) used for neutrons results also suitable for the photons attenuation coefficient generation: by means of the same structure, the photon production cross sections are exactly calculated where the photons are emitted, and then they are propagated in such a way to well represent the γ heat deposition, especially in SST-K and radial reflector elements.

3.2.7 Group-Constant-Universe generation optimisation

After illustrating the method to generate the attenuation coefficients, the second criterion for the spatial homogenisation is assessed. The general idea is kept: the division is performed by separating the non fissile regions in the SA classes from their active portions (along the axis), and the cold assemblies are treated separately (in the radial pattern). A second step in the discretisation has been introduced, taking advantage from the common universes in which the materials are defined. The coarse regions reported in Table 3.15 are further divided among the SA classes. In fact, Serpent-2 performs the scoring for the homogenisation in a universe each

time it is located in a cell of the computational domain. This second level of analyses arises from:

- avoiding the definition of SIUs to collect results in whole core, to reduce the impact on memory consumption and on the calculation time;
- avoiding the integration among mixtures that are sensible different in a single domain. An example is the axial reflector, mainly in stainless steel and the plenum, in which helium is present.

Therefore, the inner core coarse region has been expanded into sub-regions, aiming to better describe each single SA class. This expansion is reported in Table 3.16. To better understand how the generation is thus performed, the case of

Table 3.16: EBR-2 finer spatial definition for the generation of integral nuclear data for neutrons and photons.

Assembly class	**Domain**	**Sub-domain**
Fuel	Lower reflector	MARK-IIA, MARK-IIAI (full/half)
	Active region (GCU)	MARK-IIA, MARK-IIAI (full/half)
	Plenum	MARK-IIA, MARK-IIAI (full/half) XETAGS
	Upper reflector	MARK-IIA, MARK-IIAI (full/half)
HWCR		Lower reflector Active region (GCU) Poison Plenum Upper reflector
SR		Lower reflector Active region (GCU) Upper reflector 1-2
Dummy	SST-K, X320C, XY16	
Reflector		Radial Blanket
Instrumented	XX09/XX10	Lower reflector Active region/Dummy Upper reflector

fuel is illustrated: the lower reflector of the fuel assembly is common to MARK-IIAI/MARK-II, therefore the generation of the cross sections (and photons data) can be performed in each lower reflector of each MARK-IIA assembly and MARK-IIAI (full/half). At the end of the calculation, there are:

- a set of nuclear data for the MARK-IIA lower reflector, resulting from the integration of the scoring in each assembly of the MARK-IIA class

- a set of nuclear data for the MARK-IIAI lower reflector, resulting from the integration of the scoring in each assembly of the MARK-IIAI class;

This is consistent with the considerations about particles distributions, since the effects due to the position is far less significant, but the scoring results more homogeneous and representative of the heterogeneity in the core (both for photons/neutrons).

3.2.8 Generation of energy deposition coefficients for neutrons and photons

Serpent-2 does not provide the same routines for the photons generation data as well for neutrons. Therefore, an *ad hoc* procedure to get information about their production and released energy has been elaborated. To calculate an effective photons production cross section due to neutrons interactions, the strategy is:

1. to define a detector to score the reaction rate (per universe) of photon productions by neutrons;
2. to define a detector to score neutron fluxes in the six energy group structure;
3. to perform the division to get the cross section.

The reaction rates estimation for this kind of reaction is calculated by Serpent-2 as:

$$R_{(n,\gamma),g} = \frac{1}{V}\int_V d\boldsymbol{r}\int_{E_{g-1}}^{E_g} dE'\Sigma_{n,\gamma}(\boldsymbol{r},E')\phi(\boldsymbol{r},E') \tag{3.19}$$

where the $\Sigma_{\mathrm{n},\gamma}(\boldsymbol{r},\mathrm{E}')$ corresponds to the MT = -5 with respect to [38]. The corresponding neutron flux is:

$$\phi_g = \frac{1}{V}\int_V d\boldsymbol{r}\int_{E_{g-1}}^{E_g} dE'\phi(\boldsymbol{r},E') \tag{3.20}$$

For both equations, the volume V is set to 1, to have a total reaction rate instead of a reaction rate density. Performing the division, the $\Sigma_{(n,\gamma),g}$ is obtained:

$$\Sigma_{(n,\gamma),g} = \frac{\displaystyle\int_V d\boldsymbol{r}\int_{E_{g-1}}^{E_g} dE'\Sigma_{n,\gamma}(\boldsymbol{r},E')\phi(\boldsymbol{r},E')}{\displaystyle\int_V d\boldsymbol{r}\int_{E_{g-1}}^{E_g} dE'\phi(\boldsymbol{r},E')} = \frac{R_{(n,\gamma),g}}{\phi_g} \tag{3.21}$$

By means of this, the few-group (n,γ) cross sections production set can be calculated for each material (universe).

After the calculation of production cross sections, the amount of energy deposited by neutrons and photons must be evaluated. Serpent-2 presents several

models to assess the energy deposition of particles [39]. For the present study, the adopted model foresees a coupled calculation NE/PH (mode 3). In general, Serpent-2 imposes the normalisation on the total power with the next relation:

$$P_{\mathrm{TOT}} = P_{\mathrm{f}} + P_{\mathrm{n,K}} + P_{\gamma,\mathrm{K}} \tag{3.22}$$

where:

- $\mathrm{P_f}$ is the fraction due to the proper energy of fission plus the delayed contributions in the fission site;
- $\mathrm{P_{n,K}}$ is the thermal power provided by the neutrons as they travel and deposit their energy when absorption occurs;
- $\mathrm{P_{\gamma,K}}$ is the thermal power provided by the photon as they travel and deposit their energy when absorption occurs.

In order to not to lose the delayed contributions of β and γ energy, the option to include in the fission site these energies has been set. In this way, the only fraction of the total available energy when fission happen is in charge to neutrons and photons KERMA and their energy when they are absorbed after travelling in the reactor. This estimation is performed setting a detector for the total energy generated, with the response function MT = -80. Results of this estimator are given in thermal power for each universe. A distinction between photons and neutrons energy grid must be done: the neutrons are treated according to the six energy group for the GCU calculations, whereas the photons are mono-kinetic. This implies that Serpent-2 calculates six values of thermal power in each material for neutrons, and one single value for the thermal power in each material due to photons.

To be useful for the FRENETIC code, these contributions must be attributed to some energy-per-unit-length coefficient. In fact, the calculation of thermal power in the tool is performed using the same structure of the fission power definition:

$$P = \sum_{g=1}^{\mathrm{N_g}} \int_V d\boldsymbol{r} E_{f,g}(\boldsymbol{r}) \Sigma_{f,g}(\boldsymbol{r}) \phi_g(\boldsymbol{r}) \tag{3.23}$$

where the product $\mathrm{E_{f,g}}(\boldsymbol{r})\Sigma_{\mathrm{f,g}}(\boldsymbol{r})$ has the unit of MeV/cm. Therefore, the energy estimated by Serpent-2 in a certain universe is used to define this equivalent KERMA coefficient for photons and neutrons [40]. For these results the MT = -4 has been used for neutrons, and for the photons the MT = -26. Starting from the Serpent-2 results, the equivalence is obtained as:

$$K_{n,g}^{FRN} = \frac{K_{n,g}^{SRP}}{\phi_g} \tag{3.24}$$

where $K^{SRP}_{n,g}$ is the thermal power deposited in the material in the g-th group. Analogously, for the photons KERMA in FRENETIC:

$$K_{\gamma}^{FRN} = \frac{K_{\gamma}^{SRP}}{\phi_p} \tag{3.25}$$

according to have one single group for the data collapsing. The mono-kinetic photon flux is obtained by defining a proper detector to score the flux in each material between the energy range of 100 keV and 20 MeV, as Serpent-2 has the cut-off of photon libraries at 100 keV:

$$\phi_p = \int_V d\boldsymbol{r} \int_{100\ keV}^{20\ MeV} dE' \phi_p(\boldsymbol{r}, E') \tag{3.26}$$

3.3 EBR-2 results for the NE/PH coupled simulation

Here the results of calculations performed with FRENETIC are shown. The benchmark is conducted by comparing the integral results with respect to the ones of Serpent-2 and, as a consequence, the evaluation of the accuracy of the spatial discretisation for the homogenisation is assessed. A first simulation in FRENETIC is set without considering the external sodium in the blanket periphery (**Scenario A**). In a second step, an additional layer of sodium has been included nearby the blanket FAs, in order to limit the geometry discrepancies between the two models (**Scenario B**). Finally, the optimisation of the group constant generation is completed with a finer discretisation of the blanket, and a coupled simulation NE/PH is performed with the FRENETIC code (**Scenario C**).

3.3.1 Purely NE simulation performed by FRENETIC in steady state condition: Scenario A

In Scenario A, the simulation in FRENETIC has been set up by creating the geometry according to the mesh used in Serpent-2 excluding the slender volume of sodium surrounding the blanket. The core pattern is shown in Fig. 3.24. The legend entries as CMP, CMF and CMA mean, respectively, Core MARK-IIAI partially loaded, Core MARK-IIAI fully loaded and Core MARK-IIA, whereas RIB is the acronym for Reflector in the Blanket. Notwithstanding the same material of the radial reflector, these elements experience a quite different flux with respect to the ones in the radial reflector, therefore they have been treated separately.

The axial discretisation is performed following the logic reported in Table 3.16 and shown in Fig. 3.25. It is noteworthy the fact that experimental drivers X402, X412A and XETAGS, although they contain the same materials that constitute the

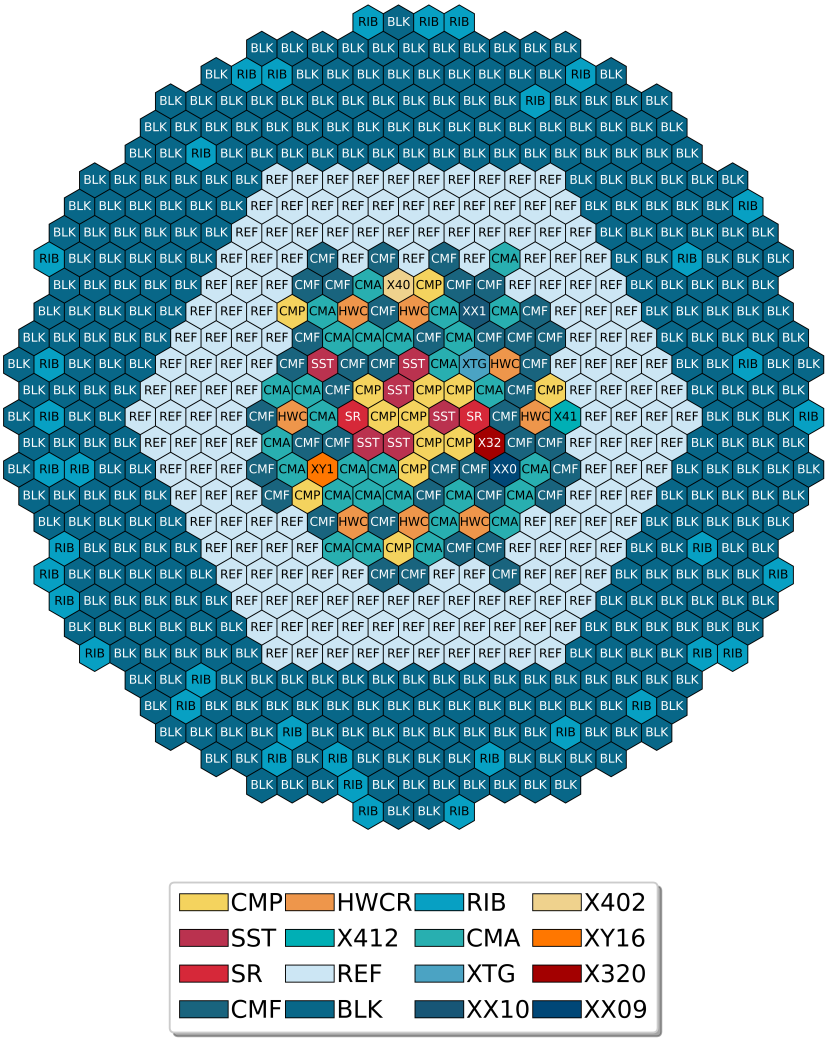

Figure 3.24: EBR-2 core pattern in FRENETIC simulation in Scenario A.

lower/upper reflectors of the most common core assemblies, have been associated to MARK-IIA/I. The black lines delimit the coarse mesh of FRENETIC along the axial direction. To refine the mesh, a finer grid has been used to further discretise the coarse region, paying attention not to have small optical regions compared with the mean free path of neutrons [26].

The multiplication eigenvalue calculated by FRENETIC, in this scenario, is compared with the one of Serpent-2 in Table 3.17, whereas the relative error between the respective fission power distributions is shown in Fig. 3.26.

From the data provided by Serpent-2, the contributes to the total thermal power are reported in Table 3.18. The difference between the two values reported Table 3.17 in can be explained with the different boundary conditions (lack of sodium in FRENETIC) between the two models and with the approximation made in the

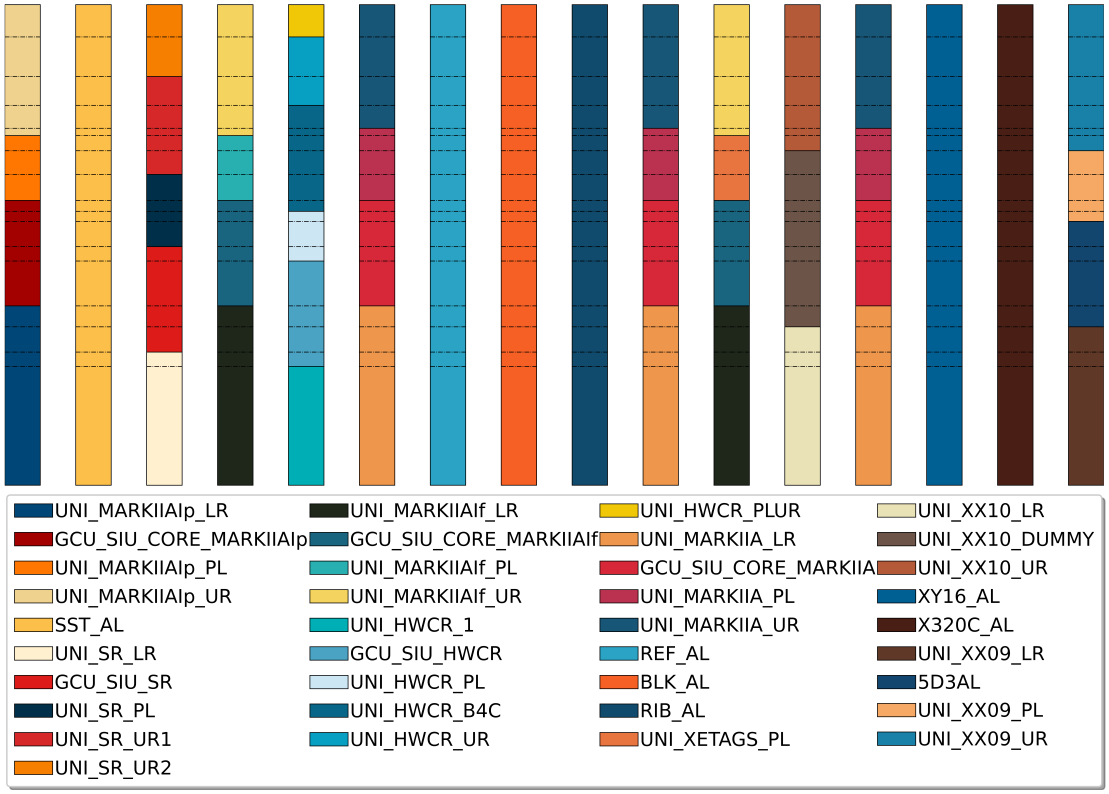

Figure 3.25: EBR-2: axial subdivision of materials in the FRENETIC simulation. The labels in the legend derive from Serpent-2.

Table 3.17: Comparison between the effective multiplication eigenvalues calculated by FRENETIC and Serpent-2 in a pure NE simulation on the EBR-2 reactor.

$k_{\text{eff,FRN}}$	$k_{\text{eff,SRP}}$	Δk_{eff}
0.98946	0.98786(2)	160 pcm

Table 3.18: Contributions to the total thermal power calculated by Serpent-2.

Thermal Power	[MW]
P_{fiss}	54.58
$P_{\text{n,K}}$	0.50
$P_{\gamma,\text{K}}$	4.92
P_{TOT}	60.00

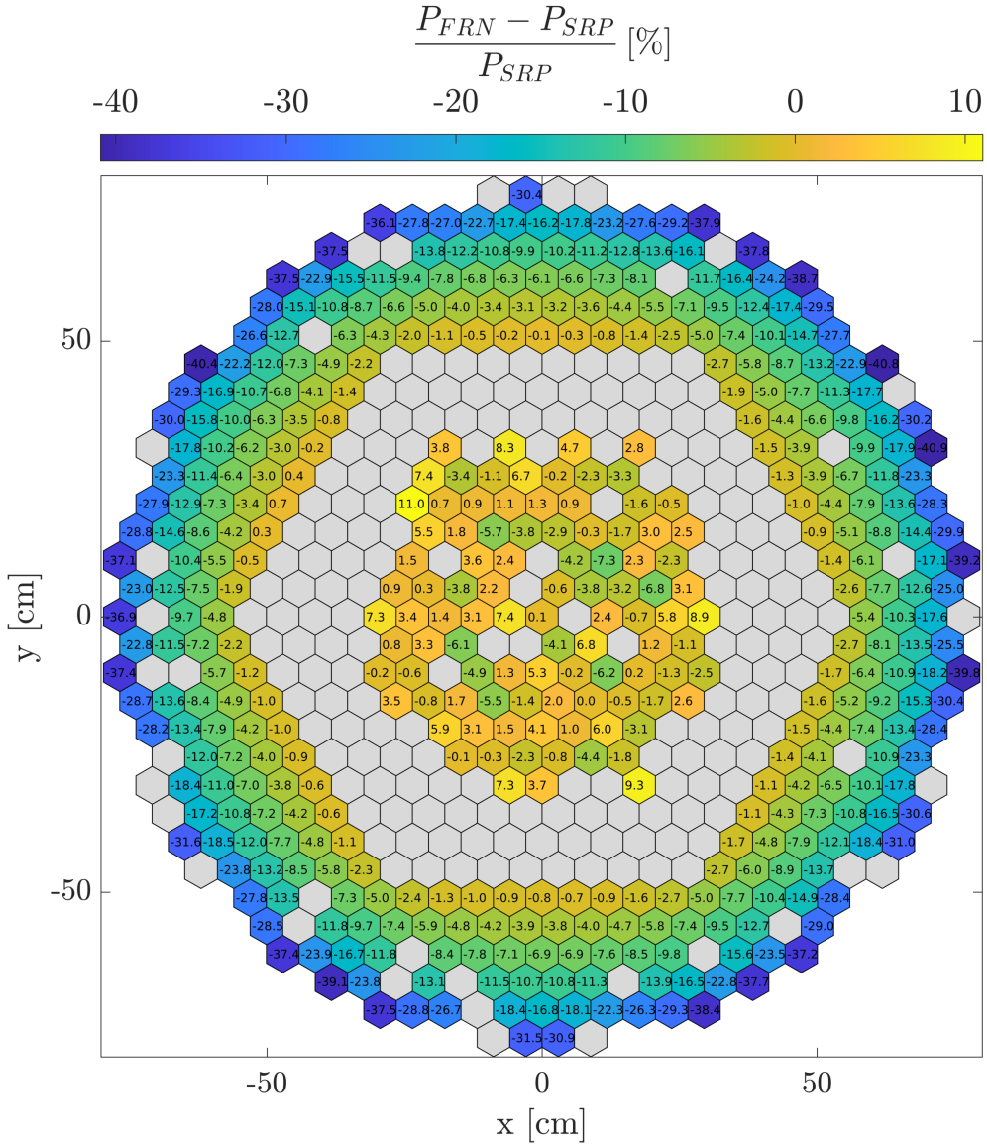

Figure 3.26: Comparison of the thermal fission power of results provided by FRENETIC and Serpent-2. The power computed by the deterministic code has been normalised on the fission power reported in Table 3.18.

blanket. The active length of the blanket, as shown in Fig. 3.15, was included between two other regions: the foot of the blanket driver (stainless steel) and the upper part where sodium is the major component. To avoid bad statistics in those peripheral regions, the generation of the data set has been performed on the entire volume. Therefore, the collapsing volume used in Serpent-2, thus FRENETIC, is the one reported in Fig. 3.25 (BLK_AL). Although the reaction rates have been preserved since there is accordance on the generation (Serpent-2) and on the integration of reaction rates (FRENETIC), this approximation behaves as a *dilution* of fertile material with respect to the spatial effects. The discrepancy of the flux nearby the boundary is caused by the different geometry considered by the two codes. In fact, the computational domain of FRENETIC is delimited exactly by the last ring of FAs, leading to a strong gradient of the flux on the boundary. On the contrary, the Monte Carlo model presents a slender volume of sodium (Fig. 3.14), moving further away the frontier from the blanket.

3.3.2 Purely NE simulation performed by FRENETIC in steady state condition: Scenario B

Having observed great discordance close to the boundaries between the two codes, the geometry of FRENETIC has been expanded by adding a representative volume of sodium which was already included in Serpent-2 and was initially neglected. For an even better consistency between the two simulation, the Serpent-2 model has been slightly changed with respect to Fig. 3.14. The new setup of the model calculated by Serpent-2 is reported in Fig. 3.27. The new setup for the FRENETIC code is shown in Fig. 3.28. In this new configuration the domain is expanded with the external sodium, and the reflector has been further refined into 4 hexagonal rings in order to better describe the flux gradient among the energy groups. As a consequence, a new set of cross section data for neutrons have been calculated as well as for the external sodium. In this condition the agreement with Serpent-2 for the thermal fission power is improved, as shown in Fig. 3.29. In the last ring of the blanket, neutrons are travelling at low energy; indeed, as reported in Table 3.12, the last group indicates a mean free path in the order of $\sim$ 1 cm. Therefore, the addition of an external sodium layer which is much larger than the mean free path of particles reduces the leakages as many outgoing neutrons experience back-scattering. Globally, the error on the fission power is thus reduced, improving the accordance in the inner core too.

In order to complete the discussion on the neutron flux, the comparison of results calculated by FRENETIC and Serpent-2 is depicted in Fig. 3.30. First, the discrepancies in the blanket are reasonably caused by having homogenised the whole region in a single domain. In fact, as the average energy of neutrons decreases (moving towards low energy groups), the distribution calculated by FRENETIC is marginally under estimated with respect to Serpent-2. This happens since the

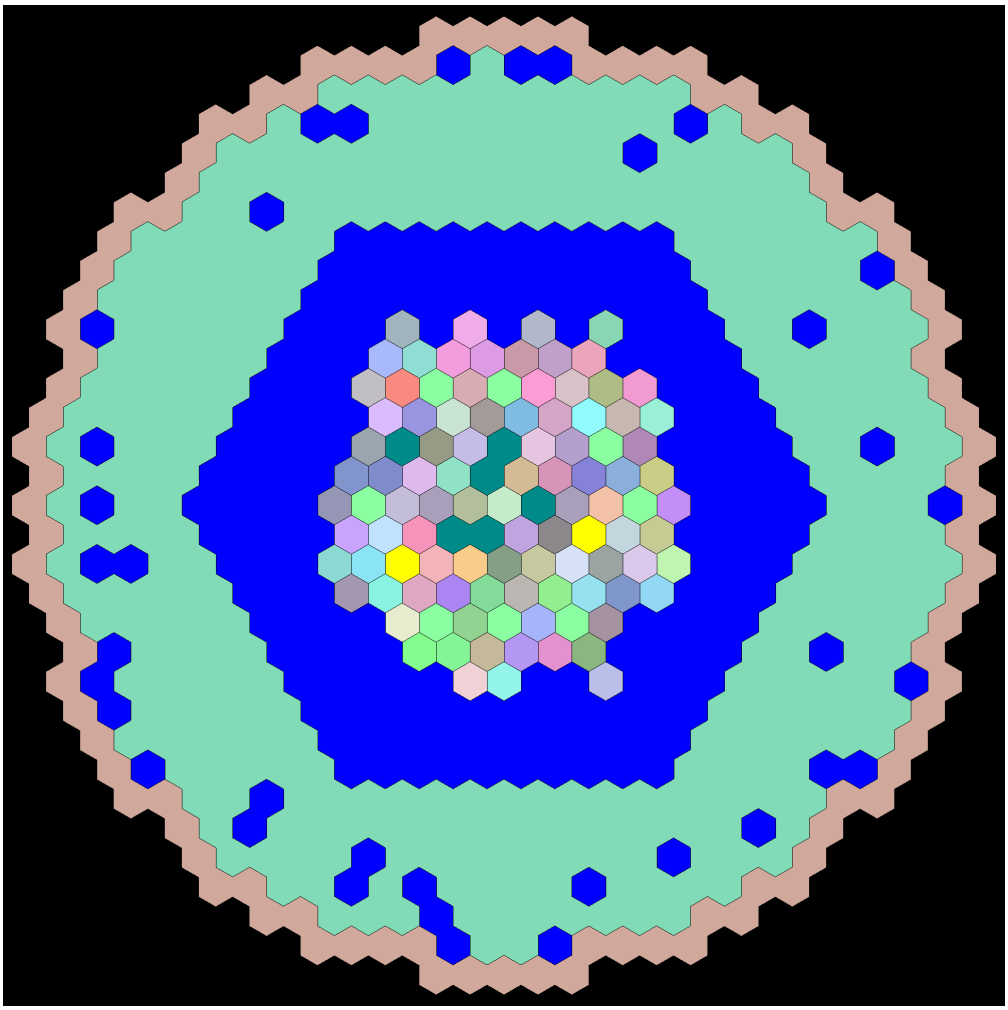

Figure 3.27: New Serpent-2 model for the generation of collapsed data for the EBR-2 reactor with the external sodium.

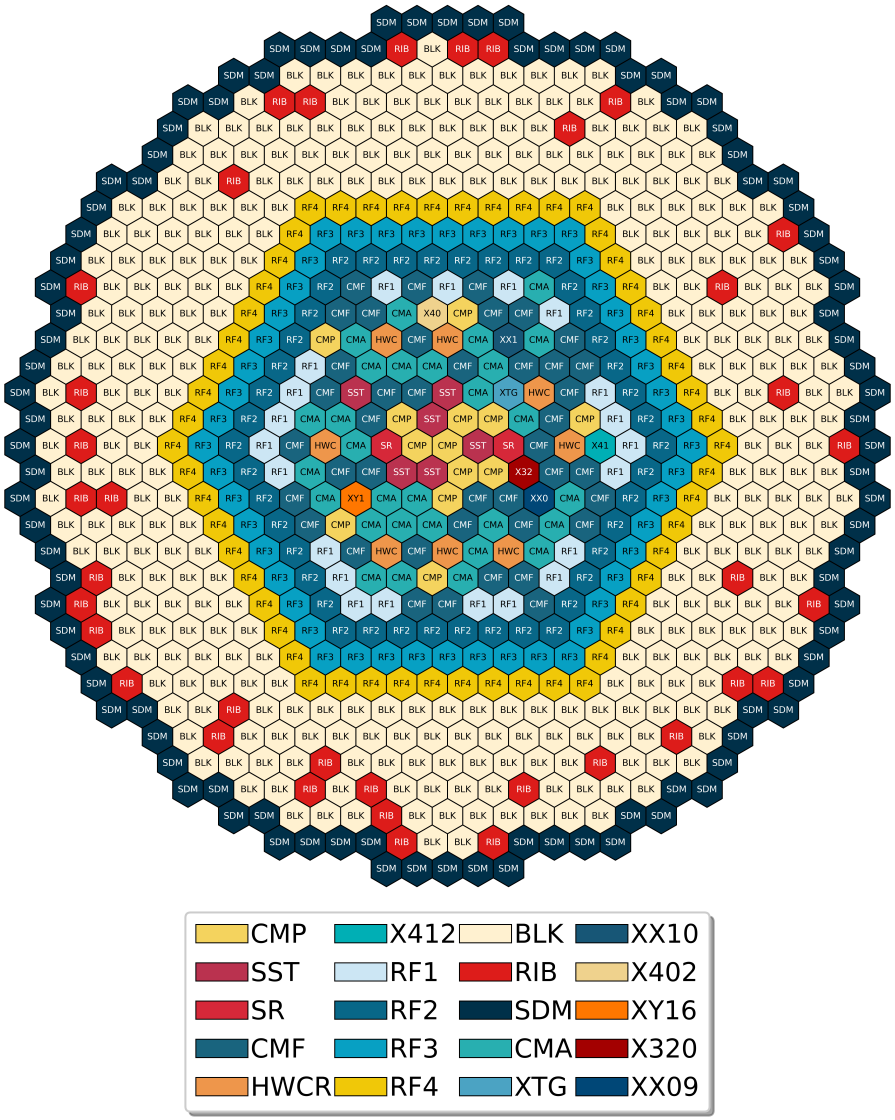

Figure 3.28: Expanded mesh for the FRENETIC code for the simulation of the EBR-2 reactor in Scenario B.

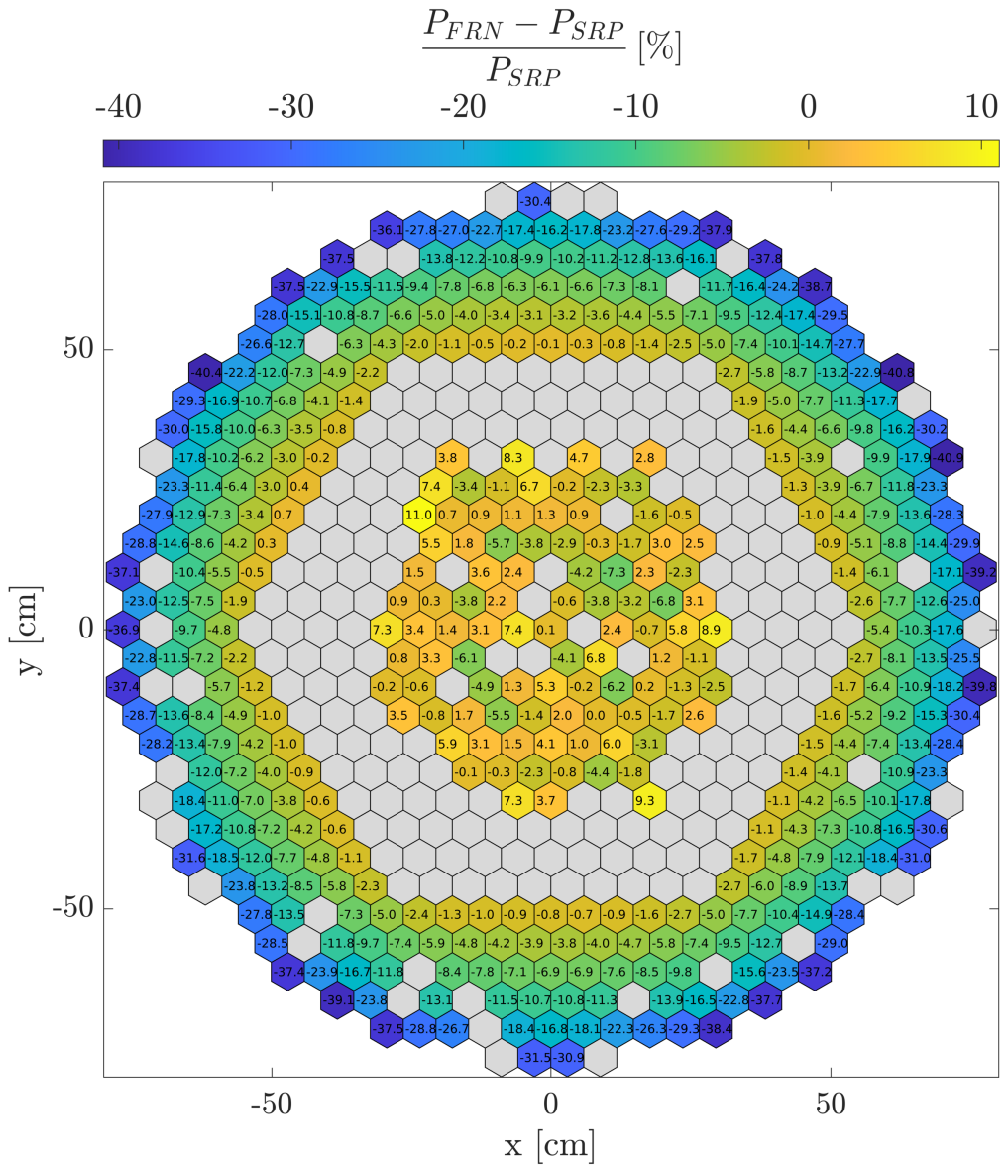

Figure 3.29: Comparison between the fission power computed by the FRENETIC with respect to the one calculated by Serpent-2 for the EBR-2 reactor in Scenario B.

blanket FAs nearby the reflector are exposed to a neutron flux which is energetically different from the ones at the core boundaries. Second, the flux shape calculated by FRENETIC is slightly over estimated in the reflector. This is confirmed by the radial flux distribution, showed in Fig. 3.31 for the SAs from 1 to 14. The reflector is present at SA 7 to 10, and the flux is always bigger than the one simulated

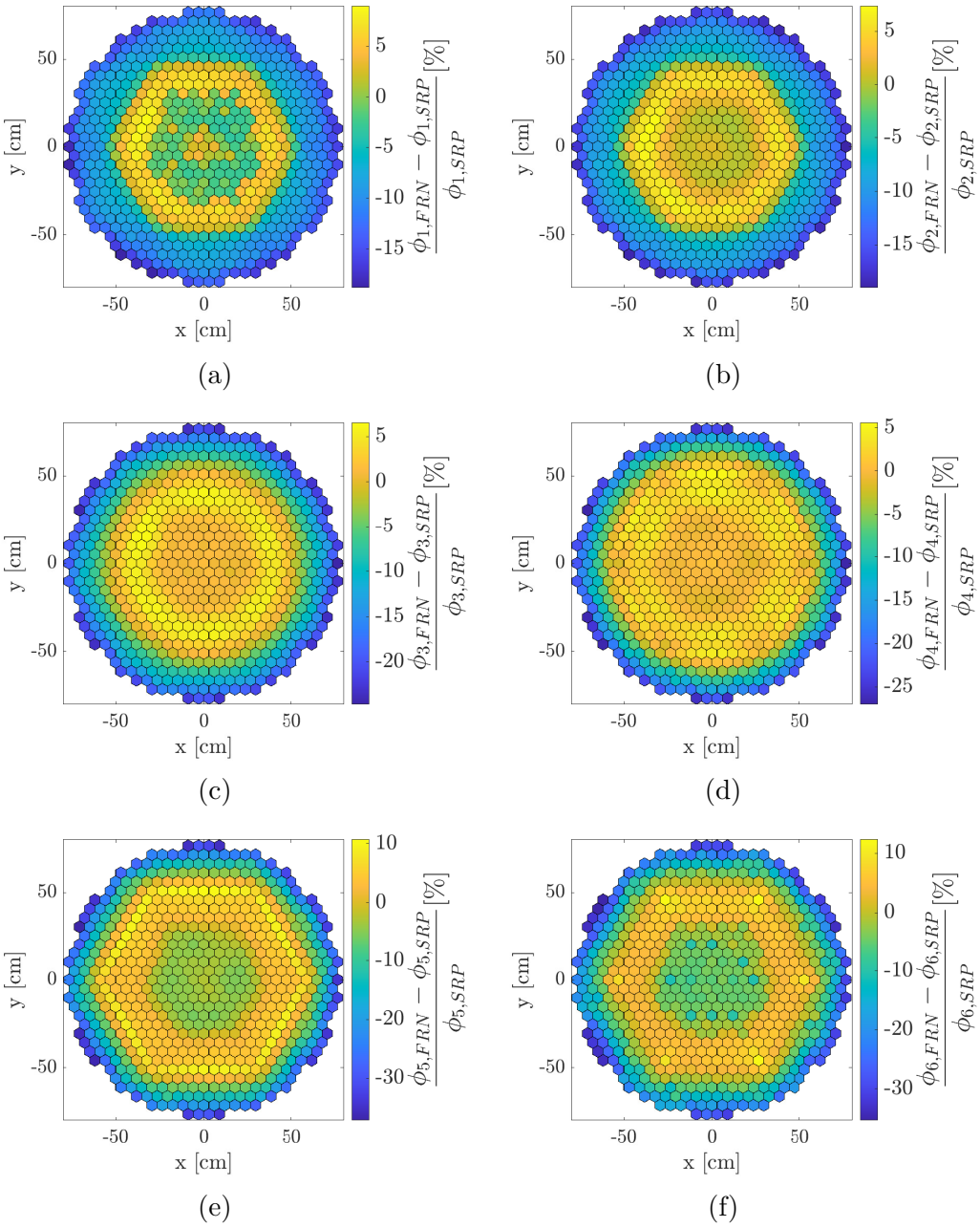

Figure 3.30: Comparison between the neutron flux computed by FRENETIC and Serpent-2 on the few-group energy structure in Scenario B.

by Serpent-2. To further improve the concordance between the two tools, a more detailed scenario for FRENETIC has been studied, and the results are showed in Section 3.3.3.

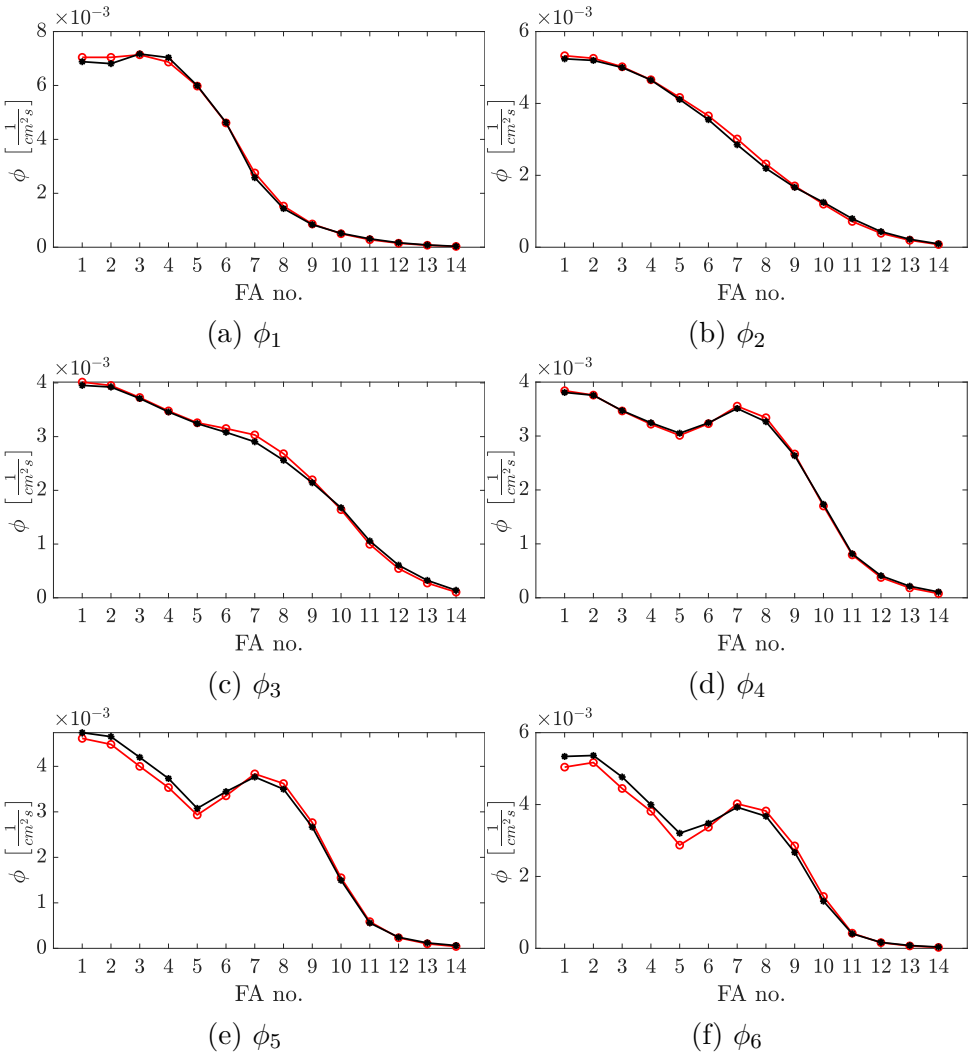

Figure 3.31: Comparison between the neutron flux computed by FRENETIC and Serpent-2 on the few-group energy structure for a selected number of FAs. Serpent-2 values are in black lines, whereas the FRENETIC ones are in red.

3.3.3 NE-PH simulation performed by FRENETIC in steady state condition: Scenario C

In this last scenario, the computational domain in Serpent-2 is the same reported in the previous section (Fig. 3.27). The new setup in FRENETIC includes the sub-division of the blanket into 5 rings, in order to improve the description of local effects due to slowing down and capture events. The mesh for FRENETIC is illustrated in Fig. 3.32.

In Table 3.19, the eigenvalues for the three scenarios are summarised. The agreement increases as the collapsed cross sections are generated on smaller volume,

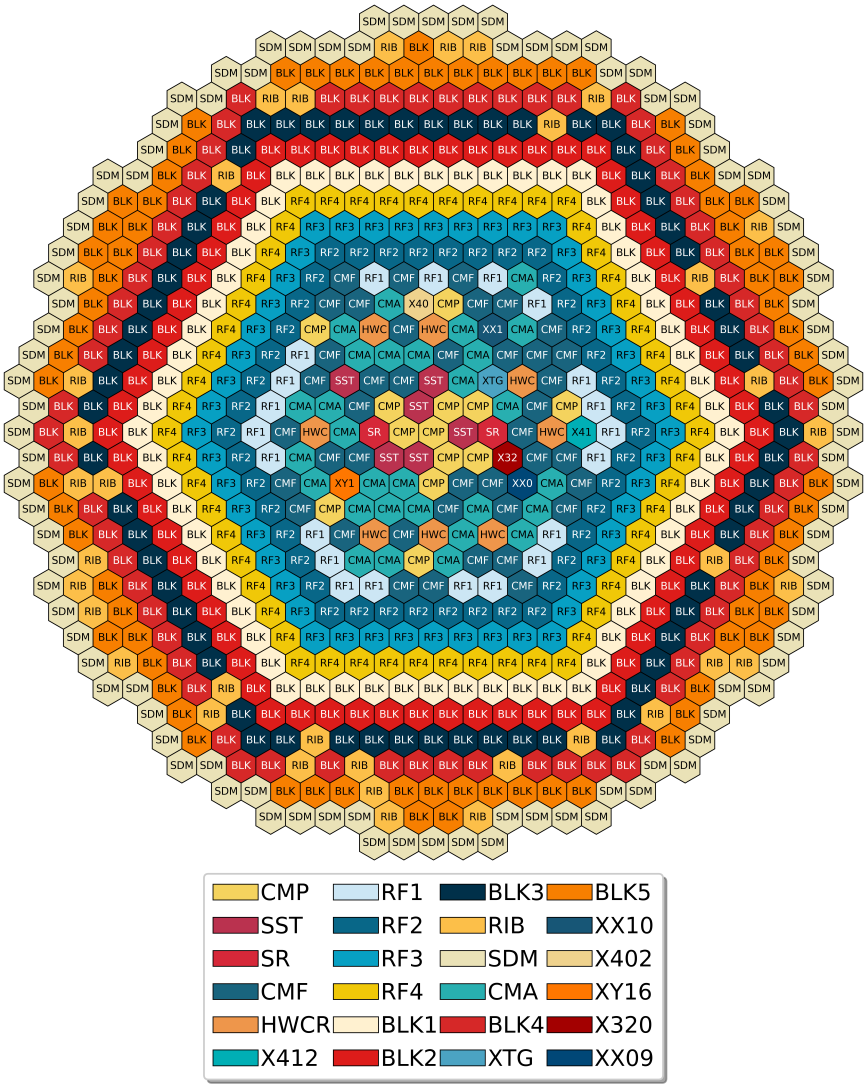

Figure 3.32: Computation mesh for FRENETIC including the refinement of the blanket in Scenario C.

where the flux does not present great azimuthal gradients. The incisive improve-

Table 3.19: Comparison among the effective multiplication eigenvalues calculated by FRENETIC and Serpent-2 for the EBR-2 reactor in Scenarios A, B and C.

Scenario	$k_{\text{eff,FRN}}$	$k_{\text{eff,SRP}}$	Δk_{eff}
A	0.98946	0.98786(2)	160 pcm
B	0.98916	0.98790(2)	125 pcm
C	0.98909		118 pcm

ment has been obtained by adding the external sodium. In this way, the reflection caused by sodium has been taken into account in the periphery of the blanket, moving further away the boundary condition (incoming neutron current equal to zero) imposed by FRENETIC on the frontier. Moreover, in Scenario B the reflector has been refined to better detail its gradient at lower energy groups (Fig. 3.31e and Fig. 3.31f, black lines). Moving to Scenario C, the comparison of the thermal fission power calculated by FRENETIC against the one of Serpent-2 is reported in Fig. 3.33. With reference to Fig. 3.29, this last result shows a good agreement with Serpent-2. The average error in the inner core region is very low, with some exceptions due to the spatial homgenisation. For instance, the FA located in the position 7A5 is a MARK-IIAI partially loaded that has been homogenised with other MARK-IIAI FAs. The latter are positioned for the major part in the centre of the core, where the fast flux is dominant. Nearby the reflector, instead, neutrons undergo scattering phenomena due to stainless steel, thus it is reasonable to assume that the energy distribution of neutrons here is quite different when compared to the centre. As a consequence, there is a substantial spectral difference among that FA and the others.

In the blanket, the relative error is lower than the previous scenarios. The finer sub-division presents a more homogeneous distribution of the error along each hexagonal ring, since neutrons emerging from the reflector have smooth distribution. At the same time, the local effects are preserved, since the blanket FAs localised in the neighbouring of the reflector are significantly different with respect the ones on the border. This is confirmed by the comparison of flux calculated for this scenario, taking again Serpent-2 as a reference (Fig. 3.34). The overall error is decreased, especially in the blanket FAs far from the boundary (Fig. 3.34a, Fig. 3.34d), whereas in the radial reflector the overestimation at lower energies is still present, compatible with the approximation performed by the diffusion theory (Fig. 3.34e).

With regards to photons, the reaction rates of γ production due to neutron interactions are shown in Fig. 3.35. Since in FRENETIC the production of γ is proportional to the neutron flux by means of the cross section in the g^{th} group, the overestimation located in the reflector is clearly visible also in the photon source.

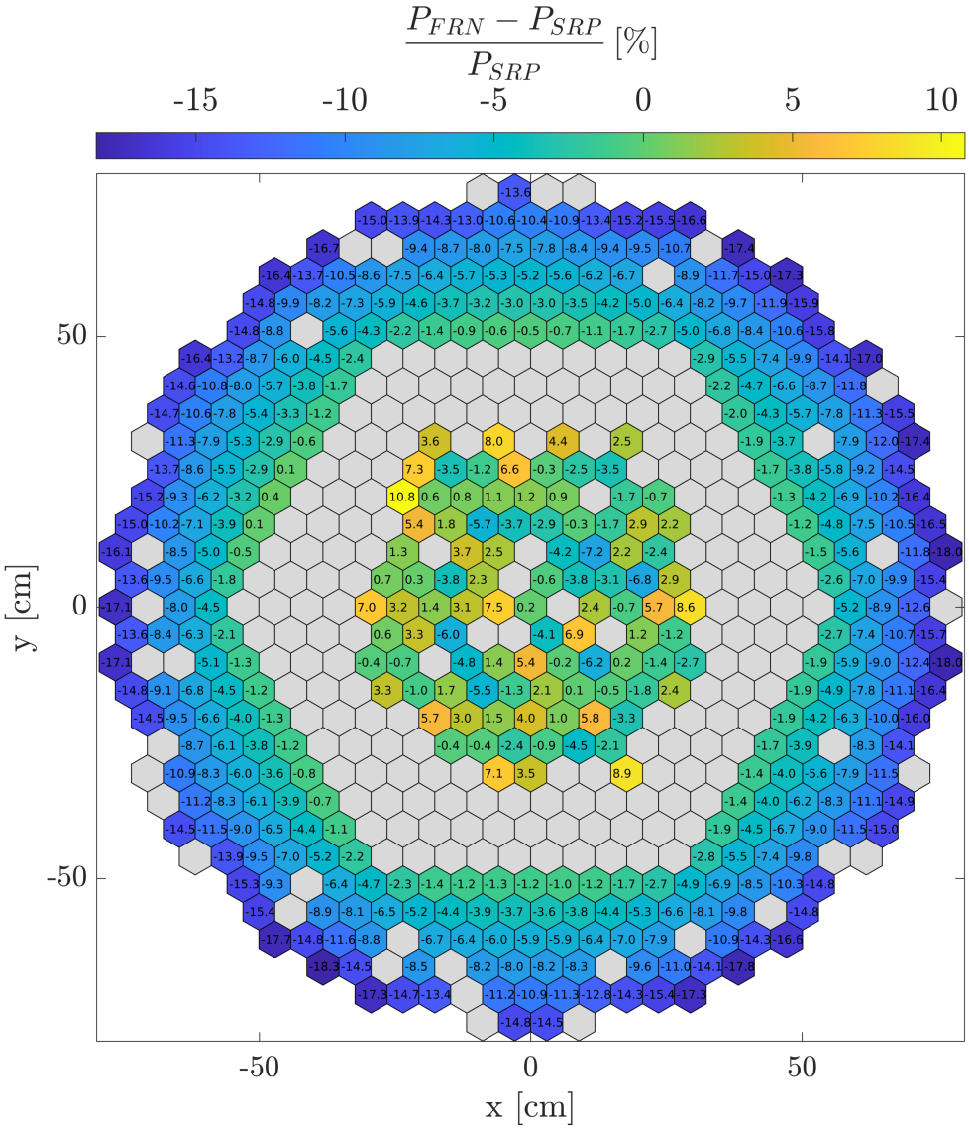

Figure 3.33: Comparison between the fission power computed by the FRENETIC with respect to the one calculated by Serpent-2 for the EBR-2 reactor in Scenario C.

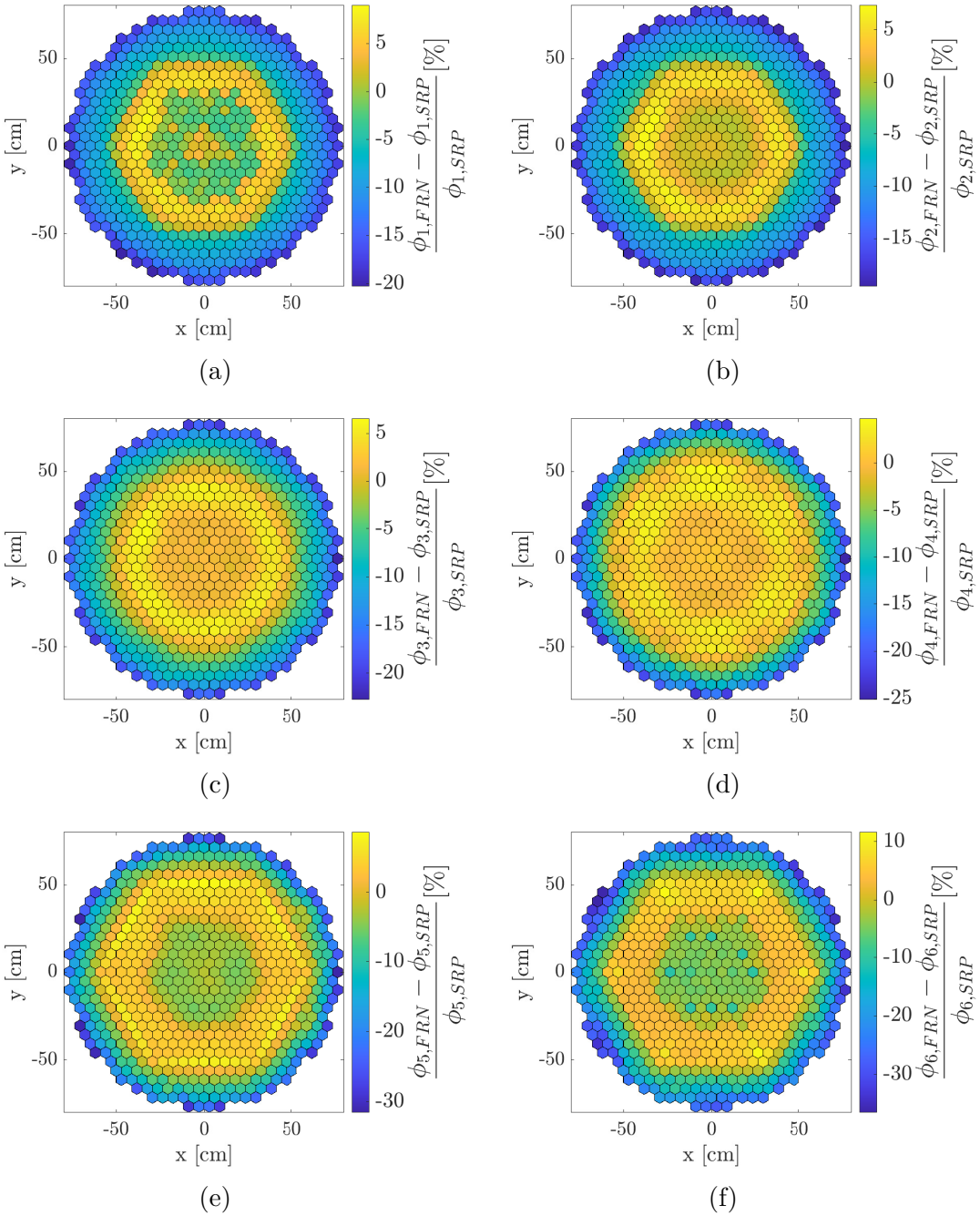

Figure 3.34: Comparison between the neutron flux computed by FRENETIC and Serpent-2 on the few-group energy structure in Scenario C.

The spots in the first group (Fig. 3.35a) are caused by the spatial homogenisation.

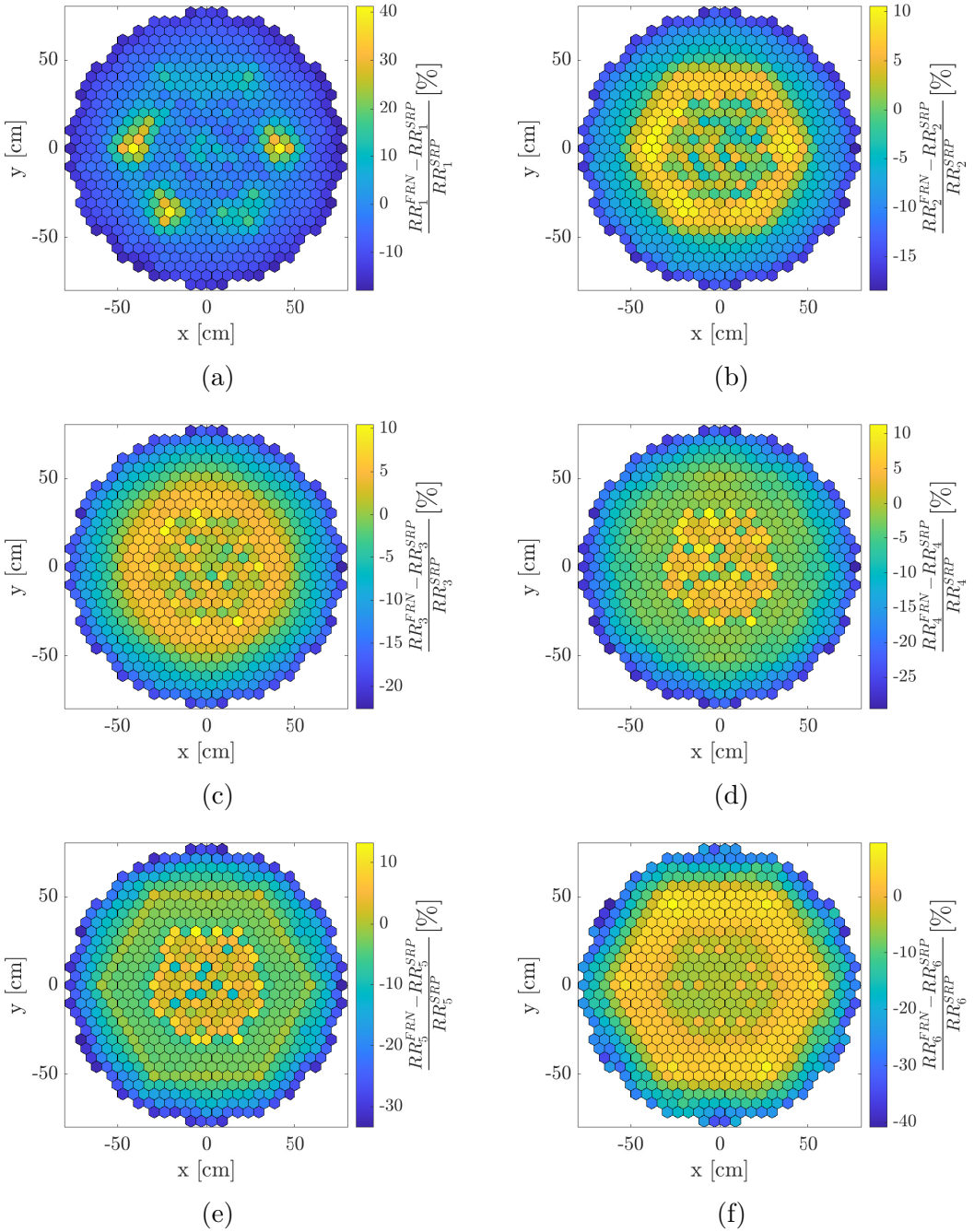

Figure 3.35: Comparison between the photon production rate computed by FRENETIC and Serpent-2 on the few-group energy structure in Scenario C.

In fact, the first ring of the radial reflector is sharply coupled with the inner region of

the core; the heterogeneities are negligible nearby the core centre, but they become predominant in proximity of the reflector. Therefore, if the homogenisation is performed according to Fig. 3.32 for the material "REF1", the effective cross section is conditioned by all this non-uniformity in the spatial distribution. A proof for this consideration can be found in the flux distribution provided by Serpent-2 for some assemblies of the ring REF1, shown in Fig. 3.36. The blue line represents the integrated flux in the first group for the assemblies of the reflector according to the index reported along the x: the assembly 539 (7A1 for the convention proposed by ANL) presents an imbalance with respect to the other elements. Therefore, the average value for the first group will overestimate that local value, leading to the hot spot in Fig. 3.35a.

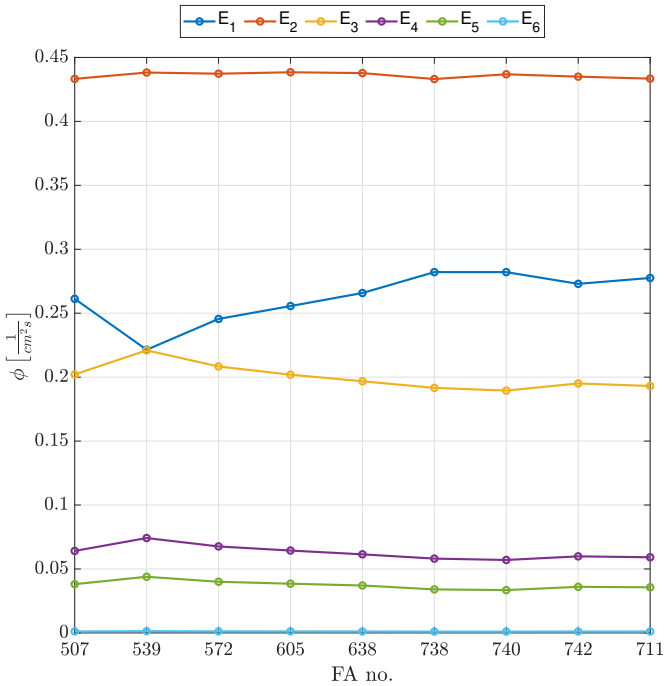

Figure 3.36: Flux distribution calculated by Serpent-2 on the six-group energy structure where the cross sections for the material "REF1" are generated.

With respect to the other groups (Fig. 3.35d and Fig. 3.35e), the reaction rates calculated by FRENETIC are overestimated in the inner core. These discrepancies arise from the spatial homogenisation of the $\Sigma_{n,\gamma}$, as already illustrated in Fig. 3.36. Indeed, although there is an good accordance among the fluxes in the few-groups energy structure, the collapsing of the neutron production cross section is performed by merging different core elements with different neutron distributions (especially near the reflector). The overestimation is, however, of order of $\sim$ 2-3 %, whereas the effect in the reflector is more evident.

Concerning the photon flux ϕ_γ, the relative error between the two codes is

pointed out in Fig. 3.37. As expected from the reaction rates for the γ production,

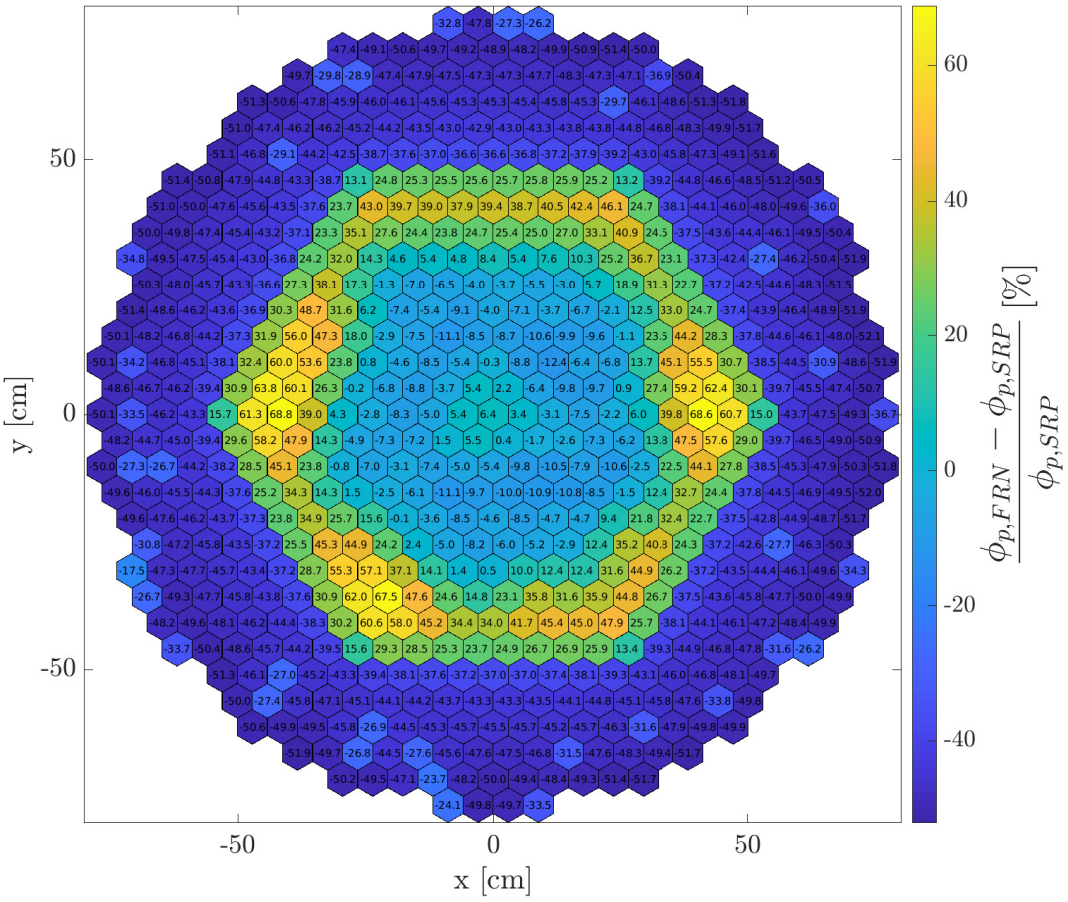

Figure 3.37: Comparison between the photon flux calculated by FRENETIC and Serpent-2 in Scenario C for the EBR-2 reactor.

the most evident error lies in the radial reflector. In fact, the overestimation in this region can be related directly with the of neutron fluxes calculated by Serpent-2 FRENETIC. The latter overestimates the neutron distribution in the stainless steel with respect to Serpent-2, leading to the higher production observed by Fig. 3.35.

In addition, the blanket presents a lower streaming of photon in FRENETIC, whereas the inner core has a good agreement with Serpent-2. As a second point, there is a lack of information about the photon multiplicity production. In fact, Serpent-2 does not provide as output an equivalent $\bar{\nu}_{n,g}$ for the photon production: the detector used for the estimation of the reaction rate of γ production, indeed,

provides the reaction rate of (n, γ) interaction, rather than the total production of photons.

FRENETIC treats the photons with same physics of neutrons (with only difference that the D_γ is isotropic): the (n, γ) interactions act as the fission for the neutrons. The neutron density production when a primary neutron undergoes fission is in the form of

$$\bar{\nu}_{n,g}\Sigma_{n,g}\phi_g \tag{3.27}$$

with $\bar{\nu}_{n,g}\Sigma_{n,g}$ being the data provided to FRENETIC as input. Similarly, the photon density production is in the form of

$$\nu_\gamma \Sigma_{\mathrm{n},\gamma}\phi_\gamma. \tag{3.28}$$

However, Serpent-2 provides only $\Sigma_{\mathrm{n},\gamma}\phi_\gamma$, while it is not possible to obtain the photon multiplicity ν_γ. The consequent underlying assumption in FRENETIC is that the each (n, γ) interaction produces exactly one photon.

Table 3.20: Comparison among the relevant photon quantities calculated by FRENETIC and Serpent-2.

Parameter	**Serpent-2**	**FRENETIC**	**Ratio (SRP/FRN)**
(n, γ) total reaction rate $\left[\frac{\gamma}{s}\right]$	2.95659E+19	3.1317E+19	0.94
total photon flux Φ_γ $\left[\frac{\gamma\ cm}{s}\right]$	1.25937E+20	4.5797E+19	2.75

- Table 3.20 shows that the average expected multiplicity is 2.75 photons per interaction. However, it is important observing that the photon multiplicity is largely variable throughout the core, as it is an inherent property of the nuclides, exactly as the fission neutron multiplicity. Moreover, the photon multiplicity features an energy dependence that should be considered too: as a consequence, the material-dependent values should be consistently condensed with the neutron spectrum.

This results in a deformed shape of photon flux, leading to a significantly different photon deposited thermal power with respect to Serpent-2. The relative error is shown in Fig. 3.38. In turn, this issue affects the normalisation for the different contributions to the total power. Since the thermal power deposited by photons is underestimated by FRENETIC, especially in the blanket, the amplitude of neutron flux is changed accordingly in order to be compliant with the normalisation at 60 MW. Furthermore, a change in the flux amplitude influences as well the thermal power due to KERMA of neutrons, as reported in Table 3.21.

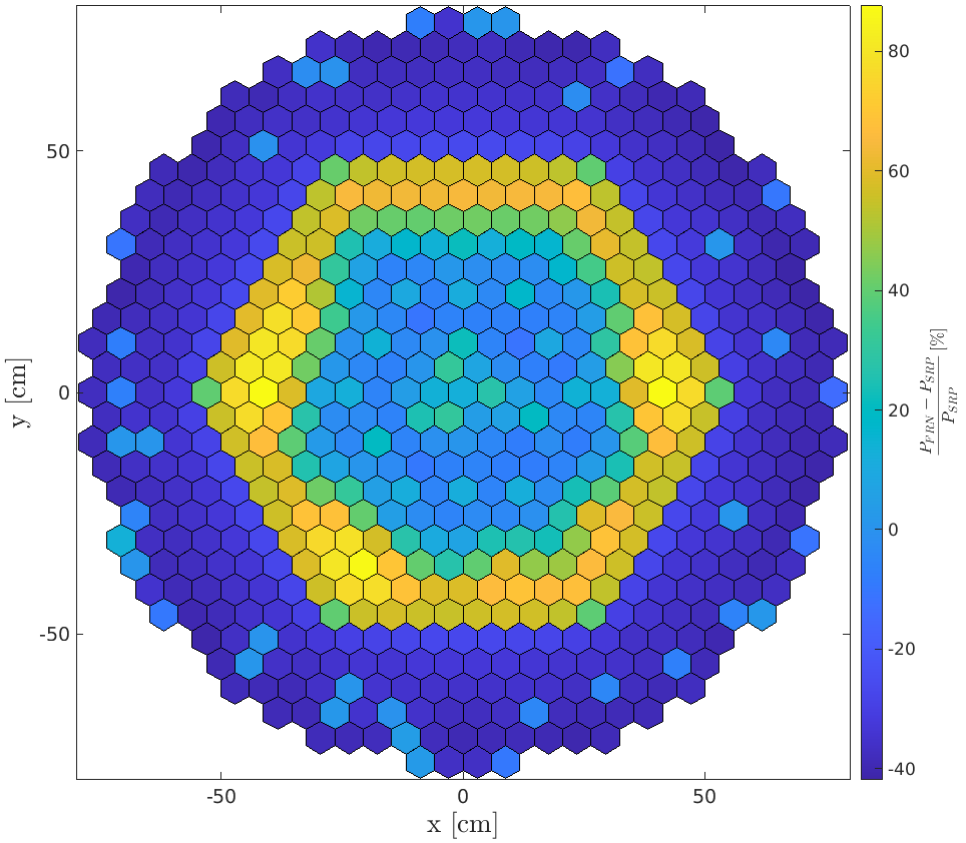

Figure 3.38: Comparison between the photon thermal power calculated by FRENETIC and Serpent-2 in Scenario C for the EBR-2 reactor.

Table 3.21: Comparison among the contributions to the total thermal power computed by FRENETIC and Serpent-2.

Parameter	**Serpent-2 [MW]**	**FRENETIC [MW]**
P_{fiss}	54.58	57.92
$P_{n,K}$	0.50	0.54
$P_{\gamma,K}$	4.92	1.54

3.4 Conclusions and perspectives

The activity conducted on the EBR-2 reactor has been addressed with the purpose to carry on the verification of the neutronic module of the FRENETIC, including also the photon heat deposition. Indeed, the FRENETIC code is able to simulate also the photon diffusion, by means of the same multi-group diffusion equations used for neutrons.

The study here reported has considered the test-case of the EBR-2, a SFR. On this reactor, an experimental campaign were performed to validate computational tools, thanks to a CRP proposed by IAEA. One of this test, namely the SHRT-45R, treated an unprotected LOFA to demonstrate the inherent physical mechanisms to passively shutdown the reactor.

During the SHRT-45R, the core was partially depleted and heavily instrumented to retrieve experimental data, as sodium temperature. Several SA typologies were loaded inside the reactor (fuelled, dummy assemblies, experimental and so on and so forth), different in their internals and fuel composition.

To perform the steady state simulation in FRENETIC, including photon diffusion, a set of cross sections for neutrons and photon data were needed. The Monte Carlo Serpent-2 has been used to generate the required data by means of a 3D full-core model at SA level. The high level of heterogeneity has been systematically treated, aiming to accurately preserve the thermal power generation: first, starting from the data collected in the framework of the CRP, the SAs have been classified with respect to their function and geometry; second, the material inventory has been reconstructed, including the burnup in each core element; third, preliminary spectral and spatial analyses have been conducted with Serpent-2 to identify a suitable few-group energy grid structure to collapse the neutron cross sections. This energy grid has been used to calculate effective parameters for neutrons, with particular attention to the spatial aspects of the homogenisation. A first attempt of a coarse spatial grouping has been used for neutron: results of this homogenisation have suggested the necessity to refine the spatial scheme for the collapsing, leading to finer spatial (radially/axially) schemes to generate the homogenised cross sections.

After having identified a suitable spatial arrangement, a methodology to compute the energy deposition by neutrons and photons in terms of fission power and KERMA has been developed. This was needed since Serpent-2 is not well optimised to generate the required homogenised photon data as well as for neutrons. By means of the Monte Carlo model used for the generation of cross sections, the single contributions to the total thermal power for both particles have been calculated. These information have been post-processed to generate the input for the FRENETIC code, as well as the attenuation coefficients for photons.

These data have been used to build a set of simulations in FRENETIC, to firstly check the accuracy of the energy/space homogenisation for neutrons, and

secondly to perform the coupled calculation with photons. Results have shown very good agreements between the thermal fission power (and the related neutron flux) computed by the deterministic code and the transport one. Successive spatial refinements have been introduced in both codes, to take into account other phenomena as the scattering due to external sodium surrounding the core or the spatial gradient in the reflector/blanket.

The overall outcomes in term of multiplication eigenvalues are in good accordance between the two tools, confirming the accuracy in the homogenising procedure to generate the effective data. The approach used for the energy deposition provides good results for the neutron KERMA, whereas for photons some difficulties have been highlighted. Although the reaction rate of (n, γ) is correctly assessed by both codes, Serpent-2 does not provide the photon multiplicity production for FRENETIC. This lack of information leads to an underestimation of the photon flux, affecting also the other contributions to the total thermal power.

Therefore, in the future the possibility to calculate the photon multiplicity (as well as for neutrons when fission happens) by Serpent-2 will be addressed to correctly retrieve the total power. With this new data, the validation of the NE/PH module of FRENETIC will be completed by using the experimental measurements of the SHRT-45R, to correctly simulate the transient with FRENETIC in a multiphysics framework (NE+PH+TH) when neutrons and photon are evaluated with the inclusion of thermal-hydraulic feedback.

Chapter 4

Preliminary development of a DOC for deformed fuel bundles in Lead Fast Reactors: the EFIALTE code

In the framework of the European joint project PASCAL, the necessity to develop fast computational tools aiming to support the design phase of the ALFRED core is currently ongoing. One of the tasks in which ENEA and the CIRTEN consortium are involved regards the development of a DOC for the assessment of the SC mixing phenomena which occur in a deformed fuel bundle (occurring, for instance, in accidental condition). This tool, namely EFIALTE (Fig. 4.1), is part of the suite of DOCs (TIFONE, ANTEO+ and TEMIDE) and their development is coordinated by ENEA Bologna.

Figure 4.1: Inferno, Canto XXXI: Ephialte in manacles among the giants.

The EFIALTE purpose is to assess the distribution of temperature, pressure and mass flow rate in a hexagonal closed fuel assembly, accounting for the coupling between the transverse and axial momentum equations. The state-of-the-art for this assessment is represented by ANTEO+, a SC code where the coupling among the SCs (Fig. 4.2) is mainly due to turbulent momentum exchange and/or buoyancy, but not to the localised pressure drops which implies a net mass exchange [6]. This approximation is well justified by the validation domain of ANTEO+: the latter aims to help the design in the nominal condition of the fuel bundle, or, at BOL. In fact, important mixing phenomena can occur not only in accidental condition, but also at the EOL condition when the reactor has experienced a certain level of thermo-mechanical stresses.

In this chapter, the general derivation for deformed fuel bundles is elaborated starting from the mass and axial/radial momentum conservation. The mathematical model is then cast into a matrix form in order to generalise as much as possible the treatment of the geometry. A preliminary application to an undeformed test case is presented, to demonstrate the possibility to solve the coupling among the sub-channels when a pressure drop among the latter is established.

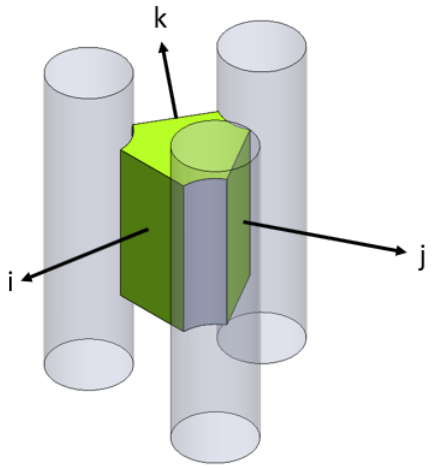

Figure 4.2: Example of sub-channels coupling in the generic fuel bundle.

4.1 Physical model

Here the physical model for the EFIALTE code is presented. The derivation for mass and momentum conservation law is treated in their integral form, assuming the flow as steady state. Consistently with the scope of the EFIALTE code design as foreseen in PASCAL, the present work is limited to the purely hydraulic modelling, thus leaving the calculation of the temperature field for future developments. As

a consequence, the derivation of energy conservation law is not discussed, and the flow is assumed to be isothermal in the whole domain.

To retrieve the equations for mass and momentum, three generic SCs i, j and k are considered. The geometry is presented as undeformed to not to complicate the discussion, although the quantities are evaluated in the generic condition.

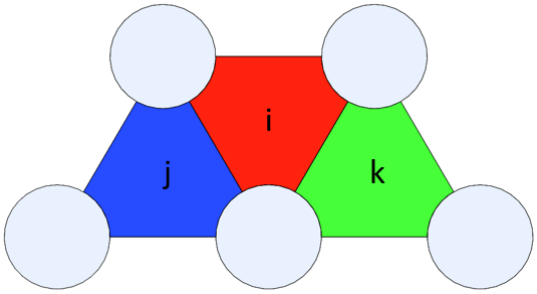

Figure 4.3: Three generic SCs i, j, k for the evaluation of diversion mass flow rates.

4.1.1 Mass law conservation

The mass conservation law allows to perform a balance in the SC i when it exchanges mass towards the gaps of the neighbouring SCs. To do this, a control volume with height dz is considered for the SC i. The latter faces the SCs j and k as reported in Fig. 4.4. The variation of mass flow rate in the SC i depends on:

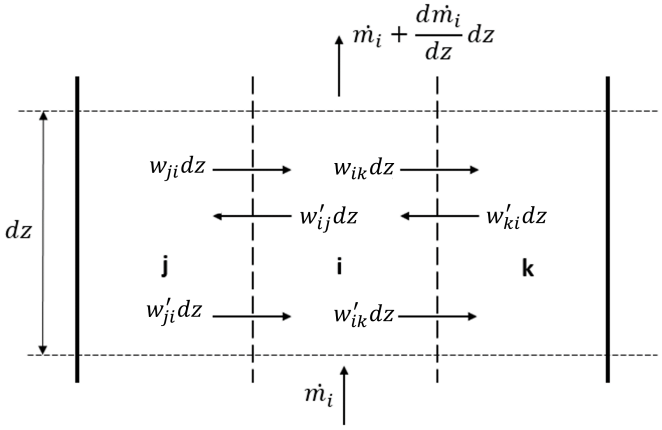

Figure 4.4: Axial mass balance on the generic control volume on the SC i.

- turbulent mixing mass flow rate w'_{ji} and w'_{ik}, and the reciprocal contributes w'_{ij} and w'_{ki};

- diversion mass flow rate w_{ji} and w_{ik};

In order to correctly retrieve the net exchange of mass flow rates among the SCs gaps, a sign convention must be adopted. The SCs of j type *gives* mass flow rates to the SC i, whereas the SCs of k type receive mass flow rate from the channel i. Since the turbulent mixing mass flow rates are equal in absolute value when they are averaged on a sufficient time interval (as in the steady state condition), their net contribution to the channel i is zero. Making a balance on the control volume, the mass conservation law is obtained as:

$$\dot{m}_i + \frac{dm_i}{dz}dz - \dot{m}_i = w_{ji}dz - w_{ik}dz \tag{4.1}$$

where the indexes ji mean that the mass flow rate goes from j to i and it is positive, and the index ik indicate that the mass flow goes from i to k ans it is negative. Therefore, for the channel i, the mass conservation law can be expressed as:

$$\frac{d\dot{m}_i}{dz} = \sum_{j=1}^{N_{\mathrm{SC}}} w_{ij} \tag{4.2}$$

where N_{SC} is the number of SCs and the negative sign is associated to the convention

$$\begin{cases} w_{ij} \geq 0 \text{ if i} < \text{j} \\ w_{ij} < 0 \text{ if i} > \text{j} \end{cases} \tag{4.3}$$

4.1.2 Axial and transverse momentum conservation laws

The momentum conservation law describes the axial and transverse momentum of the coolant in each SC. The axial momentum variation for a given SC is due to gravity, friction due to the portion of the wet perimeter in the SC, localised pressure losses and net transverse momentum exchange with neighbouring SCs. The latter can be caused by either net mass exchange (with the consequent momentum transport) or by mixing effects (which do not imply a net mass exchange).

Axial momentum conservation

The axial momentum conservation law considers the fluxes associated to the diversion mass flow rates and forces as gravity and continuous friction (See Fig. 4.5).

The local balance on the SC i leads to:

$$\begin{aligned} p_i A_{i,z} - (p_i + dp_i)A_{i,z+1} - F_i dz - \rho_i g V_i = \\ \left[f_{\mathrm{D}} w_{ik} u_i dz + f_{\mathrm{T}} w'_{ik} u_i dz + f_{\mathrm{T}} w'_{ij} u_i + \dot{m}_i u_i + d(\dot{m}_i u_i)\right] + \\ - \left[\dot{m}_i u_i + f_{\mathrm{D}} w_{ji} u_j dz + f_{\mathrm{T}} w'_{ki} u_k dz + f_{\mathrm{T}} w'_{ji} u_j dz\right] \end{aligned} \tag{4.4}$$

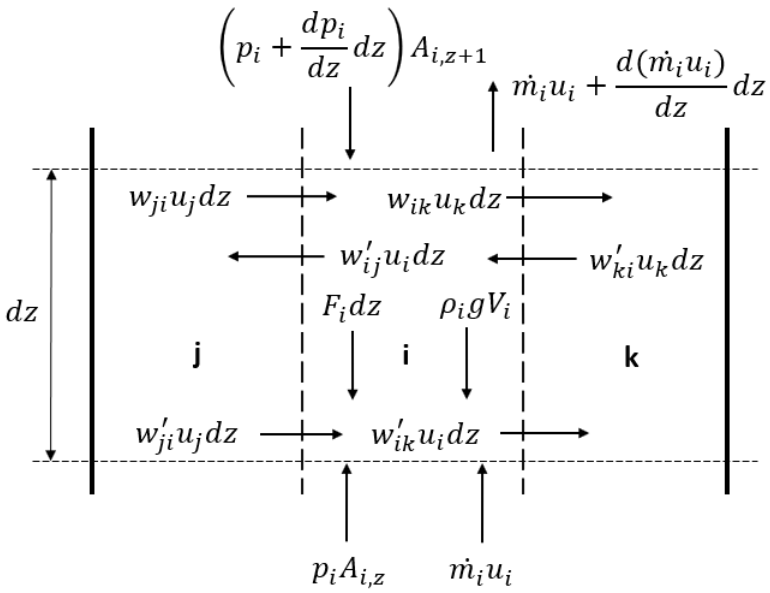

Figure 4.5: Axial momentum balance on the generic control volume on the SC i.

If the last equation is then divided by the dz, the relative pressure loss per unit length is:

$$\begin{aligned} -\frac{dp_i A_{i,z+1}}{dz} &= \rho_i g \frac{V_i}{dz} + F_i - p_i \frac{A_{i,z}}{dz} + p_i \frac{A_{i,z+1}}{dz} + f_{\mathrm{D}} w_{ik} u_i + \\ &+ f_{\mathrm{T}} w'_{ik}(u_i - u_k) + f_{\mathrm{T}} w'_{ij}(u_i - u_j) - f_{\mathrm{D}} w_{ij} u_j + \frac{d(\dot{m}_i u_i)}{dz} \end{aligned} \tag{4.5}$$

Here the mass conservation law is introduced for the last contribution. In fact:

$$\frac{d(\dot{m}_i u_i)}{dz} = \frac{d\dot{m}_i}{dz} u_i + \dot{m}_i \frac{du_i}{dz} \tag{4.6}$$

where the first term is expressed by 4.2, transforming the former equation in

$$\frac{d\dot{m}_i}{dz} u_i + \dot{m}_i \frac{du_i}{dz} = (w_{ji} - w_{ik}) u_i + \dot{m}_i \frac{du_i}{dz} = u_i w_{ji} - u_i w_{ik} + \dot{m}_i \frac{du_i}{dz} \tag{4.7}$$

The coolant can increase its speed if there are either a change in the cross section of the SC, or a variation in its density (conversely for the specific volume). These effects are taken into account by the derivative of velocity with respect to the axial direction:

$$\begin{aligned} \frac{du_i}{dz} &= \frac{d\dot{m}}{dz}\frac{v_i}{A_i} + \dot{m}_i v_i \frac{d}{dz}\left(\frac{1}{A_i}\right) + \frac{\dot{m}_i}{A_i}\frac{dv_i}{dz} = \\ &= (w_{ji} - w_{ik})\frac{v_i}{A_i} + \frac{\dot{m}_i v_i}{\Delta z}\left[\frac{1}{A_{i,z+1}} - \frac{1}{A_{i,z}}\right] + \frac{\dot{m}_i}{A_i}\frac{dv_i}{dz} \end{aligned} \tag{4.8}$$

Here, the derivative of the area along z is approximated by its finite difference, since the geometry of the SC is known at each axial point. On the contrary, the evaluation of the A_i in the first and in the third terms of 4.8 requires a further consideration. In the real condition, the coolant velocity increases/decreases by decreasing/increasing of the cross section area, which is a continuous function of the axial length. In this model, all the quantities are calculated in the *centroid* of the control volume, as sketched in Fig. 4.6. This is necessary since the velocity

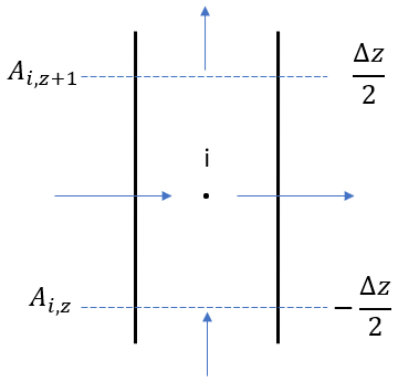

Figure 4.6: EFIALTE centroid of the control volume in the generic SC i.

is different if it is calculated at the inlet, at the middle or at the outlet of the control volume due to the changing of the cross section area. To avoid under/over estimation, the velocities can be evaluated in the centroid, assuming an *average* area given by:

$$A_i = \frac{V_i}{\Delta z} \tag{4.9}$$

This is also consistent also in the undeformed condition, where the volume V_i is constant and the A_i is equal to the $A_{i,z} = A_{i,z+1}$.

The specific volume is function of pressure and the hentalpy or, in other words, its thermodynamic state. Therefore,

$$\frac{dv_i}{dz} = \frac{\partial v_i}{\partial p}\frac{dp}{dz} + \frac{\partial v_i}{\partial h}\frac{dh}{dz} \tag{4.10}$$

Combining this result in the 4.5

$$\begin{aligned} -\frac{dp_i A_{i,z+1}}{dz} &= \rho_i g \frac{V_i}{\Delta z} + F_i - p_i\left(\frac{A_{i,z}}{\Delta z} - \frac{A_{i,z+1}}{\Delta z}\right) + w_{ik}u_i\left(f_{\mathrm{D}} - 1\right) + \\ & f_{\mathrm{T}} w'_{ik}(u_i - u_k) + f_{\mathrm{T}} w'_{ij}(u_i - u_j) + w_{ji}\left(u_i - f_{\mathrm{D}} u_j\right) + \\ & \dot{m}_i\left[\left(w_{ji} - w_{ik}\right)\frac{v_i}{A_i} + \frac{\dot{m}_i v_i}{\Delta z}\left(\frac{1}{A_{i,z+1}} - \frac{1}{A_{i,z}}\right) + \frac{m_i}{A_i}\left(\frac{\partial v_i}{\partial p}\frac{dp_i}{dz} + \frac{\partial v_i}{\partial h}\frac{dh_i}{dz}\right)\right] \end{aligned} \tag{4.11}$$

and the general (i.e. valid for both the deformed and the undeformed case) formulation for the axial momentum conservation law is obtained:

$$\begin{aligned} &-\left[A_{i,z+1}+\dot{m}_i u_i \rho_i \frac{\partial v_i}{\partial p}\right]\frac{dp_i}{dz}=\rho_i g\frac{V_i}{\Delta z}+F_i-p_i\left(\frac{A_{i,z}}{\Delta z}-\frac{A_{i,z+1}}{\Delta z}\right)+\\ &w_{ik}u_i\left(f_{\mathrm{D}}-2\right)+f_{\mathrm{T}}w_{ik}^{'}(u_i-u_k)+f_{\mathrm{T}}w_{ij}^{'}(u_i-u_j)+\\ &w_{ji}\left(2u_i-f_{\mathrm{D}}u_j\right)+\frac{A_i u_i \dot{m}_i}{\Delta z}\left(\frac{1}{A_{i,z+1}}-\frac{1}{A_{i,z}}\right)+\frac{m_i^2}{A_i}\frac{\partial v_i}{\partial h}\frac{dh_i}{dz} \end{aligned} \tag{4.12}$$

Axial momentum conservation in undeformed geometry

If in the 4.12 the geometry is undeformed, the terms which refer to variation of the cross section area are equal to zero. In fact, if $A_{i,z}=A_{i,z+1}=A_i$ the previous equation becomes:

$$\begin{aligned} &-\left[1+\left(\frac{\dot{m}_i}{A_i}\right)^2\frac{\partial v_i}{\partial p}\right]A_i\frac{dp_i}{dz}=F_i+\rho_i g A_i+w_{ik}u_i\left(f_{\mathrm{D}}-2\right)+\\ &w_{ji}\left(2u_i-u_j f_{\mathrm{D}}\right)+f_{\mathrm{T}}w_{ik}^{'}\left(u_i-u_k\right)+f_{\mathrm{T}}w_{ij}^{'}(u_i-u_j)+\frac{\dot{m}_i{}^2}{A_i}\frac{\partial v_i}{\partial h}\frac{dh}{dz} \end{aligned} \tag{4.13}$$

By dividing the last expression by A_i, the undeformed axial momentum law is found. If the condition of isothermal is applied, the derivative of enthalpy along z can be neglected,

$$\begin{aligned} &-\left[1+\left(\frac{\dot{m}_i}{A_i}\right)^2\frac{\partial v_i}{\partial p}\right]\frac{dp_i}{dz}=\left(\frac{\dot{m}_i}{A_i}\right)^2 f_i\frac{P_{\mathrm{b,i}}}{2A_i\rho_i}+\rho_i g+\\ &\frac{w_{ik}u_i}{A_i}\left(f_{\mathrm{D}}-2\right)+\frac{w_{ji}}{A_i}\left(2u_i-u_j f_{\mathrm{D}}\right)+f_{\mathrm{T}}\frac{w_{ik}^{'}}{A_i}\left(u_i-u_k\right)+f_{\mathrm{T}}\frac{w_{ij}^{'}}{A_i}(u_i-u_j) \end{aligned} \tag{4.14}$$

and considering all the possible SCs j that are facing the SC i, the latter equation becomes:

$$\begin{aligned} &-\left[1+\left(\frac{\dot{m}_i}{A_i}\right)^2\frac{\partial v_i}{\partial p}\right]\frac{dp_i}{dz}=\left(\frac{\dot{m}_i}{A_i}\right)^2 f_i\frac{P_{\mathrm{b,i}}}{2A_i\rho_i}+\rho_i g+\\ &\frac{1}{A_i}\sum_{j=1}^{N_{\mathrm{SC}}}f_{\mathrm{T}}w_{ij}^{'}\left(u_i-u_j\right)+\frac{1}{A_i}\sum_{j=1}^{N_{\mathrm{SC}}}\begin{cases} w_{ij}u_i\left(f_{\mathrm{D}}-2\right), & \text{for } w_{ij}\geq 0 \;\; i\longrightarrow j\\ w_{ij}\left(u_j f_{\mathrm{D}}-2u_i\right), & \text{for } w_{ij}<0 \;\; j\longrightarrow i\end{cases} \end{aligned} \tag{4.15}$$

Transverse momentum conservation

The transverse momentum takes into account the momentum which is transferred between a gap from the channel i to a generic channel j. It is a net contribution, due to a physical movement of coolant mass flow rate due to a pressure difference,

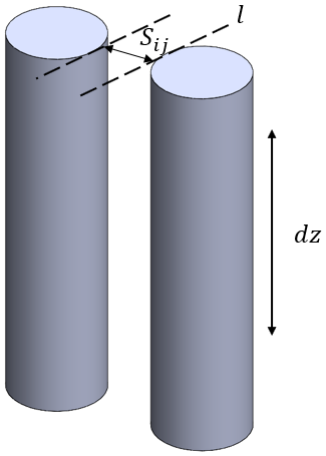

Figure 4.7: EFIALTE transverse momentum derivation

called diversion mass flow rate. If two adjacentSCs are considered, the distance between two fuel rods is S_{ij}, whereas the equivalent*length* (perpendicular to the rods) where the diversion mass flow rate experiences a pressure loss is l. With respect to Fig. 4.7, the difference between the channel i and j is due to:

$$\Delta p_t = p_i - p_j = f\frac{l}{D_{\mathrm{h,i}}}\frac{w_{ij}^2}{2A_t^2\rho_i} = f\frac{l}{4\dfrac{S_{ij}dz}{2dz}}\frac{w_{ij}^2 dz^2}{2S_{ij}^2 dz^2\rho_i} = f\frac{l}{4S_{ij}^3\rho_i}w_{ij}|w_{ij}| \tag{4.16}$$

where the $w_{ij}|w_{ij}|$ gives the sign of the pressure drop, A_t is the transversal area that the coolant faces, and the $D_{\mathrm{h,i}}$ is the hydraulic diameter of the gap. The difficult is to find a suitable value for the product fl. Moreover, if the geometry is deformed, the A_t can result as twisted with respect to the normal direction of the diversion mass flow rate. At this point of the study, the geometry is considered undeformed and the product fl is conservatively considered equal to 0.001.

4.2 Mathematical model

After presenting the general formulation for momentum and mass conservation, here the mathematical scheme to solve for the diversion cross flow w_{ij} is illustrated. Since this formulation aims to put in a suitable way the coupling between the axial and transverse momentum to get the coolant mass exchange among the SCs, the next hypotheses are considered:

- steady state condition;
- the flow is isothermal;

- the geometry is undeformed;

The general system to be solved is

$$\begin{cases} \dfrac{d\dot{m}_i}{dz} = \displaystyle\sum_{j=1}^{N_{\mathrm{SC}}} w_{ij} \\ \\ -\left[1 + \left(\dfrac{\dot{m}_i}{A_i}\right)^2 \dfrac{\partial v_i}{\partial p}\right] \dfrac{dp_i}{dz} = \left(\dfrac{\dot{m}_i}{A_i}\right)^2 f \dfrac{P_{\mathrm{b,i}}}{2A_i\rho_i} + \rho_i g + \\ \dfrac{1}{A_i} \displaystyle\sum_{j=1}^{N_{\mathrm{SC}}} f_{\mathrm{T}} w_{ij}^{'} \left(u_i - u_j\right) + \dfrac{1}{A_i} \displaystyle\sum_{j=1}^{N_{\mathrm{SC}}} \begin{cases} w_{ij} u_i \left(f_{\mathrm{D}} - 2\right), & \text{for } w_{ij} \geq 0 \; i \to j \\ w_{ij} \left(u_j f_{\mathrm{D}} - 2u_i\right), & \text{for } w_{ij} < 0 \; j \to i \end{cases} \\ \\ p_i - p_j = f \dfrac{l}{4S_{ij}^3 \rho_i} w_{ij} |w_{ij}| \end{cases} \tag{4.17}$$

where the first and the second equations solve the velocity field (i. e., the mass flow) and the pressure field, whereas the third implies the coupling among the SCs. To solve the two differential equations, a numerical scheme is required. This system has to be solved for the each SC in each axial point. To assure the unconditional stability of the numerical scheme, the Implicit Euler method is used for the integration of the space dependency. Applying the numerical scheme to the previous differential equations, velocity and pressure fields can be retrieved for each SC as

$$\begin{cases} \dot{m}_i^{z+1} = \dot{m}_i^z + \Delta z \left(\dfrac{\Delta \dot{m}_i}{\Delta z}\right)^{z+1} \\ p_i^{z+1} = p_i^z + \Delta z \left(\dfrac{\Delta p_i}{\Delta z}\right)^{z+1} \end{cases} \tag{4.18}$$

where the derivatives of mass flow rates and pressure losses are given by 4.17. In order not to complicate the discussion, all the quantities from this point onward are considered to be calculated at $z+1$ point.

The conservation of mass and axial momentum are linked among the SCs by the transverse momentum equation. In fact, the latter describes the net mass exchange among SCs consequent to the difference of pressure between two adjacent SCs (i, j). Since the diversion mass flow rate between two contiguous SCs is associated to a unique interface, the SCs couple (i, j) corresponds to a single k interface, thus a change of notation can be adopted

$$w_{ij} = w_k \tag{4.19}$$

where the index k corresponds to the index (i, j) of the SCs. As a consequence, the pressure inside the generic i SC can be written as:

$$p_i = q_i + \sum_{k=1}^{N_{\mathrm{K}}} r_{ik} w_k \tag{4.20}$$

where:

- q_i is the axial term due to gravity, continuous pressure loss and turbulent exchange mixing;
- N_{K} is the total number of the interfaces;
- r_{ik} is the driver of the transverse exchange towards all the N_{K} interfaces. This term depends on the relative velocity between two contiguous SCs (i, j).

For the i^{th} SC, the q_i contribution is defined as

$$q_i = p_i^z - \left[\left(\frac{m_i}{A_i}\right)^2 \frac{f_i}{2D_{\mathrm{h,i}}\rho} + \rho g + \frac{b_i}{A_i}\right]\left[1 + \left(\frac{m_i}{A_i}\right)^2 \frac{\partial v_i}{\partial p}\right]^{-1} \Delta z \tag{4.21}$$

where b_i is the i^{th} component of the vector related to the turbulent exchange $\boldsymbol{b}$ vector. For the sake of compactness, the last definition can be generalised in matrix form since all the quantities are solved simultaneously at the same axial node. If N_{SC} is the total number of SCs in the system, the next matrices can be defined as:

$$\boldsymbol{a} = \begin{bmatrix} A_1 \\ A_2 \\ \dots \\ A_{N_{\mathrm{SC}}} \end{bmatrix} \quad \boldsymbol{M} = \begin{bmatrix} \left(\frac{m_1}{A_1}\right)^2 & 0 & \dots & 0 \\ 0 & \left(\frac{m_2}{A_2}\right)^2 & \dots & 0 \\ \dots & \dots & \dots & \dots \\ 0 & \dots & \dots & \left(\frac{m_{N_{\mathrm{SC}}}}{A_{N_{\mathrm{SC}}}}\right)^2 \end{bmatrix} \tag{4.22}$$

$$\boldsymbol{F} = \begin{bmatrix} \left(\frac{f_1}{2D_{\mathrm{h},1}\rho}\right) & 0 & \dots & 0 \\ 0 & \left(\frac{f_2}{2D_{\mathrm{h},2}\rho}\right) & \dots & 0 \\ \dots & \dots & \dots & \dots \\ 0 & \dots & \dots & \left(\frac{f_{N_{\mathrm{SC}}}}{2D_{\mathrm{h},\mathrm{N_{SC}}}\rho}\right) \end{bmatrix} \tag{4.23}$$

$$\boldsymbol{G} = \begin{bmatrix} \rho g & 0 & \dots & 0 \\ 0 & \rho g & \dots & 0 \\ \dots & \dots & \dots & \dots \\ 0 & \dots & \dots & \rho g \end{bmatrix} \quad \boldsymbol{V} = \begin{bmatrix} \frac{\partial v_1}{\partial p} & 0 & \dots & 0 \\ 0 & \frac{\partial v_2}{\partial p} & \dots & 0 \\ \dots & \dots & \dots & \dots \\ 0 & \dots & \dots & \frac{\partial v_{N_{\mathrm{SC}}}}{\partial p} \end{bmatrix} \tag{4.24}$$

Regarding the turbulent exchange $\boldsymbol{b}$, some considerations about the connection of each SC must be discussed. The topology of the connections gives the relation

about the convention of mass exchange sign and the number of the interfaces. First, a matrix which identifies the physical connections (i, e., the interfaces) must be known. To assess this, a matrix $\boldsymbol{K}$ can be build with N_{K} rows, corresponding to the number of interfaces. The number of columns is fixed at 2 since the k interface faces always 2 single SCs: each column contains the index of the SCs across the interface, with the convention to have $i < j$. Therefore the number of rows depends on the geometry of the fuel bundle, and a generic SC can have multiple exchanges with a different number of interfaces.

By means of the $\boldsymbol{K}$ matrix, the exchange matrix $\boldsymbol{D}$ can be built. The latter contains the information related to the direction of the mass flow rates, or in other words, it defines the sign convention of the exchanges. The matrix $\boldsymbol{D}$ has N_{K} rows as the number of the interfaces, and N_{SC} columns as the number of SCs. For the k interface, the element $d_{k,i}$ of $\boldsymbol{D}$ is:

- -1 if the SC gives mass flow rate towards the interface;
- 1 if the SC receives mass flow rate towards the interface;
- 0 elsewhere, since only 2 SCs can exchange mass each other on a single interface.

These two matrices are useful to conveniently evaluate the exchange of momentum and mass, since the selection of the row in the $\boldsymbol{K}$ matrix automatically identifies which SCsare involved on the k interface, and consequently the matrix $\boldsymbol{D}$ give the signs of exchange with its element $d_{k,i}$. An example for $\boldsymbol{D}$ and $\boldsymbol{K}$ is provided in the next with $N_{\mathrm{SC}} = 6$ and $N_{\mathrm{K}} = 6$:

$$\boldsymbol{K} = \begin{bmatrix} 1 & 2 \\ 2 & 3 \\ 3 & 4 \\ 4 & 5 \\ 5 & 6 \\ 1 & 6 \end{bmatrix} \quad \boldsymbol{D} = \begin{bmatrix} -1 & 1 & 0 & 0 & 0 & 0 \\ 0 & -1 & 1 & 0 & 0 & 0 \\ 0 & 0 & -1 & 1 & 0 & 0 \\ 0 & 0 & 0 & -1 & 1 & 0 \\ 0 & 0 & 0 & 0 & -1 & 1 \\ -1 & 0 & 0 & 0 & 0 & 1 \end{bmatrix} \tag{4.25}$$

Concerning the turbulent mixing exchange $\boldsymbol{b}$, its generic term b_i is defined as:

$$\sum_{j=1}^{N_{\mathrm{SC}}} f_{\mathrm{T}} w_{ij}^{'} \left(u_i - u_j\right) \tag{4.26}$$

Using the information provided $\boldsymbol{D}$ matrix, the relative velocity between i and j can be computed as

$$\boldsymbol{\Delta u} = -\boldsymbol{D u} \tag{4.27}$$

if $\boldsymbol{u}$ is the column vector that contains the velocity of coolant in each SC. The second factor that has to be expressed is the turbulent mixing flow rate $w_{ij}^{'}$. The

constitutive relations for the numerical values of this matrix will be exposed in the next section where the closure definitions are reported. For the moment, the mathematical aspect of this matrix is analysed. The vector $\boldsymbol{w}_{\text{mix}}$ has the dimension of $N_{\text{SC}} \times 1$ rows, as well as the turbulent friction factor f_{T}. Therefore, the relation 4.26 can be now written as:

$$\boldsymbol{b} = \boldsymbol{D}^{\text{T}} \text{diag}(\boldsymbol{\Delta u}) \text{diag}(\boldsymbol{f}_{\text{T}}) \text{diag}(\boldsymbol{w}_{\text{mix}}) \tag{4.28}$$

Finally, the column matrix $\boldsymbol{q}$ can be built as

$$\boldsymbol{q} = \boldsymbol{p}^z - \left[\boldsymbol{MF} + \boldsymbol{G} + \text{diag}(\boldsymbol{a})^{-1}\boldsymbol{b}\right] \boldsymbol{I}_{N_{\text{SC},1}} \left[\boldsymbol{I}_{N_{\text{SC},1}} + \boldsymbol{MV}\boldsymbol{I}_{N_{\text{SC},1}}\right]^{-1} \Delta z \tag{4.29}$$

The sign of the generic term is conditioned by the matrix $\boldsymbol{D}$ with the logic reported in Fig. 4.8. The terms in the lowest level of the flowchart are determined

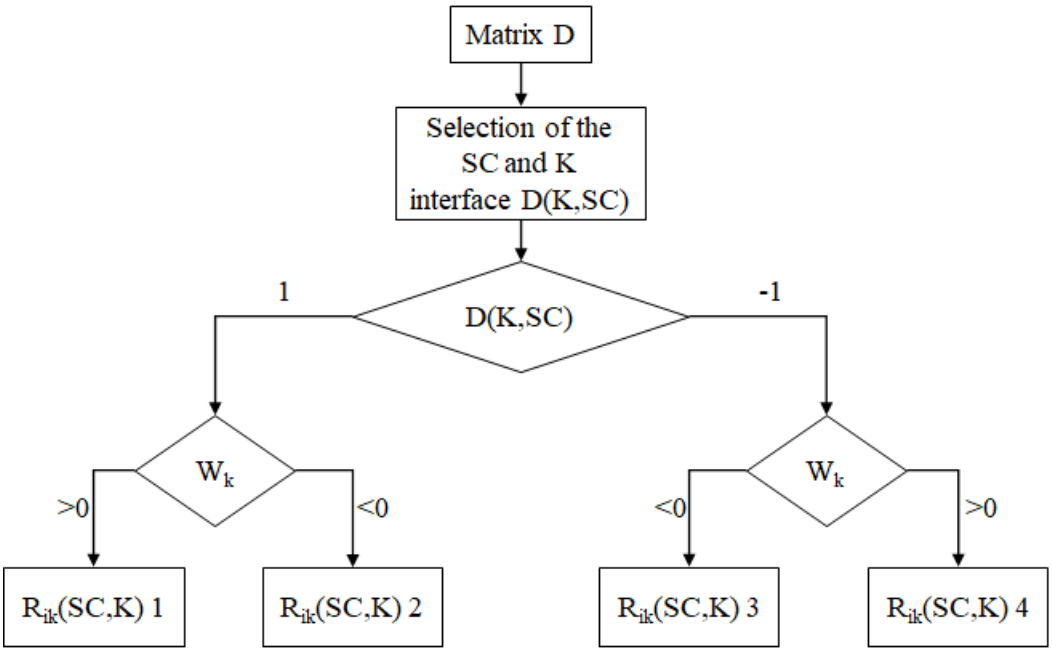

Figure 4.8: Exchange matrix **R** logic evaluation with the four formulation for the r_{ik}.

by the sign of the diversion mass flow rate. In fact, according to the 4.17, the expression of the exchange term can be:

1. if $d_{k,i}$ is equal to 1:

$$\begin{cases} r_{ik} = \dfrac{u_i}{A_i}(2 - f_{\mathrm{D}})\left[1 + \left(\dfrac{m_i}{A_i}\right)^2 \left(\dfrac{\partial v_i}{\partial p}\right)\right]^{-1} & \text{for } w_k \geq 0 \\ r_{ik} = \dfrac{1}{A_i}(2u_i - f_{\mathrm{D}} u_j)\left[1 + \left(\dfrac{m_i}{A_i}\right)^2 \left(\dfrac{\partial v_i}{\partial p}\right)\right]^{-1} & \text{for } w_k < 0 \end{cases} \tag{4.30}$$

2. if $d_{k,i}$ is equal to -1:

$$\begin{cases} r_{ik} = \dfrac{u_i}{A_i}(f_{\mathrm{D}} - 2)\left[1 + \left(\dfrac{m_i}{A_i}\right)^2 \left(\dfrac{\partial v_i}{\partial p}\right)\right]^{-1} & \text{for } w_k \geq 0 \\ r_{ik} = \dfrac{1}{A_i}(f_{\mathrm{D}} u_j - 2u_i)\left[1 + \left(\dfrac{m_i}{A_i}\right)^2 \left(\dfrac{\partial v_i}{\partial p}\right)\right]^{-1} & \text{for } w_k < 0 \end{cases} \tag{4.31}$$

These elements build a sparse matrix $\boldsymbol{R}$ which has the dimensions of $N_{\mathrm{SC}} \times N_{\mathrm{K}}$, so in general it is not squared. The pattern of $\boldsymbol{R}$ is the same of the matrix $\boldsymbol{D}^{\mathrm{T}}$ because it is build on the basis of the connection among the SCs. As last step, the pressure in all SCs of the fuel bundle can be expressed, according to the 4.20, as:

$$\begin{aligned} &\boldsymbol{p}^{z+1} = \boldsymbol{p}^z + \Delta z \left(\frac{\boldsymbol{\Delta p}}{\boldsymbol{\Delta z}}\right)^{z+1} = \\ &\boldsymbol{p}^z - \left[\boldsymbol{M}\boldsymbol{F} + \boldsymbol{G} + \mathrm{diag}(\boldsymbol{a})^{-1}\boldsymbol{b}\right] \boldsymbol{I}_{N_{\mathrm{SC},1}} \left[\boldsymbol{I}_{N_{\mathrm{SC},1}} + \boldsymbol{M}\boldsymbol{V}\boldsymbol{I}_{N_{\mathrm{SC},1}}\right] \Delta z + \boldsymbol{R}\boldsymbol{w}\Delta z \end{aligned} \tag{4.32}$$

with $\boldsymbol{w}$ as the column vector of the diversion mass flow rates.

To retrieve the transversal exchange, a single couple of SCs (i, j) is concerned. If the definition 4.20 is written for the SCs i and j, their difference leads to:

$$p_i - p_j = q_i - q_j + \sum_{k=1}^{N_{\mathrm{K}}} (r_{ik} - r_{jk})\, w_k = s_l + \sum_{k=1}^{N_{\mathrm{K}}} (r_{ik} - r_{jk})\, w_k \tag{4.33}$$

where l refers to the specific interface of the couple (i, j). At this point, the transverse equation can be used to substitute the difference between p_i and p_j. Therefore, the final expression for the interface l from 1 to N_{K} is given by:

$$\sum_{k=1}^{N_{\mathrm{K}}} (r_{ik} - r_{jk}) w_k - c_l w_l |w_l| + s_l = 0 \tag{4.34}$$

Particular attention must be drawn on this last expression: the l index refers to a specific interface where the diversion cross flow is evaluated, whereas the index

k refers to all the interfaces in the domain. Indeed, a single SC can exchange with different adjacent SCs, since it receives or gives mass and momentum by the driving term r_{ik} towards the related gaps. Therefore, the sum takes into account the different contributions to the channel i with respect to neighbouring channels that are exchanging mass and momentum with the others. The index l, which is included in the range of N_{K}, allows to evaluate the diversion mass flow rate of that specific interface, considering at the same time the net exchanges with the other SCs.

Thus, if this equation is written for all the possible l interfaces, a system $N_{\mathrm{K}} \times N_{\mathrm{K}}$ is obtained, and the transfer matrix $\boldsymbol{T}$ can be defined starting from $\boldsymbol{R}$. This is possible since the latter already contains the other physical connections of i and j when the interface k is solved. The matrix $\boldsymbol{T}$ is equal to

$$\boldsymbol{T} = \boldsymbol{R} - \boldsymbol{I}_{\mathrm{P}}\boldsymbol{R} \tag{4.35}$$

where the permutation matrix $\boldsymbol{I}_{\mathrm{P}}$ is defined starting by the information of $\boldsymbol{K}$. Each row of $\boldsymbol{K}$ contains the indexes (i, j) which correspond, respectively, to the row indexes of $\boldsymbol{R}$ to build the difference $(r_{ik} - r_{jk})$.

Regarding c_l and s_l, c_l is the component of the diagonal matrix $\boldsymbol{C}$ where the localised pressure drops of the gaps are inserted, and $\boldsymbol{s}$ is the column vector of the difference of the axial momentum of the generic couple (i, j) according to $\boldsymbol{K}$:

$$\boldsymbol{C} = \begin{bmatrix} f_1 \dfrac{l}{4S_1^3\rho} & 0 & \dots & 0 \\ 0 & f_2 \dfrac{l}{4S_2^3\rho} & & 0 \\ \vdots & & \ddots & \vdots \\ 0 & 0 & \dots & f_{N_{\mathrm{K}}} \dfrac{l}{4S_{N_{\mathrm{K}}}^3\rho} \end{bmatrix} \quad \boldsymbol{s} = \begin{bmatrix} s_1 \\ s_2 \\ \vdots \\ s_{N_{\mathrm{K}}} \end{bmatrix} \tag{4.36}$$

Finally, the diversion mass flow rate $\boldsymbol{w}$ can be obtained by solving the next system, also called *CROSSFLOW SCHEME*:

$$\Big(\boldsymbol{T} - \boldsymbol{C}|\boldsymbol{w}|\Big)\boldsymbol{w} + \boldsymbol{s} = \boldsymbol{0} \tag{4.37}$$

4.2.1 Constitutive equations and solution algorithm

The mathematical formulation of the CROSSFLOW SCHEME needs a set of constitutive equations to complete the definitions of the previous matrices. These closure relations are necessary to correctly evaluate

- the friction factor f_i;
- turbulent mixing mass flow rate $w_{ij}^{'}$ in the vector $\boldsymbol{w}_{\mathrm{mix}}$

since the turbulent and diffusive correction cross flow terms f_{T} and f_{D} are input data and they vary from 0 to 1. For the friction factor in the axial direction, the correlation given by [41] is generally suitable for liquid metals flowing in circular pipe. The physical properties have been take from [6]. The cross section area of the SC is not circular, therefore the hydraulic diameter must be used:

$$f_i = \frac{0.316}{Re_{D_{\mathrm{h,i}}}^{0.25}} \tag{4.38}$$

Other correlations shall be implemented in the final version of the code to cover the entire foreseen validation domain.

Several correlations are available in literature for the turbulent mixing mass flow rate. In general, this mass flow rate is in the form of:

$$w_{ij}^{'} = \beta_{ij} S_{ij} \overline{G_{ij}} \tag{4.39}$$

where β_{ij} is the turbulent mixing parameter which depends on position of the SC (i. e., the gap), $\overline{G_{ij}}$ is the average specific mass flow rate of the SCs (i, j). Due to the dependence of the SC typology (internal, corner or boundary), a more general relation for this quantity is used for the moment, which is in the form of:

$$w_{ij}^{'} = \rho \frac{\epsilon}{l_{ij}} S_{ij} \tag{4.40}$$

with ϵ is the turbulent diffusivity and l_{ij} is the mixing length, under the hypothesis to have the mixing momentum length and mixing thermal length as equal. If in the previous relation the correlation of Rogers and Rosehart reported in [42] is used for the mixing length, the 4.40 becomes

$$w_{ij}^{'} = K_1 S_{ij} \overline{G_{ij}} \frac{\overline{D}_{\mathrm{e,ij}}}{D_r} \left(\overline{Re}_{ij}\right)^{-0.1} \left(\frac{S_{ij}}{D_r}\right)^{K_2} \tag{4.41}$$

where K_1 is 0.0018 and K_2 is 1.4 for triangular cells, and D_r is the rod diameter.

The solution algorithm is shown in Fig. 4.9. The solver takes as input the geometry of the SCs and the temperature on which the physical properties are calculated (the dynamic viscosity and mass density of lead). On the basis of the geometry, the interfaces matrix $\boldsymbol{K}$ and the connection matrix $\boldsymbol{D}$ are determined. At this point, the whole calculation domain is assessed, since the number of axial points is defined by the user by choosing a spatial discretisation step Δz. The boundary conditions are imposed in each SC with the mass flow rate and the pressure. Here the iterative calculation starts:

1. to solve the spatial point $z + 1$, a first guess for the diversion mass flow rates is assumed;

2. to retrieve the mass flow rate in the node $z+1$, the mass conservation law is solved and the matrix $\boldsymbol{M}$ is composed;
3. the $\boldsymbol{u}$ vector is calculated:
   - the friction factor in the axial direction is found;
   - the turbulent mass flow rates are determined;
   - the relative difference between (i, j) can be built with in the vector $\boldsymbol{\Delta u}$;
4. the axial momentum law is solved for each SC, to construct the matrix $\boldsymbol{R}$;
5. here the transfer matrix $\boldsymbol{T}$ is computed and the matrix $\boldsymbol{C}$ is summed to it;
6. the diversion mass flow rates are computed in the vector $\boldsymbol{w}$.

When the point 6 is reached, error checks on pressure and diversion mass flow rates are performed, and the new values of the diversion mass flow rates are updated in the first point. It should be noted that in the compute of $\boldsymbol{C}$, the issue of the non-linearity of localised pressure drops with respect to the solution vector $\boldsymbol{w}$ is solved by using the previous value of the diversion mass flow rate. This is justified by the expected small changes of the diversion mass flow rates between an iteration and another. To assure a low level of oscillation of the solution for pressure and mass flow rates, the new values are under-relaxed to enhance the speed of convergence. The iterations are repeated until both errors are lower than the imposed tolerance, then the calculation is moved to the next axial point.

Although this procedure has been built for the undeformed condition, the extension to the deformed condition is straightforward: the geometry has to be built according to the foreseen deformation, and in the matrix formulation the terms related to the variation of the areas have to be included. Moreover, the coupling scheme between the inlet pressure and outlet pressure is foreseen: in this study, the inlet pressure is imposed together with the mass flow rate. In the practice, the inlet mass flow rate is known as well as the outlet pressure at the end of fuel bundle. Therefore, the inlet pressure must be found according to have the same value of pressure at end of SCs. In other words, a relation between the exit pressure and inlet pressure has to be included in the model, to allow the flowing of the imposed mass flow rates for each SC. Notwithstanding these *open-issues*, in the next section a test case is shown with an application to a domain composed by 6 SCs.

4.3 Test case: undeformed 6 sub-channels domain

The geometry is composed by 7 pins in a regular triangular lattice. With respect to Fig. 4.10, there are 6 SCs with 6 internal interfaces (orange ones), while the

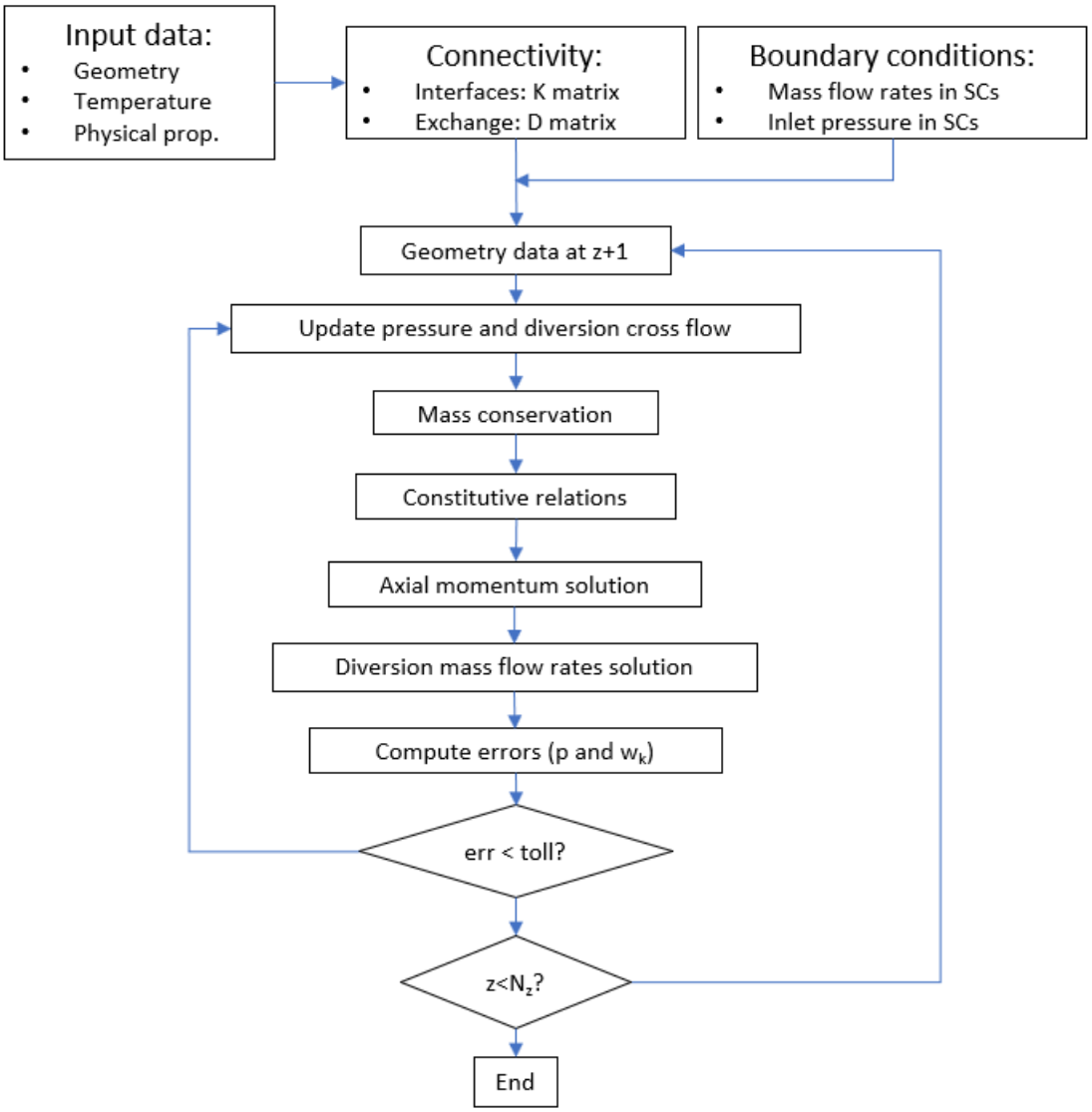

Figure 4.9: CROSSFLOW SCHEME solution alghorithm in undeformed geoemtry.

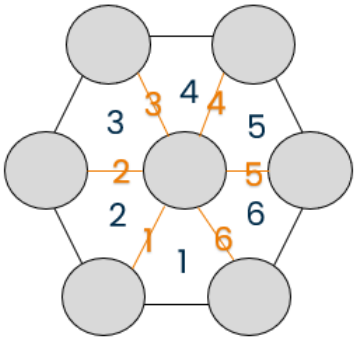

Figure 4.10: Test case for the EFIALTE solver in undeformed condition.

external ones are assumed impenetrable. Each pin has a diameter of 0.525 cm and the pitch is 1.386 cm. The axial length is 10 cm and the spatial discretisation step is Δz = 1E-4 m. In this configuration, the matrices $\boldsymbol{D}$ and $\boldsymbol{K}$ are in:

$$\boldsymbol{K} = \begin{bmatrix} 1 & 2 \\ 2 & 3 \\ 3 & 4 \\ 4 & 5 \\ 5 & 6 \\ 1 & 6 \end{bmatrix} \boldsymbol{D} = \begin{bmatrix} -1 & 1 & 0 & 0 & 0 & 0 \\ 0 & -1 & 1 & 0 & 0 & 0 \\ 0 & 0 & -1 & 1 & 0 & 0 \\ 0 & 0 & 0 & -1 & 1 & 0 \\ 0 & 0 & 0 & 0 & -1 & 1 \\ -1 & 0 & 0 & 0 & 0 & 1 \end{bmatrix} \tag{4.42}$$

Regarding the boundary conditions, the inlet mass flow rate [kg/s] for each SC and the inlet pressure [Pa] are:

$$\boldsymbol{m} = \begin{bmatrix} 0.7 \\ 0.7 \\ 0.7 \\ 0.7 \\ 0.7 \\ 0.7 \end{bmatrix} \boldsymbol{p} = 10^5 \begin{bmatrix} 4.19 \\ 4.20 \\ 4.20 \\ 4.20 \\ 4.20 \\ 4.19 \end{bmatrix} \tag{4.43}$$

The difference in the SCs 1, 3 and 6 is assumed *a priori* in order to create the driver for the initial exchange. The matrix $\boldsymbol{R}$ is in the form of (here is reported in the general form, since it is updated at each iteration):

$$\boldsymbol{R} = \begin{bmatrix} r_{1,1} & 0 & 0 & 0 & 0 & r_{1,6} \\ r_{2,1} & r_{2,2} & 0 & 0 & 0 & 0 \\ 0 & r_{3,2} & r_{3,3} & 0 & 0 & 0 \\ 0 & 0 & r_{4,3} & r_{4,4} & 0 & 0 \\ 0 & 0 & 0 & r_{5,4} & r_{5,5} & 0 \\ 0 & 0 & 0 & 0 & r_{6,5} & r_{6,6} \end{bmatrix} \tag{4.44}$$

$$\boldsymbol{T} = \begin{bmatrix} r_{1,1} - r_{2,1} & -r_{2,2} & 0 & 0 & 0 & r_{1,6} \\ r_{2,1} & r_{2,2} - r_{3,2} & -r_{3,3} & 0 & 0 & 0 \\ 0 & r_{3,2} & r_{3,3} - r_{4,3} & -r_{4,4} & 0 & 0 \\ 0 & 0 & r_{4,3} & r_{4,4} - r_{5,4} & -r_{5,5} & 0 \\ 0 & 0 & 0 & r_{5,4} & r_{5,5} - r_{6,5} & -r_{6,6} \\ r_{1,1} & 0 & 0 & 0 & -r_{6,5} & r_{1,6} - r_{6,6} \end{bmatrix} \tag{4.45}$$

4.3.1 Preliminary results

The preliminary results are reported in Figs.4.11, 4.12 and 4.13. Since the inlet

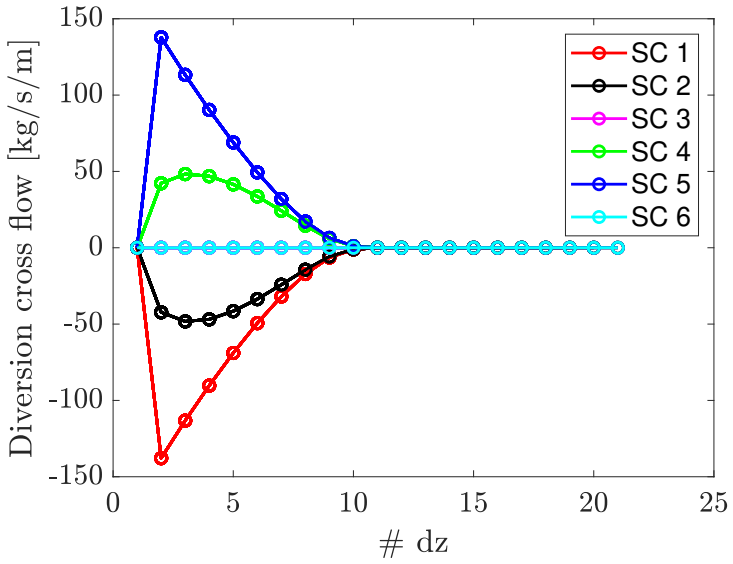

Figure 4.11: Diversion mass flow rate for the test case in undeformed condition.

pressure in the SCs is not equal, the diversion mass flow rates are established in the first axial region of the fuel bundle. As the mass is being exchanged between SC 1 and SC 6, the other SCs are involved in the process in order to compensate the difference. As the pressure in the SCs becomes equal, the diversion mass flow rate decreases to zero and the system reaches the equilibrium condition until the last axial point.

4.3.2 Conclusions and perspectives

The design and the pursuing of the LFRs is currently supported by the PASCAL project for the design of the ALFRED core. Indeed, in the framework of PASCAL, the development of new tools for the assessment of accidental condition of the FA in a HLMCRs and their validation by future experimental campaigns is one of the main targets to be achieved. Furthermore, fast computational codes for the preliminary

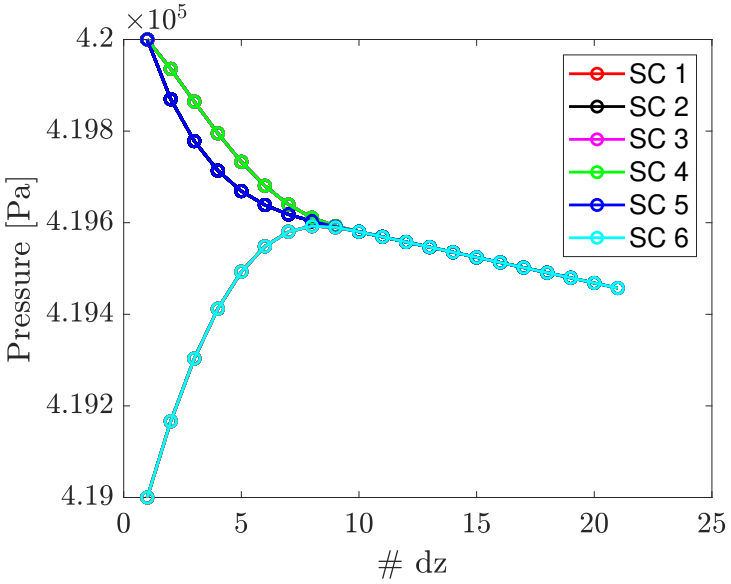

Figure 4.12: Pressure at each axial point for the test case in undeformed condition.

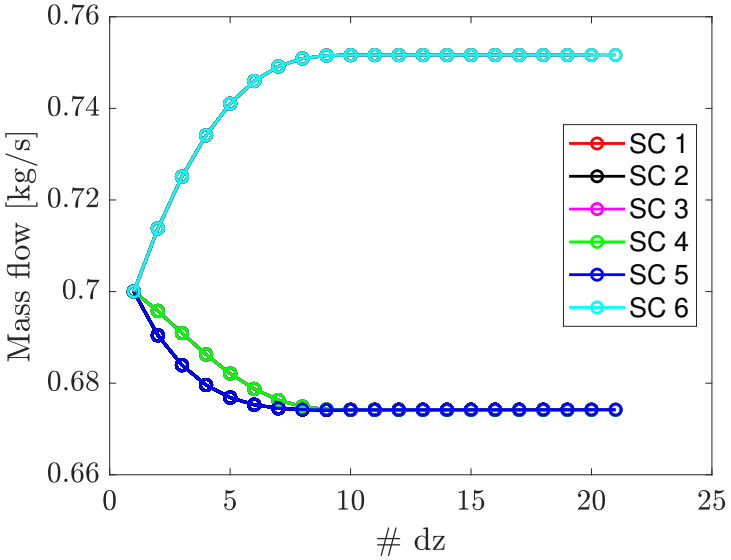

Figure 4.13: Mass flow rates for the test case in undeformed condition.

verification of operating conditions (as BOL/EOL) have to be envisaged. This type of study requires the so-called DOCs, that are computational codes able to simulate different phenomena in order to give a first verification of the conceptual design. ENEA Bologna is currently coordinating the development of a DOCs suite (ANTEO+, TIFONE, TEMIDE) for the complete analyses of LFRs, in which each code is able to verify, and thus produce an output/input, for the other codes of the group to create a consistent multi-physics framework of analysis.

The general purpose of the EFIALTE code is to assess the distribution of mass flow, temperature and pressure of SCs when the geometry of the FA in LFRs is deformed. This deformation can arise from two principal conditions. First, as natural evolution of the FA geometry in the EOL condition; second, when an accidental condition (as the displacement of a fuel rod) is considered. In both scenarios, relevant mixing phenomena occur, leading the FA to unpredictable operating condition, which requires an assessment during the design phase itself.

Therefore, the model on which EFIALTE is based has to treat the solution of mass flow, transverse and axial momentum, energy conservation laws to retrieve the diversion mass flow rates among the SCs in the single FA. It is pivotal to point out that this kind of analyses is, at present, already performed by ANTEO+ but with a different application domain. In fact, ANTEO+ is able to simulate normal operating condition of the FA as the BOL in nominal geometry, when the net mass exchanges are negligible and the pressure in each SC can be assumed constant in the transverse direction.

The preliminary work on this new model for EFIALTE deals with the solution of mixing effects in a pure hydraulic scenario. The general mathematical formulation (CROSSFLOW SCHEME) in deformed/undeformed condition for the evaluation of diversion mass flow rates has been formulated. To test the possibility to solve the transverse mixing, the undeformed situation has been studied in a simple test case constituted by 6 SCs. Since the considered geometry is assumed undeformed, the driver of the mass exchange has been obtained by imposing a different inlet pressure in 2 SCs of 6, in order to establish a forced unbalance of pressure. The CROSSFLOW SCHEME has shows promising results: the diversion mass flow rate is correctly retrieved when a proper driver (i.e., the different pressure at the inlet) is provided as boundary condition.

Future activities on this tool are foreseen by NEMOgroup at Politecnico di Torino, including in the CROSSFLOW SCHEME the implementation of the formulation for deformed geometry and the energy conservation law. In fact, at the moment the effects related to buoyancy have been neglected, as the thermal turbulent exchanges of momentum. In the end, a strategy to calculate the correct inlet pressure when the outlet pressure at the end of the sub-channels is imposed will be implemented, in order to simulate an operating condition nearer the real one.

Part II

Liquid metals for nuclear fusion reactors

Chapter 5

Tritium mass transport modelling for the PAV of the EU DEMO Tritium Extraction System

The most promising nuclear fusion reaction to be exploited for electricity production in a tokamak involves deuterium and tritium as reactants [10]; while the former can be extracted, e.g., from the seawater, the latter is radioactive with an half-life of ∼12 years [11]. Therefore, it cannot be found in nature in a quantity sufficient for the fuelling of a tokamak. For this reason, it will be produced on-site by the breeding of the lithium in the blanket [15]. For the EU DEMO reactor, aiming at demonstrating the electricity production from nuclear fusion reaction in Europe by the middle of this century, one of the options is to have a breeding blanket cooled by water [15] or helium [43] and exploiting PbLi as liquid breeder. To extract the tritium from the PbLi, a TERS should be foreseen in the plant: it will close the fuel cycle avoiding the accumulation of radioactive inventory in the machine. Several technologies are being investigated for the EU DEMO TERS [44], but currently the most promising seem to be the GLC, the VLC and the PAV [45].

While the former two rely on the direct contact between the tritium carrier (PbLi) and the secondary side of the extractor (a stripping gas, e.g. helium, in the GLC [46], or vacuum in the VLC), the PAV technology is based on tritium transport across a membrane permeable to tritium [47]. The membrane separates the PbLi, in which the dissolved tritium, after being generated within the blanket, has a given partial pressure, from the secondary side, where vacuum is pumped. The tritium pressure difference across the membrane is thus the driver of the permeation. The liquid alloy of PbLi with dissolved tritium passes through channels whose wall is the membrane itself. For the dimensioning of the PAV membrane, a proper estimation of the tritium permeated flux in nominal operating conditions is needed. To perform this estimation, suitable numerical models must be adopted.

Such models already exist, e. g. that developed in [48], where the tritium permeation was considered to be dominated by the diffusion across a Nb membrane also in view of the assumption of atomic dissolution of the tritium in the PbLi (justified in [49] and [50]). This model was already used for a preliminary dimensioning of the PAV for the EU DEMO TERS [51]. The latter, however, requires a model accounting for the fact that in some operating conditions the permeation regime can be limited by phenomena localised on the membrane surface facing the liquid metal (or the vacuum) rather than by the diffusion across the membrane itself, as shown in the next Section. Consequently, besides the surface phenomena on the vacuum side already partially included in [48] as an upgrade of the previous model based on [52], it is necessary to introduce a more detailed description of the surface partial fluxes on both the inner and outer sides of the membrane.

The permeation model in [47] can be used as a reference for that: it accounts for the surface phenomena when a gas mixture faces a metal membrane. Therefore, the gas follows the kinetic theory since the equations were developed for gas-metal-vacuum interactions. However, the liquid nature of the tritium carrier (PbLi in the EU DEMO) does not allow to use such model, developed for gaseous carriers.

Therefore, the present chapter deals with the development of a new model for the tritium permeation across a membrane from a liquid carrier, in order to support the design of the EU DEMO TERS based on PAV technology. Properly setting all the input parameters, the new model will be able to address both surface and diffusion regimes.

5.1 Permeation physics and modelling

The aim of the above-mentioned PAV design process is the calculation of the requested length for the permeator channels (i.e. the membrane) where the PbLi flows, in order to reduce the concentration of the dissolved tritium below a prescribed value before returning the carrier to the breeding blanket. This concentration reduction is usually expressed in terms of efficiency (η) of the PAV:

$$\eta = 1 - \frac{C_{\text{out}}}{C_{\text{in}}} \tag{5.1}$$

where C_{out} and C_{in} are the tritium bulk concentrations in PbLi at the PAV outlet and inlet, respectively. A detailed model of the interactions between the tritium and the involved materials (mainly the liquid metal and the membrane) is thus fundamental. Such a model will rely on several assumptions:

- steady state operation (the EU DEMO TERS will operate in this condition for most of the time, being the plasma flat top duration 2 h out of a $\sim$ 8000 s duty cycle [53])

- the velocity profile in the PbLi is considered to be fully developed in turbulent regime along the entire channel length
- the tritium velocity within the PbLi is the same as that of the PbLi flow
- the mass diffusion is driven by tritium partial pressure gradients and, as in [48], it is not influenced by the presence of helium bubbles in PbLi flow.

The PbLi flow carries the tritium within the channel; its concentration can thus be described by the advection equation

$$\nabla \cdot \overrightarrow{\boldsymbol{J}_{\mathbf{T}}} = -\overrightarrow{\boldsymbol{v}} \cdot \nabla C_{\mathrm{T}} \tag{5.2}$$

where

- $\overrightarrow{\boldsymbol{J}_{\mathbf{T}}}$ is the tritium mass flux ($[mol/m^2/s]$)
- $\overrightarrow{\boldsymbol{v}}$ is the velocity of PbLi in the channels ($[m/s]$)
- C_{T} is the tritium concentration in the PbLi ($[mol/m^3]$)

Starting from the above-mentioned assumptions, the next simplifications are introduced:

- the entire system is considered to be isothermal (the temperature directly influences the transport and permeation parameters of each involved material)
- the different species involved are in thermodynamic equilibrium
- in view of the turbulent mixing, the tritium concentration is almost uniform (and close to the bulk value) across most of the channel cross section (the concentration gradient is localised close to the membrane wall)
- the tritium mass transport in the radial direction is dominated by the turbulent mixing within the fluid bulk, the diffusion (in the fluid close to the membrane wall) and the permeation (across the membrane), while in the axial direction it is dominated by the advection driven by the PbLi flow; thus the diffusion across the channel is predominant with respect to that along the channel, that can be neglected if the advection in the same direction is considered in the model.

As a result of the last two simplifications, and similarly to what was done in [48], the analysis of the tritium concentration in the PAV can be described by the combination of two 1D models:

- pure advection of the tritium concentration in the PbLi bulk along the axial (z) channel direction, so that in the case of cylindrical coordinates, used to describe the circular pipes (inner radius r_i) adopted as channels in the design proposed in [51] and [45], (5.2) becomes:

$$2\pi r_{\mathrm{i}} \cdot J_{\mathrm{T}}(z) = -v \cdot \pi r_{\mathrm{i}}^2 \cdot \frac{dC_{\mathrm{T,b}}(z)}{dz} \tag{5.3}$$

  where v is the PbLi speed in the axial direction, $C_{\mathrm{T,b}}$ is the tritium bulk concentration in the PbLi and J_{T} is the tritium flux across the membrane surface;

- permeation across the membrane, in the radial (r) direction, influencing the tritium mass flux J_{T} across the membrane surface; the concentration gradient in the PbLi close to the membrane wall is also accounted for.

5.1.1 Physical process

The permeation across the membrane is generally influenced by phenomena occurring on the surface of the membrane and diffusion mechanisms inside its bulk. Several studies investigated how gases permeate through a metal surface, leading to the identification of two permeation regimes:

Diffusion-Limited (DL), where the permeation is driven by the gradient of concentration inside the metal bulk;

Surface-Limited (SL), where the permeation is strongly influenced by the surface effects; the contribution of the concentration gradient inside the membrane can be neglected because the diffusion across the membrane bulk is by far faster than the surface processes.

To correctly identify in which regime the device operates, the dimensionless permeation parameter described in [54] for the membrane is typically used as a criterion

$$W = \frac{2K_r t K_s \sqrt{p_{in}}}{D} \tag{5.4}$$

where the K_r is the recombination constant ($[m^4/s/mol]$), t is the membrane thickness ($[m]$), K_s is the solubility constant ($[mol/m^3/\sqrt{Pa}]$), D is the mass diffusion coefficient ($[m^2/s]$) of the membrane material, and p_{in} is the partial pressure ($[Pa]$) of the gas (to be permeated) impinging the surface. The factor 2 is present since two atoms are involved in the surface effects, as shown in [55]. The hydrogen isotope solubility constant and mass diffusion coefficient for several membrane materials are provided by [56]; if specific values for the tritium are missing, the hydrogen properties are adopted, re-scaled dividing them by $\sqrt{3}$ as suggested in [57]. The

dimensionless permeation parameter represents the ratio between the flux that would be allowed to cross the membrane surface and that allowed to cross the membrane bulk, for the same concentration gradient. Therefore, if $W << 1$ the regime can be considered SL, whereas a $W >> 1$ implies that the permeation is completely diffusion-driven. For an exhaustive explanation on the permeation parameter, please refer to [55].

The temperature and pressure influence the permeation mechanism across the membrane. Several materials (e.g. Fe, V, Nb and Ta, [51]) have been investigated in order to identify possible candidates with good resistance to the corrosion induced by the PbLi, and with high mass permeation characteristics, see e.g. the plot in figure 1 of [58]. For this study the membrane has been assumed made by Nb, one of the candidates for the PAV being designed for the EU DEMO TERS; however, in spite of a very high permeability and solubility, it shows a low recombination coefficient, see Fig. 5.1 where properties of Nb membrane by [56], [59] and [60] are reported. These values of recombination constant represent the condition

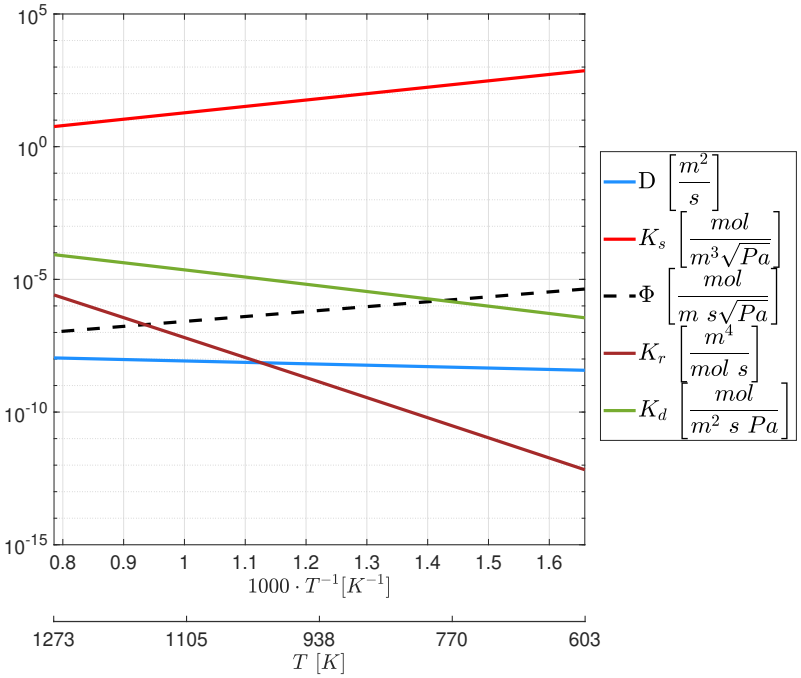

Figure 5.1: Nb mass transport properties used in this work. The dashed line refers to the permeability Φ calculated by [56], whereas mass diffusion coefficient D and Sievert constant K_s are measured by [60] and reported in [56]. The temperature relation for the recombination constant K_r in case of a contaminated surface is provided by [59].

of having the (inner or outer) surface oxidised or contaminated: at low tritium partial pressure p_{in}, even at an high temperature (leading to higher values of the

recombination constant) the regime is SL, since the higher temperature results also in much lower values of the solubility constant. At the same time, the mass diffusion coefficient increases with temperature, further reducing W. On the contrary, assuming a non-contaminated surface (e.g. at the beginning of the operation, or using a suitable coating of the Nb membrane, as done in [51] with Pd), the regime is DL for any temperature value, being the recombination constant $\sim$ 5 orders of magnitude larger (as reported in Fig. 3 of [47]). The parameters used for the evaluation of W in some different cases relevant for the PAV of the EU DEMO TERS are reported in Table 5.1. The temperature ranges from 330 °C to 500 °C, being the lower bound the foreseen outlet temperature of the PbLi from the Breeding Blanket, and the upper bound the maximum currently considered in the case of PbLi post heating to improve tritium permeation. To assess the gas permeation

Table 5.1: Comparison among different surface conditions of Nb membrane at different temperatures when the tritium pressure p_{in} and the membrane thickness t are 100 Pa and 0.4 mm, respectively. The permeation parameter W is also reported for each condition.

Nb surface	T [°C]	K_s $[mol/m^3/\sqrt{Pa}]$	K_r $[m^4/mol/s]$	D $[m^2/s]$	W [-]
Contaminated	330	726.92	$6.77 \cdot 10^{-13}$	$3.7563 \cdot 10^{-9}$	$1.048 \cdot 10^{-3}$
	500	96.11	$3.94 \cdot 10^{-10}$	$5.8816 \cdot 10^{-9}$	$5.146 \cdot 10^{-2}$
Non-contaminated	330	726.92	$6.022 \cdot 10^{-8}$	$3.7563 \cdot 10^{-9}$	93.23
	500	96.11	$6.022 \cdot 10^{-6}$	$5.8816 \cdot 10^{-9}$	787.29

through a metallic membrane when a liquid wets the surface, some considerations about the physics of permeation in the membrane are required. A reference system formed by gas-membrane-vacuum is considered first: the gas (or one of its isotopes) impinges on a solid metallic membrane with a certain thickness, while on the other side the vacuum is present. In this condition, if a pressure gradient (i.e. a concentration gradient) exists across the membrane, a molecular gas flux is established. As the behaviour of the gas can be described by the kinetic theory when the gas has a certain temperature and pressure, the concept of solubility is introduced. Since the solubility of a gas into a solid compound is a dynamic process between the metal and the gas itself, it is important to link this phenomenon to the surface condition. In fact, the permeated flux depends, firstly, on the reactivity of the surface to the impinging gas. The condition of the surface determines which permeation regime is established. In the reference system, the permeation source is imposed by temperature and pressure, according to the kinetic theory. In a system where, instead, the membrane is wet by a liquid metal, the gas source does not follow the kinetic theory. Notwithstanding this, the gas source is still a function of temperature and pressure due to the fact that a concentration gradient exists across the membrane. This dependency is explicated by the relationship between

the gas concentration and its partial pressure with the solubility, which is typical of the membrane. Therefore, in this new system configuration the membrane is supposed to behave as in the reference system, since the physics of the surfaces and of the membrane bulk does not change.

As the operation in SL regime is not excluded, the model in [48] should be completed with a more detailed description of the surface partial fluxes on both the sides of the membrane. In this new model, the membrane is graphically "expanded" to represent also the surface phenomena (conventionally taking place in the zone delimited by the real surface and the dashed lines inside the membrane in Fig. 5.2) and the mass flux cannot be anymore considered diffusion-driven. According to the model in [47], developed for the interface between a gas and a metal membrane, the relevant partial fluxes across the surface (represented also in Fig. 5.2) are:

- f_1 adsorption flux (from the gas bulk to the membrane surface);
- f_2 desorption flux (from the membrane surface to the gas bulk);
- f_3 absorption flux (from the membrane surface to the metal bulk);
- f_4 de-absorption flux (from the metal bulk to the membrane surface).
- f_5 diffusion flux (inside the metal bulk).

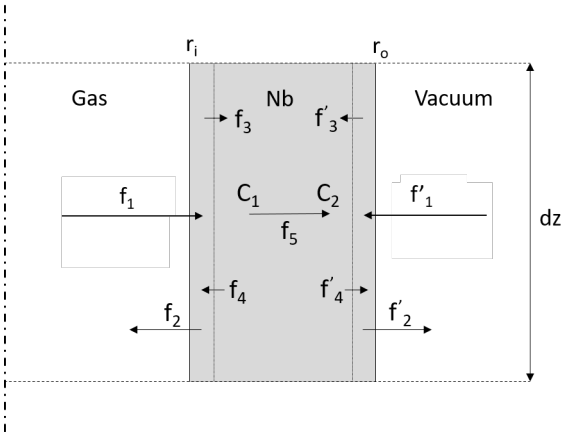

Figure 5.2: Scheme of the tritium mass fluxes across the Nb membrane, in the case of a gas carrier. The surface phenomena are conventionally represented here as taking place in the zone delimited by the real surface and the dashed lines inside the membrane.

Adsorption, desorption, absorption and de-absorption are also called *chemisorption*. In general, the membrane can be asymmetric as far as surface properties are considered: surface reactions could be different on the two membrane surfaces. For

instance, a coating could be present on the vacuum side, making $f_1^{'}$ and $f_2^{'}$ different from those on the other surface. Moreover, $f_1^{'}$ must be taken into account only if a counter pressure is considered, on the vacuum side. Hereafter, the surface is supposed to be symmetric, concentrating only on the more general case of an interface between the (bi-atomic) gas and the membrane. The equations used in [47] to compute the above-mentioned partial fluxes are:

$$f_1 = 2\Gamma s(1-\theta_i)^2 \tag{5.5}$$

$$f_2 = 2\delta\theta_i^2 \tag{5.6}$$

$$f_3 = \alpha\theta_i \tag{5.7}$$

$$f_4 = \beta C_1(1-\theta_i) \tag{5.8}$$

$$f_5 = -D\frac{\partial C}{\partial x}\bigg|_{x=r_i} \tag{5.9}$$

where:

- θ is the coverage surface fraction, i.e. the fraction of the membrane surface which is covered by tritium molecules ready to go through surface phenomena; the subscript "i" (and, in the following, "o") refers to the inner (outer) side of the membrane;
- C_{w1} (C_{w2}) is the generic isotope concentration at the inner (outer) surface;
- s ($s^{'}$) is the sticking coefficient, which expresses the probability that a molecule dissociates in contact with the inner (outer) surface;
- Γ is the mass flux of the generic isotope impinging the wall, depending on temperature and pressure (in a gas-membrane-vacuum system as that reported in Fig. 5.2, the incoming gas flux follows the kinetic theory in the form of

  $$\Gamma = \phi p_{in} \tag{5.10}$$

  where ϕ depends on the temperature as described by Eq. (2) in [47]);
- the coefficients α, β, δ express the reaction rate in the respective fluxes: they are temperature-dependent (with an Arrhenius-type dependence), and they are specific for each material since they depend on atomic superficial density;
- the mass diffusion coefficient D of the membrane expresses the diffusion flux $J_{T,D}$ according to the Fick's law.

For a complete discussion about reaction rates please refer to [47]. The major issue is the availability of direct measurements of reaction rates for each partial flux. To overcome this lack, recombination, dissociation and Sievert constants have been introduced starting from the definition of the mass fluxes. Considering the flux balance at the inner surface, the following system of equations is obtained:

$$\begin{cases} f_1 + f_4 = f_2 + f_3 \\ \\ f_5 = f_3 - f_4 \end{cases} \tag{5.11}$$

in which the first equation is valid only in steady state conditions, i.e. when there is no tritium accumulation on the surface. Using the flux definitions for $f_{1...5}$, the system becomes:

$$\begin{cases} 2\Gamma s(1-\theta_i)^2 + \beta C_1(1-\theta_i) = 2\delta\theta_i^2 + \alpha\theta_i \\ \\ -D\dfrac{\partial C}{\partial x}\bigg|_{x=r_i} = \alpha\theta_i - \beta C_1(1-\theta_i) \end{cases} \tag{5.12}$$

When the system reaches the equilibrium ($J_{T,D} = 0$), the derivative of the concentration goes to zero, therefore:

$$C_1 = \frac{\alpha}{\beta}\left(\frac{\theta_i}{1-\theta_i}\right) \tag{5.13}$$

Substituting the ratio between the coverage surface fractions from the first equation of (5.12):

$$\frac{\theta_i}{1-\theta_i} = \sqrt{\left(\frac{\Gamma s}{\delta}\right)} \tag{5.14}$$

$$C_1 = \frac{\alpha}{\beta}\sqrt{\left(\frac{\Gamma s}{\delta}\right)} = \frac{\alpha}{\beta}\sqrt{\left(\frac{\phi s}{\delta}\right)}\sqrt{p_{in}} \tag{5.15}$$

In the last equality the incoming mass flux has been expressed with (5.10). Here an important result is provided, which defines the Sievert constant for a certain material as:

$$K_s = \frac{\alpha}{\beta}\sqrt{\left(\frac{\phi s}{\delta}\right)} \tag{5.16}$$

The (5.15) expresses the relationship between the concentration and its partial pressure. According to the previous derivation, the dependency on the temperature comes from the surface fluxes definition. Due to the behaviour of reaction rates,

showing an Arrhenius-type temperature dependence, the (5.16) can be suitably formulated in the same way. If a proper solubility energy E_s is defined, the (5.15) becomes:

$$C = K_s\sqrt{p} = K_{s0}e^{-E_s/(KT)}\sqrt{p} \tag{5.17}$$

The same derivation can be applied also for recombination and dissociation constants (please refer to [47], [55], and [61]), simplifying the modelling: K_s, K_r and K_d phenomenological constants defined as *volume* properties for a certain material that convey surface effects, not related anymore to the atomic density and reactivity of the considered surface.

5.1.2 Model

In the next section the model is presented, applying the previous analysis to the membrane when the PbLi wets the metal. Turbulence and related transport phenomena in the PbLi are coupled to the dissociation and recombination fluxes in the membrane.

Mass transport across PbLi flow

In the model presented in [47], these equations were developed for gas-metal-vacuum interactions; so the gas follows the kinetic theory and the source term Γ in f_1 is a function of temperature and pressure. The inner side of the membrane is now wet by a liquid, with a radial tritium concentration profile supposed to be almost uniform (and close to the bulk value) in view of the turbulent mixing, except close to the membrane wall where the concentration gradient is localised (see the simplifications in Section 5.1 above). The source term Γ is therefore driven by that gradient:

$$J_T = h_T\Big(C_{T,b}(z) - C_{T,l}(z)\Big) \tag{5.18}$$

where h_T ($[m/s]$) is the mass transport coefficient in PbLi (temperature dependent) and $C_{T,l}$ is the tritium concentration nearby the membrane wall on the PbLi side (note that the temperature and pressure dependence is included in both tritium concentration values). The molecular gas flux is established by the concentration gradient across the membrane; being the concentration on the other side of the membrane nearly zero (if vacuum is present), the concentration $C_{T,l}$ nearby the wall promotes the permeation, behaving as the "source" of the impinging gas on the membrane. The mass transport coefficient quantifies how fast the tritium crosses the flow boundary layer. It has the physical meaning of the tritium radial velocity, which results from the combination of diffusion and mass transport by the PbLi turbulent motion (being the latter dominant with respect to the former). The mass

transport coefficient is evaluated by means of empirical formulations, some of which are listed in [52]; that used in this model was developed by [62]:

$$Sh = 0.0096 Re^{0.913} Sc^{0.346} \tag{5.19}$$

where Sh is the Sherwood number, Re the Reynolds number and Sc the Schmidt number, defined as:

$$Sh = \frac{d_i h_T}{D_{PbLi}} \tag{5.20}$$

$$Re = \frac{\rho_{PbLi} v d_i}{\mu_{PbLi}} \tag{5.21}$$

$$Sc = \frac{\mu_{PbLi}}{\rho_{PbLi} D_{PbLi}} \tag{5.22}$$

and in turn depending on the PbLi mass density ρ_{PbLi} $[kg/m^3]$, the channel internal diameter d_i $[m]$, the PbLi dynamic viscosity μ_{PbLi} $[Pa\ s]$ and the tritium mass diffusivity in the PbLi D_{PbLi} $[m^2/s]$. Since the correlation for the mass transfer coefficient was developed for water, its application to the PbLi leads to an extrapolation of the results, due to the out far-ranging of the Sc number [48]. For further information about the validity of this correlation please refer to [62]. For the complete set of PbLi properties, please refer to [63].

The partial pressure can be expressed by the Sievert's law, with the hypothesis of thermodynamic equilibrium between the gas and its atomic form:

$$C_T = K_s \sqrt{p_T} \tag{5.23}$$

Note that this relation between the concentration and its partial pressure is in principle valid only in equilibrium conditions, i.e. if the net permeated flux is zero. However, the relation (5.23) is still adopted part of developed permeation models, even if the permeated flux is not actually zero, but it is very low. Through the (5.23), the concentration nearby the Nb membrane can be expressed with its partial pressure as:

$$C_{T,l}(z) = K_s^{PbLi} \sqrt{p_{T,l}(z)} \tag{5.24}$$

where K_s^{PbLi} is the solubility constant of the tritium in the PbLi and $p_{T,l}$ is the partial pressure.

Mass transport across the membrane

In the DL case, as surface mechanisms are orders of magnitude faster than the mass diffusion in the membrane itself (and can thus be neglected), the partial pressure on the membrane surface ($p_{T,l}$) and in its bulk ($p_{T,w}$), i.e. at the interface between the PbLi and the membrane, can be considered in equilibrium. Moreover, if the equilibrium across the membrane is (almost) satisfied ($p_{T,b} = p_{VC}$), the overall

net permeated flux is (almost) zero, and the (5.23) can then be used to evaluate (almost) exactly the concentration from the equilibrium partial pressure.

On the contrary, in the SL case at the (inner, but possibly also outer) surface of the membrane non-negligible recombination and dissociation phenomena occur, as presented in [55], leading to a non-equilibrium in the partial pressure between the surface ($p_{T,l}$) and the bulk ($p_{T,w}$) of the membrane.

To obtain an expression for recombination $J_{T,r}$ and dissociation $J_{T,d}$ mass molecular fluxes, the equilibrium condition is considered. In the general case of a bi-atomic gas impinging the wall to permeate across it, the molecular recombination flux involves two atoms which could reconstitute the original impinging molecule if the proper energy ΔE_r is provided by the membrane. Being $2C_{T,w1}^2$ the probability to have in the lattice two atoms close to each other, the recombination flux $J_{T,r}$ is proportional to the square of the concentration through the *phenomenological* (recombination) constant K_r^{Nb}:

$$J_{T,r} = 2K_r^{Nb}C_T^2 \tag{5.25}$$

This equation expresses the flux that leaves the membrane in the *molecular* form, and it depends on the tritium concentration inside the membrane $C_{T,w}$. The dissociation mass flux represents the flux that penetrates the membrane in atomic form after a dissociation process of the impinging molecule on the membrane surface. Since the impinging gas flux depends on pressure and temperature as described in [47], it is suitable to relate $J_{T,d}$ to the partial pressure of the tritium in the PbLi near the membrane wall $p_{T,l}$ by the *phenomenological* dissociation constant K_d^{Nb} as:

$$J_{T,d} = 2K_d^{Nb}p_{T,l} \tag{5.26}$$

The factor 2 means that two atoms are involved in the process. If the equilibrium is reached

$$J_{T,r} = J_{T,d} \tag{5.27}$$

and therefore follows

$$C_T^2 = \frac{K_d^{Nb}}{K_r^{Nb}}p_T \tag{5.28}$$

giving an expression for the K_d as function of the solubility and recombination, as the (5.23) shows:

$$K_d^{Nb} = K_r^{Nb}(K_s^{Nb})^2 \tag{5.29}$$

This approach can be applied on both membrane surfaces, considering how the tritium behaves in the PbLi and in the vacuum (See Fig. 5.3). On the inner surface of the membrane, i.e. where the PbLi wets the Nb, the tritium is supposed to be dissolved in atomic form, as reported in [49]. Consequently, the recombination and

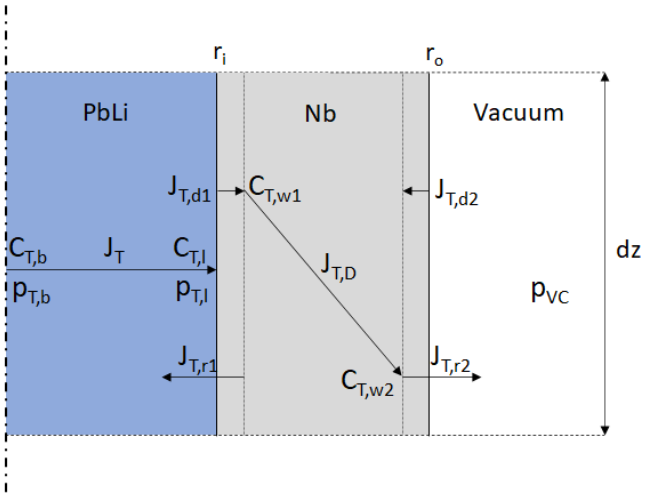

Figure 5.3: Scheme of the tritium mass fluxes included in this model. Surfaces have been expanded according to Fig. 5.2 to show where superficial mass fluxes origin.

dissociation fluxes expressed in (5.25) and in (5.26) on this surface do not involve two atoms. Therefore, at the inner surface $J_{T,r1}$ and $J_{T,d1}$ are defined as:

$$J_{T,r1}(r_i, z) = K_r^{Nb} C_{T,w1}^2(z) \tag{5.30}$$

$$J_{T,d1}(r_i, z) = K_d^{Nb} p_{T,l}(z) \tag{5.31}$$

where $p_{T,l}$ is the tritium partial pressure related to $C_{T,l}$ as expressed by (5.23). On the outer surface, i.e. where the Nb membrane faces the vacuum, the recombination is supposed to form tritium molecules. Thus, two atoms produce one tritium molecule. Moreover, if the counter pressure p_{VC} is (realistically) larger than 0, an incoming dissociation mass flux will be present. Respectively,

$$J_{T,r2}(r_i, z) = 2\frac{r_o}{r_i} K_r^{Nb} C_{T,w2}^2(z) \tag{5.32}$$

$$J_{T,d2}(r_i, z) = \frac{r_o}{r_i} K_d^{Nb} p_{VC} \tag{5.33}$$

where the $\frac{r_o}{r_i}$ is introduced to account for the different area the flux is referred to.

The mass diffusion flux inside the membrane bulk can be expressed by the Fick's law, depending on concentrations underneath the surfaces of the membrane. Considering the cylindrical geometry of the membrane and assuming the mass diffusion coefficient to be isotropic:

$$J_{T,D}(r_i, z) = -D_{Nb} \nabla C_T = D_{Nb} \frac{C_{T,w1}(z) - C_{T,w2}(z)}{r_i log\left(\frac{r_o}{r_i}\right)} \tag{5.34}$$

where $C_{w,1}$ and $C_{w,2}$ are the concentrations underneath the inner and the outer surfaces, respectively. If the permeation is SL, the contribution of the diffusion could be neglected: due to the different velocity of the two mechanisms, the diffusion is much faster than the recombination/dissociation processes on the surfaces, and the concentration gradient inside the bulk would be smoothed.

These equations can be coupled in a system that includes the diffusion of the tritium and its solubility in the PbLi mass flow, the surface effects on the inner surface of the Nb and on the outer surface, where there is the vacuum pressure p_{VC}:

$$\begin{cases} J_T(r_i, z) = h_T\left(C_{T,b}(z) - C_{T,l}(z)\right) \\ J_T(r_i, z) = 2\dfrac{r_o}{r_i}K_r^{Nb}C_{T,w2}^2(z) - \dfrac{r_o}{r_i}K_d^{Nb}p_{VC} \\ C_{T,l}(z) = K_s^{PbLi}\sqrt{p_{T,l}(z)} \\ J_T(r_i, z) = D_{Nb}\dfrac{C_{T,w1}(z) - C_{T,w2}(z)}{r_i \log\left(\dfrac{r_o}{r_i}\right)} \\ J_T(r_i, z) = K_d^{Nb}p_{T,l}(z) - K_r^{Nb}C_{T,w1}^2(z) \end{cases} \tag{5.35}$$

The previous system is non-linear in the unknowns $p_{T,l}$ (or the concentration $C_{T,l}$), in the $C_{T,w1}$ and in the $C_{T,w2}$, being the permeated flux $J_T(r_i, z)$ referred to the inner radius of the membrane r_i. The set of equations must be solved at each axial coordinate along the z-axis. The aforementioned system produces one real solution for the mass flux $J_T(r_i, z)$ which depends only on partial pressures, i.e the tritium concentration, once the temperature is fixed. Coupling this system with the 5.3, the concentration distribution inside the PbLi bulk can be determined:

$$\begin{cases} \dfrac{dC_{T,b}(z)}{dz} = -\dfrac{2}{r_i v}J_T(r_i, z) \\ J_T(r_i, z) = h_T\left(C_{T,b}(z) - C_{T,l}(z)\right) \\ J_T(r_i, z) = 2\dfrac{r_o}{r_i}K_r^{Nb}C_{T,w2}^2(z) - \dfrac{r_o}{r_i}K_d^{Nb}p_{VC} \\ C_{T,l}(z) = K_s^{PbLi}\sqrt{p_{T,l}(z)} \\ J_T(r_i, z) = D_{Nb}\dfrac{C_{T,w1}(z) - C_{T,w2}(z)}{r_i \log\left(\dfrac{r_o}{r_i}\right)} \\ J_T(r_i, z) = K_d^{Nb}p_{T,l}(z) - K_r^{Nb}C_{T,w1}^2(z) \end{cases} \tag{5.36}$$

The first equation of (5.36) allows computing the gas concentration in the PbLi bulk along the hydraulic channel; this concentration is reduced as the axial coordinate increases because the tritium flux permeates through the membrane in the

r-direction. To solve the first order ordinary differential equation, a Forward Euler scheme has been used:

$$C_{T,b}(z_{n+1}) = C_{T,b}(z_n) - \frac{2\Delta z}{r_i v} J_T(r_i, z_n) \tag{5.37}$$

where the $C_{T,b}(z_{n+1})$ is the unknown of the problem and n is the index of the nodal discretisation along the channel length.

With the system of equations in (5.36) is possible to calculate the membrane length needed to obtain the desired permeation (extraction) efficiency in the PAV, following these steps for each node z_n:

1. The mass flux $J_T(r_i, z_n)$ at z_n can be calculated from (5.35);
2. The tritium bulk concentration in the PbLi at z_{n+1} is then computed from (5.37);
3. The value of the tritium concentration $C_{T,b}(z_{n+1})$ becomes the known term in the (5.36) for the node z_{n+1}, and the system can be solved again for the $J_T(r_i, z_{(n+1)})$;

The procedure is repeated until the efficiency expressed by (5.1) is higher than (or equal to) the desired value: the axial coordinate of the z-node is the membrane length required to provide that efficiency.

5.2 Verification

The model verification is performed here in two steps:

- Order-of-Accuracy (OoA) test;
- Code-to-code comparison (or benchmark).

5.2.1 Order-of-Accuracy test

To rigorously apply the code verification procedure, the Method of the Manufactured Solution (MMS) [64][65][66][67][68] is adopted here to assess the OoA of the model. From the system (5.36), the variables to be solved are:

- J_T: mass flux of gas isotope;
- $C_{T,b}$: gas concentration inside the PbLi bulk;
- $C_{T,l}$: gas concentration nearby the membrane wall in the PbLi;
- $C_{T,w1}$: gas isotope concentration inside the Nb bulk on the inner side;

- $C_{T,w2}$: gas isotope concentration inside the Nb bulk on the outer side;
- $p_{T,l}$: partial pressure of the gas isotope nearby the membrane wall damped by the PbLi (related to $C_{T,l}$);

The manufactured solution approach foresees the introduction of fictitious source terms in the original system:

$$\begin{cases} \dfrac{dC_{T,b}(z)}{dz} = -\dfrac{2}{r_i v} J_T(r_i, z) + Q_1 \\ J_T(r_i, z) = h_T\left(C_{T,b}(z) - C_{T,l}(z)\right) + Q_2 \\ J_T(r_i, z) = 2\dfrac{r_o}{r_i} K_r^{Nb} C_{T,w2}^2(z) - \dfrac{r_o}{r_i} K_d^{Nb} p_{VC} + Q_3 \\ C_{T,l}(z) = K_s^{PbLi}\sqrt{p_{T,l}(z)} + Q_4 \\ J_T(r_i, z) = D_{Nb}\dfrac{C_{T,w1}(z) - C_{T,w2}(z)}{r_i \log\left(\dfrac{r_o}{r_i}\right)} + Q_5 \\ J_T(r_i, z) = K_d^{Nb} p_{T,l}(z) - K_r^{Nb} C_{T,w1}^2(z) + Q_6 \end{cases} \tag{5.38}$$

The source terms $Q_{1,\dots,6}$ are obtained imposing the shape of the variables as reported in Table 5.2:

$$\begin{cases} Q_1 = \dfrac{dC_{T,b}(z)}{dz} + \dfrac{2}{r_i v} J_T(r_i, z) \\ Q_2 = J_T(r_i, z) - h_T\left(C_{T,b}(z) - C_{T,l}(z)\right) \\ Q_3 = J_T(r_i, z) - 2\dfrac{r_o}{r_i} K_r^{Nb} C_{T,w2}^2(z) + \dfrac{r_o}{r_i} K_d^{Nb} p_{VC} \\ Q_4 = C_{T,l}(z) - K_s^{PbLi}\sqrt{p_{T,l}(z)} \\ Q_5 = J_T(r_i, z) - D_{Nb}\dfrac{C_{T,w1}(z) - C_{T,w2}(z)}{r_i \log\left(\dfrac{r_o}{r_i}\right)} \\ Q_6 = J_T(r_i, z) - K_d^{Nb} p_{T,l}(z) + K_r^{Nb} C_{T,w1}^2(z) \end{cases} \tag{5.39}$$

Due to the low values of physical constants involved in the model, the former have been re-normalised as reported in Table 5.2. Results of verification are presented in Fig. 5.4b in black dash line, showing the correctness of equations in the model.

The convergence analysis is performed on a case-study where the channel length is imposed and the temperature is fixed at 330 °C. For the reference case has been used a $\Delta z = 10^{-5}$ m to discretise a length of 2 m, comparing the gas isotope concentration in the PbLi bulk at $z = 1$ m. Results are shown in Fig. 5.4a. Two different values of PbLi velocity are compared to point out the effect of the turbulence on the permeated mass flux. As expected, the order of accuracy is of the 1^{st} order, as the forward Euler foresees.

Table 5.2: Function shapes applied to variables set for the manufactured solution verification and parameters. The constants A, L, ϕ and ω have been fixed to $A = 10$, $L = 1$, $\omega = 0.5$, $\phi = \frac{\pi}{4}$, $d_i = 9.2\ mm$, $d_o = 10\ mm$.

Variable	Shape	Parameter	Value
$J_T(r_i, z)$	$A\left[\frac{1}{2}\sin\left(\frac{\pi z}{L}\right) + 1\right]$	T_{PbLi}	330 °C
$C_{T,b}(z)$	$A\left[1 + \sin\left(\frac{\pi z}{L}\right)\right]$	$p_{T,b}$	100 Pa
$C_{T,l}(z)$	$\frac{A}{2}e\frac{z}{L}$	K_s^{Nb}	$2\ \frac{mol}{m^3\sqrt{Pa}}$
$C_{T,w1}(z)$	$\frac{A}{4}e\frac{z}{L}$	D_{Nb}	$10^{-3}\ \frac{m^2}{s}$
$C_{T,w2}(z)$	$A\left[\frac{1}{2}\sin\left(\frac{\pi z}{L}\right) + 2\right]$	p_{VC}	0.1 Pa
$p_{T,l}(z)$	$A\sin(\omega z + \phi)$	K_r^{Nb}	$1\ \frac{m^4}{mol\ s}$

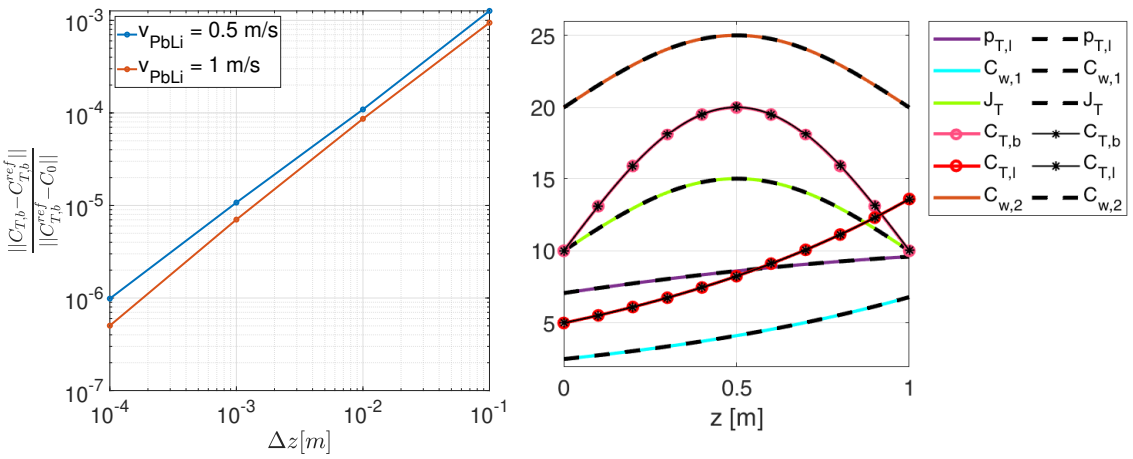

(a) (b)

Figure 5.4: Results of verification and convergence study. In 5.4b dash and symbolic lines are the variables set calculated imposing the fictitious source terms. The manufactured solutions reported in Table 5.2 are in continuous and symbolic lines. In 5.4a results of convergence analysis are shown. Two different values of v_{PbLi} are reported.

5.2.2 Code-to-code comparison

Here the code-to-code comparison is presented. As stated before, the model introduced in this work can describe the tritium permeation, encompassing all the possible phenomena which affect the tritium mass flux across a metallic membrane. In order to perform the benchmark, the reference model which has been taken into account is the one presented by [52]. In the latter, the tritium permeation is completely DL, neglecting the superficial effects. Under this hypothesis, the interface between the PbLi and the Nb membrane can be modelled imposing the equilibrium of the partial pressure according to:

$$\frac{C_{w,s}}{K_s^{Nb}} = \frac{C_{w,l}}{K_s^{PbLi}} \tag{5.40}$$

where the K_s^{PbLi} is the solubility of the PbLi and the $C_{w,s}$ the concentration of the tritium in the inner side of the Nb membrane. The radial motion of the tritium is still due to the turbulence of the PbLi from the concentration in the bulk (C_B) to the one near the Nb wall ($C_{w,l}$), with the mass transport coefficient K_T. Inside the membrane, the mass diffusion is expressed by the Fick's law by the mass diffusion coefficient D_s.

On the outer side of the metallic membrane, the recombination process is not considered and the tritium concentration C is supposed to be zero since the vacuum is present. In Fig. 5.5 the reference scheme of the model presented by [52] is reported. According to what is said in the latter, the behaviour of the tritium bulk

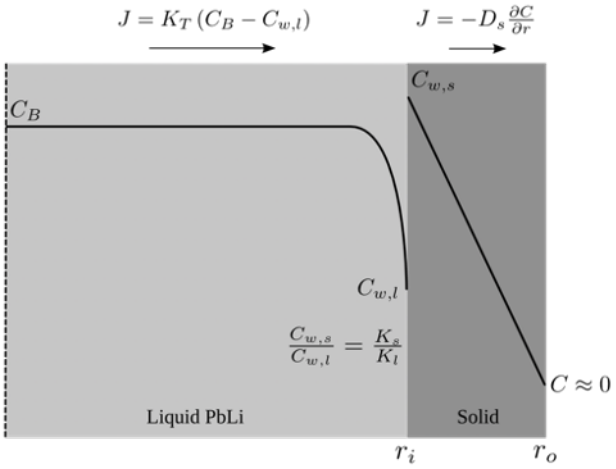

Figure 5.5: Scheme of tritium permeation model reported in [52]. The permeation is completely DL, and the concentration of tritium on the outer side of the membrane is zero due to absence of recombination process together with the vacuum condition.

concentration at a certain axial point along the extractor can be expressed by:

$$C_{T,b}(z) = C_0 \exp\left(- \frac{4K_T z}{v d_i} \frac{\xi}{\xi + 1} \right) \tag{5.41}$$

in which the C_0 is the initial tritium concentration inside the PbLi and the ξ is an dimensionless parameter that weights the permeation on the solid or on the liquid. In particular, if ξ is larger than 1, the permeation is controlled by the liquid metal, whereas in the other case it is dominated by the solid membrane. For further description please refer to [52]. The other parameters involved in the model are the same of the ones used in this work. In particular, the effect of PbLi velocity is still present with the mass transport coefficient K_T, i. e. the grade of turbulence, together with the geometrical impact due to the inner diameter d_i. Therefore, apart from the treatment of the superficial effect of the membrane, the evolution of the tritium concentration in this model is ruled by temperature, geometry and mass properties of all the materials.

The aim is to compare the results, in terms of tritium extraction efficiency, between the reference model and the model of this work when the same permeation regime is considered. Since the reference one is completely DL, the first step is to put the other one through the same condition. As Table 5.1 reports, when a non-contaminated membrane is concerned, the permeation regime is DL. The latter results as a consequence for taking into consideration a higher value of the recombination constant, which affects only the model to be tested. Thus, the same set of properties is used for both models. The other condition is to have the same boundary conditions. In particular, the outer side of the membrane is assumed to be exposed to vacuum ($p_{VC} = 0$), and to have the concentration $C_{T,w2}$ equals to zero. The latter corresponds to force the tritium to instantaneously leave the membrane in atomic form. Consequently, the balance equation on the outer side of the membrane interfacing the vacuum

$$J_T(r_i, z) = 2\frac{r_o}{r_i} K_r^{Nb} C_{T,w2}^2(z) - \frac{r_o}{r_i} K_d^{Nb} p_{VC} \tag{5.42}$$

becomes redundant, since the unknown $C_{T,w2}$ is turned into a known value.

In Fig. 5.6 the benchmark results are shown when an extractor length of 1 m is concerned at $v_{PbLi} = 0.5\ m/s$. The geometrical parameters are $d_i = 9.2\ mm$, $d_o = 10\ mm$, and the partial pressure $p_{T,in} = 100\ Pa$. The tested model reproduces with a maximum relative error of 0.38%, at the end of the channel, the extraction efficiency with respect to the DLM at 330 °C. In the other cases, the maximum relative error at the end of extractor is, respectively, 0.07% for 400 °C and 0.12% for 500 °C.

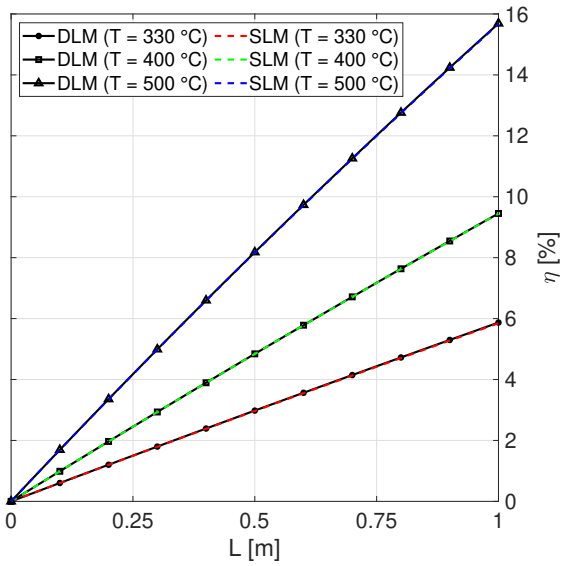

Figure 5.6: Comparison between the model developed by [52] (DLM) and the one presented in this work (SLM). Three different operational temperatures are shown for both models. The coloured dash lines are for the SLM, whereas the symbolic black lines are for the DLM.

5.3 Surface-Limited vs. Diffusion-Limited modelling on a test-case

In this section, the current model is applied to a test-case when the permeation regime is SL. The results are then compared with the ones foreseen by the DLM one [52]. According to what is reported in Table 5.1, if the Nb is contaminated the regime will be SL. One reason for this condition is the presence of the oxidised compounds formed by the Nb itself. In fact, the Nb tends to be oxidised quite easily when it is exposed to air: the perfect vacuum is not achievable in the extractor, therefore it is reasonable to analyse how the formation and/or the presence of contaminating compounds affects the extraction efficiency.

With respect to the previous analysis performed in the benchmark, now the tritium concentration on the outer side of the membrane is not set at zero anymore. This causes the recombination phenomenon to be taken into consideration, as devised in (5.42). On the contrary, the condition on the perfect vacuum is still present for both models, by the fact that the DLM does not make allowance for the incoming flux from the vacuum. As result, the balance equation on this side becomes:

$$J_T(r_i, z) = 2\frac{r_o}{r_i} K_r^{Nb} C_{T,w2}^2(z) \tag{5.43}$$

The setup for the test-case is the one used in the benchmark analysis. Results of

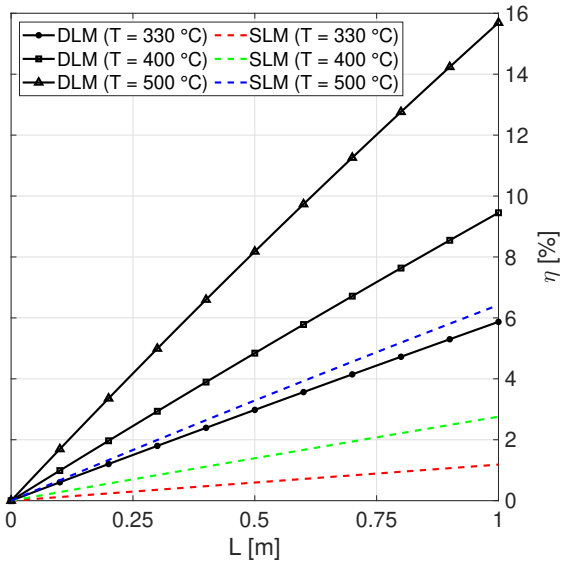

Figure 5.7: Comparison between the model developed by [52] (DLM) and the one presented in this work (SLM) when the latter models the SL regime. Three different operational temperatures are shown for both models. The coloured dash lines are for the SLM, whereas the symbolic black lines are for the DLM.

the comparison are shown in Fig. 5.7. The extraction efficiency tends to increase due to the higher value of the recombination constant as well as the temperature increases, always keeping the efficiency of the SL regime lower than the DL one. Firstly, the mass diffusion in the membrane is faster than chemisorption effects on the interfaces, leading to a flattening of the concentration profile. In this way, the mass flux is not influenced by the diffusion due to the Nb, instead the recombination/dissociation phenomena *limit* the mass flux from the PbLi bulk towards the vacuum. As a consequence, the mass gradient tends to be lower. Secondly, the DLM assumes that tritium leaves the membrane instantaneously in atomic form. All the tritium which arrives on the vacuum side is immediately extracted. Instead, the SLM foresees that the tritium leaves the membrane in molecular form: this can happen only if two atoms are located sufficiently close with a proper *recombination energy*. Thus, the recombination phenomenon is a statistical event, with a probability lower than 1. The same happens in the interface between the liquid metal and the Nb, furthermore reducing the permeated tritium.

5.4 Conclusions and perspective

The tritium extraction in the future EU DEMO Reactor is today an open issue to close the fuel cycle in situ. Promising technology as the GLC and the PAV technology are under investigation, in order to achieve the design efficiency for the isotope extraction. The latter is based on the extraction by pressure difference across a metallic membrane of the tritium from the PbLi, where the it is formed by the breeding of the Li-7. Although models there are permeation models to estimate the mass flux, the presence of a liquid metal wetting the membrane introduces a significant difference for the permeation rate with respect to a pure extraction where the gas impinges on the metal. Moreover, the operative conditions of the membrane (low pressure, high temperature) lead to surface effects which can strongly changed the permeation mechanism. The model here presented aims to include the transport due to turbulence of the liquid metal in the channel together with the recombination and the dissociation phenomena on membrane interfaces. Starting from a deep analysis of the previous model which have properly investigated the behaviour of several materials for fusion application about the gas extraction, two different permeation regimes have been identified (DL and SL regimes). The Nb membrane is one of the candidate for the membrane of the PAV due to its high mass permeability, although it has a lower value of recombination constant when contaminating compounds are present. Therefore, considering the case in which the permeation is SL, surface effects (recombination and dissociation) have been included in the tritium mass flux balance on both membrane sides, also when the pressure in the vacuum side is not actually zero. In this way, as the theory confirms, the mass diffusion in the metal bulk can be neglected: velocities of recombination/dissociation rates are much lower than diffusion one, leading to a smoothness in the concentration profile. By the solution membrane equations, the permeated mass flux can be finally figured out. Coupling this with the transport in the PbLi of the tritium concentration, the tritium concentration along the extractor can be foreseen. As result, the membrane length to achieve the design efficiency can be estimated, to correctly sizing the extractor.

Some mathematical analyses have been conducted on the aforementioned model. The verification activity has been done with the manufactured solutions approach, proving the correctness of the equations. Then, the OoA has been carried on to assure the convergence of the numerical scheme adopted for the discretisation of the tritium evolution along the permeator length. In conclusion, two test cases have been simulated to perform extraction efficiency analyses. Firstly, a benchmark with a pure DLM has been carried on with three different values of the temperature. Using a set of value for the recombination constant which represents the condition to have a non-contaminated membrane, the permeation regime has been put through DL condition. The proposed model has shown a successful agreement with the reference DL one. Secondly, a comparison between the two regimes (SL and DL)

has been done. When the permeation is SL, i. e. the membrane is contaminated, the extraction efficiency results lower than the DL regime, even at high temperature. Therefore, a longer membrane in the extractor will be required to get the target efficiency if the permeation regime is SL.

In perspective, validation activities are foreseen, thanks e.g. to the experimental campaign that is going to start at the research centre in ENEA Brasimone, where a mock-up for the PAV extractor will be tested in the facility TRIEX-II (Chapter 6).

Chapter 6

Design of the EU DEMO Tritium Extraction System mock-up based on PAV technology

In this chapter the conceptual design of the mock-up based on the PAV technology is discussed. The mock-up has been sized based on the constraints on the TRIEX-II facility at ENEA Brasimone, starting from the basic equations for the thermo-mechanical assessment for the vessel and holed plate where the niobium pipe are allocated. Then, the CFD analyses have been carried out, to verify if the mass flow rate is well distributed within the manifolds and among the parallel pipes. After verifying the PbLi flow repartition, a Finite Element assessment of the mechanical behaviour of the mock-up has been conducted, since the analytical formulas are not able to correctly model the critical points as border effect or junction. Finally the permeation model developed in the previous chapter has been applied to investigate how the hydrogen is extracted from the carrier. Moreover, an uncertainty analyses has been performed to guide the experimental campaign. However, the evolution of COVID-19 pandemic has postponed the validation activity beyond the end of this PhD program. Therefore, the expected results of the uncertainty analyses have been used to assess the effects of the parameters on the extraction efficiency to support the development of the PAV technology up to EU DEMO scale. The final results of the mock-up engineering can be found in the work presented at SOFT2020 where an advancement [69] in the design has been made for the experimental campaign.

6.1 TRIEX-II facility

TRIEX-II is a facility located in ENEA Brasimone (See Fig. 6.1) where experiments for the TERS are conducted. In the facility a loop is present where PbLi with dissolved hydrogen or deuterium (in order to substitute the tritium and reduce

the radiobiological risk) is circulated. In the facility, the actual constraints on the

Figure 6.1: TRIEX-II facility in ENEA Brasimone.

mock-up mainly concern the geometrical dimensions of the extractor (related to the space allocated for its installation) and the allowable pressure drop, see Table 6.1. The pump can provide a pressure head of 2 bar when the maximum mass flow rate is circulated. Therefore, the maximum pressure drop allowed in the mock-up is 0.5 bar, since ∼1.5 bar are taken by the distributed and localised pressure drops in the loop. Concerning the permeator pipe length, it is limited by the installation point of the component within the loop: the height of the highest point of the PAV pipes must be lower than the pressuriser height, to avoid a depressurisation in the pipes. Consequently, the allowed height of the pipes is 0.9 m (including the U curve), resulting in a vessel height of ∼1.1 m. The maximum external diameter of the vessel is also constrained by the allowable encumbrance within the circuit.

Table 6.1: Constraints for the PAV in the TRIEX-II facility.

Item	**Limit Value**
PbLi mass flow rate	$\leq$ 4.6 kg/s
Pump pressure head	$\leq$ 2 bar
PbLi temperature	$\leq$ 530 °C
Pipe material	Pure niobium
U-pipe height	$\leq$ 0.9 m
Manifold height	$\leq$ 15 cm
Vessel external diameter	$\leq$ 20 cm
Vacuum pressure	$\geq 10^{-6}$ mbar

The PAV technology is based on the extraction of the radioisotope from the LM by mass transport mechanisms when a pressure gradient is kept across the membrane. The PbLi mass flow rate flows inside pipes (i.e. the membranes) while the vacuum is pumped on the other side (see Fig. 6.2a) from the top of the vessel (see Fig. 6.2b). Each vessel contains the channels for the PbLi flow: the wall of the channels is the hydrogen permeation membrane. The parallel channels are "U-shaped" and shown in Fig. 6.2b.

Three manifolds are present at the bottom of the vessel:

- an inlet manifold, taking ¼ of the entire manifolds volume
- an outlet manifold, also taking ¼ of the entire manifolds volume
- a mixing manifold, taking ½ of the entire manifolds volume; it contains also a draining pipe to allow the PbLi discharge from the mock-up in case of accidents.

The PbLi is collected at the inlet section in a manifold, then passes through a first set of U-pipes reaching an intermediate manifold. From the latter and through a second set of U-pipes the PbLi flows to the outlet manifold (see Fig. 6.2).

6.2 Aim of the work

The aim of this work is to provide a preliminary dimensioning of the mock-up based on PAV technology. The results are obtained starting from the design proposed for the PAV mock-up in [45] with the final constraints imposed in the TRIEX-II facility at ENEA Brasimone. The sizing is followed by a transport analysis to investigate the hydrogen permeation across the membrane with a newly developed surface limited model, aiming at estimating the extraction efficiency.

In order to dimension the component, it will be necessary to determine:

- the number and the location of pipes;
- the thickness of both plate and vessel;
- the dimensions of the manifolds (i.e. the height of PbLi chamber).

The detailed assessment of the design is carried out with CFD analyses for the calculation of the mass flow repartition in each channel and with a TM analysis to verify the mechanical stress in operating and test conditions. The transport model provides the extraction efficiency given the geometry. A comparison with the results of the model presented in [52] is showed. As in [70] and [45], the PAV system must meet a given extraction efficiency η (with a desired target, in EU DEMO, of at least 80%), defined as

$$\eta = 1 - \frac{C_{\text{out}}}{C_{\text{in}}} \tag{6.1}$$

In 6.1 C_{in} (the hydrogen concentration at the PAV inlet) is an input parameter depending on hydrogen dissolved in the LM, while C_{out} depends on the mock-up design. The design process is divided into three preliminary steps, followed by a detailed check of the results:

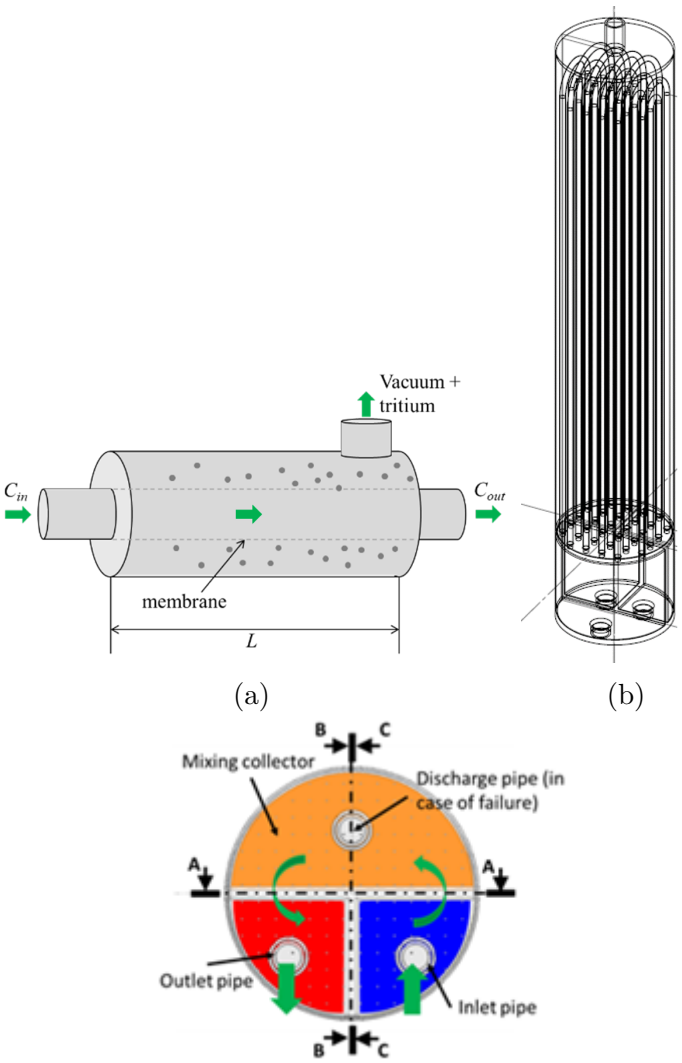

Figure 6.2: Schematics of the PAV system (a) and (b) 3D view of the PAV design proposed here. In (c) the wiew of the mock-up design proposed is shown: the inlet, outlet and intermediate manifolds are highlighted. The PbLi pattern is shown with green arrows.

1. the sizing of the vessel thickness starting from its outer diameter (prescribed by the installation in TRIEX-II) and estimated firstly using the thick shell theory; also the plate thickness is estimated following the same procedure;
2. the sizing of the PAV pipes (membrane), namely their diameter and length in order to have a pressure drop lower than the prescribed limit and satisfy the constraints on its maximum height when installed in the facility, see above;
3. the design of the layout (and definition of the number) of the PAV pipes to be inserted in the holed plate, satisfying the given constraint on the pitch;

The detailed assessment of the design PbLi flow distribution by CFD analyses and of the mechanical stress by a TM model is then performed to assess the preliminary sizing obtained from the three steps reported above.

6.3 Sizing of the mock-up

This section contains the description of the dimensioning of the mock-up following the three steps described above.

6.3.1 Sizing of the vessel thickness

In order to estimate the thickness of the plate and vessel, analytical formulas have been applied. In a second step, a finite element approach is adopted for the TM analysis, see Section 6.3.5, to compensate the limits of the analytical formulas and confirm the design. The material of the vessel and plates is the martensitic steel 10CrMo9-10 [71] due to low corrosion rate compared with austenitic steel. Its TM properties were taken from a data sheet of the Gruppo Lucefin company [72] and are referred to the standard UNI EN 10273: 2008. The temperature-dependent adopted properties, reported in Table 6.2, refer to a temperature of 330 °C.

Note that the upper part of the vessel is not in direct contact with PbLi, so that it can in principle be made using a non-martensitic steel. However, its connection with the martensitic steel plate would require a welding between two different materials; for this reason, the same material has been adopted for the plate and vessel in this design and analysis. For the pipe (membrane), the pure niobium has been chosen for its mass transport properties together with its good TH properties (see Table 6.2). The maximum von Mises stress in the plates must be lower than the maximum allowable stress. The cylindrical vessel design instead, in addition to this requirement, must consider also the collapse due to instabilities, as it is a component under vacuum conditions subject to external atmospheric pressure.

As regards the vessel thickness, the stress distribution can be computed with analytical formulas, valid in zones far from geometrical discontinuities, if the following assumptions hold:

Table 6.2: Thermo-mechanical properties of the mock-up materials at 330 °C.

Material	**Density [kg/m^3]**	**Young Modulus (E) [GPa]**	**Poisson coefficient (ν)**	**Thermal expansion coefficient (α) [K^{-1}]**	**Yield strength (σ_y) [MPa]**	**Max allowable stress [MPa]**
10CrMo9-10	8700	169.5	169.5	14.2e-6	162	108
niobium	8570	96.65	96.65	7.09e-6	16.2	10.8

- cylindrical wall;
- thick shell;
- axial symmetry.

Adopting the thick shell theory, the radial and the circumferential stress can be computed as:

$$\begin{aligned} \sigma_\theta &= A + \frac{B}{r^2} \\ \sigma_{\mathrm{rr}} &= A - \frac{B}{r^2} \end{aligned} \tag{6.2}$$

as discussed in [70], where r is the radius of the vessel. The constants A and B depend on the external and internal load where $p_\mathrm{i} = 1.7$ bar and $p_\mathrm{e} = 1$ bar

$$\begin{aligned} A &= p_\mathrm{i}\frac{r_\mathrm{i}^2}{r_\mathrm{e}^2 - r_\mathrm{i}^2} - p_\mathrm{e}\frac{r_\mathrm{e}^2}{r_\mathrm{e}^2 - r_\mathrm{i}^2} \\ B &= p_\mathrm{i}\frac{r_\mathrm{i}^2 r_\mathrm{e}^2}{r_\mathrm{e}^2 - r_\mathrm{i}^2} - p_\mathrm{e}\frac{r_\mathrm{i}^2 r_\mathrm{e}^2}{r_\mathrm{e}^2 - r_\mathrm{i}^2} \end{aligned} \tag{6.3}$$

To be conservative, the equivalent stress is then calculated with the Tresca criterion:

$$\sigma_{\mathrm{Tresca}} = \sigma_\theta - \sigma_{\mathrm{rr}} \tag{6.4}$$

where σ_θ and σ_{rr} are, respectively, the maximum and minimum stresses. The calculation is performed starting from a proper value of the Safety Factor (SF) with respect to the maximum allowable stress and, consequently, the correct value of the radius is found:

$$SF = \frac{\sigma_{\max}}{\sigma_{\mathrm{Tresca}}} \tag{6.5}$$

Since the sizing must consider the accidental condition of the internal pressure of 10 bar, a value of 5 has been chosen for the SF above, whereas the safety factor (SF_{ASME}) for the materials has been selected by the ASME VIII Div.1 (See

Table 6.2). Therefore, a 4.25 mm vessel thickness is proposed with a SF of 5. This value will be assessed with a Finite Element Method (FEM) analysis in both normal operation, where the internal pressure is imposed at 10^{-6} mbar (the operational value), and test conditions (10 bar of internal pressure, if a pipe collapses).

For the plate, the analysis starts from the analytical formulas for a non-perforated planar plate. This case is just an indication of the real value of the thickness since the plate of the mock-up is perforated: the holes will locally increase the stress, so that the analytical estimation is expected to be non-conservative. Furthermore, this approach averages the stresses along the thickness. Consequently, the FEM analysis is necessary.

In the case of a plate with constrained edges, the maximum radial and circumferential stresses are located at the edges and are equal to:

$$\begin{aligned} \sigma_{\mathrm{r,max}} &= \frac{6}{s^2}\left(\frac{p r_{\mathrm{e}}^2}{8}\right) \\ \sigma_{\theta,\mathrm{max}} &= \nu\frac{6}{s^2}\left(\frac{p r_{\mathrm{e}}^2}{8}\right) \end{aligned} \tag{6.6}$$

where $p = 10$ bar and r_{e} is the plate radius which coincides with the internal radius of the vessel of 9.57 cm. The axial stress is equal to 0, as the plates have usually low thickness with respect to the other dimensions. Applying the relation 6.6 with the definition of SF equal to 2, the thickness of the plate can be found equal to 12 mm.

6.3.2 Sizing of the PAV pipes

In this part the geometry of the PAV membrane (namely, the pipes) is addressed. The principal constraint is on the pressure drop which influences the choice of the pipe internal diameter and therefore, the external encumbrance on the plate. The allowable Δp in the pipes is 0.5 bar with the velocity v of 0.5 m/s of mass flow rate of PbLi as desired value inside each channel. The contributions to the total pressure drop are:

- localised: inlet and outlet nozzle, inlet and outlet regions to the pipes in the manifold, curves;
- distributed along the pipes.

Since the total length of the pipes is about 4 m, using the definition of pressure drop due to distributed friction

$$\Delta p = \frac{4f}{d_{\mathrm{i}}} L \frac{1}{2}\rho v^2 \tag{6.7}$$

where the friction factor f is calculated by [41], d_i is the internal diameter of pipes, and L is the length of the straight part of pipes, the contribution to the total pressure losses results more than two order of magnitude larger than the sum of localised pressure drops. In order to find a good compromise between the encumbrance on the plate (related to the maximum number of allowable pipes) and the pressure drop, two diameters are considered, see Table 6.3. The diameter

Table 6.3: Comparison of possible solutions for the membrane dimension.

Inner diameter	Δp	$\dot{m}$
5 mm	1.2 bar	0.77 kg/s
9.2 mm	< 0.5 bar	2.57 kg/s

of 5 mm leads to non-allowable pressure drop, therefore this solution could be adopted only if the velocity of PbLi was decreased to 0.3 m/s with a lower value of inlet mass flow rate. In this way, the constraint on the pressure drop is satisfied, but the decrease of PbLi speed causes a lower value of Re number, reducing the transport phenomena from the bulk to the membrane interface. This will lead to the adoption of pipes with the inner diameter of 9.2 mm (outer diameter of 10 mm) to have acceptable pressure drop with a sufficient value of Re number.

6.3.3 Number and layout of the PAV pipes

According to the constraint on the pitch between the pipes, dictated by the space required to weld them (see Table 6.1), a layout of the pipes maximising their number (in order to maximise the total mass flow rate processed by the mock-up) is proposed. It consists in a disposition in square lattice as reported in Figure 6.3 As

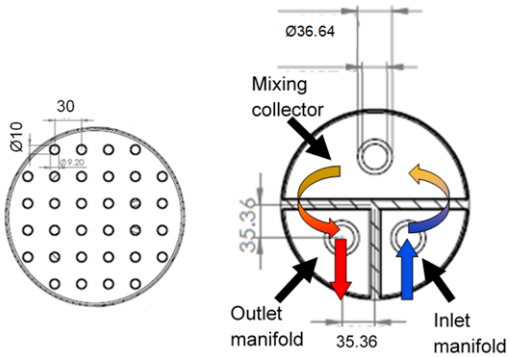

Figure 6.3: Plate and bottom view of the mock-up. Quotes are in mm.

a result, a maximum number of 8 U-pipes per passage can fit in the allocated area of the plate within the vessel; the inlet mass flow rate in Table 6.3 is calculated

Table 6.4: Geometrical dimensions for the plate and the inlet/outlet manifolds.

Dimension	[mm]
Pipes pitch p	30
Plate diameter	191.5
Inlet/outlet/draining pipe outer diameter	36.64
Inlet/outlet/draining pipe inner diameter	26.32
Mock-up height	1022
Mock-up diameter	200
Nb pipe length	872
Vessel thickness	4.25
Plates thickness	12
PbLi manifold height	50
Inlet/outlet length	10

considering that number of pipes while the other geometry details are in Table 6.4.

6.3.4 Detailed TH analyses

In this paragraph, the flow distribution among the different pipes is assessed by means of a suitable CFD analysis with STAR-CCM+ [73] of the manifolds (see Figure 6.4), as the flow speed influences the extraction efficiency.

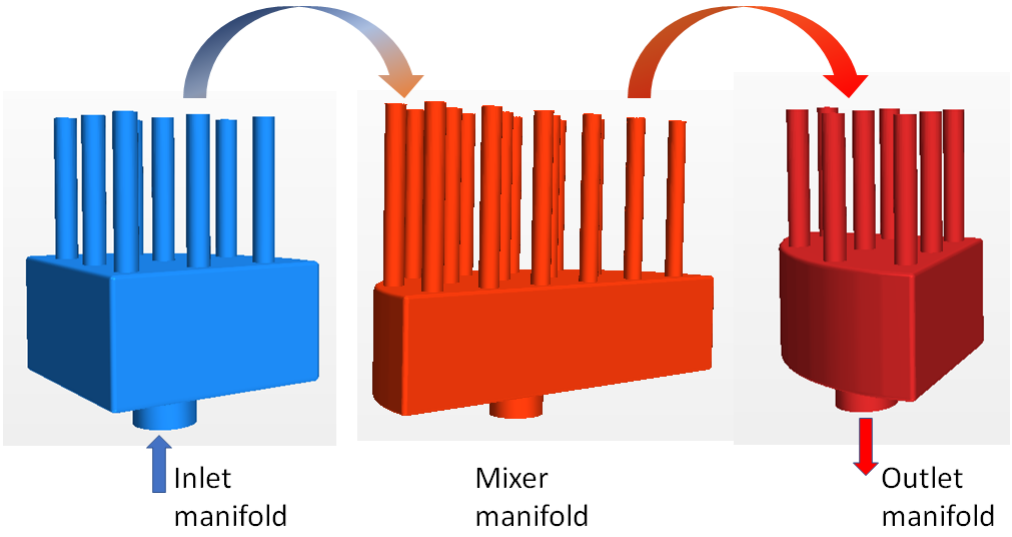

Figure 6.4: 3D view of the subdomains adopted for the CFD analysis of the manifolds: inlet manifold (light blue), mixing manifold (orange), outlet manifold (red).

In order to reduce the computational cost of the analysis, the three manifolds are analysed separately following this flow chart:

1. Analysis of the inlet manifold, prescribing the total mass flow rate on the inlet pipe and a 0-gauge pressure in correspondence of the outlet surface of the 8 pipes (cut 5.2 cm from the plate), see Fig. 6.4. The output of this analysis is the mass flow rate in each of the 8 pipes where the PbLi exits the subdomain *inlet manifold*.

2. The output of the calculation in point 1, namely the mass flow rate in each of the 8 pipes at the outlet of the subdomain *inlet manifold*, is prescribed in the corresponding 8 pipes where the PbLi enters the subdomain *mixer manifold*. A 0-gauge pressure is also prescribed on the outlet surface of all the 8 pipes where the PbLi exits the subdomain *mixer manifold*, i.e. at the beginning of the second passage (the discharge pipe is considered closed, as normal operation is analysed). The result of this CFD simulation is the flow repartition among the 8 pipes at the outlet of the subdomain *mixer manifold*.

3. The output of the analysis in point 2, i.e. the mass flow rate in each of the 8 pipes at the outlet of the subdomain *mixer manifold*, is used as input to be prescribed in the corresponding pipes where the PbLi enters the subdomain *outlet manifold*. The other condition prescribed is a 0-gauge pressure on the outlet surface of the outlet pipe. The outcome of the simulation is the pressure on each of the 8 pipes at the inlet of the subdomain *outlet manifold*.

The pressure drop in the mock-up pipes is then estimated according to [41] for the friction factor, considering the different pipe lengths and the different mass flow computed in each pipe. In the curved region of the pipe, the following formula is adopted to compute the pressure drop [74].

$$\Delta p = \rho v^2 \left(\frac{d_\mathrm{i}}{R_\mathrm{c}} \right) + 4 f_\mathrm{c} \left(\frac{L_\mathrm{c}}{d_\mathrm{i}} \right)^{0.5} \rho v^2 \tag{6.8}$$

where R_c is the curvature radius, L_c is the averaged curved length and

$$f_\mathrm{c} = f + 0.01 \left(\frac{d_\mathrm{i}}{2R} \right)^{0.5} \tag{6.9}$$

$$f = \frac{0.07725}{\left[log_{10} \left(\frac{Re}{7} \right) \right]^2} \tag{6.10}$$

After this first iteration, the following steps are performed:

4. CFD analysis of the *mixer manifold* prescribing, on the outlet surface of the *mixer manifold* outlet pipes, the pressure computed at point 3 on the *outlet*

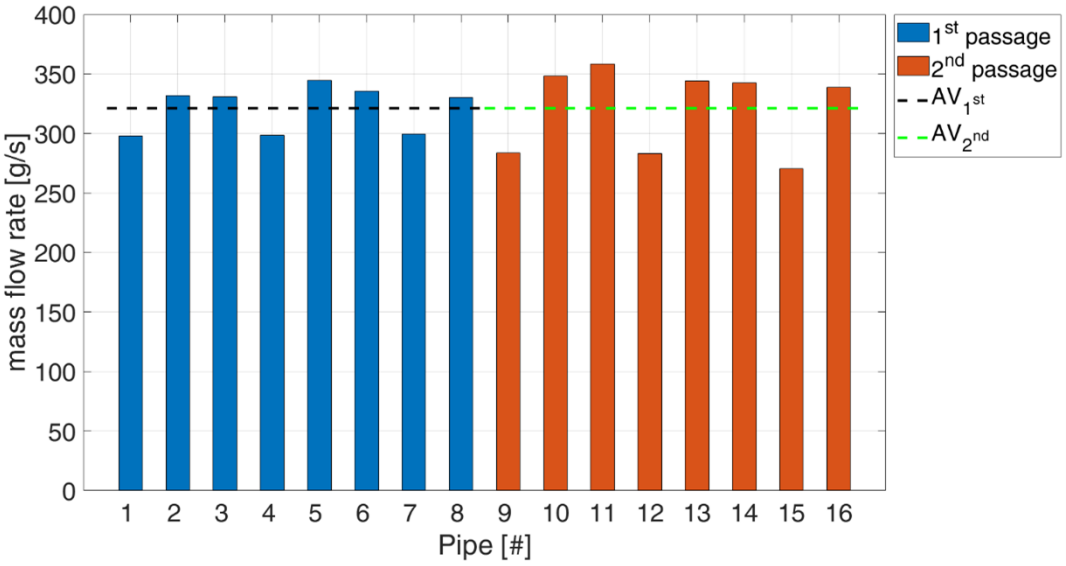

Figure 6.5: Mass flow rate repartition in the mock-up. The pipes of the first passage are indicated in blue, those of the second passage are indicated in orange.

manifold inlet pipes incremented by the pressure drop in the different pipes. The flow repartition among the *mixer manifold* inlet pipes, equal to that computed at point 1 for the *inlet manifold* outlet pipes, is also prescribed. The result of the calculation is the pressure on each inlet surface of the *mixer manifold* inlet pipes and the mass flow rate repartition among the *mixer manifold* outlet pipes.

5. CFD analysis of the *inlet manifold*, prescribing on the outlet surface of the *inlet manifold* outlet pipes the pressure computed at point 4 on the inlet surface of the corresponding *mixer manifold* inlet pipes incremented by the pressure drop in the different pipe, and prescribing the total inlet mass flow rate on the inlet pipe. The outcome of the calculation is the pressure on the inlet pipe surface and the mass flow rate repartition among the *inlet manifold* outlet pipes.

The results in terms of flow repartition among the different pipes in the first passage (connecting the inlet and the mixing manifolds) and second passage (connecting the mixing and the outlet manifolds), respectively, are reported in Figure 6.5. From the results, the average value (named in the legend $AV_{1/2}$) 0.321 kgs of the mass flow rates for both passages can be computed. In the first passage (from inlet manifold to the mixer) the maximum spread related to the average value is 7.23 % in the pipe 1, whereas for the second passage (from the mixer to the outlet manifold) in the pipe 15 is 15.8 %. In the inlet manifold the pipe 5 presents the highest value of mass flow rate, since it is collocated along the axes of the feeding pipe. In the

mixer manifold, pipes 9, 12, 15 get a lower value of the mass flow because they experiment a larger pressure drop due to the short curvature radius as well as in pipes 1, 4, 7.

6.3.5 Detailed TM analyses

A preliminary 3D TM analysis with FEM (using COMSOL 5.1 Multiphysics tool [75]) has been carried out on the vessel. Normal operating condition and accidental operating condition have been studied, where environmental temperature and pressure are 20 °C and 1 bar. Even if the vessel has been designed to resist to an internal pressure of 10 bar, a relief valve is supposed to open to discharge the pressure wave when the internal pressure reaches 1.7 bar. Consequently, the FEM analyses is performed in these cases:

- normal condition: $p_{\text{in}} = 0$ bar, at $T_{\text{PbLi}} = 330$ °C and $T_{\text{PbLi}} = 500$ °C;
- accidental condition: $p_{\text{in}} = 1.7$ bar, at $T_{\text{PbLi}} = 330$ °C and $T_{\text{PbLi}} = 500$ °C

In Fig. 6.6, the bottom plate deformation can be seen, respectively, at $T_{\text{PbLi}} = 330$°C and $T_{\text{PbLi}} = 500$°C during normal operating conditions: The deformation of the upper plate is presented in the next figures. In corresponding of welding between the vessel and the plate, the analytical theory (suitable for cylindrical wall, thick shell and axial symmetry, far from geometrical discontinuities) loses its validity. This effect can be solved with a series of clamps to compensate the discontinuity, to assure the structural resistance in both operating conditions (respectively, normal in Fig. 6.7a and accidental in Fig. 6.7b). The analysis has revealed that the maximum stress is reached in the junction where the plates are welded to the vessel. For the holed plate, the behaviour is different: in Fig. 6.7c the deformation in the accidental condition is negligible. With respect to the upper plate, the presence of the septum that divides the inlet/outlet manifold works as a joint. The same effect can be appreciated in the normal operating condition, where the bend is lower than upper plate.

6.4 Study on the extraction efficiency

After the sizing of the mock-up, the hydrogen extraction performances are analysed. In this case, the membrane length is fixed, therefore the free parameters are the temperature of the PbLi and its flow velocity. In fact, the latter influences the permeation due to the degree of turbulence for the mass transport coefficient, as in the Chapter will be shown.

The temperature affects all the physical properties both for PbLi and the membrane. Since the operating condition is steady state, the temperature field

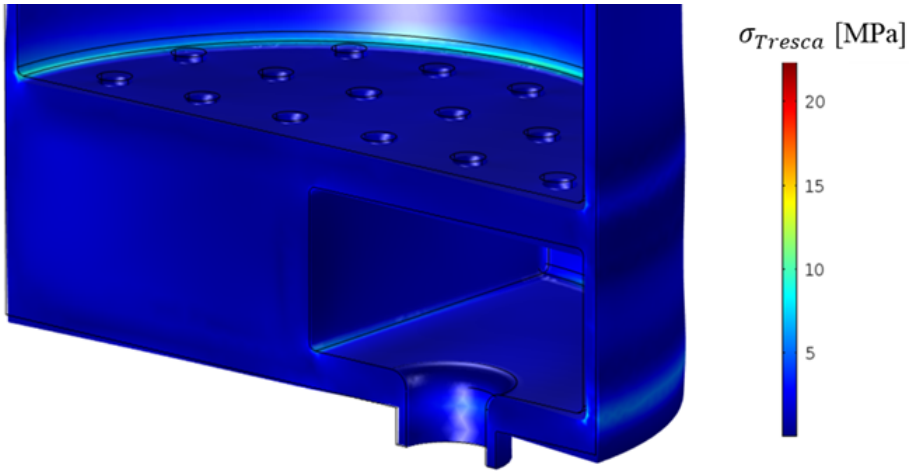

(a)

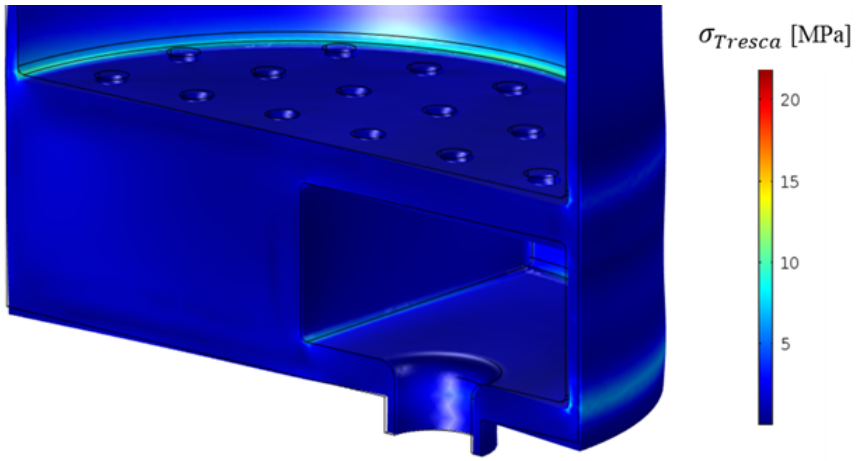

(b)

Figure 6.6: Stress distribution close to the holed plate in normal operating conditions. In a) the PbLi temperature is 330 °C, in b) the PbLi temperature is 500 °C.

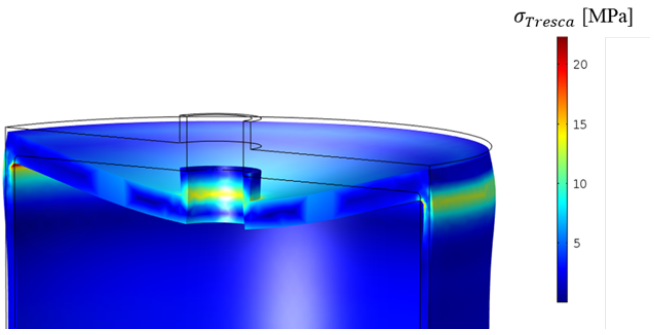

(a)

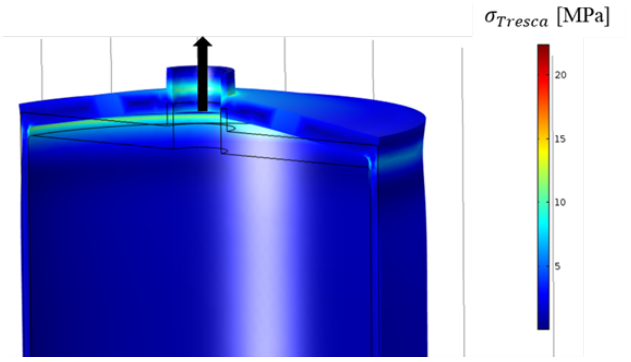

(b)

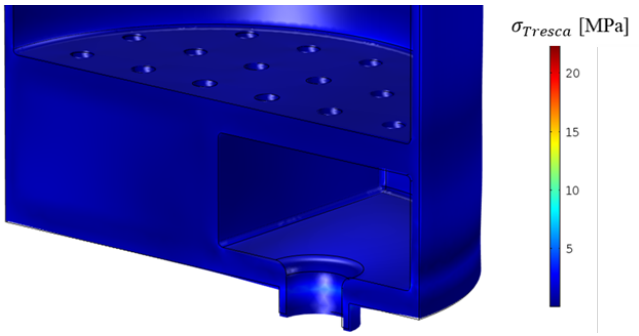

(c)

Figure 6.7: Stress distribution close to the upper plate in normal operating conditions, when the external pressure is 1 bar while the internal pressure is 0 bar when the PbLi temperature is 330 °C a). In b) the details on upper plate when the external pressure is 1 bar while the internal pressure is 1.7 bar and the PbLi temperature is 330 °C are shown. In c) the details on bottom plate stress can be appreciated in the same case.

is assumed to be isothermal. For this reason, the temperature is an independent uniform variable uniform for each material. The needed PbLi properties are ρ_l[76],μ_l[76],D_l[50],K_l[50].

6.4.1 Surface-Limited Regime vs. Diffusion-Limited Regime

In this section the results of the application of the model described in the Chapter 5 are reported. Both cases of permeation regime in SL and DL are shown in Fig. 6.8. When the mock-up operates at low temperature, the permeation regime is SL, leading to a lower mass flux across the membrane than the one in DL. This is due, in particular, to a lower value of recombination phenomena (and consequently the dissociation mechanism) that acts a further resistance to the permeation. This effect is evident at 330 °C, where the pure DL regime has an efficiency of ∼20%, whereas the corresponding case in SL regime the extraction efficiency is ∼5%. As the temperature increases, the surface mechanisms become lesser important,

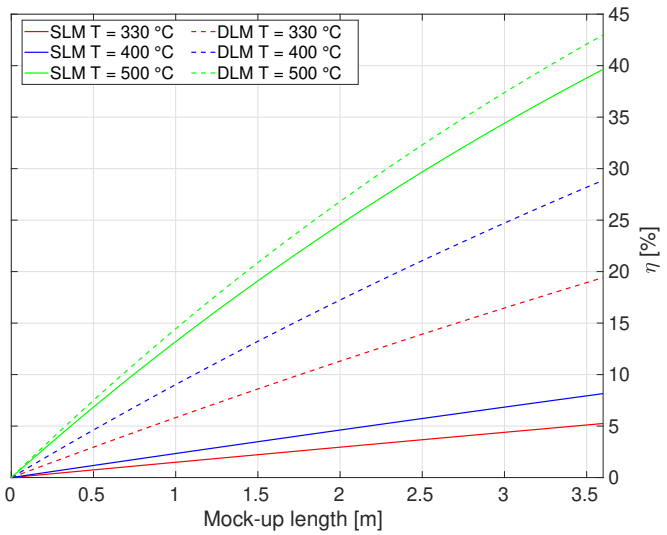

Figure 6.8: Effect of the variation of the PbLi temperature on the hydrogen extraction efficiency when the flow velocity is fixed at 0.5 m/s.

moving the permeation to the DL regime, in which the mass flux is only affected by the mass resistance of diffusion in the membrane bulk. Indeed, when the considered temperature is 500 °C, the extraction efficiencies are similar. It must be noted that these effects are consistent even if the membrane is contaminated, since the permeation is forced to be SL. In fact, a lower value of recombination constant can be also a consequence of impurities in the membrane. In this case, a temperature increase leads to a permeation in diffusion-limited regime, since the chemisorption effects are attenuated.

6.4.2 Sensitivity analyses

To show the effect of the other parameters as the turbulence of the PbLi in the pipes and/or the membrane properties, an uncertainty analysis has been performed. This activity was foreseen for the experimental campaign on the mock-up on the TRIEX-II facility, but due to the COVID-19 pandemic, the validation activities was postponed beyond the end of this PhD program.

The analysed parameters are:

- mass transport coefficient;
- mass flow repartition;
- permeation condition.

Notwithstanding this, an evaluation of the possible scenarios for the validation has been prepared to support the conceptual design of the TERS based on the PAV technology. A test matrix has been elaborated, considering as input the following data:

- Temperature range: 330 °C - 450°C;
- PbLi mass flow: 1.2 kg/s - 4.6 kg/s;
- inlet partial pressure of H_2: 200 Pa;
- Pressure vacuum side: 0.01 Pa;

With this range of operating parameters, the text matrix example is shown in Table 6.5. The target of the analysis is to investigate how the uncertainty on the mass transport coefficient (related to the adopted correlation) in the PbLi, the degree of turbulence (the mass flow rate) in the pipes and the permeation properties affect the performance of extraction.

Table 6.5: Test matrix example for the uncertainty analyses of the experimental campaign of the mock-up on TRIEX-II facility.

	PbLi mass flow [kg/s]		
T [°C]	1.2	2.9	4.6
330	$\eta_{1,1}$	$\eta_{1,2}$	$\eta_{1,3}$
390	$\eta_{2,1}$	$\eta_{2,2}$	$\eta_{2,3}$
450	$\eta_{3,1}$	$\eta_{3,2}$	$\eta_{3,3}$

Effect of mass transport coefficient h_T

Considering the effect of the mass transport coefficient h_T, the correlation adopted for its estimation is reported in [77] and it has a confidence interval of ± 13%. To show only this effect, the other parameters are fixed. In particular, the average values for each mass flow rate is retained in the pipe, and the properties for the niobium membrane are taken from [56]. In this condition, the mass transport coefficient is manually altered up to the minimum/maximum value starting from the average one. In Fig. 6.9 two phenomena are highlighted. The first one, in Fig. 6.9a, is the efficiency increase when the mass flow rate decreases: this is due to the increase of the residence time of the hydrogen molecule in the PbLi as the transport effect along the pipe is reduced. In this figure the mass transport coefficient is fixed at the nominal value. The highest efficiency value is reached when the temperature is 450 °C (reduction of surface phenomena) and the mass flow rate is 1.2 kg/s (lower diffusion time with respect to the transport time). In this operative condition, the membrane is more permeable than the other points, and the reduction of PbLi velocity enhances the diffusion towards the membrane surface.

The second one is the impact of the mass transport coefficient when the PbLi velocity is fixed. If h_T is altered in its confidence interval, the importance of the transport towards the wall becomes more evident (See Fig. 6.9b for the case of 1.2 kg/s). In fact, if the mass flow rate value is kept constant (i. e., the PbLi flow velocities in the pipes), a reduction of the mass transport resistance enhances the permeation (higher h_T), confirming the impact of the velocity both on transport of hydrogen along the pipe and its transport towards the wall.

The two effects are summarised in Fig. 6.9c where the operating condition is at the maximum temperature (450 °C) and the mass flow rates encompass the range [1.2-4.6] kg/s. As the figure shows, an increase in the mass flow rate induces an increase of outlet partial pressure of hydrogen, due to the predominance of PbLi transport with respect to the permeation. The highest value is reached again when the mass flow rate is 1.2 kg/s and the h_T has its maximum. To conclude, the major resistance to the permeation is due to the PbLi since two opposing effects are present: the transport towards the membrane due to a higher mass transport coefficient (higher turbulence) and the advection of hydrogen along the pipe.

Effect of mass flow repartition

Here the effect of the mass flow repartition is discussed, since each pipe contributes to the extraction efficiency by the proper mass transport coefficient. Indeed, the split of mass flow rate due to the pressure drops, which is different for each pipe as showed in Fig. 6.5, induces small differences about h_T in each tubes. This implies that, in principle, the hydrogen is differently extracted in the permeator as the level of turbulence is concerned. To retrieve this effect, an example of flow repartition

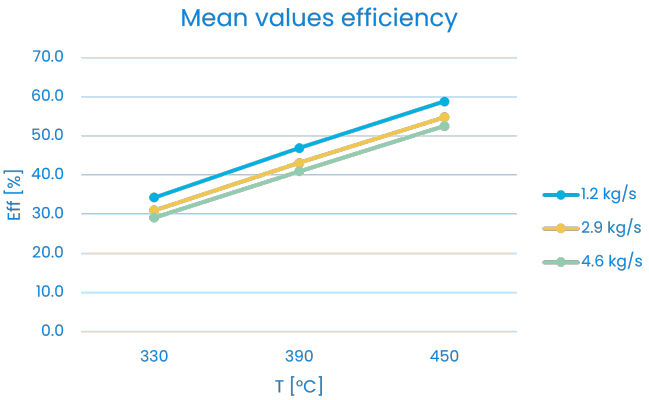

(a)

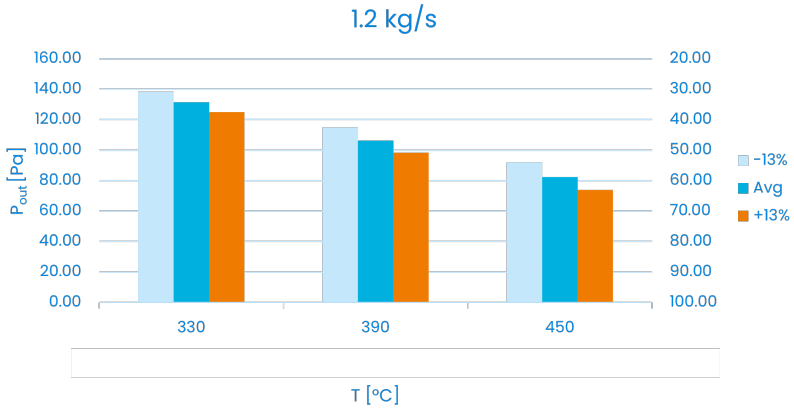

(b)

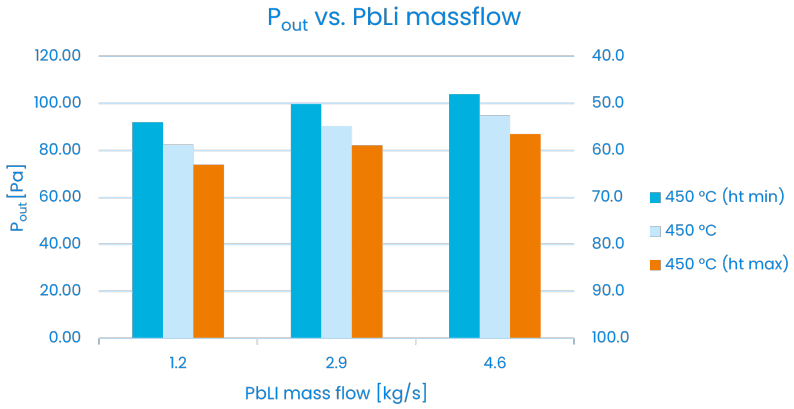

(c)

Figure 6.9: Effect of mass transport coefficient on the hydrogen extraction efficiency in the mock-up. In (a) the average value of the h_T is used. In (b) variation of h_T is reported for a single case of mass flow rate. In (c) the effect of mass flow rate at fixed temperature is showed.

is taken as a reference from [69], and it is applied to the investigated mass flow rate range. Each outlet concentration is evaluated at the end of pipe (entry of each manifold). Here, the average concentration $\overline{C}$ is calculated as:

$$\overline{C} = \frac{\sum_{i=1}^{N_\mathrm{p}} C_i \frac{\dot{m}_i}{\rho}}{\sum_{i=1}^{N_\mathrm{p}} \frac{\dot{m}_i}{\rho}} \tag{6.11}$$

where N_p is 8 as the number of pipes, and ρ is the PbLi mass density. The average concentration of hydrogen is thus calculated in each manifold, setting a new initial value for the permeation in the next collector. Concerning the niobium properties, the ones calculated by Steward [56] are used.

In Fig. 6.10 the results of analysis are shown. It is evident that a slightly difference in the mass transport coefficient does not affect in significant way the outlet concentration of hydrogen. This is due to the fact that the mixing effect in each collector averages the different concentration at the outlet of each pipe. Moreover, a rebalance effect on the permeation is present: if a pipe receives less mass flow rate, the permeated flux is increased, as stated in the previous section. In conclusion, the permeation is not affected with significant effect when there are slightly differences in the mass flow rate in each pipe.

Permeation properties of the niobium membrane

Recently, CIEMAT has measured a new set of niobium properties [78] that confute those calculated by Steward. In the results of CIEMAT, the recombination constant K_r decreases by increasing of temperature. To show the effects of this implication, the next case has been calculated keeping the average mass flow velocity in each pipe since it has no influences on the permeation. With respect to Fig. 6.11a, the case calculated with the Steward's properties is reported for direct comparison. In Fig. 6.11b the calculation performed with the set of properties measured by CIEMAT is shown. The permeation is always negligible since the surface resistances increase as the temperature increase. This means that if this new set of properties was confirmed, the niobium membrane would not be suitable for the extractor based on PAV technology.

Niobium surface condition

The last examined case regards the state of the surface of the niobium membrane. In fact, according to [79], if the metal is contaminated, the value of recombination constant is lower than that for a clean surface. This implies a greater resistance on the walls with respect to the case of pure membrane, which leads to a SL permeation

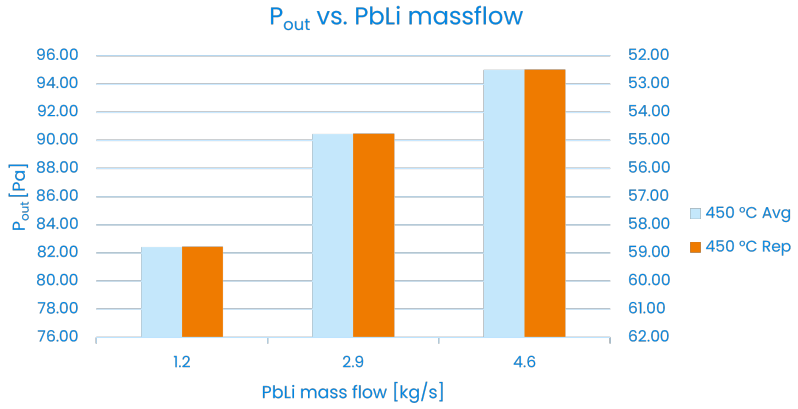

(a)

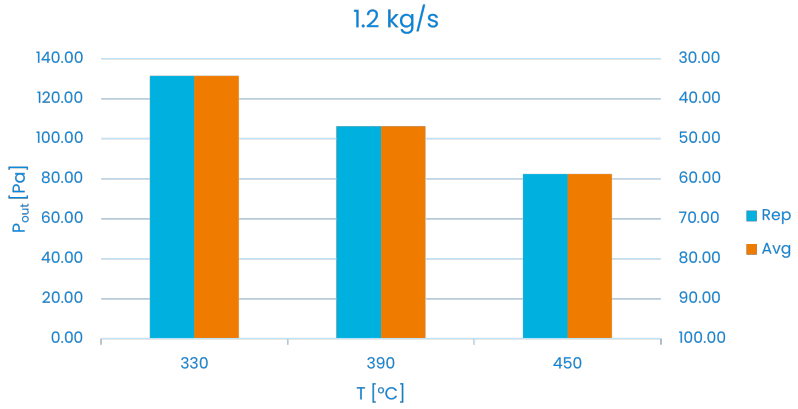

(b)

Figure 6.10: Effect of mass flow repartition on the extraction efficiency in PAV mock-up. In the right axis the efficiency is reported. In (a) the effects of mass flow repartition is showed for different temperatures, while in (b) the case with 1.2 kg/s is showed at vary temperatures.

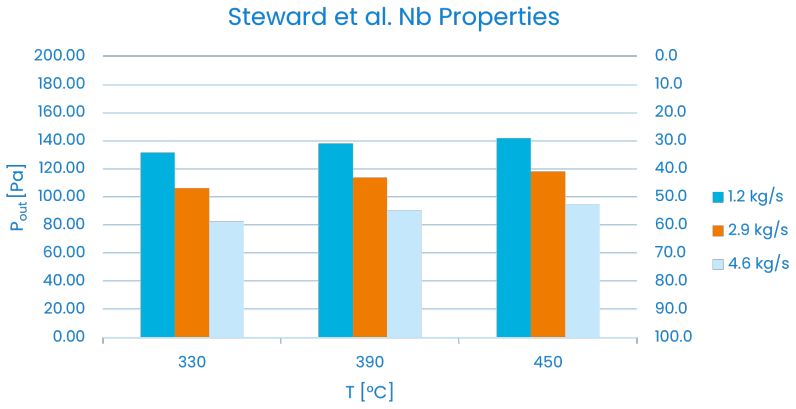

(a)

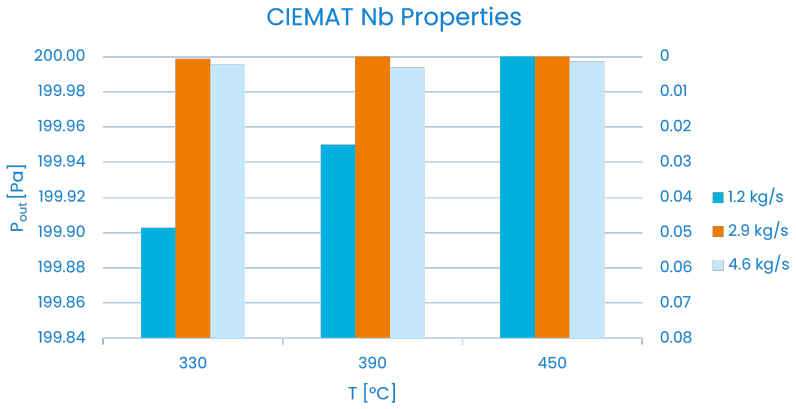

(b)

Figure 6.11: Effect on the extraction efficiency with two different sets of niobium properties: in (a), the property of Steward are used, whereas in (b) the new set measured by CIEMAT is adopted.

regime. To show the influence of the membrane condition, the extraction efficiency is computed and compared in both operating scenarios.

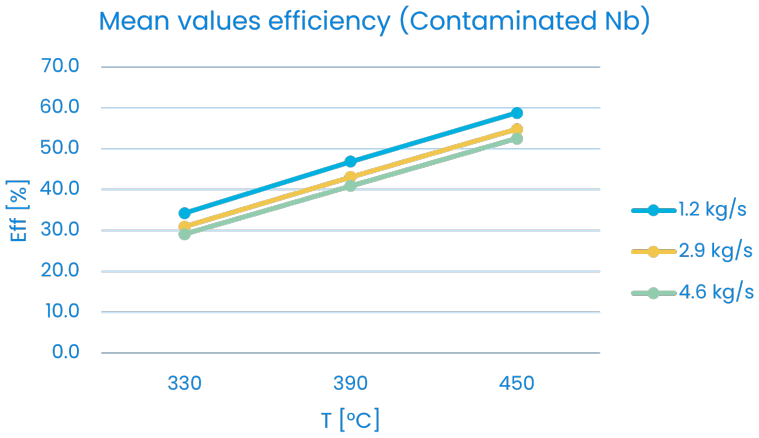

(a)

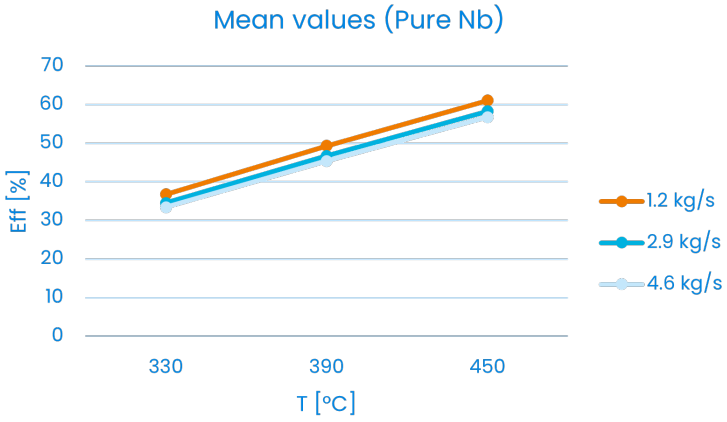

(b)

Figure 6.12: Effect on the extraction efficiency depending on the niobium membrane surface. In (a) the niobium is contaminated, while in (b) the membrane is clean.

From Fig. 6.12 it is evident that in presence of a clean niobium surface, the extraction efficiency is quite higher than the case of contaminated niobium. This is due to the recombination constant, because it behaves as an enhancer of the permeation: higher value implies a major number of hydrogen atoms that are able to recombine and leave the membrane faster, avoiding the flattening of the gradient concentration in the membrane. In fact, the flattening of the gradient is mainly due to the different velocities of surface effects: if the latter are slower than the diffusion in the membrane bulk, the chemisorption acts as stopper for the diffusion,

leading to lower efficiencies. To conclude, the niobium membrane performs worse extraction when its surface is contaminated, as by the formation of oxides.

6.5 Conclusions and perspectives

The primary purpose of this effort was to develop a PAV mock-up with a niobium membrane with the intention of installing it sequentially in the TRIEX-II facility and characterising its performance. A cylindrical structure with U-tubes was chosen to reduce the total size of the components, and the membrane thickness in comparison to a planar arrangement. niobium was chosen as the membrane material due to its high hydrogen permeability, low susceptibility to oxidation, and reduced cost. A FEM analysis hes been carried on to verify the preliminary sizing by means of analytical formulas. As well, a CFD study has been perform to assure the level of turbulence in the pipe, since the hydrogen transport towards the membrane is mainly affected by PbLi velocities.

The design was adjusted to minimise the spread of PbLi speed between the pipes, taking into consideration criteria for overall dimensions and pressure losses. The ideal PbLi speed for hydrogen isotopes penetration was determined to be 0.5 m/s, where at 500 °C, the mock-up demonstrates a potential maximum extraction efficiency of around 40-45%.

In the framework of the validation activity foreseen in TRIEX-II, an uncertainty analysis has been carried out. The main parameters have been deeply investigated in order to optimise the extraction efficiency and to understand how the latter is affected by the temperature, partial pressure and niobium condition. Considering the niobium surface, a possible foreseen solution to avoid corrosion and thus enhance the permeation, is to use the PdAg coating. The recombination constant of the coating is higher than the niobium one, leading to a reduction of surface resistance to the permeated flux at lower temperature.

Chapter 7

Conceptual design of a PAV-based tritium extractor for the WCLL BB of the EU DEMO

In this chapter, the scalability of device analysed in Section 6 is assessed for the TERS up to EU DEMO scale. The design is performed considering the foreseen constraints for the WCLL BB.

The methodology is carried on by means of the new permeation model developed in Chapter 5, taking into account the results achieved in the uncertainty analyses on the PAV mock-up. The prescribed constraints impose a certain limit of the pressure drops which results in a limit for the membrane length. The latter is the main parameter to be determined in order to achieve the nominal efficiency of 80-90%.

To carry on the study, a parametrically analysis is conducted varying the inlet temperature of the PbLi and the membrane geometry in order to be compliant with the prescribe pressure drop. As showed in the previous section, the temperature in the main parameter which affects the permeation regime. Therefore, a comparison among the solutions found with the SL and the DL are showed, to identify the best options. Most of this work has been presented at SOFT2020 [80].

7.1 TERS based on PAV up to EU DEMO scale

In this conceptual design of the TERS, the working principle is the same proposed in the Section 6.2. The PbLi that exits the BB is collected in the intake manifold, which distributes the flow via a first set of U-pipes before reaching the mixing manifold. From the latter, where the PbLi mixing enables the tritium concentration to be homogenised in the event of non-homogeneity in the first passage, and via a second set of U-pipes, the PbLi flows eventually to the outlet manifold. See

Fig. 7.1. In the extractor foreseen for the EU DEMO, each set has U-pipes placed in a square lattice with a 5 cm pitch, which enables the pipes to be correctly welded to the plate.

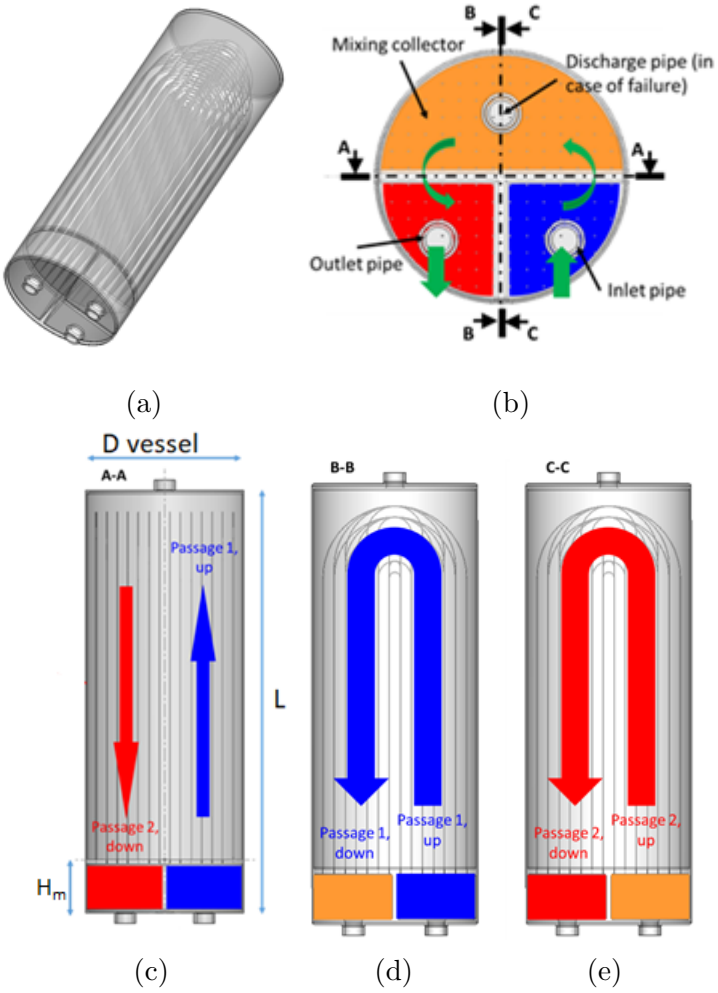

Figure 7.1: View of the PAV design proposed here: a) 3D view, b) top view of the vessel internals (with the inlet/outlet and discharge pipes in transparency), c) side view of the vessel internals (with inlet and outlet manifolds) and side view of the passage 1 d) and passage 2 e).

Concerning the TERS for the WCLL BB at system level, a possible configuration is presented in Fig. 7.2. This P&ID is similar to that described in [81] for the TERS of the Dual Coolant Lithium Lead (DCLL) BB. Following its escape from the BB, the liquid PbLi from the loop enters the PAV, where tritium is removed, and then returns to the PbLi loop, where it is extracted again. The efficiency of the PAV is dependent on several factors, including the pressure gradient established across the permeator membrane; consequently, the vacuum level established on the vessel side

of the membrane is critical and must be carefully selected, as it has implications for the vacuum system. The vacuum line is comprised of an extraction line connecting the PAV to the tritium plant, which is powered by a pair of vacuum pumps (HVP01 and RVP01). In the event of a tritium plant emergency shutdown, the vacuum line directs the extracted tritium to the GETTER systems, which store the tritium until the tritium plant is restored. V16 is closed while V07 is opened. During the start-up phase, the helium line is necessary to fill the PAV vessel. The vessel air is removed through the V03-V05 line: the PAV is supplied with helium at a high pressure from the He main line, avoiding the need for pumps, and is diverted to the low pressure helium line. Helium is also utilised as a stripping gas in the GETTER systems after they exceed their tritium storage capacity. A tritium extractor is planned to separate the tritium from the helium, recovering the helium (which will be returned to the low pressure pipe), and transporting the pure tritium to the tritium plant. The potential of encountering non-standard operating situations has been considered, necessitating, for example, the discharge of the PbLi to the T01 through the three parallel sets of valves and rupture discs under the PAV.

7.2 Conceptual design strategy

The preliminary dimensioning of the PAV for the EU DEMO TERS begins with an assessment of the required length for the permeator membranes, i.e. the U-pipes. Along with defining the pipe diameter, this result also defines the vessel size. The pipe length is calculated by specifying the required extraction efficiency η and estimating the distribution of the tritium concentration in the PbLi using appropriate permeation models. The findings obtained using a SLM will be compared to those obtained using a pure DLM, as described below. To optimise the shape of the permeator while still adhering to the design limitations, parametric scanning is performed by

- the pipe diameter, using available commercial values for Nb pipes;
- the PbLi inlet temperature, that can be increased by means of suitable heaters, if the permeation process must be enhanced to reach the desired target efficiency (even though this will result in an overall plant efficiency reduction, due to the heater power consumption).

7.2.1 Design constraints and inputs

The primary limits on PAV dimensioning are space occupancy (which is determined by the amount of space provided for its installation in the plant) and permitted pressure drop, as shown in Table 7.1. The maximum permeator length (40 m) is

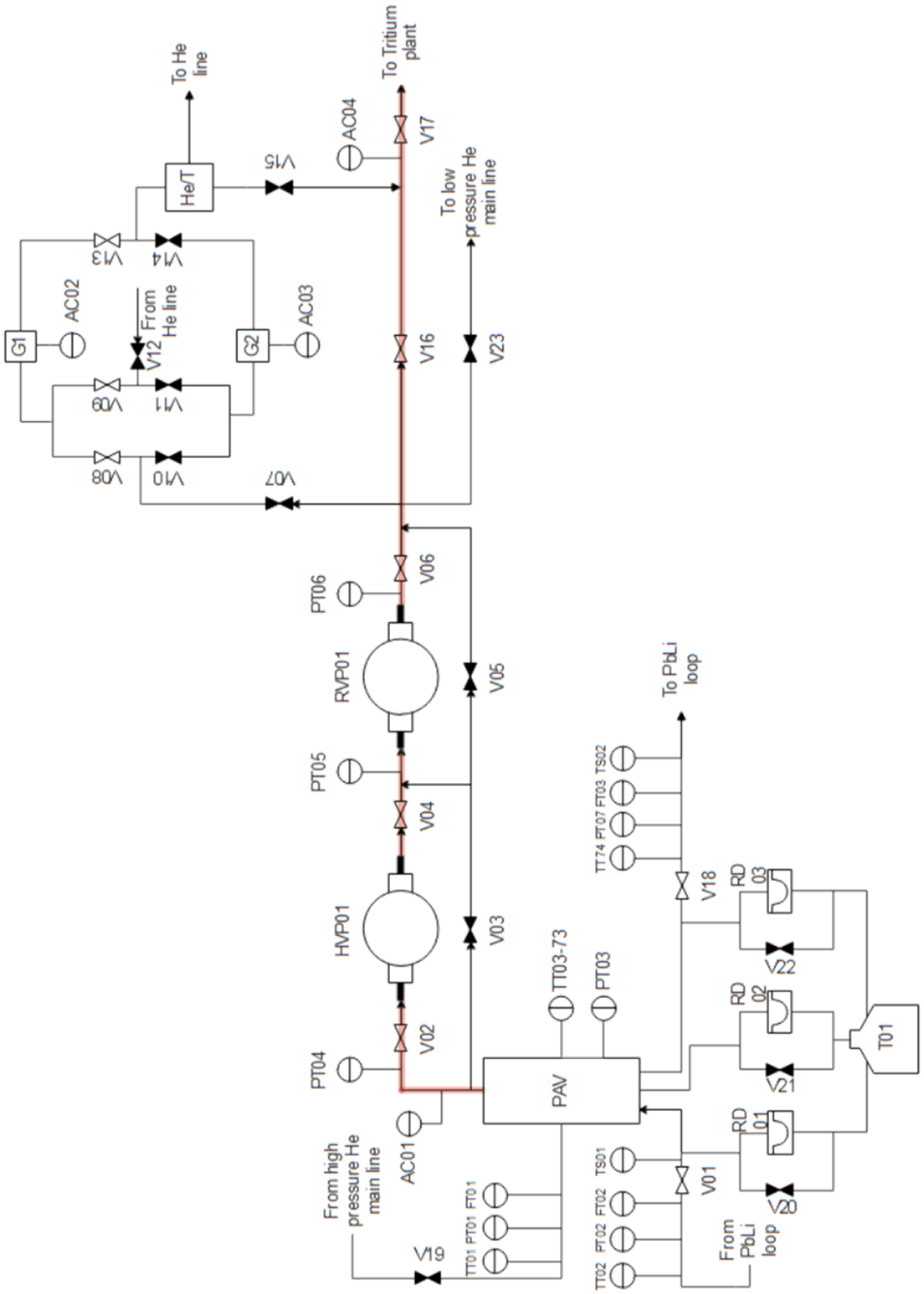

Figure 7.2: P&ID of the PAV system for theEU DEMO TERS. PAV; G: getter system; HVP: high vacuum pump; RVP: rough vacuum pump; TT: temperature sensor; PT: pressure transducer; TS: tritium sensor in PbLi; AC: tritium sensor in gas phase; V: valve; FT: flowmeter; RD: rupture disk; T: storage tank; He/T: He - tritium separator. The tritium path in normal operation mode is highlighted in red.

Table 7.1: Constraints for the EU DEMO TERS design.

Variable	Constraint
Pressure drop in the extractor	$\leq$ 2 bar
Vessel diameter D_V	$\leq$ 7 m
Devices for each BB loop	max 2 in parallel
Vessel height L	10 m
Efficiency η	$\geq$ 80%

determined by the vessel maximum height and the presence of two U-pipe passageways. The WCLL BB design incorporates four PbLi loops for OutBoard (OB) segments and two loops for InBoard (IB) segments. The dimensioning of the PAV required to extract tritium from one of the OB loops is carried out here, as they have the highest mass flow rate (up to 264 kg/s), as shown in Table 7.2: if the dimensioning demonstrates that the PAV is capable of processing that mass flow, it will also be capable of processing the lower mass flow in the IB loops. Additionally, a maximum of two parallel vessels is specified for each circuit to ensure redundancy in the event of a failure without exceeding the maximum space occupancy. The efficiency must be at least 80% and, if feasible, raised to 90% [82] in order to decrease tritium inventory within the PbLi loop. The extractor will be situated near the reactor, at the highest point of the PbLi circuit. The design inlet pressure is 4.6 bar, with a relief valve that allows the PbLi content in a tank to be released in the event of a component pipe rupture.

Apart from the PbLi mass flow rate to be processed, the model used to design the permeator also takes into account its thermodynamic properties, as well as the tritium partial pressure at the membrane inlet, as shown in Table 7.2. The latter has a list of all the inputs.

Table 7.2: Input data for the dimensioning of the OB PAV.

Parameter	Value
Tritium inlet partial pressure ($p_{T,b}$)	100 Pa
Design PbLi inlet temperature (T)	330 °C
PbLi inlet pressure (p)	~15 bar
PbLi mass flow rate (W_t)	264 kg/s

7.2.2 Design approach

Due to the fact that all thermophysical characteristics are temperature dependent, the latter is the first independent variable: because the PAV operation is isothermal, it is consistent across all materials. Following that, the following qualities are evaluated:

PbLi: $\rho_{PbLi}, \mu_{PbLi}, D_{PbLi}, K_{sPbLi}$;

Nb: $D_{Nb}, K_{sNb}, K_{rNb}, K_{dNb}$;

The following stage is to determine the geometrical dimensions of the pipes, most notably the inner diameter. To generate credible results from the model, the correlation used for the mass transfer coefficient must change within the validity range of the Reynolds number (Re). This constraint, when paired with the correct inner diameter d_i of the pipes (as determined by commercial sheets [83], results in a predefined PbLi speed. As a result, at the specified temperature value

$$v\left(d_i, T\right) = \frac{Re \cdot \mu_{PbLi}}{d_i \cdot \rho_{PbLi}} \tag{7.1}$$

moving between the lowest and maximum values of the Re number, as defined by the correlation validity range described in [77]. Each combination of (d_i, T) results in a unique mass flow per pipe, allowing the total number of pipes required to handle the whole mass flow rate to be calculated. Even though the membrane length is unknown at this point, the pressure drop per unit length [Pa/m] for any combination of (d_i, T) is already calculable at this point. The friction factor f is correlated using the formula provided by [41]:

$$f = \frac{0.316}{Re^{0.25}} \tag{7.2}$$

and it is applicable to circular pipelines carrying liquid metal. As a result, the pressure decrease per unit length is as follows:

$$\Delta p_l = \frac{4f}{d_i}\frac{1}{2}\rho_{Pbli}v^2 \tag{7.3}$$

Using both models for the two tritium penetration regimes within the permeator and the temperature, the inner pipe diameter, and the PbLi speed, it is feasible to determine the length necessary to achieve the required extraction efficiency. The required membrane length is highly dependent on the permeation regime and is calculated by assessing the bulk tritium concentration $C_{T,b}$ at each axial coordinate z inside the pipes using 5.3, until the desired extraction efficiency is obtained. After determining the length, the total pressure drop may be calculated.

The parametric analysis is carried out by modifying the temperature and inner diameter of the pipe. The final design will then be chosen by the solution that minimises the overall pressure loss in the PAV and the maximum encumbrance. The inner diameter of the pipes through which the PbLi flows determines the number of tubes required to handle the total mass flow while fulfilling the fluid speed limitation; with a fixed pitch of 5 cm between the pipes, this defines the diameter of the vessel(s).

Due to the fact that varying the PbLi speed results in varied membrane length, pressure drop, and mass flow rate behaviours in the pipes, the acceptable option for successfully completing the design is represented by a trade-off between all parameters (temperature, pipe diameter and membrane length). This trade-off occurs as a result of the membrane length and the number of pipes, after the selection of an appropriate PbLi speed that ensures a total pressure drop less than the relevant limit. Fig. 7.3 illustrates the design process, which may be resumed as:

1. a temperature value determined by parametrically raising it from the design to 400 °C and 500 °C;
2. the speed is determined by the permitted Re range and the temperature; as a result, the mass flow rate per pipe and the number of pipes may be determined;
3. the pressure loss per unit length is calculated using the speed and temperature at the preceding step;
4. the permeation model calculates the membrane length necessary to attain the required efficiency for each speed value;
5. within the constrained encumbrance, the best solution is developed that satisfies all of the requirements (pressure drop, membrane length, and vessel diameter).

7.3 Results

The dimensioning results, including the parametric investigations, are presented here. They are produced by enforcing an extraction efficiency of 90%, which is greater than the required minimum of 80%, in order to limit the tritium inventory inside the PbLi loop. The dimensioning process seeks to determine the membrane length and vessel diameter (which are directly proportional to the number of pipes) that fulfil all restrictions. According to the design procedure (Fig. 7.3), the PbLi speed is predetermined using 7.1, after the required range of Re values is chosen. As seen in Fig. 7.4, the membrane length and the number of pipes behave differently as a function of the total pressure drop (i.e. the PbLi speed):

- The mass flow rate per pipe (and hence the pressure drop) increases as the PbLi speed increases, resulting in a reduction in the number of pipes as the pressure drop grows.

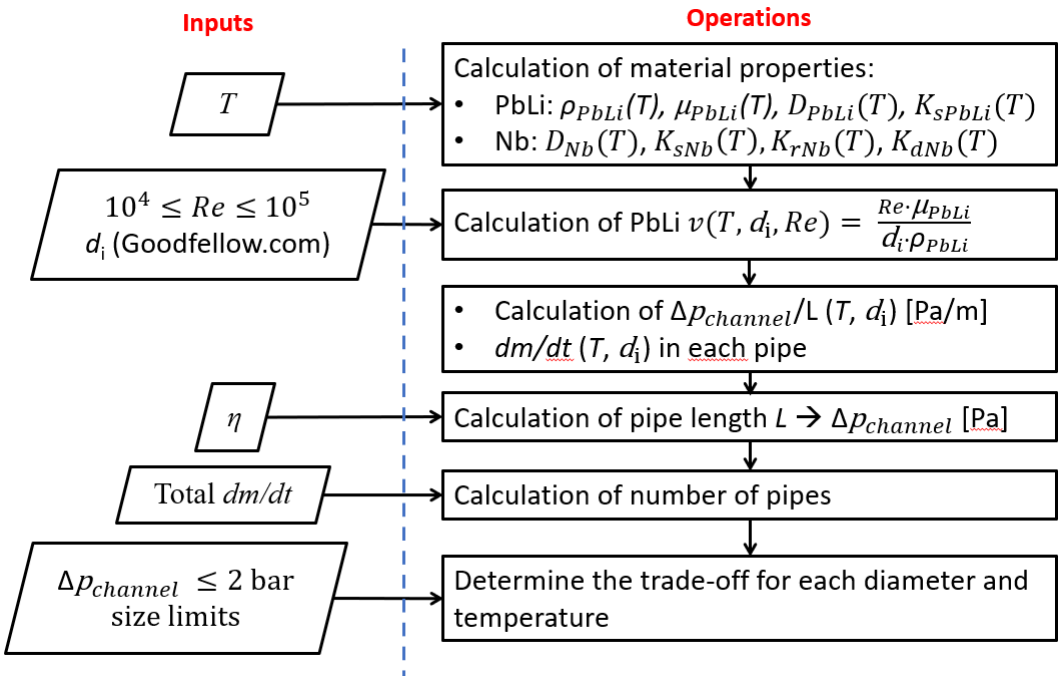

Figure 7.3: Flowchart of the design process for the PAV proposed here: on the left the constraints given in input are present, and on the right the operations are reported.

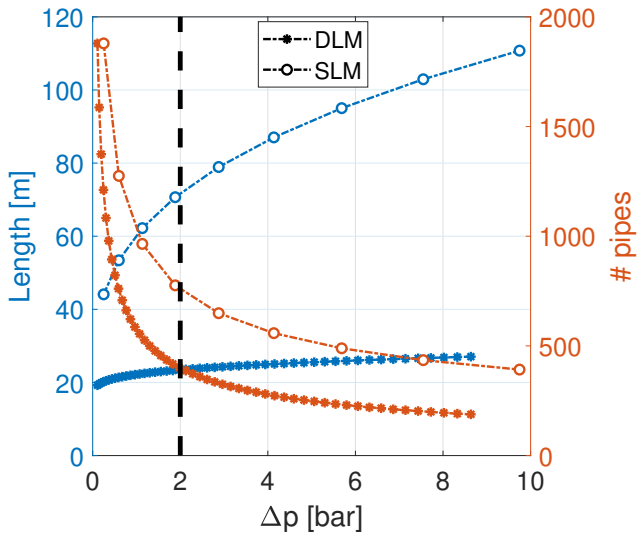

Figure 7.4: Comparison between the trade-off when both permeation regimes are considered at $\eta = 90\%$. Here the $d_i = 13\ mm$ at $T = 500$ °C case is reported. The orange lines show the membrane length (left axis) and the light blue lines show the pipe number (right axis). The trade-off for each regime is highlighted by a black circle.

- On the contrary, when the speed increases, the membrane length tends to grow due to the decrease in the residence period of the tritium during extraction; accordingly, longer membranes are necessary to achieve the goal efficiency (and consequently the total pressure drop tends to further increase).

The spatial restrictions impose a limit on both the membrane length (left axis in Fig. 7.4) and the number of pipes (indirectly) (right axis in Fig. 7.4). Finally, the pressure drop limits impose a limit on the x-axis of Fig. 7.4. Due to the behaviours described above, the latter restriction places a limit on the minimum number of pipes and the maximum length that are permitted. The space of acceptable design values is defined as the intersection of these acceptable values and those imposed by encumbrance limitations. This space can be limited (but not necessarily tiny) or infinite. In the first scenario, because the number of pipes is the more strict limitation (because more pipes require more welds, which are crucial structurally), the maximum pressure drop is kept, although at the expense of a longer membrane. The second scenario retains the pressure drop nearest to the threshold, while maintaining a manageable amount of pipes. The pressure drop constraint is regarded indicative for the time being, as the circulator pressure head is not yet determined throughout the design phase. As a result, only solutions within twice the 2 bar threshold are maintained in Fig. 7.5: this is true only for the membrane operating in the SL regime at 330°C.

The findings of both models are compared in Fig. 7.5a: for both specified diameters, the surface-limited model predicts a longer membrane than the pure DLM, suggesting that contamination of the Nb membrane (requiring the employment of an SLM) reduces efficiency. Notably, only heating the PbLi to 500°C allows for a design solution that satisfies almost all constraints (with a 90% efficiency); at 400°C, the pipe length required to achieve the target extraction efficiency is more than twice the acceptable value, while at 330°C, the pressure drop is unacceptably high. If the mass flux of tritium is restricted by surface phenomena, and the recombination/dissociation mechanisms are orders of magnitude slower than the mass diffusion in the membrane, the limiting factor is no longer the mass diffusion in the membrane. The membrane becomes shorter as the temperature increases, as the recombination constant (for the SLM) and diffusion coefficient (for the DLM) tend to increase, resulting in a greater tritium flux across the membrane.

As shown previously, the pressure decrease recorded in Fig. 7.5b is nearly always close to the maximum permissible amount. Larger values are preserved only in a few circumstances where a suitable solution cannot be found.

The diameters of the permeator vessel computed by the SLM (and by the DLM at 330°C) are shown in Fig. 7.5c: the constraint on maximum encumbrance is always satisfied when a single vessel is used for each loop. The diameter of the vessel, in particular, is determined only by the number of pipes it should contain (after the pitch between the pipes in the lattice is established), as seen in Fig. 7.5d.

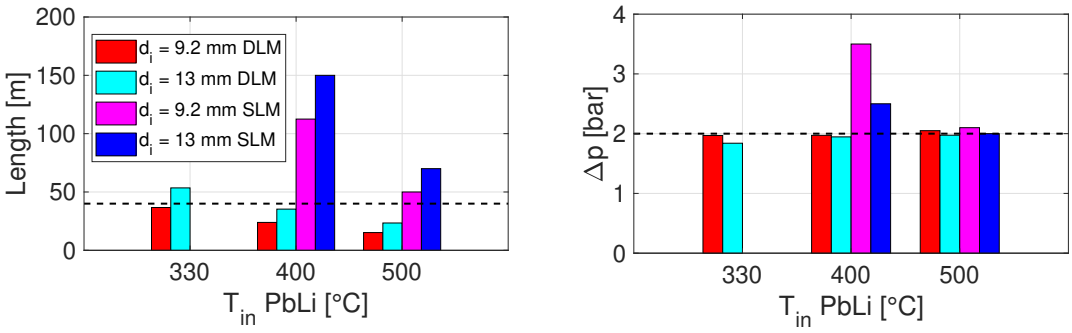

(a)

(b)

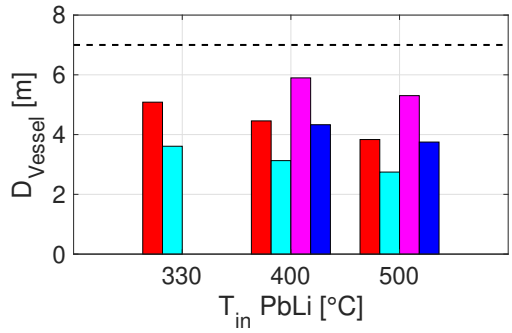

(c)

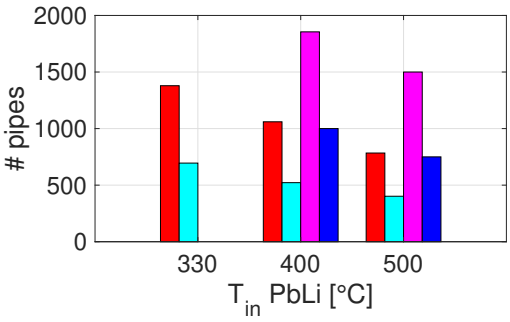

(d)

Figure 7.5: Results of the PAV dimensioning considering different pipe diameters and PbLi temperature, and a 90% target extraction efficiency. a) Permeator length; b) pressure drop; c) vessel diameter; d) number of pipes in each vessel. Where available, the maximum allowed value is reported as a black dashed line. The color legend is the same for all figures.

The latter is the ratio of the overall mass flow rate to the mass flow rate carried in each pipe, which is determined only by the pipe diameter and PbLi speed chosen in the design process.

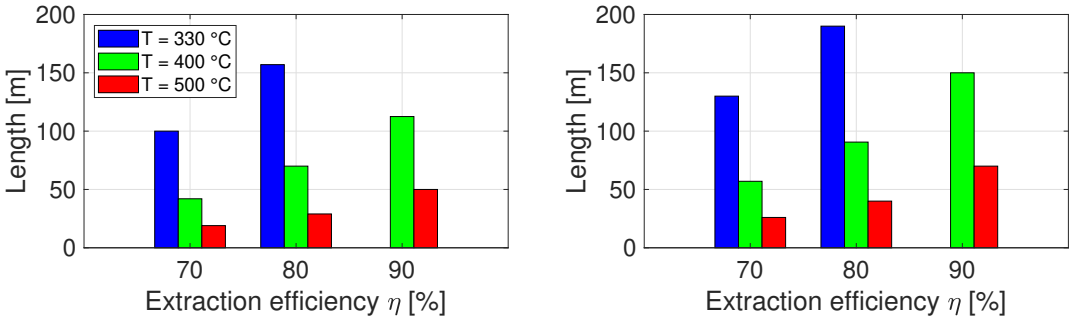

(a) (b)

Figure 7.6: Comparison of the requested membrane length in SL regime at different temperatures for different target extraction efficiencies for a) $d_i = 9.2\ mm$ and b) $d_i = 13\ mm$.

The comparison of membrane lengths produced with varied target extraction efficiencies is shown in Fig. 7.6. Both situations of $d_i = 9.2\ mm$ (Fig. 7.6a) and $d_i = 13\ mm$ (Fig. 7.6b) are illustrated, with the temperature being parametrically varied in the SL regime. Due to the increased penetrated flow as the temperature rises, the desired duration tends to decrease. On the other hand, if the desired efficiency is increased while maintaining the same temperature, longer membranes are necessary to force a lower tritium concentration at the PAV exit. At 330°C, the extraction efficiency of 90% cannot be achieved without a significant pressure drop; so, that example is not included in Fig. 7.6.

To summarise, as seen in Fig. 7.5 and Fig. 7.6, it is conceivable to operate the EU DEMO TERS presented here with the extraction efficiency (conservatively) up to 90% in order to minimise the tritium inventory:

- in a DL regime at any temperature, including the WCLL working temperature of 330°C;
- at 400 °C, also in a SL regime, but with at least two permeators connected in series (or with a drop to 70% of the goal extraction efficiency);
- at 500 °C, as well as in a SL regime, to achieve the desired extraction efficiency.

Future advancements of the overall EU DEMO design will result in the optimal alternative being chosen from those presented here, mostly based on the permissible TERS operation temperature and the relaxing of certain space limits.

7.4 Conclusion and perspectives

The EU DEMO TERS conceptual design, based on PAV technology, has been detailed. The permeator geometry is shell-and-tube in nature, with the Nb membrane serving as the pipe wall and the tritium recovered from the PbLi flowing through the pipes through vacuum pumping. Additionally, a preliminary P&ID for the TERS has been shown, highlighting certain critical valve functioning.

The preliminary dimensioning of one vessel for the PAV has been completed for one of the BB OB WCLL loops, with a target tritium extraction efficiency of 90% and a tritium inventory of less than one kilogram. Two distinct models of tritium permeation were utilised, as the permeation will be SL or DL depending on the membrane surface conditions, contaminated or uncontaminated. The results demonstrate that, in the event of a polluted membrane, the efficiency, space, and pressure drop requirements imposed by the design may be met by raising the PbLi temperature to increase permeability. On the other hand, with a non-contaminated membrane, the full flow of a WCLL loop may be processed in a single permeator without heating the PbLi and yet meet all limitations.

To assess the performance of the PAV, a mock-up is being produced [69]: it will be tested at ENEA Brasimone under EU DEMO-like working conditions. Moreover, a new set of permeation properties for Nb is being measured to update the current mass properties available in literature. In general, these tests will be utilised to determine the permeator effective operating regime and to validate the associated model.

Chapter 8

Final conclusions and perspectives

This thesis deals with the modelling of LMs in future fission and fusion machines. Due to the versatile properties of LM as coolant (for LMCRs) or as coolant/breeder/carrier (for future fusion reactors) for tritium, a multi-physics approach is needed to correctly model the phenomena involved by its exploitation. In particular, the development of this type of computational codes to be used during the firstly design phases addresses this target by means of fast analyses for the inherent safety of the design (as in the case of FRs). Moreover, some aspects have to be investigated to develop new systems which will be able to increase the reliability and the safety of processes (for instance, as in the EU DEMO reactor for the tritium cycle). To do this, the European framework is currently supporting the research and the development of these tools for both fission and fusion machines, by means of consortium as EUROfusion or FALCON.

The work presented in this thesis has the scope to verify, test and develop tools and new models for the multi-physics assessment of advanced nuclear system based on LMs.

For the fission machines (Section 8.1), the main target is the benchmark of the results calculated by the FRENETIC code on relevant test cases as ALFRED (LFR) and EBR-2 (SFR) with respect to other state-of-the-art tools, as Serpent-2 or SIMMER. Furthermore, to broaden the application domain of FRENETIC when multi-physics simulations are required, a methodology to test the capability of the PH module has to be developed to obtain the needed data from Monte Carlo simulations. Concerning the development of new models, the necessity to study the mixing phenomena due to deformation or accidental conditions in FAs of LFRs with respect to the nominal condition is one of the main activities of the PASCAL project, which is currently supporting the design of the ALFRED reactor. Mixing phenomena of coolant among fuel rods become important when there is a net mass flux due to deformation, therefore a new mathematical model to assess these exchanges has to be formulated. Then, the latter has to be implemented in the EFIALTE code, one of the DOCs suite developed by ENEA Bologna. In this

context, the purpose of the EFIALTE code is the assessment of different scenarios with respect to the ones already treated by the ANTEO+ code, whose application domain is restricted to the nominal or BOL conditions.

Concerning the fusion machines (Section 8.2), the extraction of tritium from the PbLi is the main topic of the discussion. As the tritium is produced (and thus dissolved) inside the LM due to the capture of a neutron by Li-7, the necessity to close the fuel cycle is one of the most important target of the EU DEMOs reactor to guarantee the sustainability of the fusion reaction and to minimise the loss of the radioactive isotope for safety aspects. One of the candidate technology to accomplish these features for the EU DEMO reactor is the PAV, where the tritium can permeate through a metallic membrane when a pressure difference across the latter is established. Since the permeation is strongly affected by the operating (temperature and pressure) and membrane conditions (contaminated or not-contaminated), a new model to assess the total quantity of extracted tritium from the LM has to be derived, encompassing all the possible permeation regimes (SL or DL). The scope of this model is the estimation of the required length to achieve the prescribed extraction efficiency for the extractor, including the surface phenomena together with the mass diffusion inside the metal bulk. Then, the model has to be applied for the sizing and study of extraction performances on a mock-up based on the PAV concept, that is being installed in TRIEX-II in ENEA Brasimone. The validation activity was also foreseen, but due to pandemic COVID-19 situation, it has been postponed beyond the end of this PhD program. The assessment of the mock-up has to be conducted following a multi-physics approach, by means of CFD and FEM analyses of the component, together with the permeation study. As final application, the TERS up to EU DEMO scale has to be carried out, in order to find the best operating conditions for the extractor that are compliant with the foreseen constraints.

8.1 Fission-related activities

The fission-related activities have been carried on with the scope to pursue the verification activities of the FRENETIC code, a multi-physics code that has been being developed in the last years in Politecnico di Torino. FRENETIC is able to fast simulate steady state and transient condition of LMCRs by means of two modules which solve the NE aspects with a multi-group diffusion equations, and TH ones by a 1D+2D approach for the temperature, pressure and velocity distributions. In this way, the code is capable to take into consideration the thermal feedback of the system is proper cross sections libraries temperature-dependent are provided.

Due to the strongly interest of Italy in the development of LFRs technology in the European context by its involving in the joint PASCAL project for supporting the design of the ALFRED reactor, the latter has been analysed with FRENETIC.

To perform the study, a cross section libraries temperature-dependent has been build by means of the Monte Carlo code Serpent-2. The optimisation of the model have been carried on considering different level of modelling in FRENETIC, in order to increase the accordance between the results of the two tools. Results have shown excellent agreement when the external regions of the core are included in the FRENETIC code when the thermal feedback are also included in the transport model to perform the comparison.

With this improved model, the NE module of FRENETIC have been verified with the SIMMER code. The activity has been conducted with the same set of cross sections library in the HZP condition calculated by Serpent-2. The aim of the benchmark was to test the capabilities of FRENETIC to solve the neutronic parameter by multi-group diffusion theory with respect to discrete-ordinate methods used by SIMMER. Results of the 3D analyses have shown good concordance between the two codes, aiming to demonstrate the accuracy of the diffusion model in FRENETIC compared with the SIMMER transport solution.

As stated before, a methodology for the inclusion of thermal energy deposited by photons in FRENETIC when the code works in a coupled scenario NE/PH has been developed. Indeed, in FRENETIC a NE module is available and it uses the same multi-group diffusion equations adopted for neutrons. To test this capability of the code, a complex case on the EBR-2 Sodium-cooled FR has been studied. On the EBR-2 several experimental campaigns were conducted, aiming to demonstrate the effect of thermal feedback on reactivity to passively shutdown the reactor, when a series of unprotected accidents were simulated. The reactor configurations of these tests (SHRT-45R and Shutdown Heat Removal System 17 (SHRT-17)) have been released during a CRP of IAEA. The EBR-2 was very heterogeneous during the SHRT-45R, both for the core configuration and fuel composition. By means of a 3D Monte Carlo simulation with Serpent-2, a set of cross section data have been calculated, studying in particular the effect of the spatial homogenisation to preserve the generation of thermal power. A methodology for the generation of photon data (i.e, attenuation coefficients, the deposited energy per particles, the (n, γ) production) has been developed to retrieve also the thermal power due to KERMA of neutrons and photon. The set of collapsed data have been used in the FRENETIC code, by adding successive levels of detail both in transport and diffusion model. Results have shown the correctness of the methodology for the generation of photon data, as well as the spatial homogenisation. The thermal fission power and the neutron KERMA power is correctly retrieved, whereas for photon the incapability of Serpent-2 to provide the photons multiplicity production has led to an underestimation of photon flux. As a consequence, the related photon power is not well reproduced by FRENETIC. Notwithstanding this, the complex case of the SHRT-45R has been deeply exploited for photon, giving the possibility to pursue the validation of the FRENETIC code in theSHRT-45R transient if a complete set of photon data is provided.

As final activity in the framework of the European project PASCAL, a preliminary design of a DOC for the deformed fuel bundle in LFRs has been assessed. This code, namely EFIALTE, aims to model the SC mixing in accidental conditions (or in EOL condition) when the deformation of fuel rods is concerned. Since one of the foreseen capabilities in the code is to evaluate also the power and temperature distributions inside the bundle, the code purpose is to work in a multi-physics context, together with other DOCs as ANTEO+, TIFONE and TEMIDE. Starting from the integral equations for mass flow, transverse and axial momentum in a pure hydraulic deformed scenario, the general formulation for evaluation of the diversion cross flow has been achieved. To test the possibility to solve the transverse mixing, the undeformed situation has been studied. The so-called CROSSFLOW SCHEME shows promising results: the diversion mass flow rate is correctly retrieved when a proper driver (i.e., a different pressure in the inlet pressure) is provided as boundary condition. Foreseen activities on this tool are foreseen by NEMOgroup in Politecnico di Torino, including the general formulation of deformed geometry and a scheme which is able to calculate the correct inlet pressure, if an outlet pressure at the end of the SCs is imposed.

8.2 Fusion-related activities

This part of thesis is has been devoted to the design of an extractor of tritium from the PbLi, the LM breeder which is foreseen in one of the concepts of the WCLL BB for the future EU DEMO reactor. Several technologies are being investigated, and one of the promising solutions is based on PAV technology.

The first part of the work consists in the development of a new model for the evaluation of the permeated flux from the carrier (the PbLi) by means of an extractor where a pressure drop is established across a metallic membrane. A deeply study has been carried on regards the mass transport properties of PbLi and metals as niobium, identify two regimes of permeation. When the permeation is strongly conditioned by surface effects of the membrane, as the recombination and dissociation, the diffusion in the metal bulk is neglected and the permeation is called SL. On the contrary, when the the surface effects are faster than the diffusion in the bulk of membrane, the permeation is driver by the gradient of concentration, and the operating condition is called DL. The model has been developed starting from previous works, where systems as gas-membrane-vacuum were studied in order to identity the mass flexes due to surface and bulk of the membrane, when a pressure drops is established across the membrane. The physics modelling has been extended to the case of liquid-membrane-vacuum (or counter pressure, if it is present), treating the transport from the LM bulk towards the wet side of the membrane as the source of permeation.

The model has been verified with respect to other DLMs. Indeed, this model

can encompass the two permeation regimes by changing the physical constants as diffusion mass coefficient, recombination constant and solubility constant. Therefore, a parametric analyses on the foreseen mock-up of the extractor have been carried on, to estimate the extraction performances if the geometry is imposed.

The PAV mock-up has been designed starting from the constraints of geometry prescribed in TRIEX-II facility (ENEA Brasimone), where an experimental campaign was foreseen to test the technology with hydrogen. Unfortunately, due to the outbreak of COVID-19 pandemic in the 2020, the tests have been postponed beyond the ending of this PhD. The design of the mock-up has been conducted by a preliminary sizing of the vessel and holed plate where the pipes (the membrane) are located. The assessment have been performed with analytical formulas for thin shell and plates, and then verified with a set of FEM analyses considering the operational and accidental conditions.

A set of CFD analyses have been assessed to study the effects of the mass flow repartition (i.e, the turbulence level in each single pipe) on the extraction efficiency. These results have been parametrically studied to highlight the effects of the temperature, partial pressure and surface condition on the outlet concentration of hydrogen. As final results, the most influencing parameters are the temperature of the system (which affects the surface phenomena of the membrane) and the hydrogen transport from the PbLi to the membrane. Moreover, the presence of impurity in the membrane changes significantly the permeation, leading to lower efficiencies in the SL condition than DL one.

The final application of the developed model has been exploited on the extractor up to EU DEMO scale. By assessing of the most affecting variables on the extraction efficiency, the TERS has been sized to achieve the required extraction efficiency foreseen in EU DEMO. A methodology to design the membrane, the vessel encumbrance and the number of pipes has been developed, if a set of constraints are provided. The sizing have been carried on by changing the operative conditions, in order to find the best solution for the permeation. Indeed, if the permeation is moved towards DL regime, the employed length are shorter than theSL regime. This implies lower pressure drops per unit length, which promotes also the turbulence by higher mass flow rate for single pipe.

As perspectives for this work, the implementation of the model in a system-level tool is foreseen to study the performance of the whole extraction system, encompassing SL and DL permeation condition. Furthermore, the possibility to coat the membrane on the vacuum side to avoid contamination (for instance, the oxidation) are currently understudy, could lead to have higher extraction efficiency since also in SL condition due to lower impact of surface phenomena at low operating temperature.

Bibliography

[1] *GIF*. [Online]. Available: https://www.gen-4.org/gif/ (cit. on p. 2).

[2] IAEA, "Status and Advances in MOX Fuel Technology", Tech. Rep. 415, 2003, p. 179. [Online]. Available: http://www-pub.iaea.org/books/IAEABooks/6562/Status-and-Advances-in-MOX-Fuel-Technology (cit. on p. 2).

[3] G. Grasso, C. Petrovich, D. Mattioli, *et al.*, "The core design of ALFRED, a demonstrator for the European lead-cooled reactors", *Nuclear Engineering and Design*, vol. 278, pp. 287–301, 2014 (cit. on pp. 2, 13).

[4] *PASCAL*. [Online]. Available: https://www.pascalworkspace.eu/ (cit. on p. 2).

[5] R. Bonifetto, S. Dulla, P. Ravetto, L. S. Richard, and R. Zanino, "A full-core coupled neutronic/thermal-hydraulic code for the modeling of lead-cooled nuclear fast reactors", *Nuclear Engineering and Design*, vol. 261, pp. 85–94, Aug. 2013. DOI: 10.1016/J.NUCENGDES.2013.03.030. [Online]. Available: https://www.sciencedirect.com/science/article/pii/S0029549313001726 (cit. on pp. 3, 11).

[6] F. Lodi, G. Grasso, D. Mattioli, and M. Sumini, "ANTEO+: A subchannel code for thermal-hydraulic analysis of liquid metal cooled systems", *Nuclear Engineering and Design*, vol. 301, pp. 128–152, 2016. DOI: 10.1016/j.nucengdes.2016.03.001. [Online]. Available: http://dx.doi.org/10.1016/j.nucengdes.2016.03.001 (cit. on pp. 3, 112, 125).

[7] J. Leppänen, *Development of a new Monte Carlo reactor physics code*. Espoo: VTT Technical Research Centre of Finland, 2007 (cit. on pp. 3, 9).

[8] W. Maschek, A. Rineiski, M. Flad, *et al.*, "The SIMMER safety code system and its validation efforts for fast reactor application", English, in *International Conference on the Physics of Reactors 2008, PHYSOR 08*, ser. International Conference on the Physics of Reactors 2008, PHYSOR 08, Paul Scherrer Institut, 2008, pp. 2370–2378 (cit. on pp. 3, 10, 37).

[9] *EUROfusion*. [Online]. Available: https://www.euro-fusion.org/ (cit. on p. 4).

[10] K. M. McGuire and et al., "Review of deuterium-tritium results from the Tokamak Fusion Test Reactor", *Physics of Plasmas*, vol. 2, no. 6, pp. 2176–2188, 1995. DOI: 10.1063/1.871303 (cit. on pp. 4, 135).

[11] A. M. Bradshaw, T. Hamacher, and U. Fischer, "Is nuclear fusion a sustainable energy form?", *Fusion Engineering and Design*, vol. 86, no. 9-11, pp. 2770–2773, 2011. DOI: 10.1016/j.fusengdes.2010.11.040. [Online]. Available: http://dx.doi.org/10.1016/j.fusengdes.2010.11.040 (cit. on pp. 4, 135).

[12] G. Federici, R. Kemp, D. Ward, *et al.*, "Overview of EU DEMO design and R&D activities", *Fusion Engineering and Design*, vol. 89, no. 7-8, pp. 882–889, 2014. DOI: 10.1016/j.fusengdes.2014.01.070. [Online]. Available: http://dx.doi.org/10.1016/j.fusengdes.2014.01.070 (cit. on p. 4).

[13] A. J. Donné, "The European roadmap towards fusion electricity", *Philosophical Transactions of the Royal Society A: Mathematical, Physical and Engineering Sciences*, vol. 377, no. 2141, 2019. DOI: 10.1098/rsta.2017.0432 (cit. on p. 4).

[14] D. Demange, R. Antunes, O. Borisevich, *et al.*, "Tritium extraction technologies and DEMO requirements", eng, *Fusion engineering and design*, vol. 109-111, pp. 912–916, 2016 (cit. on p. 4).

[15] A. Del Nevo, E. Martelli, P. Agostini, *et al.*, "WCLL breeding blanket design and integration for DEMO 2015: status and perspectives", *Fusion Engineering and Design*, vol. 124, pp. 682–686, 2017. DOI: 10.1016/j.fusengdes.2017.03.020. [Online]. Available: http://dx.doi.org/10.1016/j.fusengdes.2017.03.020 (cit. on pp. 4, 135).

[16] I. Ricapito, A. Ciampichetti, G. Benamati, and M. Zucchetti, "Tritium extraction systems for the European HCLL/HCPB TBMs", *Fusion Science and Technology*, vol. 54, no. 1, pp. 107–112, 2008. DOI: 10.13182/FST08-A1775 (cit. on p. 5).

[17] M. Utili, A. Aiello, L. Laffi, A. Malavasi, and I. Ricapito, "Investigation on efficiency of gas liquid contactor used as tritium extraction unit for HCLL-TBM Pb-16Li loop", *Fusion Engineering and Design*, vol. 109-111, pp. 1–6, 2016. DOI: 10.1016/j.fusengdes.2016.03.067. [Online]. Available: http://dx.doi.org/10.1016/j.fusengdes.2016.03.067 (cit. on p. 5).

[18] R. Zanino, R. Bonifetto, A. Ciampichetti, I. Di Piazza, L. Savoldi Richard, and M. Tarantino, "First validation of the FRENETIC code thermal-hydraulic model against the ENEA integral circulation experiment", *Transactions of the American Nuclear Society*, vol. 107, no. 6, pp. 1395–1398, 2012 (cit. on pp. 9, 11).

[19] G. F. Nallo, N. Abrate, S. Dulla, P. Ravetto, and D. Valerio, "Neutronic benchmark of the FRENETIC code for the multiphysics analysis of lead fast reactors", *The European Physical Journal Plus*, vol. 135, p. 238, 2020. DOI: 10.1140/epjp/s13360-020-00171-8. [Online]. Available: https://doi.org/10.1140/epjp/s13360-020-00171-8 (cit. on pp. 10, 16, 31, 38, 40).

[20] M. Massone, G. F. Nallo, D. Valerio, S. Dulla, and P. Ravetto, "Code-to-code SIMMER / FRENETIC comparison for the neutronic simulation of lead-cooled fast reactors", *submitted to Annals of Nuclear Energy*, 2021 (cit. on pp. 10, 38).

[21] D. Caron, R. Bonifetto, S. Dulla, *et al.*, "Full-core coupled neutronic/thermal-hydraulic modelling of the EBR-II SHRT-45R transient", *International Journal of Energy Research*, vol. 42, no. 1, pp. 134–150, Jan. 2018. DOI: 10.1002/er.3571. [Online]. Available: http://doi.wiley.com/10.1002/er.3571 (cit. on p. 11).

[22] D. Caron, S. Dulla, P. Ravetto, L. Savoldi, and R. Zanino, "Models and methods for the representation of decay and photon heat in spatial kinetics calculations", in *Proceedings of the International Conference PHYSOR 2016*, Sun Valley, ID, May 2016, pp. 2416–2425 (cit. on pp. 11, 47).

[23] L. Savoldi Richard, F. Casella, B. Fiori, and R. Zanino, "The 4C code forthe cryogenic circuit conductor and coil modeling in ITER", *Cryogenics*, vol. 50, pp. 167–176, 2010 (cit. on p. 11).

[24] A. Alemberti, L. Mansani, G. Grasso, *et al.*, "The European Lead Fast Reactor Strategy and the Roadmap for the Demonstrator ALFRED", in *IAEA Conference FR13*, 2013, pp. 1–10 (cit. on p. 13).

[25] J. Leppänen, M. Pusa, and E. Fridman, "Overview of methodology for spatial homogenization in the Serpent 2 Monte Carlo code", *Annals of Nuclear Energy*, vol. 96, pp. 126–136, 2016. DOI: 10.1016/j.anucene.2016.06.007 (cit. on p. 13).

[26] D. Caron, "Neutronics methods for the multiphysics analysis of nuclear fission systems", Ph.D. dissertation, Politecnico di Torino, 2017 (cit. on pp. 19, 90).

[27] D. Caron, R. Bonifetto, S. Dulla, *et al.*, "Full-core coupled neutronic/thermal-hydraulic modelling of the EBR-II SHRT-45R transient", *International Journal of Energy Research*, vol. 42, no. 1, pp. 134–150, Jan. 2016 (cit. on pp. 36, 48).

[28] S. Kondo, H. Yamano, and T. Suzuki, *SIMMER-III: A computer program for LMFR core disruptive accident analysis. Version 2. H model summary and program description*, 2000. [Online]. Available: https://inis.iaea.org/search/search.aspx?orig_q=RN:33004688 (cit. on p. 37).

[29] M. Massone, F. Gabrielli, and A. Rineiski, "A genetic algorithm for multi-group energy structure search", *Annals of Nuclear Energy*, vol. 105, pp. 369–387, Jul. 2017. DOI: 10.1016/J.ANUCENE.2017.03.022 (cit. on pp. 37, 45).

[30] D. Valerio, N. Abrate, G. F. Nallo, S. Dulla, and P. Ravetto, "Coupled Modelling of the EBR-II SHRT-45R Including Photon Heat Deposition", *Proceedings of the PHYSOR 2020, Cambridge, United Kingdom*, 2020 (cit. on p. 47).

[31] C. Batra, V. Kriventsev, and S. Monti, *IAEA's Coordinated Research Project on EBR-II Shutdown Heat Removal Tests: An Overview*. [Online]. Available: https://inis.iaea.org/search/search.aspx?orig_q=RN:49085715 (cit. on p. 48).

[32] T. Fei, A. Mohamed, and K. T. Kim, "Neutronics Benchmark Specifications for EBR-II Shutdown Heat Removal Test SHRT-45R – Revision 1", Nuclear Engineering Division, Argonne National Laboratory, Tech. Rep., 2013, pp. 1–56 (cit. on pp. 52–55, 60).

[33] V. Sobolev, "Database of thermophysical properties of liquid metal coolants for GEN-IV", Tech. Rep. 12, 2010, pp. 3496–3502. [Online]. Available: http://www.iaea.org/inis/collection/NCLCollectionStore/_Public/43/095/43095088.pdf (cit. on p. 67).

[34] R. E. Macfarlane, C. Authors, D. W. Muir, *et al.*, "The NJOY Nuclear Data Processing System, Version 2016", Tech. Rep., 2018 (cit. on p. 73).

[35] D. Caron, S. Dulla, and P. Ravetto, "New aspects in the implementation of the quasi-static method for the solution of neutron diffusion problems in the framework of a nodal method", *Annals of Nuclear Energy*, vol. 87, pp. 34–48, 2016, Special Issue of The 3rd International Conference on Physics and Technology of Reactors and Application. DOI: https://doi.org/10.1016/j.anucene.2015.02.035. [Online]. Available: https://www.sciencedirect.com/science/article/pii/S0306454915001127 (cit. on pp. 76, 78).

[36] T. Kaltiaisenaho, "Photonuclear reactions in serpent 2 monte carlo code", in *Proceedings of the ANS International Conference M&C2019*, Portland, OR, Aug. 2019 (cit. on p. 82).

[37] M. Bassani, F. Martelli, G. Zaccanti, and D. Contini, "Independence of the diffusion coefficient from absorption: experimental and numerical evidence", *Opt. Lett.*, vol. 22, no. 12, pp. 853–855, 1997. DOI: 10.1364/OL.22.000853. [Online]. Available: http://opg.optica.org/ol/abstract.cfm?URI=ol-22-12-853 (cit. on p. 84).

[38] M. Herman and A. Trkov, "ENDF-6 Formats Manual", Tech. Rep., 2009, p. 392. [Online]. Available: http://scholar.google.com/scholar?hl=en&btnG=Search&q=intitle:ENDF-6+Formats+Manual.+Data+Formats+and+Procedures+for+the+Evaluated+Nuclear+Data+Files+ENDF/B-VI+and+ENDF/B-VII#0 (cit. on p. 87).

[39] R. Tuominen, V. Valtavirta, and J. Leppänen, "New energy deposition treatment in the Serpent 2 Monte Carlo transport code", *Annals of Nuclear Energy*, vol. 129, pp. 224–232, 2019 (cit. on p. 88).

[40] D. Caron, S. Dulla, P. Ravetto, L. Savoldi, and R. Zanino, "Models and methods for the representation of decay and photon heat in spatial kinetics calculations", in *Proceedings of PHYSOR 2016*, USA, 2016, pp. 2416–2425 (cit. on p. 88).

[41] P. R. H. Blasius, "Das aehnlichkeitsgesetz bei reibungsvorgangen", *Forschungsheft*, vol. Flüssigkei, 1913 (cit. on pp. 125, 166, 168, 188).

[42] O. S. Eiff and M. F. Lightstone, "On the modelling of single-phase turbulent energy transport in subchannels", *Proceedings - Annual Conference, Canadian Nuclear Association*, vol. 2, 1997 (cit. on p. 125).

[43] F. A. Hernández, P. Pereslavtsev, G. Zhou, *et al.*, "Consolidated design of the HCPB Breeding Blanket for the pre-Conceptual Design Phase of the EU DEMO and harmonization with the ITER HCPB TBM program", *Fusion Engineering and Design*, vol. 157, p. 111 614, 2020. DOI: 10.1016/j.fusengdes.2020.111614. [Online]. Available: https://doi.org/10.1016/j.fusengdes.2020.111614 (cit. on p. 135).

[44] M. Utili, A. Tincani, L. Candido, *et al.*, "Tritium Extraction from HCLL/WCLL/DCLL PbLi BBs of DEMO and HCLL TBS of ITER", *IEEE Transactions on Plasma Science*, vol. 47, no. 2, pp. 1464–1471, 2019. DOI: 10.1109/TPS.2018.2886409. [Online]. Available: https://doi.org/10.1109/TPS.2018.2886409 (cit. on p. 135).

[45] R. Bonifetto, M. Utili, D. Valerio, and R. Zanino, "Conceptual design of a PAV-based tritium extractor for the WCLL breeding blanket of the EU DEMO: Effects of surface-limited vs. diffusion-limited modeling", *Fusion Engineering and Design*, vol. 167, p. 112 363, 2021. DOI: https://doi.org/10.1016/j.fusengdes.2021.112363. [Online]. Available: https://www.sciencedirect.com/science/article/pii/S0920379621001393 (cit. on pp. 135, 138, 161).

[46] S. Tosti, A. Pozio, L. Farina, M. Incelli, A. Santucci, and D. Alique, "Membrane gas-liquid contactor for tritium extraction from Pb-Li alloys", *Fusion Engineering and Design*, vol. 158, p. 111 737, 2020. DOI: https://doi.org/10.1016/j.fusengdes.2020.111737. [Online]. Available: https://www.

sciencedirect.com/science/article/pii/%20S0920379620302854 (cit. on p. 135).

[47] M. A. Pick and K. Sonnenberg, "A model for atomic hydrogen-metal interactions-application to recycling, recombination and permeation", *J. Nucl. Mater*, vol. 131, pp. 208–220, 1985 (cit. on pp. 135, 136, 140–144, 146).

[48] V. D'Auria, S. Dulla, P. Ravetto, L. Savoldi, M. Utili, and R. Zanino, "Tritium extraction from lithium-lead in the EU DEMO blanket using permeator against vacuum", *Fusion Science and Technology*, vol. 71, no. 4, pp. 537–543, 2017. DOI: 10.1080/15361055.2017.1291252. [Online]. Available: https://doi.org/10.1080/15361055.2017.1291252 (cit. on pp. 136, 137, 141, 145).

[49] D. Masuyama, T. Oda, S. Fukada, and S. Tanaka, "Chemical state and diffusion behavior of hydrogen isotopes in liquid lithium-lead", *Chemical Physics Letters*, vol. 483, no. 4-6, pp. 214–218, 2009. DOI: 10.1016/j.cplett.2009.10.079. [Online]. Available: http://dx.doi.org/10.1016/j.cplett.2009.10.079 (cit. on pp. 136, 146).

[50] Y. Maeda, Y. Edao, S. Yamaguchi, and S. Fukada, "Solubility, diffusivtty, and isotopic exchange rate of hydrogen isotopes in Li-Pb", *Fusion Science and Technology*, vol. 54, no. 1, pp. 131–134, 2008. DOI: 10.13182/FST54-131 (cit. on pp. 136, 173).

[51] V. D'Auria, S. Dulla, P. Ravetto, L. Savoldi, M. Utili, and R. Zanino, "Design of a permeator-against-vacuum mock-up for the tritium extraction from PbLi at low speed", *Fusion Engineering and Design*, vol. 121, p. 198.203, Jul. 2017. DOI: http://dx.doi.org/10.1016/j.fusengdes.2017.07.006 (cit. on pp. 136, 138–140).

[52] P. W. Humrickhouse and B. J. Merrill, "Vacuum permeator analysis for extraction of tritium from DCLL blankets", *Fusion Science and Technology*, vol. 68, no. 2, pp. 295–302, 2015. DOI: 10.13182/FST14-941 (cit. on pp. 136, 145, 152–155, 161).

[53] G. Federici, C. Bachmann, L. Barucca, *et al.*, "Demo design activity in europe: Progress and updates", *Fusion Engineering and Design*, vol. 136, pp. 729–741, 2018, Special Issue: Proceedings of the 13th International Symposium on Fusion Nuclear Technology (ISFNT-13). DOI: https://doi.org/10.1016/j.fusengdes.2018.04.001. [Online]. Available: https://www.sciencedirect.com/science/article/pii/S0920379618302898 (cit. on p. 136).

[54] E. A. Denisov, M. V. Kompaniets, T. N. Kompaniets, and V. I. Spitsyn, "Surface-limited permeation regime in the study of hydrogen interactions with metals", *Measurement: Journal of the International Measurement Confederation*, vol. 117, no. August 2017, pp. 258–265, 2018. DOI: 10.1016/j.measurement.2017.12.018. [Online]. Available: https://doi.org/10.1016/j.measurement.2017.12.018 (cit. on p. 138).

[55] I. Ali-Khan, K. J. Dietz, F. G. Waelbroeck, and P. Wienhold, "The rate of hydrogen release out of clean metallic surfaces", *Journal of Nuclear Materials*, vol. 76-77, no. C, pp. 337–343, 1978. DOI: 10.1016/0022-3115(78)90167-8 (cit. on pp. 138, 139, 144, 146).

[56] S. A. Steward, "Review of Hydrogen Isotope Permeability Through Materials", Lawrence Livermore National Laboratory, Tech. Rep., 1983. DOI: 10.2172/5277693. [Online]. Available: http://www.osti.gov/servlets/purl/5277693/ (cit. on pp. 138, 139, 175, 177).

[57] R. Causey, R. Karnesky, and C. San Marchi, "Tritium barriers and tritium diffusion in fusion reactors", *Comprehensive Nuclear Materials*, vol. 4, pp. 511–549, Dec. 2012. DOI: 10.1016/B978-0-08-056033-5.00116-6 (cit. on p. 138).

[58] A. Sushil and F. Sandun, "Hydrogen membrane separation techniques", *Industrial and Engineering Chemistry Research*, vol. 45, no. 3, pp. 875–881, 2006. DOI: 10.1021/ie0506441 (cit. on p. 139).

[59] M. I. Baskes, W. Bauer, and K. L. Wilson, "Tritium permeation in fusion reactor first walls", *Journal of Nuclear Materials*, vol. 112, no. 111&112, pp. 663–666, 1982 (cit. on p. 139).

[60] E. Veleckis and R. K. Edward, "Thermodynamic Properties in the Systems V-H, Nb-H, and Ta-H", *Journal of Physical Chemistry*, vol. 73, no. 3, 1969 (cit. on p. 139).

[61] P. L. Andrew and A. A. Haasz, "Models for hydrogen permeation in metals", *Journal of Applied Physics*, vol. 72, no. 7, pp. 2749–2757, 1992. DOI: 10.1063/1.351526 (cit. on p. 144).

[62] P. Harriot and R. M. Hamilton, "Solid-liquid mass transfer in turbulent pipe flow", *Chem. Eng. Sci.*, vol. 20, no. 12, pp. 1073–1078, Jul. 1965 (cit. on p. 145).

[63] E. Mas de les Valls, L. A. Sedano, L. Batet, *et al.*, "Lead-lithium eutectic material database for nuclear fusion technology", *Journal of Nuclear Materials*, vol. 376, no. 3, pp. 353–357, 2008. DOI: 10.1016/j.jnucmat.2008.02.016 (cit. on p. 145).

[64] W. Oberkampf and C. Roy, *Verification and Validation in Scientific Computing*. Jan. 2010. DOI: 10.1017/CBO9780511760396 (cit. on p. 149).

[65] P. J. Roache, *Verification and validation in computational science and engineering*. Hermosa Albuquerque, NM, 1998, vol. 895 (cit. on p. 149).

[66] A. I. of Aeronautics and Astronautics, "Guide for the verification and validation of computational fluid dynamics simulations", *American Institute of Aeronautics and Astronautics*, vol. 1998, 1998 (cit. on p. 149).

[67] W. L. Oberkampf, F. G. Blottner, and D. P. Aeschliman, "Methodology for computational fluid dynamics code verification/validation", Jul. 1995. [Online]. Available: https://www.osti.gov/biblio/90701 (cit. on p. 149).

[68] W. L. Oberkampf and F. G. Blottner, "Issues in computational fluid dynamics code verification and validation", *AIAA Journal*, vol. 36, pp. 687–695, 1998 (cit. on p. 149).

[69] F. Papa, M. Utili, A. Venturini, *et al.*, "Engineering design of a Permeator Against Vacuum mock-up with niobium membrane", *presented at SOFT2020*, Sep. 2020 (cit. on pp. 159, 177, 194).

[70] V. D'Auria, S. Dulla, P. Ravetto, L. Savoldi, M. Utili, and R. Zanino, "Design of a Permeator-Against-Vacuum mock-Up for the tritium extraction from PbLi at low speed", *Fusion Engineering and Design*, vol. 121, pp. 198–203, 2017. DOI: 10.1016/j.fusengdes.2017.07.006 (cit. on pp. 161, 164).

[71] G. Lucefin, "Chemical composition and Mechanical properties of 10CrMo9-10", Tech. Rep., 2005. [Online]. Available: https://www.lucefin.com/wp-content/files_mf/0410crmo91023.pdf (cit. on p. 163).

[72] *Gruppo Lucefin*. [Online]. Available: www.lucefin.com/wp-content/files_mf/10crmo910.pdf. (cit. on p. 163).

[73] SIEMENTS, *STAR-CCM+* (cit. on p. 167).

[74] J. Hart, J. Ellenberger, and P. J. Hamersma, "Single- and two-phase flow through helically coiled tubes", *Chemical Engineering Science*, vol. 43, no. 4, pp. 775–783, 1988. DOI: 10.1016/0009-2509(88)80072-1 (cit. on p. 168).

[75] COMSOL, *COMSOL 5.1 Multiphysics* (cit. on p. 170).

[76] E. Mas de les Valls, L. A. Sedano, L. Batet, *et al.*, "Lead-lithium eutectic material database for nuclear fusion technology", *Journal of Nuclear Materials*, vol. 376, no. 3, pp. 353–357, 2008. DOI: 10.1016/j.jnucmat.2008.02.016 (cit. on p. 173).

[77] P. Harriott and R. M. Hamilton, "Solid-liquid mass transfer in turbulent pipe flow", *Chemical Engineering Science*, vol. 20, no. 12, pp. 1073–1078, 1965. DOI: 10.1016/0009-2509(65)80110-5 (cit. on pp. 175, 188).

[78] M. Malo, B. Garcinuno, and D. Rapisarda, "Experimental refutation of the deuterium permeability in vanadium, niobium and tantalum", *Fusion Engineering and Design*, vol. 146, no. A, SI, 224–227, September 2019, 30th Symposium on Fusion Technology (SOFT), Messina, Italy, SEP 16-21, 2018. DOI: {10.1016/j.fusengdes.2018.12.025} (cit. on p. 177).

[79] M. A. Pick and K. Sonnenberg, "A model for atomic hydrogen-metal interactions-application to recycling, recombination and permeation", *Journal of Nuclear Materials*, vol. 131, pp. 208–220, 1985 (cit. on p. 177).

[80] D. Valerio, R. Bonifetto, M. Utili, and R. Zanino, "Effects of surface-limited vs. diffusion-limited modeling on the conceptual design of a PAV-based TERS for the WCLL blanket of the EU DEMO", *presented at SOFT2020*, Sep. 2020 (cit. on p. 183).

[81] B. Garcinuno, D. Rapisarda, R. Antunes, *et al.*, "The tritium extraction and removal system for the DCLL-DEMO fusion reactor", *Nuclear Fusion*, vol. 58, no. 9, 2018. DOI: 10.1088/1741-4326/aacb89 (cit. on p. 184).

[82] F. Cismondi, G. A. Spagnuolo, L. V. Boccaccini, *et al.*, "Progress of the conceptual design of the European DEMO breeding blanket, tritium extraction and coolant purification systems", *Fusion Engineering and Design*, vol. 157, no. September 2019, p. 111 640, 2020. DOI: 10.1016/j.fusengdes.2020.111640. [Online]. Available: https://doi.org/10.1016/j.fusengdes.2020.111640 (cit. on p. 187).

[83] G. LDT. "Goodfellow: Supplier of materials for research and development". (), [Online]. Available: https://www.goodfellow.com (visited on 04/01/2019) (cit. on p. 188).

This Ph.D. thesis has been typeset by means of the TEX-system facilities. The typesetting engine was pdfLATEX. The document class was `toptesi`, by Claudio Beccari, with option `tipotesi=scudo`. This class is available in every up-to-date and complete TEX-system installation.